NASA CONTRACTOR REPORT

NASA CR-184253

RESEARCH REPORTS - 1991 NASA/ASEE SUMMER FACULTY
FELLOWSHIP PROGRAM

The University of Alabama in Huntsville
Huntsville, Alabama
and
The University of Alabama
Tuscaloosa, Alabama

October 1991

Final Report

Prepared for
NASA, Geo. C. Marshall Space Flight Center
Marshall Space Flight Center, Alabama   35812

RESEARCH REPORTS

1991 NASA/ASEE SUMMER FACULTY FELLOWSHIP PROGRAM

George C. Marshall Space Flight Center

The University of Alabama in Huntsville

and

The University of Alabama

EDITORS:

Dr. Gerald R. Karr
Chairman of Mechanical Engineering
The University of Alabama in Huntsville

Dr. Charles R. Chappell
Associate Director for Science
Marshall Space Flight Center

Dr. Frank Six
University Affairs Officer
Marshall Space Flight Center

Dr. L. Michael Freeman
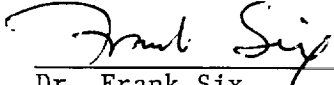Associate Professor of Aerospace Engineering
The University of Alabama

NASA CR - 184253

REPORT DOCUMENTATION PAGE

Public reporting burden for this collection of information is estimated to average 1 hour per response, including the time for reviewing instructions, searching existing data sources, gathering and maintaining the data needed, and completing and reviewing the collection of information. Send comments regarding this burden estimate or any other aspect of this collection of information, including suggestions for reducing this burden, to Washington Headquarters Services, Directorate for Information Operations and Reports, 1215 Jefferson Davis Highway, Suite 1204, Arlington, VA 22202-4302, and to the Office of Management and Budget, Paperwork Reduction Project (0704-0188), Washington, DC 20503.

1. AGENCY USE ONLY (Leave blank)	2. REPORT DATE October 1991	3. REPORT TYPE AND DATES COVERED Contractor Report

4. TITLE AND SUBTITLE
Research Reports - 1991 NASA/ASEE Summer
Faculty Fellowship Program

5. FUNDING NUMBERS
G: NGT-001-008-021

6. AUTHOR(S)
G. Karr, R. Chappell, F. Six, M. Freeman, Editors

7. PERFORMING ORGANIZATION NAME(S) AND ADDRESS(ES)
The University of Alabama in Huntsville and
The University of Alabama, Tuscaloosa, Alabama

8. PERFORMING ORGANIZATION REPORT NUMBER

9. SPONSORING/MONITORING AGENCY NAME(S) AND ADDRESS(ES)
National Aeronautics and Space Administration
Washington, DC 20546

10. SPONSORING/MONITORING AGENCY REPORT NUMBER
NASA CR-184253

11. SUPPLEMENTARY NOTES

12a. DISTRIBUTION/AVAILABILITY STATEMENT
Unclassified/Unlimited

Dr. Frank Six   11-7-91
                       Date
University Affairs Officer

12b. DISTRIBUTION CODE

13. ABSTRACT (Maximum 200 words)

For the 27th consecutive year, a NASA/ASEE Summer Faculty Fellowship Program was conducted at the Marshall Space Flight Center (MSFC). The program was conducted by The University of Alabama in Huntsville and MSFC during the period June 3, 1991 through August 9, 1991. Operated under the auspices of the American Society for Engineering Education, the MSFC program, as well as those at other NASA centers was sponsored by the Office of Educational Affairs, NASA Headquarters, Washington, D.C. The basic objectives of the programs, which are in the 28th year of operation nationally, are (1) to further the professional knowledge of qualified engineering and science faculty members; (2) to stimulate an exchange of ideas between participants and NASA; (3) to enrich and refresh the research and teaching activities of the participants' institutions; and (4) to contribute to the research objectives of the NASA centers.
The Faculty Fellows spent 10 weeks at MSFC engaged in a research project compatible with their interests and background and worked in collaboration with a NASA/MSFC colleague. This document is a compilation of their research reports for summer 1991. Further information can be obtained by contacting any of the editors.

14. SUBJECT TERMS
Advanced projects; information and electronic systems; materials and processes; propulsion; space science; structures and dynamics; mission operations; public affairs

15. NUMBER OF PAGES
266

16. PRICE CODE
NTIS

17. SECURITY CLASSIFICATION OF REPORT	18. SECURITY CLASSIFICATION OF THIS PAGE	19. SECURITY CLASSIFICATION OF ABSTRACT	20. LIMITATION OF ABSTRACT
Unclassified	Unclassified	Unclassified	

TABLE OF CONTENTS

K. Frederick, Jr., Robert A.
    The University of Alabama in Huntsville
    "Experimental Investigation of a Solid Rocket Combustion
    Simulator"

L. Gambrell, Jr., Samuel C.
    The University of Alabama
    "Use of Photostress Techniques to Characterize the
    Mechanical Behavior of Weldments"

M. Goss, Ernest P.
    University of Southern Mississippi
    "Recommendations for an Executive Information System
    (EIS) for the NASA Accounting and Financial Information
    System (NAFIS)"

N. Han, Samuel S.
    Tennessee Technological University
    "Ignition Transient Analysis of Solid Rocket Motor"

O. Hassan, Razi A.
    Alabama A&M University
    "Failure Analysis of the Lithium Battery: A Study of the
    Header Deposit on the Cell Top and Diffusion Within the
    Electrode Glass Seal Using Nuclear Microanalysis and
    FFTIR Spectroscopy"

P. Helmicki, Arthur J.
    University of Cincinnati
    "On the Development of System-Theoretic Tools for the
    Design of Integrated Health Monitoring and Controls for
    Rocket Propulsion Systems"

Q. Hodel, A. Scottedward
    Auburn University
    "Numerical Methods for the Analysis of Sampled-Data
    Systems and for the Computation of System Zeros"

R. Johnson, Jacqueline U.
    Alabama A&M University
    "Biological   Patterns: Novel   Indicators   for
    Pharmacological Assays"

S. Karimi, Majid
    Alabama A&M University
    "Disordering and H-embrittlement of Pb(110)* Surface
    Using Embedded Atom Method and Molecular Dynamics"

T. Lawrence, Stella
    Bronx Community College
    "Development of a Calibrated Software Reliability Model
    for Flight and Supporting Ground Software for Avionic
    Systems"

FF. Palazzolo, Alan B.
     Texas A&M University
     "Linearized Force Representations for Turbopump Liquid
     Annular Seals"

GG. Pangia, Michael J.
     LaGrange College
     "A Theoretical Study of the Steady State of a Space
     Plasma"

HH. Peterson, Lennart R.
     University of Florida
     "Studies of the Charging of a Thin Dust Layer in a
     Plasma"

II. Pierson, William E.
     West Virginia Institute of Technology
     "SEDS1 Mission Software Verification Using a Simulator"

JJ. Ray, Paul S.
     The University of Alabama
     "Emergency Egress Requirements for Space Station Freedom"

KK. Richardson, James A.
     The University of Alabama
     "Using Probabilistic Analysis to Assess the Reliability
     of Predicted SRB Aft-Skirt Stresses"

LL. Richie, James E.
     Marquette University
     "Space Station Internal Propagation"

MM. Rosmait, Russell L.
     Pittsburg State University
     "Space System Production Cost Benefits from Contemporary
     Philosophies in Management and Manufacturing"

NN. Sheldon, John W.
     Florida International University
     "High Voltage Plasma Sheath Analysis Related to TSS-1"

OO. Shen, Hayley H.
     Clarkson University
     "Group Evaporation"

PP. Shiva, Sajjan G.
     The University of Alabama in Huntsville
     "Nickel Hydrogen Battery Expert System"

QQ. Shyy, Wei
     University of Florida
     "Development of a Pressure Based Multigrid Solution
     Method for Complex Fluid Flows"

RR. Simmons, David R.
     Louisiana College
     "A High-Fidelity N-Body Ephemeris Generator for
     Satellites in Earth Orbit"

SS. Slattery, Kerry T.
     Washington University in St. Louis
     "A Statistical Model of Carbon/Carbon Composite Failure"

TT. Solakiewicz, Richard
     Chicago State University
     "Transport of Photons Produced by Lightning in Clouds"

UU. Taneja, Vidya S.
     Western Illinois University
     "Reliability Growth Models for NASA Applications"

VV. Walsh, Daniel W.
     Cal-Poly State University, SLO
     "Characterization of the Corrosion Resistance of
     Biologically Active Solutions - The Effects of Anodizing
     and Welding"

WW. Warren, Charles W.
     The University of Alabama
     "Automation of Cutting and Drilling of Composite
     Components"

XX. Watt, George W.
     Utah State University
     "HP9-4-.30 Weld Properties and Microstructure"

YY. Wikstrom, Carl V.
     University of Arkansas
     "Computerized Reduction of Elementary Reaction Sets for
     Combustion Modeling"

ZZ. Woodbury, Keith A.
     The University of Alabama
     "Assessment of the NASA Code FDNS2D for Computation of
     Film Cooling Effectiveness"

1991

NASA/ ASEE SUMMER FACULTY FELLOWSHIP PROGRAM

MARSHALL SPACE FLIGHT CENTER
THE UNIVERSITY OF ALABAMA

HEAT SINK EFFECTS IN
VARIABLE POLARITY PLASMA ARC WELDING

Prepared By:	Amanie N. Abdelmessih, Ph.D.
Academic Rank:	Assistant Professor
Institution:	Northrop University Mechanical and Aeronautical Engineering Department

NASA/ MSFC

Office:	Materials and Processes
Division:	Process Engineering
Branch:	Metals Processes
MSFC Colleague:	Arthur C. Nunes, Jr., Ph.D.
Contract No.:	NGT-01-008-021 The University of Alabama

A

INTRODUCTION

The space shuttle external tank is fabricated by the variable polarity plasma arc (VPPA) welding process. In VPPA welding a noble gas, usually argon, is directed through an arc to emerge from the torch as a hot plasma jet. This jet is surrounded by a shielding gas, usually helium, to protect the weld from contamination with air. The high velocity, hot plasma jet completely penetrates the workpiece (resembling a line heat source) when operated in the "keyhole" mode. The metal melts on touching the side of the jet, as the torch travels in the perpendicular direction to the direction of the jet, and melted metal moves around the plasma jet in the keyhole forming a puddle which solidifies behind the jet.

Heat sink effects are observed when there are irregularities in the workpiece configuration especially if these irregularities are close to the weld bead. These heat sinks affect the geometry of the weld bead, i.e. in extreme cases they could cause defects such as incomplete fusion. Also, different fixtures seem to have varying heat sink effects.

Steranka (2,3) has worked on heat sink effects in VPPA welding, but he only experimented on one configuration where the heat sinks were attached externally to the workpiece and developed a complicated model.

The objective of this research is to study the effect of irregularities in workpiece configuration and fixture differences (heat sink effects) on the weld bead geometry with the ultimate objective to compensate for the heat sink effects and achieve a perfect weld. Experiments were performed on different workpiece geometries and compared to approximate models.

MODELS

Nunes (1) has introduced an approximate model to express the diameter d of the weld puddle, i.e. the width of the weld bead:

$$d = 4.492 \frac{\alpha}{V} e^{\frac{-2\pi k w (Tm - To)}{\eta P}} \qquad [1]$$

where α = thermal diffusivity of the workpiece metal
   V = velocity of welding torch
   k = thermal conductivity of the workpiece metal
   w = thickness of the workpiece
   Tm = melting temperature of the weld piece metal
   To = ambient temperature of the workpiece
   ηP = fraction of power absorbed by the workpiece

Equation [1] is applicable to an infinite adiabatic plate, i.e. it ignores the heat losses from the workpiece due to radiation and convection to the air and the heat losses due to conduction through the fixture and grounding connections.

From equation [1] changes in the weld diameter due t · ambient temperature changes ΔTo (caused by heat sinks) can be cal·ulated as follows:

$$\frac{\Delta d}{d} = e^{\frac{2\pi k w \Delta To}{\eta P}} - 1 \qquad [2]$$

EXPERIMENTS

Six, 24 in. long, aluminum 2219 T87 plates were prepared for welding. Three plates were flat, 0.25 in. thick, with widths 6, 8, and 12 in., respectively. The remaining three plates, 24 in. by 8 in., were milled down according to desired shapes, as shown in Figure 1, from 0.75 in. to 0.25 in. as follows:

Plate with step: The step, 0.5 in. thicker than the rest of the plate, had a length of 12 in. leaving 6 in. at the start and end of the plate. The width of the step extended from the edges of the plate to 0.25 in. from the longitudinal center of the plate, thus leaving a 0.5 in. gap at the center.

Plate with ridges: Three ridges, 0.5 in. thicker than the rest of the plate, extended through the width of the plate except for 0.5 in. gap at the center. One ridge 0.5 in. wide was located at the middle of the plate (centered 12 in. from the start), the other two (1.5 in. wide started 5 in. from the bottom and top edges of the plate.

Fig. 1: Configuration of heat sinks

Plate with protuberances: As in the previous two cases this plate was milled down from 0.75 in. to 0.25 in. leaving four square protuberances. The first protuberance is 2 by 2 in., and starts 5 in. from the bottom of the plate and 0.25 in. to the right of the longitudinal center line. The second, third and fourth protuberances, each starts 3 in. after the previous one ends. The second (2 x 2 in.) and the third (1 x 1 in.) protuberances are located 1 in. to the left of the center line, while the fourth protuberance (1 x 1 in.) is 0.25 in. to the right of the center line and 4 in. before the top of the plate.

One pass, bead on plate welds were performed on all six plates, without wire feed. The plates were welded vertically starting at the longitudinal center, 1 in. above the bottom edge of the plate, with the torch located 3/8 in. away from the flat side of the plate. All welding conditions were kept the same for the six plates, e.g. the weld length was 22.22 in., the torch velocity 11 in./min. and the power was set to produce 4185 W with fluctuations on the order of ±0.2 kW.
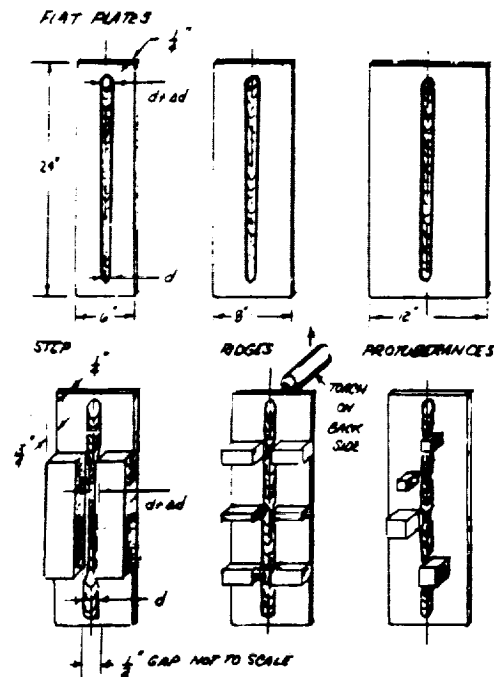
A-2

In crder to minimize heat losses that would mask the effect of plate size the sides of the plates were insulated with Acculam (high pressure phenolic laminate) except for 4 in. along the center, which were not insulated to avoid interference with welding. This eliminated heat sink effects from the fixture, and necessitated joining the power supply coupling and grounding lines to the bottom of the plates.

RESULTS AND DISCUSSION

The crown and root diameters of the welds were measured with a vernier caliper at intervals of 0.38 in. The standard deviation in measurement was almost 0.02 in. compared to diameters less than 0.3 in. This high standard deviation arose from human error in measuring the diameters due to illumination and reflection of the metal, to avoid this problem representative samples were cut and macroscopically treated then measurements of the weld were taken with a microscope, a summary of these measurements is given in table 1.

TABLE I: Microscopic Weld Bead Dimensions.

TIME min.sec	POSITION in.	ARC POWER kW	CROWN DIAMETER in.	ROOT DIAMETER in.	AVERAGE DIAMETER in.	WELD HEIGHT in.	PLATE THICKNESS in.
TWELVE	INCH	WIDE	FLAT	PLATE			
0.26	3.47	4.10	0.3202	0.2906	0.3054	0.2877	0.2467
1.50	18.90	4.17	0.3191	0.2522	0.2857	0.2910	0.2502
EIGHT	INCH	WIDE	FLAT	PLATE			
0.24	3.10	4.11	0.3121	0.2392	0.2757	0.2369	0.2456
1.48	18.52	4.14	0.3187	0.2430	0.2809	0.2812	0.2458
SIX	INCH	WIDE	FLAT	PLATE			
0.24	3.10	4.21	0.3148	0.2702	0.2925	0.2935	0.2490
1.48	18.52	4.12	0.3165	0.2575	0.2870	0.2863	0.2501
PLATE	WITH	STEP					
0.24	3.10	4.15	0.3335	0.2583	0.2959	0.2748	0.2543
0.34	4.95	4.15	0.2872	0.2137	0.2505	0.2175	0.2540
0.38	5.67	4.17	0.2924	0.1688	0.2306	0.2709	0.2541
1.04	10.47	4.17	0.3044	0.1477	0.2261	0.2566	0.2574
1.38	16.69	4.17	0.3197	0.1576	0.2387	0.2857	0.2590
1.48	18.52	4.17	0.3271	0.2190	0.2731	0.2958	0.2584
PLATE	WITH	RIDGES					
0.24	3.10	4.11	0.3143	0.2412	0.278	0.2931	0.255
0.34	4.95	4.17	0.2964	0.1435	0.220	0.2561	0.2576
1.06	10.82	4.18	0.311	0.1678	0.239	0.2852	0.2594
1.36	16.33	4.08	0.3013	0.1883	0.245	0.2748	0.2544
1.50	18.90	4.11	0.3037	0.2386	0.271	0.2949	0.2586
PLATE	WITH	PROTUBRANCES					
0.24	3.10	4.20	0.2997	0.2220	0.2609	0.2940	0.2640
0.38	5.67	4.17	0.2970	0.1838	0.2404	0.3081	0.2734
1.04	10.47	4.09	0.3064	0.2332	0.2698	0.3038	0.2667
1.26	14.49	4.12	0.4065	0.2379	0.3222	0.2978	0.2618
1.48	18.52	4.17	0.3116	0.1903	0.2510	0.3063	0.2668

From table II it is obvious that the theoretically estimated variations in diameters are higher than the measured values. In an attempt to explain discrepancies rough estimates of heat losses, not included in the theoretical estimates, were performed. The heat lost

by conduction through the power supply coupling and grounding connections is approximately 2% of the heat absorbed. Convection from the workpiece is roughly in the proximity of 10%. Heat lost by radiation from the workpiece is expected to be very high near the moving heat source and diminish rapidly towards the edges of the plate. An average temperature can not be used to estimate the radiative heat losses, because these vary with the fourth power of the local absolute temperature.

TABLE II: Comparison Between Measured and Estimated Variations in Diameters Due to Taper or Heat Sink Effects.

PLATE	MEASURED $\frac{\Delta d}{d}$ *	ESTIMATED $\frac{\Delta d}{d}$	REMARKS
Flat, 12 in. wide	-0.0800	0.185	Variation in thickness is evaluate.
	-0.0276		
Flat, 8 in. wide	0.0075	0.322	
	0.0357		
Flat, 6 in. wide	-0.0233	0.434	Variation in thickness is evaluated.
	0.0267		
Step	-0.1534	-	Start of step.
	-0.1800		
	-0.2207	-0.632	0.5 in. from start of step.
	-0.1213		
	-0.2359	-0.632	Middle of step.
	-0.1542		
	-0.1933	-	close to end of step.
	-0.0811		
	-0.0771	-	Flat, 1.75 in. from end of step
	-0.0032		
Ridge	-0.2081	-0.657	Bottom wide ridge.
	-0.1661		
	-0.1382	-0.657	Middle narrow ridge.
	-0.0813		
	-0.1188	-	Start of top wide ridge.
	-0.0900		
	-0.0238	-	Flat, 1 in. after end of top ridge
	-0.0084		
Protuberance	-0.0786	-0.172	First (2x2 in.).
	-0.0115		
	0.0341	-0.017	Second (2x2 in.).
	0.0337		
	0.2350	-0.03	Third (1x1 in.)
	0.1173		
	-0.0380	-0.119	Fourth (1x1 in.)
	0.0040		

*Top measurement is based on the average diameter of the weld, while the bottom is based on a combination of the average diameter and weld height.

Time ran)u before a theoretical estimate of radiation losses could be completed, but a arge value for radiation losses might explain the difference in theoretically estimated taper and observed taper.

CONCLUSION

The approximations used overestimated the change in weld diameter, possibly in the case of taper calculations at least, due to heat losses by radiation. Convection to the surrounding and conduction through the connections from the workpiece were not powerful enough heat sinks to substantially affect the theoretical computations. Also, the exact energy transferred from the arc to the workpiece is not known. In order to better understand the observed discrepancies between theory and observation it is proposed that detailed observations of the temperature fields within the workpiece be taken during welding.

REFERENCES

1. Nunes, Jr., A. C., "Modeling of the VPPA Welding Process," Metals Processes lab. at MSFC, Huntsville, Al., unpublished, pp 4.
2. Steranka, Jr., P.O., "Heat Sink Effects on Weld Bead - VPPA Process," Report for the NASA/ASEE Summer Faculty Research Program, The University of Alabama, Contract No. NGT-01-008-021, July 28, 1989, pp XXVIII 1-25.
3. ibid, Contract No. NGT-01-002-099, 1990.

1991

NASA/ASEE SUMMER FACULTY FELLOWSHIP PROGRAM

MARSHALL SPACE FLIGHT CENTER
THE UNIVERSITY OF ALABAMA IN HUNTSVILLE

OVERHAULING, UPDATING AND AUGMENTING

NASA SPACELINK ELECTRONIC INFORMATION SYSTEM

Prepared By: Jean A. Blake

Academic Rank: Professor

University and Department Alabama A & M University
                           Mathematics

NASA/MSFC

      Division: Public Services & Education Office

      Branch: Education

NASA Colleagues: William E. Anderson
                           Jeffrey S. Ehmen

Date: August 2, 1991

Contract No: The University of Alabama in
                           Huntsville
                           NGT-01-008-021

NASA/ Spacelink is a collection of NASA information and educational materials stored on a computer at the Marshall Space Flight Center in Huntsville, Alabama. It is provided by the NASA Educational Affairs Division and is operated by the Education Branch of the Marshall Center Public Affairs Office.

It is designed to communicate with a wide variety of computers and modems, especially those most commonly found in classrooms and homes. It was made available to the public in February, 1988. The system may be accessed by educators and the public over regular telephone lines. NASA/Spacelink is free except for the cost of long distance calls.

Overhauling and updating Spacelink was done to refurbish NASA/Spacelink, a very valuable resource medium. Several new classroom activities and miscellaneous topics were edited and entered into Spacelink. One of the areas that received a major overhaul (under the guidance of Amos Crisp) was the SPINOFFS BENEFITS, the great benefits resulting from America's space explorations. The Spinoff Benefits include information on a variety of topics including agriculture, communication, the computer, consumer, energy, equipment and materials, food, health, home, industry, medicine, natural resources, public services, recreation, safety, sports, and transportation.

In addition to the Space Program Spinoff Benefits the following is a partial list of some of the material updated and introduced:

1. Astronaut Biographies
2. Miscellaneous Aeronautics Classroom Activities
3. Miscellaneous Astronomy Classroom Activities
4. Miscellaneous Rocketry Classroom Activities
5. Miscellaneous Classroom Activities
6. NASA and Its Centers
7. NASA Areas of Research
8. NASA Patents, Licensing
9. NASA Technology Transfer
10. Pictures from Space Classroom Activities
11. Status of Current NASA Projects
12. Using Art to Teach Science
13. Word Puzzles for Use in the Classroom

A close scrutiny of the NASA/Spacelink Usage Statistics chart (shown overleaf) indicates that Spacelink is being widely used. Usage peaks seem to surround shuttle launches.

NASA/Spacelink Usage Statistics
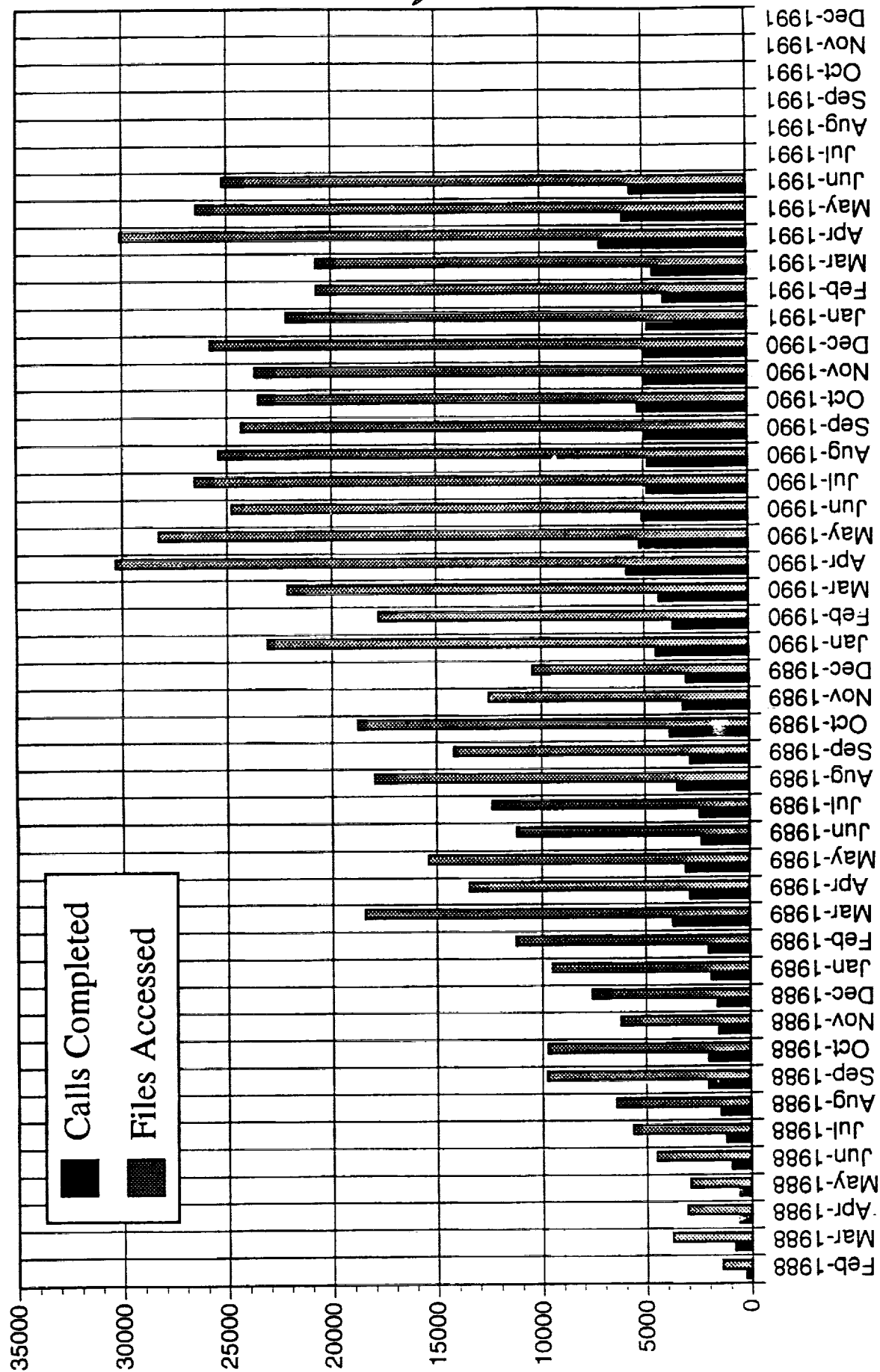
Legend:
- ■ Calls Completed
- ▨ Files Accessed

B-2

1991

NASA/ASEE SUMMER FACULTY FELLOWSHIP PROGRAM

MARSHALL SPACE FLIGHT CENTER
THE UNIVERSITY OF ALABAMA

DATA SIMULATION FOR THE LIGHTNING IMAGING SENSOR (LIS)

Prepared By: William L. Boeck, Ph.D.

Academic Rank: Professor

Institution: Niagara University
                                    Department of Computer and
                                    Information Sciences

NASA/MSFC:

        Laboratory: Space Science Laboratory
        Division: Earth Science and Application
        Branch: Remote Sensing

MSFC Colleague: Richard Blakeslee, Ph.D.

Contract No.:   NGT-001-008-021
                                    The University of Alabama

This project aims to build a data analysis system that will utilize existing video tape scenes of lightning as viewed from space. The resultant data will be used for the design and development of the Lightning Imaging Sensor (LIS) software and algorithm analysis. The desire for statistically significant metrics implies that a large data set needs to be analyzed. Before 1990 the quality and quantity of video was insufficient to build a usable data set. At this point in time, there is usable data from missions STS-34, STS-32, STS-31, STS-41, STS-37 and STS-39. During the Summer of 1990 a manual analysis system was developed to demonstrate that the video analysis is feasible and to identify techniques to deduce information that was not directly available. Because the closed circuit television system used on the space shuttle was intended for documentary TV, the current value of the camera focal length and pointing orientation, which are needed for photoanalysis, are not included in the system data. A large effort was needed to discover ancillary data sources as well as develop indirect methods to estimate the necessary parameters.

Any data system coping with full motion video faces an enormous bottleneck produced by the large data production rate and the need to move and store the digitized images. The manual system bypassed the video digitizing bottleneck by using a genlock to superimpose pixel coordinates on full motion video. Because the data set had to be obtained point by point by a human operating a computer mouse, the data output rate was small. The loan and subsequent acquisition of a Abekas digital frame store with a real time digitizer moved the bottleneck from data acquisition to a problem of data transfer and storage. The semi-automated analysis procedure was developed using existing equipment and is described below. A fully automated system can be described in the hope that the components may come on the market at reasonable prices in the next few years. The fully automated system would control an external videocassette recorder by reading a time code on the tape then capturing a sequence of frames, transfer the digitized images to the computer memory and then extract the lightning data using the LIS0 algorithm. If the system were fully automated, it would rewind the video tape and capture the next section of data until several minutes of data were processed. The ideal system would also capture data encoded in the vertical blanking interval of the original video, decode these pixels to determine GMT and camera motion. The ideal system would also have sufficient multitasking capacity to update the orbiter position on a second by second basis.

Semi-automated Analysis Procedure
Several aspects of video analysis need to be addressed. Video data is produced rapidly. Thirty frames are recorded in a second but a low cost digitizer may need five seconds to digitize a single frame and it would consume the better part of a minute to label the file, store the data and use the mouse to get pixel location data at several features in the image. Each second of data produces about 10 Megabytes of monochrome digitized image

data and could take about a half hour to digitize. A "real time digitizer" (1/30 second for a frame) speeds up the digitizing work but aggravates the data storage problem. One way to avoid the data storage problem is to superimpose a crosshair on the video and read data points without ever digitizing the images. That was the idea behind the manual analysis method. The automated method digitizes every frame in a sequence then discards pixel information not related to lightning. A typical video sequence would be of the order of one hundred seconds in length. The digitized images files for one hundred seconds would contain about 1 gigabyte of data which would exceed the throughput of existing equipment. One hundred seconds of data would have to be captured as many shorter sequences. If one manually started and stopped the VCR some overlap of the start and end of the short sequences would be necessary to be certain there were no gaps in the digitized records. This would produce a large volume of duplicate data that would have to be sorted and discarded.

The semi-automated analysis procedure starts by linking a Sony 3/4 inch tape recorder to the Abekas input and connecting the channel 2 audio (SMPTE code) output to the input of a SMPTE time code generator to regenerate a control signal to start the frame capture sequence. In order to record frames with accurate start and stop frames, the SMPTE code for the start frame must be entered into the ABEKAS as well as the number of frames to capture. After the tape is started, the time code generator is reset in order to slave the generator to the video source. The Abekas digital frame store will automatically capture several hundred frames. The starting frame for the next segment would be hand calculated and the recording process repeated until the entire video scene was captured. It is necessary to move the data from the Abekas via ethernet to a computer to proceed with the analysis. Paul Meyer has written a utility LISGRAB that moves a sequence of image files over ethernet and stores them on the Stardent in sequentially labeled files.

Level 0 data will be raw instrument data at original resolution, time ordered, with duplicates removed. This data will be downlinked from the LIS instrument. The LIS00 algorithm produces lightning data by extracting illuminated video pixels from a background as it scans a sequence of data files. This code reads one image file at a time and builds a background buffer that is the average of the last four valid background intensities for each pixel of interest. Data which exceed background and a threshold are not added to background but are sent to the output. The LIS00 output stream consists of the file ID (based on the GMT), video pixel X, Y and amplitude. Test cases will be used to determine the ability of simple, quick algorithms to separate lightning from nighttime background lights. Examples of interference include video noise introduced at the camera focal plane, the video downlink, the copying and digitizing process as well as aircraft beacons and explosions.

The output of LIS00 is sent to LIS0 which uses pan, tilt, altitude and focal length information to map the original oblique view video pixels into a nadir view with 10 km resolution. Because the higher resolution video data will map several pixels into the same 10 km resolution pixel the data will be sorted to remove duplicates. The output of LIS0 is a data stream consisting of time, pixel location and amplitude. This data is called imitation LIS level 0 data because the video data is at lower time resolution than the LIS level 0 data and the video oblique view produces data that would be out of view of the real LIS.

The LIS0 algorithm also removes duplicates by retaining the maximum value for a particular LIS pixel. Present LIS plans call for downlinking the background scene at fixed intervals. The background scene will be examined to verify the location and orientation of the platform as well as pixel calibration. Decisions are needed concerning the frequency of the background transmission, the source of this data (real time or averaged background), and whether to report this as part of LIS 0 data or store locally and discard. The background scene will be helpful in identifying optical events that are not produced by lightning. Optical pulses from cloud-free areas near cities can be discarded because they are generated by human activity.

LIS Level 1 data consist of the level 0 data stream packed with geo-referencing information and ancillary data. This data product will also contain a time stamp computation and calibration information. The LIS1 algorithm combines two data streams: the LIS 0 data stream and reference data from the platform. At present the content and format of the platform data has not been determined. Simulated time and location data will be generated to provide a data stream. Since LIS data will be asynchronous with respect to the orbital motion a decision is needed on whether to report platform data when there is no LIS data.

Level 1A data products are transformed values of full resolution instrument measurements. The data stream will consist of individual optical pulses with Universal time of origin, Latitude and Longitude of source, radiance of pulse and threshold setting. This data stream provides the most detailed set of calibrated data. Decisions are needed on the format of the output product.

Level 2 data consist of geophysical parameters located in time and space. The items of interest here are lightning stroke and flash identification. Optically, a single lightning flash is comprised of a series of discrete short duration optical pulses associated with energetic discharge processes occurring within a cloud. The individual optical pulses will be grouped to provide a single location (initial location) and starting time for a stroke. If another stroke is found in close time and spatial proximity, the combined event will be classed as a multistroke

lightning flash. Other luminous events such as meteors, sun glint, explosions, strobe lights and search lights may have to be identified at this stage. It must be noted that not all optical events in a flash will exceed the LIS threshold and be detected. The most important derived parameter is the lightning flash rate. The platform will be in a polar orbit which limits the time of continuous observation of any point within the field of view to about two minutes. This implies that strokes occurring at a particular location must be averaged for an observation period. Decisions are needed about which location to report for a lightning flash that extends over several pixel locations. Since the flash extends over time a second decision is needed regarding the choice of time tag.

The primary task of the level 2 algorithm is to group optical pulses into strokes, group strokes into flashes and count flashes at a location. It is desirable to perform the initial grouping as the time sequential data stream arrives. After a particular location has passed out of view and the incoming data stream will no longer contain relevant data, then the final summary of the data for a particular location can be constructed. A preliminary look at the algorithm suggests that the classification could be done on the level 0 data stream using coordinates relative to the LIS instrument. After the optical pulses are grouped, the location and start time of a grouping could be computed using platform data. With the flashes identified, the level 1A data could be organized on a flash by flash basis rather than a time of arrival basis. This algorithm would be more efficient because the level 1A data stream is larger than the level 0 data.

Level 3 data products consist of LIS geophysical parameters mapped and time averaged onto a uniform Earth based grid. Standard level 3 products will be produced with spatial resolution between 0.1 degree and 2.5 degrees. The data will be accumulated to produce global pentads, monthly, seasonal, yearly, annual and interannual maps of lightning. LIS level 3 products will include maps and statistics of total optical pulses, total flashes, flash densities, radiant intensities, discharge type and flash duration as well as mean and extreme value statistics. Since these mapping and statistical function are common to most EOS instruments, the EOSDIS contractor is expected to produce a tool kit for consistent mapping and statistical treatment of many different data sets. The run time of these tools may be improved by producing the LIS level 1A data grouped by flash. The polar orbit provides for extensive overlap of the viewing area during successive passes of polar locations. Since the observing time enters into the statistical significance of the data the EOS contractor is expected to address this need for all instruments.

1991

NASA/ASEE SUMMER FACULTY FELLOWSHIP PROGRAM

MARSHALL SPACE FLIGHT CENTER
UNIVERSITY OF ALABAMA

END-EFFECTOR FOR ROBOTIC ASSEMBLY
OF
WELDED TRUSS STRUCTURES IN SPACE

Prepared by: William V. Brewer, Ph.D.

Academic Rank: Associate Professor

Institution: Jackson State University
                         School of Science & Technology
                         Department of Technology

NASA/MSFC:

        Office: Materials & Processes Laboratory
        Division: Process Engineering
        Branch: Metals Processes

MSFC Colleague: Clyde S. Jones, III

Contract No.:   NGT-01-008-021
                         University of Alabama

D

INTRODUCTION

In June 1987 work was initiated at LaRC on end-effectors and preloaded joints for robotic truss assembly. This is part of an on-going research effort centered on a test facility that assembles 1"x 2m identical struts into an 8m diameter x 1.5m deep platform truss. A detailed description of the test facility was published (2).

The end-effector being used for the LaRC assembly demonstration is quite suitable for the Precision Segmented Reflector or other precision applications. These require high stiffness provided by mechanical joint preloads. Stiffness thus obtained is only required and provided over a load range far less than the ultimate strength of the strut tubes. Beyond this useful range, truss behavior is somewhat unpredictable.

THE PROBLEM

Mechanically preloaded joints of this type are less suitable for applications such as the Aero Brake where predictable strength and stiffness are required over a greater fraction of the load bearing capacity of component parts.

Preliminary studies of the Aerobrake support truss indicate that struts of at least 3 different diameters and various lengths would improve performance (3, p.3.1.1.2-3). The double-ended end-effector in service currently is designed for only one diameter and length. Anticipated single-ended versions can accomodate varing lengths but not multiple diameters.

THE WELDED ALTERNATIVE

Tradeoff considerations for welded joints relative to their mechanically preloaded counterparts:

Advantages -

    1.   High Strength & Stiffness / Mass
    2.   Preload Not Required
    3.   Predictable Behavior, linear in both tension and
            compression to the material proportional limit.
    4.   Simplified Low Mass Strut-End

Disadvantages -

    1.   Bulky Complex End-Effector
    2.   High In-Orbit Power Demand
    3.   Modest Environmental Contamination
        a.   Gas (inert and metalic)
        b.   Particle (metalic / repair mode only)
    4.   Inspection Difficult

WELDED JOINT TYPES

Joints proposed by the MSFC Structures Group for automated
assembly of welded truss structures have been placed into four
representative catagories. Each catagory was evaluated based on
the items listed below. The fractional representation of
"Alignment" shows the division of alignment effort between strut-
end and end-effector corresponding to the usual six degrees of
freedom. Progressing from catagory 1 to 4 , joint structural
performance is degraded as the joints become more complex.
Complexity in the joint reduces tasks that must be performed by
the end-effector thus simplifing it. The tradeoff is an inverse
relation between strut-end and end-effector complexity. Also
note that only catagories 1. and 4. do not require special struts
for the repair mode. This advantage supposes that the weld seam
can be cut and rewelded on the original weld site.

1.   Simple Butt Weld Joint –

Strength / Mass: best   Weld Seam: continuous, circular
Stiffness/ Mass: best   Welds / Strut: 2
Alignment   End-Effector:
    end effector: 6 / 6   double-ended
    strut end: 0 / 6   variable length
Grasp Sites / End: 2   Special Struts for Repair: NO

2.   Butt or Lap Weld with Threaded Sleeve –

Strength / Mass: good   Weld Seam: continuous, circular
Stiffness/ Mass: good   Welds / Strut: 4
Alignment   End-Effector:
    end effector: 1.5 / 6   double-ended
    strut end: 4.5 / 6   variable length
Grasp Sites / End: (n + 2)
    where n = repair sites   Special Struts for Repair: YES

3.   Butt or Lap Weld with Turnbuckle –

Strength / Mass: average   Weld Seam: continuous, circular
Stiffness/ Mass: average   Welds / Strut: 4 or 5
Alignment   End-Effector:
    end effector: 1 / 6   single ended
    strut end: 5 / 6
Grasp Sites / End: (n + 2)   Special Struts for Repair: YES

4.   Butt Weld with Slip Joint –

Strength / Mass: fair   Weld Seam: 2 eliptical segments
Stiffness/ Mass: fair   Welds / Strut: 2
Alignment   End-Effector:
    end effector: 0 / 6   single ended
    strut end: 6 / 6
Grasp Sites / End: 1   Special Struts for Repair: NO

SLIP JOINT

Joint type 4 was chosen for initial development because it allows the simplest and lowest mass end-effector. The " slip joint " required for welded assembly is a modification of the one under development at MSFC (3, p.3.1.1.3-8). Two modifications are required:

1.   the flat circular cross-sectional interface separating strut from node must be tilted 5.7 degrees wrt the strut axis to make the strut-end virtually double-action. A description of the nature and benefits of double action strut-ends has been published (3). Briefly, they allow assembly to continue when the node spacing is more or less than anticipated.

2.   the interface to be welded should present to the welding torch a material thickness of not more than 1/4" for a high quality weld seam.

END-EFFECTOR

A design to assemble and weld the joint described above would incorporated the following:

Features -
        1.   Simplified low mass strut-end.
        2.   Modified " slip " joints are virtually "double action".
        3.   Range of strut dimensions can be manipulated:
                Diameters from 2.25" to 6.0"
                Lengths variable (single-ended end-effector)
        4.   Struts retrievable from a hexagonal-close-packed tray.

Specifications -
        5.   End-Effector Envelope   (including repair subassembly)
                Axial Length: 3'
                Transverse Depth: 2'
                Transverse Width: 1'
        6.   Strut-End Dimensions
                Diameters: 2.25" to 5.0"
                Length: 2.0' to 2.5'   (plus scar length)
        7.   Torch Travel
                Axial: 2.5"
                Radial: 1.5"
                Orbital: +/- 190 degrees

Components and Subassemblies -
        (* indicates subassemblies that can be eliminated if
            only one strut diameter must be accomodated   )

I.   Weld Functions -
        1.   Torch -   Plasma arc welding adaptation planned.
                (contract with Electric Propulsion Laboratory)
        2.   Shielding (line of sight containment)
             a.   Hood (semi-cylinder)
        *   b.   End Curtains (semi-iris)
        3.   Torch and Shield Motions
        *   a.   Radial
             b.   Orbital
             c.   Axial
        *   4.   Torch Assembly Retractor
            5.   Torch Supply Line Dispenser

II. Strut Manipulation Functions –
      1. Retrieval and Location (stud inserted into Zip-Nut)
  ** 2. Release Plunger (push off from Zip-Nut)
      3. Nodal Scar Aquisition (slip joint lock bolt driver)
  *   a. Slip Joint Lock Bolt Insertion
          b. Slip Joint Lock Bolt Torque
III. Repair Functions –
      1. Stearable Saw (like inboard-outboard boat drive)
      2. Inertial Chip Collector
              (impeller integral with saw drive shaft)
      3. Saw and Collector Motions
              (components are mirror images of items
                  I.3 and I.4 above)

SUMMARY

Compared to robotically assembled & preloaded mechanical joints,
welded joints:
1. have higher strength and stiffness for any given mass,
2. exhibit linear behavior to the failure load of components,
3. are relatively permanent and not as easily repaired.

End-Effectors devised to assemble welded joints:
1. will be less complex and massive if a simple mechanical
    joint is employed to facilitate alignments,
2. can accomodate struts of varing diameter and length,
3. will be able to repair and replace failed members,
4. allow very compact launch packaging of strut components.

CONCLUSIONS

Repair by cut and re-weld on the original weld site should be
researched. Repair complexity would be significantly reduced.

Welded joints, though repairable, should not be used where high
repair frequencies are anticipated.

Welded joints should be considered for an Aero Brake truss.

REFERENCES

(1) Brewer, W. V.,"Simplified Double Action Mechanism to Preload
        Joints for Robotic Assembly of Structures in Space",
NASA/LaRC/HBCU Grant No. NAG-1-1125, proceedings of 14th IASTED
International Symposium on Manufacturing & Robotics,
Lugano, Switzerland, 6/25/91.

(2) Rhodes, M. D., Will, R. W., Wise, M.,"A Telerobotic System
        for Automated Assembly of Large Space Structures", NASA
        Technical Memorandum 101518, LaRC, Hampton VA 23665, 3/89.

(3) Thomson, M., ORBITAL CONSTRUCTION DESIGN DATA HANDBOOK,
        AAC-TN-1160, for NASA/LaRC, NAS1-18567, Task 7,
        Astro Aerospace, Carpinteria CA 93013-2993, 4/30/90.

1991

NASA/ASEE Summer Faculty Fellowship Program

Marshall Space Flight Center
The University of Alabama

Development and Application of Virtual Reality for
Man/Systems Integration

Prepared By: Marcus Brown, Ph.D.

Academic Rank: Assistant Professor

Institution: The University of Alabama
                          Computer Science Department

NASA/MSFC:
        Office: Science & Engineering
        Division: Missions Operations Lab
        Branch: Man/Systems Integration

MSFC Colleague: Joe Hale

Contract No.:   NGT-01-008-021
                          The University of Alabama

E
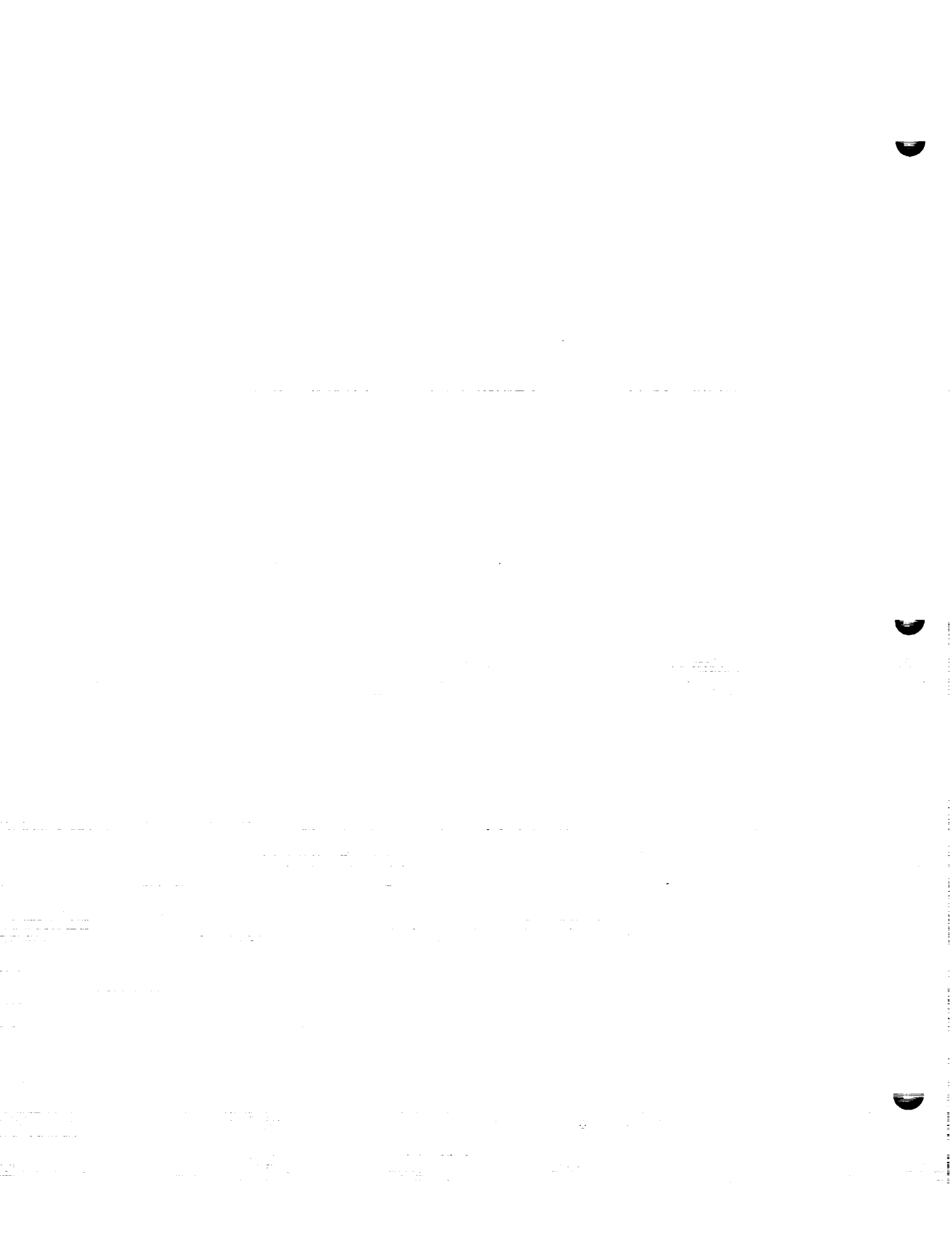
Since the first applications of the earliest computers, one question which has always been present is the question of presenting the information in the computer to the human who uses the computer. Through different computers and applications, different answers to this problem have been presented. Many of these answers have been appropriate for a small class of highly trained individuals, but even when users have learned the computer's output language, the patterns and relationships in the data have not always been evident. This is particularly true when attempting to present data about various physical models. The computer has been used to model automobiles, rockets, buildings, road systems, and many other physical models. While some applications of these models have been designed to produce textual or numerical results for special requirements, results in this form often fail to convey a complete picture of the model. This results in the user having some misconceptions which are only rectified later, perhaps when a physical model is built.

An alternative approach to textual and/or numerical results from these computer models has been to present a graphical image of the model. The user is able to perceive the model in a form similar to what she might perceive in an actual physical model. This has often lead to a better appreciation of the model, and perhaps to corrections when the model has needed adjustments.

While the graphical presentation of computer models signified a quantum leap over presentations limited to text and numbers, it still has the problem of presenting an interface barrier between the human user and the computer model. The user must learn a command language in order to orient herself in the model. For example, to move left from the current viewpoint of the model, she might be required to type 'LEFT' at a keyboard. This command is fairly intuitive, but if the viewpoint moves far enough that there are no visual cues overlapping with the first view, the user does not know if the viewpoint has moved inches, feet or miles to the left, or perhaps remained in the same position, but rotated to the left. Until the user becomes quite familiar with the interface language of the computer model presentation, she will be prone to loosing her bearings frequently. Even a highly skilled user will occasionally get lost in the model.

A new approach to presenting type type of information is to directly interpret the user's body motions as the input language for determining what view to present. When the user's head turns 45 degrees to the left, the viewpoint should be rotated 45 degrees to the left. Since the head moves through several intermediate angles between the original view and the final one, several intermediate views should be presented, providing the user with a sense of continuity between the original view and the final one.

Since the primary way a human physically interacts with her environment is by using her hands to manipulate objects, this type of interface should monitor the movements of the users hands, and alter objects in the virtual model in a way consistent with the way an actual object would move when manipulated using the same hand movements.

Since this approach to the computer-human interface closely models the same type of interface that humans have with the physical world they have lived in since long before computers were invented, this type of interface is often called **virtual reality**, and the model is referred to as a **virtual world.**

This summer's fellowship task was to set up a virtual reality system at Marshall Space Flight Center, and begin applying it to some of the questions which concern scientists and engineers involved in space flight.

Setting up the virtual reality system was fairly straightforward. Most of the hardware and basic software was ready at the beginning of the summer.

The input devices are unusual, and deserve explanation. First, the position of various body parts must be sensed, and that information fed into the computer model. While various devices might be used to sense this information, this system uses a magnetic sensing device. A magnetic source is put in a fixed location, and a sensor is put on the part of the body where information is desired, such as on the head and right hand. This allows the user's movements to be communicated to the computer without unduly interfering with the user's freedom of movement. This magnetic sensor gives information about the position and orientation, so when the user turns her head, the computer is able to compensate for that

movement, even though the head may not have moved to a different position.

Sensing the movement of the hand presents an additional problem. Not only is it necessary to know the position and orientation of the hand, but for realistic interaction, the computer system must also have information about the flexion of the fingers and thumb. This is accomplished by wearing a glove which uses fiberoptics to sense joint flexion. Two joints on each finger are measured. This allows the user a small repertoire of gestures, such as 'Point' and 'Grab', which allow her to interact with the objects in the virtual world of the computer model.

There are two parts to building a virtual world. First, a 3D modelling package is used to define the objects in the virtual world. These objects may include walls, floors, tables, etc. It is usually appropriate to define a set of constraints for the objects. It may be desirable to fix the position of a wall so that the user cannot move it. Other objects may be moveable, but only through a limited range.

After the objects are built, a certain amount of programming must be done to determine the properties of the objects, and how they will interact with the user. Most objects, by default, will allow other objects to intersect and completely pass through them. This property is sometimes desirable, but in many cases it is more appropriate to force objects to move away from each other rather than intersect. This type of interaction must be programmed into the system for each pair of objects.

Once the virtual reality system was working, the next task was to apply the tool to a specific problem facing NASA. The first problem approached dealt with the placement of the Crystal Growth Furnace in a rack in the Space Station. The CGF is large enough that it fills the racks using in the space station. This means that there is not enough room to load the 24-inch long samples which must be inserted into the top of the CGF. The solution to this problem is to tilt the CGF forward and allow more room to work. Three different pivot points have been proposed, but each has concerns about the amount of clearance required, particularly about whether the human operator would have the room necessary to manipulate the different samples and pieces necessary to the job.

A virtual world has been created which holds a section of the space station, several racks, and a model of the CGF in a rack. This virtual world will be used to check for adequate room to work, using each of the three proposed pivot points. The alternative to solving the problem this way is to build a physical mockup at a cost of $30,000. Using a virtual world has a large startup cost for the necessary computers, but the cost of the model and the trials is almost negligible.

It is hoped that further applications of virtual reality can realize additional cost savings, and allow a more intuitive interface between the human user and the computer model.

N92-15856

1991

NASA/ASEE SUMMER FACULTY FELLOWSHIP PROGRAM

MARSHALL SPACE FLIGHT CENTER
THE UNIVERSITY OF ALABAMA IN HUNTSVILLE

**EVALUATION OF SCHEDULING TECHNIQUES FOR
PAYLOAD ACTIVITY PLANNING**

Prepared By: Stanley F. Bullington, Ph.D., PE

Academic Rank: Assistant Professor

Institution: Mississippi State University,
                        Department of Industrial
                        Engineering

NASA/MSFC:

    Office: Mission Operations Laboratory
    Division: Mission Analysis
    Branch: Planning Systems

MSFC Colleague: John P. Jaap

Contract No.:   NGT-01-008-021
                        The University of Alabama
                        in Huntsville

F

Two tasks related to payload activity planning and scheduling were carried out. The first task involved making a comparison of space mission activity scheduling problems with production scheduling problems. The second task consisted of a statistical analysis of the output of runs of the Experiment Scheduling Program (ESP). Details of the work which was performed on these two tasks are presented in the separate sections which follow.

TASK 1

Description. A paper entitled "A Comparison of Space Mission Activity Scheduling Problems with Production Scheduling Problems" was written (reference 1). This paper will be submitted for possible publication as a NASA Reference Publication.

Objectives. It was felt that a need existed for a "bridge" between the literature in space mission activity scheduling and the literature in production scheduling. Writing a document which compared the two problems was seen as the best means of providing this bridge. This document could then serve to introduce the two problems to those not familiar with one, or both, of them. For example, those who are familiar with space mission activity scheduling problems (generally NASA personnel and NASA contractor personnel) might use the document to gain a better understanding of the literature on production scheduling problems, and how it relates to space mission activity scheduling. Similarly, those who are familiar with production scheduling problems, including academic and industrial researchers, as well as newly-graduated engineers, could use such a document as an introduction to space mission activity scheduling problems.

Another objective of this task was to identify possible areas for further research in space scheduling problems. This was done by examining the literature for both types of scheduling problems to see which approaches had been successful, and by considering the effects of the important differences in the two types of problems.

Approach. The document produced in Task 1 begins with a brief discussion of scheduling problems in general. This is followed by a comparative description of space mission activity scheduling problems and production scheduling problems. For each of the problem types, the associated terminology is reviewed. This is followed, for each case, by a detailed problem description which covers the problem environment, typical objectives, and typical constraints. A discussion of the solution approaches which have been applied to each problem type is included. Finally, some areas for further research in space scheduling problems are identified.

Results. The comparison of the two scheduling problems pointed out the similarities between them, especially in terms of their level of difficulty and the solution approaches which have been applied to them. However, several important differences in the problems were identified. Some of these differences are discussed below.

In production scheduling problems, machine capacity is often assumed to be the only constraining resource. In a very few studies, other resources such as labor or tooling are considered. In space mission scheduling, on the other hand, many different types of resources act as important constraints on the system, and must be considered when solving the scheduling problem. This consideration of multiple resource types makes the space mission activity scheduling problem an extremely difficult one.

The objectives of the two scheduling problems are quite different. In production problems, the objectives of interest generally include those related to job completion times (e.g., flowtime and makespan), those related to due dates (e.g., mean or maximum tardiness or lateness, number of tardy jobs, etc.), and/or those related to inventory and utilization costs (e.g., average number of jobs waiting, machine utilization percentages, etc.). In space mission activity scheduling, the single major objective is the maximization of the scientific return from the mission. Because of the difficulty of measuring this objective directly, surrogate measures such as the number of activity model performances scheduled, the amount of crew time scheduled, the amount of experiment time scheduled, or a subjectively weighted schedule grade, are generally used.

There are a number of important differences in the constraints on the two types of scheduling problems. In general, space mission activity scheduling problems tend to have many more constraints than production scheduling problems. One major difference in the two problem types is that space missions have a finite duration. Because of this, only a subset of the activities which could be scheduled actually will be scheduled. In production problems, on the other hand, all jobs are generally scheduled eventually. Those which cannot be completed in one week will be completed in the following week, for example.

In space scheduling problems, another important type of constraint is the existence of time windows in which the activities must be scheduled. These constraints arise because of the position or attitude of the spacecraft or target objects, the nature of the scientific experiment or activity being performed, the duty cycles of the crew members, etc. In most production scheduling problems, the analogous types of constraints are either unimportant or are ignored for convenience.

Some of the other complicating constraint types in the space mission activity scheduling problem include the existence of complex resource availability profiles for the multiple resource types, the possibility of concurrent activities, the existence of variable step durations, the requirement that there be a certain minimum time delay between adjacent steps in an activity model or between different performances of the same model, the requirement that certain resources remain unavailable for use during such time delays, the requirement that certain steps in an activity be performed by the same crew member(s), and the possible existence of

alternate scenarios for an activity. Some of these constraints have analogies in the production scheduling environment, but these are usually not considered in such problems.

The document produced in Task 1 provides a review of the solution approaches which have been applied to each of the types of scheduling problems. Much of the general scheduling literature deals with theoretical issues and very small scheduling problems (e.g., single-machine scheduling). Optimization approaches have been applied in both problem environments, but have been of limited practical use because of their computational burden. Because of this, heuristic approaches have generally been used to solve realistic problems of both types. Various heuristic approaches are reviewed in the paper, with special emphasis on ESP (see reference 2) and other robust payload activity scheduling programs. Finally, artificial intelligence approaches to scheduling are discussed.

The last result of the Task 1 document is the identification of areas where further research is needed. In the short term, the most promising area appears to be the investigation of methods for improving heuristic approaches such as ESP. Three specific areas of possible improvement were identified. First, the decomposition of the scheduling problem by defining "artificial" time windows for activities should be examined. In ESP, such a decomposition can be easily accomplished by using the macro windows feature of the program. Currently, macro windows are used merely to define the mission duration. However, they could be used to help control the placement of activities onto the mission timeline, and to artificially break a large scheduling problem into several smaller problems in order to reduce the time required to obtain a solution. Research is needed to determine effective methods for defining the macro windows, and to determine the effects of their use on solution time and the quality of the schedule obtained.

In ESP, activities are placed onto the mission timeline one at a time. The order in which activities are selected for placement has a significant impact on the final schedule. Several selection methods are currently available, but more robust methods are needed. Finally, the use of rescheduling in heuristics such as ESP should be examined. In some heuristics, including ESP, an activity which has been placed on the timeline will not be rescheduled. Other heuristics do reschedule activities. Rescheduling promises improved schedules, but this improvement is at the expense of increased computational requirements. An analysis of the relative costs and benefits of rescheduling, as well as the definition of appropriate rescheduling methods, needs to be performed.

The relatively new field of artificial intelligence holds promise for scheduling applications, particularly in the long term. Further research in this area is needed.

TASK 2

Description. A statistical analysis of the output from ESP runs for two space station data cases was performed. Using the random activity selection rule, 60 runs were made for a relatively difficult data case, and 95 runs were made for a relatively easy data case.

Objectives. It was hoped that Task 2 would provide knowledge on the number of ESP runs required to reach a specified level of confidence in the results. A closely related objective was to suggest how analysts could, after obtaining the results from several runs, make their own determination as to the need for making additional runs.

Approach. For the difficult data case, the 60 runs were randomly divided into groups of size 1, 2, 3, 5, and 10. The best run of each group for each of four performance measures (schedule grade, number of performances scheduled, crew time scheduled, and experiment time scheduled) was then identified. Within each group size/performance measure combination, statistical analyses were performed on the best runs of each group to find the mean value, minimum and maximum value, upper and lower tolerance limits (see reference 3), and a crude estimate (mean value plus three standard deviations) of the optimal value. The same approach was used for the easier data case, with the 95 runs being randomly divided into groups of size 1, 3, 5, and 10.

Results. As expected, the data for the two cases indicates that the number of runs needed to reach a given confidence level is highly dependent upon the amount of variation within the data. After making several runs (e.g., five), it is recommended that the mission planner carry out an analysis like the one performed here. The closeness of the best solution obtained to the upper tolerance limit and estimated optimal value should then indicate whether additional runs should be made.

REFERENCES

1. Bullington, S.F., and Jaap, J.P., "A Comparison of Space Mission Activity Scheduling Problems with Production Scheduling Problems," submitted for publication to NASA, 1991.
2. Jaap, J.P., and Davis, E.K., "Experiment Scheduling Program User's Manual," NASA Marshall Space Flight Center, 1989.
3. Miller, I.R., Freund, J.E., and Johnson, R., Probability and Statistics for Engineers, 4th Ed., Prentice-Hall, Englewood Cliffs, New Jersey, 1990.

1991

NASA/ASEE SUMMER FACULTY FELLOWSHIP PROGRAM

MARSHALL SPACE FLIGHT CENTER
THE UNIVERSITY OF ALABAMA

NONLINEAR OPTICAL PROPERTIES OF ORGANIC MATERIALS:
A THEORETICAL STUDY

Prepared By: Beatriz H. Cardelino, Ph.D.

Academic Rank: Assistant Professor

Institution: Spelman College, Department of
                    Chemistry; Atlanta University Center,
                    Inc., D.E. Milligan Science Research
                    Institute

NASA/MSFC:

    Office: ES-74

    Division: Microgravity Science and Applications

    Branch: Chemistry and Polymeric Materials

MSFC Colleague: Craig E. Moore, Ph.D.

Contract No.:   NGT-01-008-021
                    The University of Alabama

Replacement of electronic switching circuits in computing and telecommunication systems with purely optical devices offers the potential for extremely high throughput and compact information processing systems. The potential application of organic materials containing molecules with large nonresonant nonlinear effects in this area have triggered intensive research during the last decade. Interest on this area was due to two facts: (a) that many organic materials show nonlinearities that are orders of magnitude larger than those of conventional inorganic materials such as lithium niobate and potassium dihydrogen phosphate, and (b) that organic materials much flexibility in terms of molecular designs.

Some of the desirable characteristics that these materials should have are that they be transparent to the frequency of the incident laser and its second or third harmonic, that they have a high damage threshold and, in the case of second-order effects, that their crystal structure or molecular orientation be acentric. Since polymeric assemblages can enhance the nonlinear response of organic molecules severalfold, efforts have been directed toward the synthesis of thin films with interpenetrating lattices of electroactive molecules. The goal of this theoretical investigation is to predict the magnitude of the molecular polarizabilities of organic molecules that could be incorporated into films. These calculations are intended to become a powerful tool to assist material scientists in screening for the best candidates for optical applications.

There are two possible approaches in the theoretical prediction of the magnitude of molecular susceptibilities of organic molecules: the sum-over-state approach, which is based on a perturbative expansion in terms of molecular eigenstates, and the finite-field-perturbation approach, which diagonalizes a molecular Hamiltonian that includes a static-field dipolar perturbation. In the first approach, a perturbation expansion in terms of excited states of the unperturbed molecule is used. In the second approach, ground state energies are calculated directly by a variational method in the presence of a perturbing field. In either case, any semiempirical or ab-initio method may be utilized. In general, ab-initio theories are used in attempting to reproduce absolute magnitudes but semiempirical models have been useful to detect trends among related molecules. For a summary of theoretical screening methods, please see Penn, Cardelino, Moore, Shields and Frazier, 1991 [5]).

The procedure that was developed for the present calculations is based on the static-field approach, and is a modification to the method developed by Dewar and Stewart, 1984 [2] for calculating molecular linear polarizabilities. When a molecule is placed in an electric field, a given

component of its polarization can be expressed by the following summation:

$$p_q = \mu_q + \sum_j \alpha_{qj} F_j + \sum_{jk} \beta_{qjk} F_j F_k + \sum_{jkl} \gamma_{qjkl} F_j F_k F_l + \ldots \quad [1]$$

where p_q represents the **q** component of the polarization, F_i the **i** component of the applied electric field, μ the permanent dipole moment, α the linear polarizability, β the second-order polarizability, γ the third-order polarizability, etc. The magnitude of the vector part of β, corresponds to the effective measure of hyperpolarizability for second harmonic generation (SHG):

$$\beta_{vec} = (\beta_x^2 + \beta_y^2 + \beta_z^2)^{1/2} \quad [2]$$

where x, y, and z are the molecular coordinate axes. The symmetry of β with respect to interchange of the last two indices determines that the vector components be:

$$\beta_q = \beta_{qqq} + (\sum_j \beta_{qjj} + 2 \sum_j \beta_{jqj})/3 \quad [3]$$

Finally, the value of the average (scalar part) third-order polarizability γ, which is related to third-harmonic generation, can be expressed as:

$$\gamma = (\gamma_{xxxx} + \gamma_{yyyy} + \gamma_{zzzz} + 2\gamma_{xxyy} + 2\gamma_{yyzz} + 2\gamma_{xxzz})/5 \quad [4]$$

Dewar and Stewart [2] method utilizes four isolated point charges (or sparkles, with no associated electrons or atomic orbitals) in the description of the molecule, allowing for the corresponding changes in polarization and energy to be calculated directly. The polarization and energy are obtained within the MNDO approximation, implemented in the MOPAC [4] quantum mechanical package.

The computer coding required for the calculation of second-order polarizabilities was developed before the summer of 1991 (Cardelino et al., 1991 [1]). The original version of MOPAC used involved the use of fields along the three Cartesian coordinates. In order to obtain the 27 required elements of the β tensor, calculations with fields along the bisector of all quadrants were added to MOPAC. In total, molecules are subjected to electrical fields of 14 different strengths along each of the molecular axes and along the bisector line of each quadrant. Thus, MOPAC is used to obtain polarization data which are subsequently utilized by another program to perform polarization expansions in terms of field strengths.

The procedure to obtain second-order polarizabilities was applied to nitroanilines (Cardelino, Moore and Stickel, 1991 [1]) and benzophenone derivatives (Moore and Cardelino, 1991 [3]). During the summer of 1991, this code was

reviewed and substantially simplified. The simplified procedure was applied to mono-, di-, and tri-substituted naphthalene, quinoline and isoquinoline. A manuscript to be submitted for publication is under preparation.

Most of the effort during the summer of 1991 was directed toward extending the procedure for second-order polarizabilities to obtain third-order polarizabilities. Based on equation [1], a polarization expansion for fields along one Cartesian coordinate are as follows:

$$P_q = \mu_q + \alpha_{qi} F + \beta_{qii} F^2 + \gamma_{qiii} F^3 + \ldots \qquad [5]$$

where $F = F_j$. When the fields are along the bisector of a quadrant, the polarization expansion can be expressed with two different equations, depending if the two components have the same or opposite signs:

$$P_q = \mu_q + (\alpha_{qi} + \alpha_{qj}) F + (\beta_{qii} + \beta_{qjj} + 2 \beta_{qij}) F2 +$$

$$(\gamma_{qiii} + \gamma_{qjjj} + 3 \gamma_{qiij} + 3 \gamma_{qijj}) F^3 \ldots \qquad [6]$$

where $F = F_i = F_j$; and,

$$P_q = \mu_q + (\alpha_{qi} - \alpha_{qj}) F + (\beta_{qii} + \beta_{qjj} - 2 \beta_{qij}) F^2 +$$

$$(\gamma_{qiii} - \gamma_{qjjj} - 3 \gamma_{qiij} + 3 \gamma_{qijj}) F^3 \ldots \qquad [7]$$

where $F = F_i = -F_j$. Sumation and subtraction of the third-order coefficients of equations [6] and [7] result in:

$$2 \gamma_{qiii} + 6 \gamma_{qijj} \qquad [8]$$

$$2 \gamma_{qjjj} + 6 \gamma_{qiij} \qquad [9]$$

To calculate γ from equation [4], the only terms that are needed are those in which q=i or q=j. If Kleinman symmetry is assumed and if q=i then qij=iij=jii and qiij=iiij=jiii; similarly, if q=j then qij=jij=ijj and qijj=jijj=ijjj. Then, equations [6] and [7] may be written as:

$$P_i - \mu_i - (\alpha_{ii} \pm \alpha_{ij}) F - (\beta_{iii} + \beta_{ijj} \pm 2 \beta_{jii}) F^2$$

$$- (\gamma_{iiii} \pm \gamma_{ijjj} \pm 3 \gamma_{jiii}) F^3 = + 3 \gamma_{iijj} F^3 \qquad [10]$$

and

$$P_j - \mu_j - (\alpha_{ji} \pm \alpha_{jj}) F - (\beta_{jii} + \beta_{jjj} \pm 2 \beta_{ijj}) F^2$$

$$- (\gamma_{jiii} \pm \gamma_{jjjj} + 3 \gamma_{ijjj}) F^3 = \pm 3 \gamma_{iijj} F^3 \qquad [11]$$

in which case, all terms in the left side of the equations can be obtained from calculations over fields along only one Cartesian coordinate at a time. In summary, the nonlinear

terms needed to obtain the iijj terms are: ijj, jii, ijjj, and jiii. Figures 1 and 2 show the dependence of the coefficients required for the calculation of γ with the degree of the polynomial expansions for one particular molecule. All terms are very stable except for two 4th degree terms: yyyy and yxxx. These instabilities deserve further study. The section of the computer program that performs calculation of γ is under way.

Third-order polarizability calculations will be performed on 1-pyrryl-5-x-(1,3)-dipentyne and 1-pyrryl-6-x-(1,3)-dihexyne, where x will be hydroxyl, nitro, or amino groups. In particular, there has been a patent disclosure by Samuel P. McManus, Donald O. Frazier, and Mark S. Paley on the hydroxyl molecule. During this summer, energy calculations on these molecules were also performed.
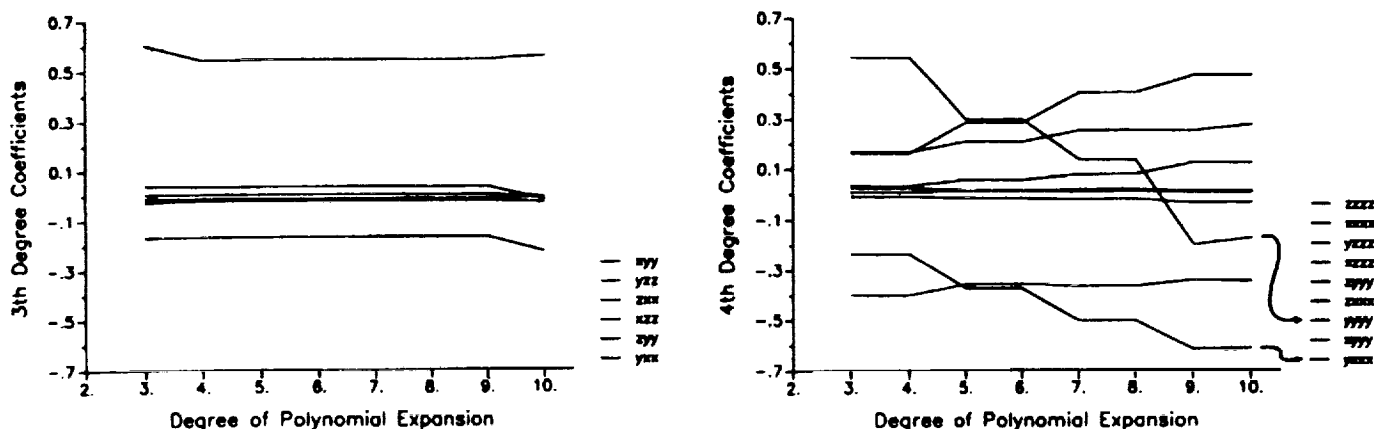
Figures 1 and 2. Values of the third and fourth degree coefficients of the expansions of polarization as a function of field strength.

References

[1] Cardelino, B.H.; Moore, C.E.; and Stickel, R.E. "Static Second-Order Polarizability Calculations for Large Molecular Systems"; J.Phys.Chem., October 1991.
[2] Dewar, M.J.S.; and Stewart, J.J.P. "A New Procedure for Calculating Molecular Polarizabilities; Applications Using MNDO"; Chem.Phys.Lett. Volume 111, 416 (1984).
[3] Moore, C.E.; and Cardelino, B.H. "Static Second-Order Polarizabilities of Aminobenzophenones and Nitro-benzophenones"; J.Mol.Struc.: Theochem, August 1991.
[4] MOPAC, Quantum Chemistry Program Exchange, No. 455 Version 4.0 (1987).
[5] Penn, B.J.; Cardelino, B.H.; Moore, C.E.; Shields, A.W.; and Frazier, D.O. "Growth of Bulk Single Crystals of Organic Materials for Nonlinear Optical Devices: An Overview"; Prog. Crystal Growth and Charact. Volume 22, Pages 19-51 (1991).

1991

NASA/ASEE SUMMER FACULTY FELLOWSHIP PROGRAM

MARSHALL SPACE FLIGHT CENTER
THE UNIVERSITY OF ALABAMA

A MINIMUM PROPELLANT SOLUTION TO AN ORBIT-TO-ORBIT TRANSFER USING A LOW THRUST PROPULSION SYSTEM

Prepared By: Shannon S. Cobb, Ph.D.

Academic Rank: Assistant Professor

Institution: University of Alabama
in Huntsville, Department
of Mathematical Sciences

NASA/MSFC:

         Division: Systems Analysis
         Branch: Flight Mechanics

MSFC Colleague: John Hanson, Ph.D.

Contract No.:   NGT-01-008-021
The University of Alabama

H

Introduction

The Space Exploration Initiative is considering use of low thrust (nuclear electric, solar electric) and intermediate thrust (nuclear thermal) propulsion systems for transfer to Mars and back. Due to the duration of such a mission, a low thrust minimum-fuel solution is of interest; a savings of fuel can be substantial if one allows the propulsion system to be turned off and back on. This switching of the propulsion system helps distinguish the minimum-fuel problem from the well-known minimum-time problem.

Optimal orbit transfers are also of interest to the development of a guidance system for orbital maneuvering vehicles which will be needed, for example, to deliver cargoes to Space Station Freedom.

The problem of optimizing trajectories for an orbit-to-orbit transfer with minimum-fuel expenditure using a low thrust propulsion system was discussed in (1), but the code, SECKSPOT (2), which was used is incapable of handling a general minimum propellant problem.

Analysis

To avoid the singularities that may occur when using the classical elements a, e, i, ω, Ω, (semi-major axis, eccentricity, angle of inclination, argument of perigee, longitude of the ascending node) the equinoctial elements a, h, k, p, and q are used to define the spacecraft's state. The sixth state element is the eccentric longitude F, which represents the angular position of the satellite in its orbit. Thus, the spacecraft's state, z, is

$z = (a, h, k, p, q)^T$, or in classical elements,

$$z = (a, e\sin(\omega + \Omega), e\cos(\omega + \Omega), \tan(i/2)\sin(\Omega), \tan(i/2)\cos(\Omega))^T,$$

and [1]

$$F = E + \omega + \Omega.$$

The convention of denoting vectors in bold print and unit vectors with the circumflex $\wedge$ is used.

It follows that the equations of motion in terms of these equinoctial elements are

$$\dot{z} = 2P \hat{Mu} / mc,$$

[2]

$$\dot{m} = -2P / c^2,$$

where P (≥ 0) = power due to thrusters, m (> 0) = mass of the spacecraft,

c (> 0) = jet exhaust speed, M = 5 × 3 matrix representing the partial derivative of z with respect to the velocity vector r, and the unit vector in the direction of thrust is $\hat{u}$, which is also the control for this optimization problem.

Applying the maximum principle to the optimal pair $(\hat{u}, z)$, it is clear that one should maximize the Hamiltonian function, H, with respect to the thrust direction at each point along the optimal trajectory of the transfer to obtain the minimum-fuel solution. The Hamiltonian function is defined in terms of the costate (adjoint) variables λ_z and λ_m so that

$$\dot{z} = \partial H / \partial \lambda_z, \quad \dot{m} = \partial H / \partial \lambda_m,$$

[3]

$$\dot{\lambda}_z = - \partial H / \partial z, \quad \dot{\lambda}_m = - \partial H / \partial \lambda_m,$$

where

$$H(z, m, \lambda_z, \lambda_m, \hat{u}) = 2P / mc \; \lambda_z^T M \hat{u} - 2P / c^2 \lambda_m.$$

[4]

Hence, the Hamiltonian H in [4] is maximized by aligning $\hat{u}$ in the direction of the primer vector, $\lambda_z^T M$. Let λ denote the magnitude of this primer vector. Then define the switching function, σ, by $\sigma = \lambda - m\lambda_m / c$. With this definition, H can be rewritten as $H = (2P / mc)\sigma$.

At any point along the trajectory for which σ, and hence H, is negative, H can be maximized by taking P = 0, which amounts to turning the propulsion system off; while if σ, and hence H, is positive, then allow the propulsion system to be used at full power in the optimal direction of thrust $\hat{u}$. So $\sigma < 0$ determines a "coast phase", while $\sigma > 0$ yields a "thrust phase". The points at which $\sigma = 0$ are called switch points.

Around each orbit the equinoctial elements vary "slowly" and can be held constant; thus only the "fast" variable F remains. However, in this situation the actual position in an orbit of the spacecraft is not of interest, so the dependence on this variable is removed by integration. Using Kepler's equation which relates the time t to the mean anomaly and hence the eccentric anomaly, one can perform averaging over an orbit of some specified period by changing the variable of integration from time t to the eccentric longitude F. Thus the Hamiltonian and hence the equations of motion can be averaged; note that since the Hamiltonian is zero for coast phases, one needs only integrate over thrust phases. In order to perform this integration using a Gaussian quadrature method, it is necessary to predetermine the switch points along the trajectory and integrate only over thrust periods, which will begin and end with a switch point. These averaged derivatives are then solved using a Runge-Kutta method.

To find the solution it is necessary to determine the initial values for the costate variables λ_z such that the boundary conditions are satisfied; that is, the desired final state is reached. The transversality conditions at the final time (which is unspecified) t_f, are $\lambda_z(t_f) = \alpha$, where α is a vector of parameters and $\lambda_m(t_f) = 1$.

Numerical Algorithm

The minimum-fuel solution is found by an iterative method which determines the initial costate values $\lambda_z(t_0)$ and $\lambda_m(t_0)$ such the boundary conditions $a - a_f = 0$, $h - h_f = 0$, $k - k_f = 0$, $p - p_f = 0$, $q - q_f = 0$ and $\lambda_{mf} - 1 = 0$ (and $f - f_f$ if not averaging) are satisfied. This is a system of nonlinear equations in terms of $\lambda_z(t_0)$, whose solution can be found by a secant method. For an initial guess, an optimal trajectory is found in the following manner: call the Runge-Kutta integrator,which calls RKFCT which calculates the derivatives . RKFCT calls SWCHPTS to find the thrust periods over and orbit, by finding the switchpoits and calls INTEG to prepare the integrands for quadrature if AVGTST determines that the variables are changing slowly enough, and if not averaging the partial derivatives of the equations of motion are calculated; INTEG calls QUAD4 for integration. QUAD4 calls FCT, which calculates the Hamiltonian, and calls EVALMP and PRIMER to find the thrust direction. From this Runge-Kutta integrator, a new state and costate is found. The stopping criterion used is the size of the semi-major axis.

Conclusions

It appears that one of the difficulties involved with this problem is convergence of the method considering the sensitivity to slight perturbations in the initial costate values. Another problem is the accurate determination of the switch points for the case of averaging and also not averaging.

References

(1) Horsewood, J.L., Suskin, M.A., Pines, S., Moon Trajectory Computational Capability Development. Technical Report 90-51, NASA Lewis Research Center, July 1990.

(2) Sackett, L.L., Malchow, H.L, Edelbaum, T.N., Solar Electric Geocentric Transfer with Attitude Constraints: Analysis. Technical Report NASACR-134927,The Charles Stark Draper Laboratory, Inc. August 1975.

1991

NASA/ASEE SUMMER FACULTY RESEARCH FELLOWSHIP PROGRAM

MARSHALL SPACE FLIGHT CENTER
UNIVERSITY OF ALABAMA IN HUNTSVILLE

AN ASSESSMENT OF SECONDARY LOSS REDUCTION TECHNIQUES
FOR STME LOX TURBINE

Prepared by	Mingking K. Chyu, Ph.D.
Academic Rank:	Associate Professor
Institution	Carnegie Mellon University Department of Mechanical Engineering
NASA/MSFC: Office: Branch:	Structure and Dynamics Lab. Computational Fluid Dynamics ED 32
MSFC Colleague:	Lisa W. Griffin
Date:	August 1991
Contract No.:	The University of Alabama in Huntsville NGT-01-008-021

One of the primary objectives of the National Launch System (NLS) program, explored jointly by NASA and several other government agencies, is to develop a new Space Transportation Main Engine (STME) which will perform better and is more reliable than the present Space Shuttle Main Engine (SSME). Preliminary design of the Oxidizer (LOX) turbine in STME has recently been completed by Pratt and Whitney (P&W). It is a single-stage, highly impulsive turbine with an approximately 170-degree deflection angle across the rotor. Due mainly to strong flow turning, the secondary loss in the rotor passage accounts for nearly 50% of the total loss over the entire stage, based on a mean-line prediction reported by P&W. To reduce such a significant loss with an aim to further improve STME performance has recently become one of the major research tasks for the Consortium Turbine Team at MSFC. As part of this team effort, the primary objective of the present study is to identify and examine prospective approaches for secondary loss reduction. Relevant information reported earlier in the open literature, primarily for jet-engine applications, has also been reviewed to a great extent. It is hoped that information gained from this study will promote further understanding toward these approaches and their potential applicability in STME turbines.

SECONDARY LOSS

The secondary loss is due to energy dissipation induced by the secondary flow in a blade passage. By definition, secondary flow is a recapitulation of flow motions which are deviated from the primary flow pattern in the passage. In classical turbine flow dynamics, the primary flow is governed by the potential theory, and it is two-dimensional in nature. The secondary flow in a turbine passage consists of two fundamental modes. The first mode is similar to the Dean-type flow motion existing in curve ducts and rotating channels. The velocity differential between the pressure side and suction side of a blade passage, which further induces non-uniform vortex stretching in the streamwise direction, is responsible for this phenomenon. Details of cascade flowfield in this respect have been extensively investigated in recent years as reported by Sieverding (1985).

The second mode, as a result of endwall-blade interaction, is initiated by a three-dimensional flow separation occurred upstream to the blade stage. This flow mode inherits more complex motion and is considered to be more accountable for the overall secondary loss, especially for blades with low aspect ratios. Figure 1 reveals a schematic sketch of cascade endwall flow structure given earlier by Sharma and Butler (1987). The separation occurred upstream forces boundary layer to roll-up and forming a flow structure similar to the well-known horseshoe vortex. Further downstream, the vortex splits into two legs, normally termed the pressure and the suction side legs, and they then enter the passage in a counter-rotating fashion and interact strongly with the mainstream. Immediately after it enters the passage, the pressure side-leg vortex is driven by the blade-to-blade pressure gradient and convected toward the suction side, meeting the surface near the minimum pressure point. This forms the well-known "passage vortex" which represents one of the most dominant features of the secondary flow and a key factor responsible for the overall secondary loss. Having reached the suction surface, the passage vortex and the suction-leg vortex roll up altogether from the endwall, and the size of this combined vortex increases toward the blade trailing edge. An increase in vortex size on the passage exit plane generally leads to a greater secondary loss. With this underlying notion in mind, an effective means for reducing the secondary loss must be capable of suppressing the growth of passage vortex.

MEANS FOR SECONDARY LOSS REDUCTION

The ways to reduce secondary loss can be classified into two different categories: active reduction and passive reduction. The former typically involves boundary layer blown off and/or sucked off, and it requires additional flow movers, which may complicate the system and induce other undesirable loss (e.g. coolant loss). Hence the present study focuses exclusively on passive

loss reduction techniques. A literature review reveals that methods for passive reduction include (1) blade endwall fillet, (2) blade leaning, (3) boundary layer fences or grooves.

Blade Endwall Fillet

Implementing a fillet at the junction between endwall and blade suction side is to temper the corner sharpness so as to form a rounded corner in the region. The resulting effect is a weakened suction-side leg vortex (horseshoe vortex), especially in the leading section of a blade passage. Therefore, its reduction mechanism lies primarily on reducing the turbulent transport and frictional loss near the endwall and, on the other hand, has little effect on the dominance of passage vortex originated from the pressure side of the neighboring blade. The reduction of turbulence transport has recently been confirmed by Chyu (1990) in a thermal study on cylinders with endwall fillets.

Based on his theoretical analysis, Debruge (1980) has posed several interesting features concerning the influence of fillet geometry on compressor blade rows. He has pointed out that an effective fillet can induce a boundary layer with thinner displacement thickness near the corner junction, which generally implies a lower frictional loss. However, the interference between the boundary layers from the blade sidewall and endwall in actual blade configurations often presents severe limitation to yield a rigorous prediction near the corner region. The conventional two-dimensional, thin-layer approximation appears to be invalid for this case as the transport characteristics in both streamwise and cross-stream directions are comparable. The boundary layer is clearly three-dimensional in nature. In addition, implementing different sizes of fillet along the chordwise direction, which varies in compliance with the thickness of local boundary layer, may be desirable for an effective loss reduction. Most of the assessments aforementioned, while fundamentally sensible, still lack experimental confirmation, especially for actual turbine configurations. This undoubtedly is necessary for STME LOx turbine where blade design involves strong turning. The effects of fillet can become secondary as the turn-induced flow separation likely prevails in the region.

Blade Leaning

One of the major effects for using leaned (bowed) blades is to re-structure the radial pressure gradient near the lower corner of the suction surface. Figure 2 displays a schematic view of curvilinearly lean blades, which has an essential feature that the angle between the suction surface and the endwall must be dihedral. From the standpoint of radial momentum balance, such an arrangement can establish a negative radial pressure gradient along the suction surface. Hence the fluid particles with low momentum originally residing in the corner of blade/endwall junction will migrate toward mainstream. By continuity, this region will be replenished by fluid with higher momentum from mainstream. This overall reduces boundary layer separation or vortex roll-up from the lower corner of suction surface.

According to studies by Hubner (1985) and Wang et al. (1987, 1988), implementing leaned blades usually results in a more uniform radial pressure distribution at the passage exit plane as compared to the straight blades. This, in fact, is considered to be the most important mechanism for secondary loss reduction with leaned blade, especially for multiple stage turbine. A uniform outlet flow condition from the upstream stage generally enhances the stage performance downstream. It also alleviates the loss involving flow unsteadiness. Because of rotating stress consideration, leaned blades are more favorably used in the stator rather than in the rotor. Caution must be taken to avoid any blade-leaning induced deviation from the designed turbine loading characteristics.

Boundary Layer Fences or Grooves

Using fences for secondary loss reduction consists of two different approaches: (1) fences on blade, and (2) fences on endwall. For the former, two fences, both conforming the blade chordwise profile, are mounted on the suction surface, one locates slightly away from the endwall and the other is near the tip. An effective blade fence can suppress the growth of boundary layer and prevent significant vortex roll up near the suction surface. With this concept in mind, the fence size should be in the order of boundary layer thickness. According to the data shown in studies by Prumer (1972) and Gallus and Kummel (1977), the local loss in the vicinity of fences is generally greater than that of a plain blade, but this is offset by considerable loss reduction in the section across mid-span. In a similar context, Gallus and Kummel (1977) also evaluated the effectiveness of grooves cut on the blade surface rather than mounting fences. Their data have suggested that grooves generally perform better than fences; however, this trend may be limited to the specific turbine and operating conditions tested.

Attaching fences on the endwall is a viable technique which presents direct blockage to the movement of passage vortex. Figure 3 shows a configuration of a fence placed in the mid-pitch between adjacent blades. With this geometry, Kawai et al. (1989) has reported that a fence with its height approximately 1/3 of inlet boundary layer thickness is the most effective for control of secondary flow and associated loss. Compared to the case without fence, this optimal condition can reduce the secondary loss by nearly 22%. However, velocity mappings measured at the blade exit plane reveal that the secondary flow structure is very sensitive to the fence height and pitchwise location. This implies that such an optimal condition may vary with differences in turbine design and operating conditions. In a earlier study, Prumper (1972) has used multiple fences to expand the range of effectiveness; nevertheless redundant fences may introduce additional endwall loss.

CONCLUDING REMARKS

It is conceivable that adopting one or several of the methods aforementioned can effectively reduce the secondary loss in the future STME LOx turbine. The most effective approach appears to be using leaning blades for the stator and endwall fences for the rotor. As a research initiative for turbine loss reduction undertaken by the Consortium Turbine Team at MSFC, this advanced concept will be investigated rigorously using numerical modeling. This will be followed by actual testings, possibly conducted at Technology Turbine Rig (TTR) presently being developed at MSFC. Knowledge gained from this research will not only benefit space shuttle turbine performance in the future, but will also improve fundamental understanding in controlling secondary loss for other turbine engines.

ACKNOWLEDGEMENT

REFERENCES

Chyu, M.K. (1990), "Heat Transfer and Pressure Drop for Short Pin-Fin Arrays with Pin-Endwall," *J. Heat Transfer,* Vol. 112, pp. 926-932.

Debruge, L.L. (1980), "The Aerodynamic Significance of Fillet Geometry in Turbocompressor Blade Rows," J. Engrg. for Power, Vol. 102, pp. 984-993.

Gallus, H.E. and Kummel, W. (1977), "Secondary Flows and Annulus Wall Boundary Layers in Axial-Flow Compressor and Turbine Stages," AGARD CP 214, Paper 4.

Hubner, J.H. (1985), "3-D Design of Turbine Airfoils," ASME Paper 85-GT-188.

Kawai, T., Shinoki, S. and Adachi, T. (1989), "Secondary Flow Control and Loss Reduction in a Turbine Cascade Using Endwall Fences," JSME Int. J., Ser. 2, Vol. 32, No. 3, pp. 375-387.

Prumer, H. (1972), "Application of Boundary Layer Fences in Turbomachinery," AGARDograph, No. 164, p.311-331.

Sieverding, C.H. (1985), "Recent Progress in the Understanding of Basic Aspects of Secondary Flows in Turbine Blade Passages," J. Engrg. for Power, Vol. 107, pp. 248-257.

Sharma, O.P. and Butler, T.L. (1987), "Predictions of Endwall Losses and Secondary Flows in Axial Flow Turbine Cascades," J. Turbomachinery, Vol. 109, No. 2, pp. 209-236.

Wang, Z-Q, Han, W-J and Xu, W-Y (1987), "An Experimental Investigation into the Influence of Diameter-Blade Height Ratios on Secondary Flow Losses in Annular Cascades with Leaned Blades," ASME Paper 87-GT-131.

Wang, Z-Q, Xu, W-Y, Han, W-J and Bai, J. (1988), "An Experimental Investigation into the Reasons of Reducing Secondary Flow Losses by Using Leaned Blades in Rectangular Turbine Cascades with Incidence Angle," ASME Paper 88-GT-4.
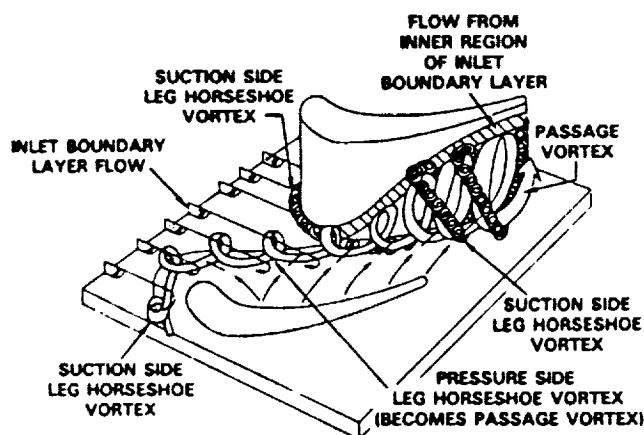
Figure 1. Secondary Flow
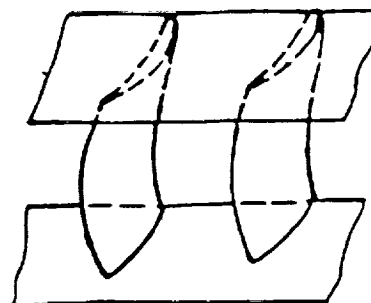
Figure 2. Curvilinearly Leaned Blade
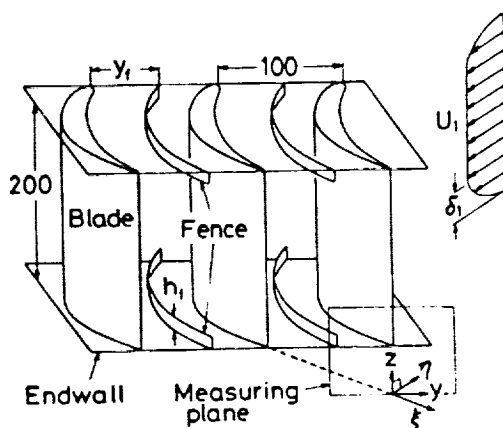
Figure 3. Endwall Fences

1991
NASA/ASEE SUMMER FACULTY FELLOWSHIP PROGRAM

Marshall Space Flight Center
The University of Alabama

An Overview of the Current Technology Relevant to the Design and Development of the Space Transportation Main Engine (STME)

Prepared By: Digendra K. Das, Ph.D.

Academic Rank: Associate Professor

Institution: SUNY Institute of Technology
UTICA/Rome, NY

NASA/MSFC Office: Science & Engineering

Laboratory: Structures & Dynamics
Laboratory

Division: Thermal Engineering and
Life Support Division

Branch: Thermal Analysis Branch (ED64)

MSFC Colleague: James W. Owen
Brian K. Goode

Contract No: NGT 01-008-021
The University of Alabama

NATIONAL LAUNCH SYSTEM (NLS)

The National Launch System (NLS), previously known as Advanced Launch System (ALS), is a joint program of the Department of Defense (DoD) and National Aeronautics and Space Administration (NASA). The program was initiated in July 1987 and was subdivided into several phases. The first phase was completed in August 1988 and the seven contractors participating in it were Martin Marietta, General Dynamics, Boeing, McDonnell Douglas, Rockewell, Hughes, and United Technologies. The Phase II of the NLS program is currently in progress. According to the current planning, NLS should achieve an initial launch capability (ILC) in 1998 and initial operational capability (IOC) in 2000 (References 1 and 2).

NLS has three primary objectives:

1. First, it is envisioned as a family of new generation launch systems, applying both existing and new technology to achieve the desired operability and cost goals, ultimately providing a capability for delivering a rang of cargo sizes from approximately 1000 to 220,000 lbs., to low earth orbit.

2. Second, ALS deployment will enable deployment of an ambitious Strategic Defense Initiative (SDI) architecture or a Lunar and Mars infrastructure program-a feat that is physically and fiscally unattainable with current systems.

3. Third, and equally important, current launch vehicle programs such as Titan, Delta, and Altas, will clearly benefit from ALS advanced technologies that will yield cost reductions, increased capacity, and improved overall system performance.

The NLS program is cost-optimized rather than performance-optimized and will utilize advanced technology and innovative management and design approaches to achieve an ambitious, congressionally mandated cost goal of $300/lb to low earth orbit by the year 2005.

Concepts for the Reference Vehicles

Several basic concepts were identifed for the reference vehicles at the end of phase I of the NLS program. Each of these concepts uses a common cryogenic (liquid oxygen and hydrogen) core engine called Space Transportation Main Engine (STME) being developed by the Marshall Space Flight Center (MSFC).

The three contractors involved in the design and development of STME are: Aerojet,

The three contractors involved in the design and development of STME are: Aerojet, Pratt & Whitney, and Rocketdyne.

The tasks assigned to each of these contractors are indicated below:

Electromechanical Propellant Control, (Aerojet)

Engine Controller Development, (Aerojet)

Full Scale Split Expander Contract, (Not Awarded)

LOX Turbopump, (Pratt & Whitney)

Liquid Hydrogen Turbopump (Aerojet)

Liquid Fuel Turbopump, (Rocketdyne)

Main Injector Thrust Chamber, Nozzle, and Gas Generator, (Aerojet)

Subscale and Large Scale Thrust Chamber, (Rocketdyne)

Large Scale Injector, (Aerojet, Rocketdyne, Pratt & Whitney)

The Current Summer Project

The project described in this report was undertaken by the author as a part of the NASA/ASEE Summer Faculty Fellowship Program 1991, for the Thermal Analysis Branch (ED64) of NASA, Marshall Space Flight Center, Alabama. The duration of the project was ten weeks (June 3-August 9, 1991).

The development of the STME being in its early stage, it was decided that the objective of this ten week summer project should be to review the latest literature relevant to STME. It was also decided that this literature search and review should be directed toward the specific topics of interest to the Thermal Analysis Branch (ED64), MSFC. Hence, the search was focused on the following engine components:

1. Gas Generator

2. Hydrostatic/Fluid Bearings

3. Seals/Clearances

4. Heat Exchanges

5. Nozzles

6. Nozzle/Main Combustion Chamber joint

7. Main Injector Face Plate

8. Rocket Engine - General

The Methodology of the Literature Search

The research was broadly divided as follows:

1. Conference papers

2. Journal papers.

The selection of the time period chosen for this search was influenced by the following two factors:

a. The ALS/STME program was initiated in July 1987

b. Limited time available for the summer program (ten weeks).

Hence, the literature scan was targeted to the following time periods:

1. Conference papers (June 1991 - 1986) 6 years

2. Journal papers - approximately from June 1991-1980 about 11 years

At the end of the search process, approximately about 150 papers were identified as being relevant to the components indicated earlier. The distribution of the papers/models are shown below:

Components	No. of Papers/Models
Gas Generator	7
Hydrostatic/Fluid Bearings	25
Seals/Clearances	22
Heat Exchangers	17
Nozzles	32
Nozzle/Main Combustion Chamber Joint	2
Main Injector Face Plate	2
Rocket Engines-General	42
Total	149

The majority of the papers/models indicated above are found in the following journals/conferences:

1) Journal of Space Craft & Rockets

2) Transactions of the ASME-Journal of Heat Transfer

3) International Journal of Heat and Mass Transfer

4) AIAA/ASME/SAE/ASEE Joint Propulsion Conference

5) AIAA Aerospace Sciences Meeting

A report with brief reviews of some of these papers/models is available at the Thermal Analysis Branch (ED64) of MSFC.

REFERENCES

1.   Stofan, A.J. & Isakowitz S.J. "Design Challenges for the Advanced Launch System." AIAA-89-2748, AIAA/ASME/SAE/ASEE, 25th Joint Propulsion Conference, Montery, CA. July 10-12, 1989

2.   Wolfe, M.G. "Joint DoD/NASA Advanced Launch System: Pathway to Low-Cost, Highly Operable Space Transportation." Space Commercialization Launch Vehicles and Programs. Edited by Shahrokhi etall. Progress in Astronautics and Aeronautics. Vol. 126,1990. ISBN 0-930-403-75-4 (AIAA)

1991

NASA/ASEE SUMMER FACULTY FELLOWSHIP

MARSHALL SPACE FLIGHT CENTER
THE UNIVERSITY OF ALABAMA

EXPERIMENTAL INVESTIGATION OF A SOLID ROCKET COMBUSTION SIMULATOR

Prepared by:	Robert A. Frederick, Jr., PhD.
Academic Rank:	Assistant Professor
Institution:	University of Alabama in Huntsville

NASA/MSFC:

Office:	Propulsion Laboratory
Division:	Propulsion Systems
Branch:	Solid Propulsion
MSFC Colleague:	Benjamin Goldberg
Contract No.:	NGT-01-008-021 University of Alabama

K

INTRODUCTION:

The response of solid rocket motor materials to high-temperature corrosive gases is usually accomplished by testing the materials in a subscale solid rocket motor. While this imposes the proper thermal and chemical environment, a solid rocket motor does not provide practical features that would enhance systematic evaluations such as: the ability to throttle for margin testing, on/off capability, low test cost, and a low-hazards test article. Solid Rocket Combustion Simulators (SRCS) are being evaluated by NASA to test solid rocket nozzle materials and incorporate these essential practical features into the testing of rocket materials.

The SRCS, sketched in Figure 1, is designed to generate the thermochemical environment of a solid rocket. It uses hybrid rocket motor technology in which gaseous oxygen (Gox) is injected into a chamber containing a solid fuel grain. Specific chemicals are injected in the aft mixing chamber so that the gases entering the test section match the temperature and a non-dimensional erosion factor B' to insure similarity with a solid motor. Because the oxygen flow can be controlled, this approach allows margin testing, the ability to throttle, and an on/off capability. The fuel grains are inert which makes the test article very safe to handle.

The objective of this work was to establish the baseline operating characteristics of a Labscale Solid Rocket Combustion Simulator (LSRCS). This included establishing the baseline burning rates of plexiglass fuels and the evaluation of a combustion instability for hydroxy-terminated polybutadyene (HTPB) propellants. The scope of the project included: 1) activation of MSFC Labscale Hybrid Combustion Simulator, 2) testing of plexiglass fuel at Gox ranges from 0.025 to 0.200 lb/s, 3) burning HTPB fuels at a Gox rate of 0.200 lb/s using four different mixing chamber configurations, and 4) evaluating the fuel regression and chamber pressure responses of each firing.

APPROACH:

A complete facility for testing the LSRCS was established at Marshall Space Flight Center during this project. The basic motor hardware was acquired from Thiokol Corporation, Utah. The system was installed in Building 4583, Cell 103. Specific work accomplished included adaptation of an existing Gox feed system, modification of the motor hardware to accept four additional pressure measurements, and installation of a dedicated instrumentation and control system.

Motor controls allowed the starting and stopping of the motor. The Gox flowrate was metered by controlling the pressure upstream of a venturi. Ten seconds prior to ignition, Gox flow was initiated. A current applied to an NSI squib ignited the motor which was allowed to burn for two seconds. Termination of the Gox flow and the immediate introduction of nitrogen gas stopped the combustion.

Instrumentation supplied basic data on the motor pressure, temperature, and fuel burning rate. A forward, an aft, and a differential (forward minus aft) pressure gage measured the low-frequency (0-50 hz, digital; 0-6,500 hz analogue) chamber pressures. High-frequency (10 to 20,000 hz analogue) pressure transducers monitored the pressure fluctuations forward and aft. Eight thermocouples measured the forward and aft external temperature of the motor. A precision balance was used to weigh the grains before and after each test to determine the mass consumed during the test. Video cameras monitored the motor hardware and plume emissions.

The first series of firings determined the effect of Gox flow rate on the burning rate of plexiglass fuel. Flow rates of 0.025, 0.050, 0.100, and 0.200 lb/sec covered the desired operating range. The fuel segments were machined from cast material and pressed into phenolic sleeves. Four 2.5-in. long segments with a 0.82-in. port were stacked inside the motor. The motor was run with a long aft mixing section and a 0.309-in. diameter stainless steel nozzle.

The second series of firings investigated the effect of mixing chamber length on combustion chamber pressure oscillations. A Gox flow rate of 0.200 lb/sec was specified for each of the tests. The HTPB fuel was vacuum cast and contained 85% R45 and 15% N-100 curative. The grains were cast into 2.5-in. long phenolic sleeves. Four grains were used for each motor firing. The motor was tested in four configurations: A) short mixing section, no baffle; B) long mixing section, no baffle; C) short mixing section, stainless steel baffle; and D) long mixing section, wood baffle.

RESULTS/DISCUSSION:

Table 1 summarizes the test data and results for the LSRCS firings. The test number references the test requests for test series P252A. The table lists the average chamber pressure during firing, CP; the maximum skin temperature of the motor; the mass flow rate of the fuel; the actual oxidizer-to-fuel ratio; the motor characteristic velocity, C^*; and the burning rates of each segment and their test average.

Figure 2 shows the average burning rate as a function Gox flow for all the tests. A least-squares curve fit for the plexiglass results yields:

$$r = 0.032 \ Gox^{0.029}$$

The excessive scatter in the plexiglass burning rates was unexpected . Examination of the burning rates of individual segments within each firing showed no extreme deviation from the mean rate for the test. Examination of the data yields no immediate explanation for the scatter. The HTPB average burning rates were more consistent.

The results of two HTPB mixing chamber tests are shown in Figure 3. The plots show the head-end chamber pressure

measurements for the short and long aft mixing section tests that were performed without a baffle. The pressure showed 100 psi peak-to-peak oscillations for the short mixing configuration. The amplitude of the oscillation decreased slightly during the burn. The oscillations were greatly attenuated when the HTPB propellant was burned with a long aft mixing section. The peak-to-peak amplitude of the fluctuations was about 50 psi. The attenuation of the pressure oscillations suggest a combustion source rather than an issue related to the Gox feed system.

CONCLUSIONS:

This project established a 6-test-per day testing capability for the LSRCS at the MSFC. Initial studies with plexiglass fuel showed unexpected variability in average burning rates. The HTPB study showed a combustion chamber pressure oscillation that is influenced by the length of the aft mixing chamber. The Labscale Solid Rocket Combustion Simulator will be an effective instrument to investigate the physical mechanisms that control this pressure instability. Validating these combustion mechanisms on a small test provide information for the design of larger scale (more expensive) systems.

Table 1. Test Results for LSRCS Firings

TEST	GOX(DER) LBS/S	GOX(ACT) LBS/S	M/C	FUEL	THROAT DIA. (IN)	PRE TEST WT FWD-AFT (g)	POST TEST WT FWD-AFT (g)	DP PSI	PMAX FWD (P)	PMIN AFT (P)	m (F wt) LBS/S	O/F	C* (FT/S)	r (WPeak) IN/S	r (SAvg) IN/S
001	0.025	.070	LONG MIXING SECTION NO BAFFLE	PLEX	0.348	66.728 / 66.364 / 66.467 / 66.555	56.9853 / 57.7727 / 56.179 / 56.2143	56	66	63	0.01303	2.1	7956	0.01103	0.010 / 0.011 / 0.008 / 0.008
002	0.005	.061	LONG MIXING SECTION NO BAFFLE	PLEX	0.348	50.961 / 66.737 / 66.341 / 66.515	53.662 / 56.4300 / 56.7606 / 56.036	100	175	67	0.0100	2.5	3597	0.01782	0.024 / 0.015 / 0.014 / 0.018
003	0.05	.064	LONG MIXING SECTION NO BAFFLE	PLEX	0.308	66.1645 / 66.5468 / 56.5353 / 50.6423	64.6573 / 56.7870 / 56.6053 / 56.66	100	175	66	0.01035	2.0	3166	0.01733	0.024 / 0.015 / 0.014 / 0.016
666	0.1	.077	LONG MIXING SECTION NO BAFFLE	PLEX	0.308	66.7079 / 66.3645 / 66.1267 / 66.1374	66.4655 / 37.8173 / 37.7178 / 57.1503	140	110	65	0.01345	3.7	3797	0.0123	0.017 / 0.010 / 0.010 / 0.012
006	0.2	.150	LONG MIXING SECTION NO BAFFLE	PLEX	0.308	66.4628 / 66.1736 / 66.7771 / 66.7124	55.7064 / 57.2216 / 57.5565 / 56.9945	270	110	65	0.01655	6.6	3667	0.01482	0.018 / 0.012 / 0.013 / 0.017
007	0.2	.100	LONG MIXING SECTION NO BAFFLE	HTPB	0.308	50.8217 / 49.7474 / 50.2640 / 50.1949	42.340 / 46.0065 / 42.2100 / 42.0957	350	160	66	0.03481	5.5	3584	0.03045	0.036 / 0.041 / 0.030 / 0.026
008	0.2	.201	LONG MIXING SECTION NO BAFFLE	HTPB	.300	50.3065 / 43.2467 / 50.164 / 49.4608	41.8378 / 40.7473 / 38.6490 / 40.0795	480	185	66	0.03066	5.1	4543	0.04063	0.040 / 0.038 / 0.042 / 0.040
009	0.2	.262	LONG MIXING SECTION WOOD BAFFLE	HTPB	.360	50.5364 / 50.0072 / 50.714 / 50.0521	42.011 / 43.000 / 41.6653 / 40.497	470	191	91	0.03500	5.0	4497	0.03643	0.036 / 0.038 / 0.044 / 0.046
010	0.2	.210	SHORT MIXING SECTION NO BAFFLE	HTPB	.300	50.565 / 50.1400 / 48.566 / 50.471	37.0125 / 38.0633 / 38.0365 / 40.1464	490	NA	NA	0.045	4.7	4375	0.04714	0.053 / 0.035 / 0.041 / 0.043
011	0.2	.214	SHORT MIXING SECTION STEEL BAFFLE	HTPB	.300	50.5077 / 52.7764 / 50.6356 / 50.0930	42.9956 / 43.331 / 42.4073 / 40.9015	500	>210	90	0.03786	5.8	4516	0.04020	0.037 / 0.042 / 0.036 / 0.044
012	0.2	.210	LONG MIXING SECTION NO BAFFLE	PLEX	0.306	66.0782 / 66.365 / 66.758 / 66.4468	51.6707 / 54.7000 / 54.0034 / 51.430	340	130	65	0.03109	7.6	3446	0.02721	0.032 / 0.032 / 0.034 / 0.031
013	0.1	0.1	LONG MIXING SECTION NO BAFFLE	PLEX	0.308	66.7153 / 66.8064 / 56.5696 / 66.7541	56.376 / 56.2021 / 56.8700 / 57.7952	*	*	*	0.01441	5.8	N/A	0.01506	0.017 / 0.011 / 0.011 / 0.013
014	0.05	0.05	LONG MIXING SECTION NO BAFFLE	PLEX	0.308	66.3736 / 66.642 / 66.0775 / 70.061	56.1872 / 57.3040 / 57.5657 / 56.4047	*	*	*	0.01662	3.8	N/A	0.01496	0.020 / 0.013 / 0.012 / 0.014
015	0.025	0.025	SECTION NO BAFFLE	PLEX	0.308	66.6421 / 66.6784 / 56.4914 / 60.1496	56.7706 / 56.7116 / 56.7386 / 56.3640	*	*	*	0.00073	2.6	N/A	0.00666	0.013 / 0.008 / 0.007 / 0.006
017	0.2	.205	LONG MIXING SECTION NO BAFFLE	HTPB	0.308	40.7601 / 40.7107 / 40.5815 / 40.5215	40.4700 / 41.0294 / 30.2753 / 30.329	450	165	65	0.0447	4.6	4262	0.04665	0.043 / 0.041 / 0.040 / 0.056
018	0.2	.207	LONG MIXING SECTION NO BAFFLE	HTPB	0.308	40.567 / 56.7579 / 56.1386 / 56.415	40.8042 / 41.5030 / 30.5330 / 37.9782	450	160	65	0.04070	4.5	4270	0.04765	0.044 / 0.041 / 0.040 / 0.057

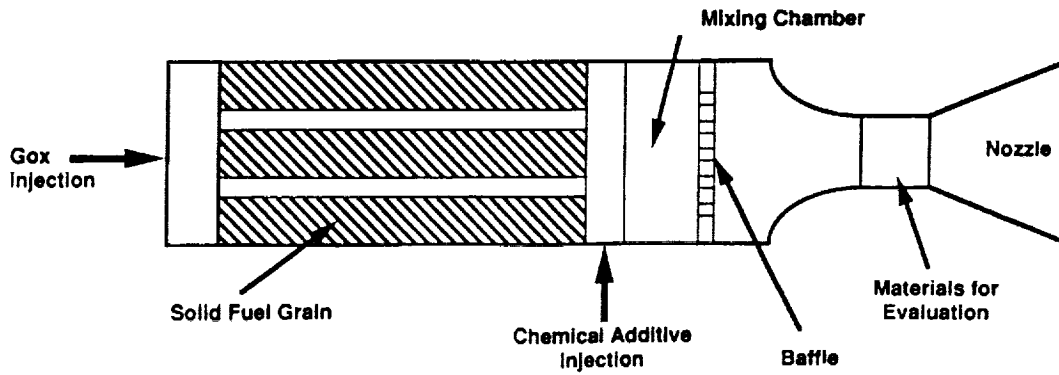*DIGITAL AND ANALOG DATA INCOMPLETE

K-3

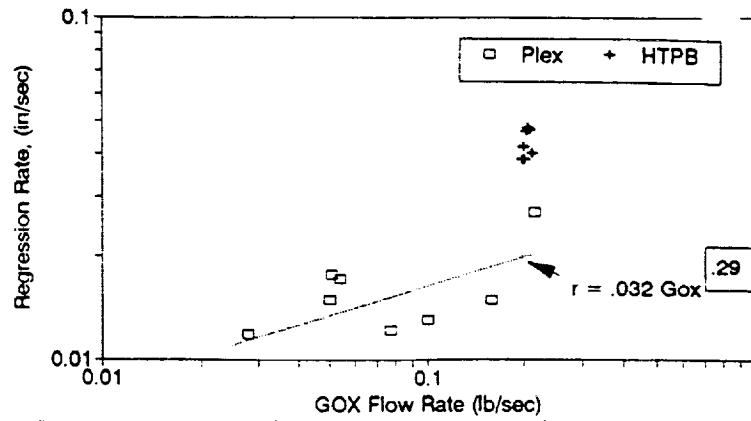Figure 1. Solid Rocket Combustion Simulator

Figure 2. LSRCS Average Burning Rates vs. Gox Flow Rate

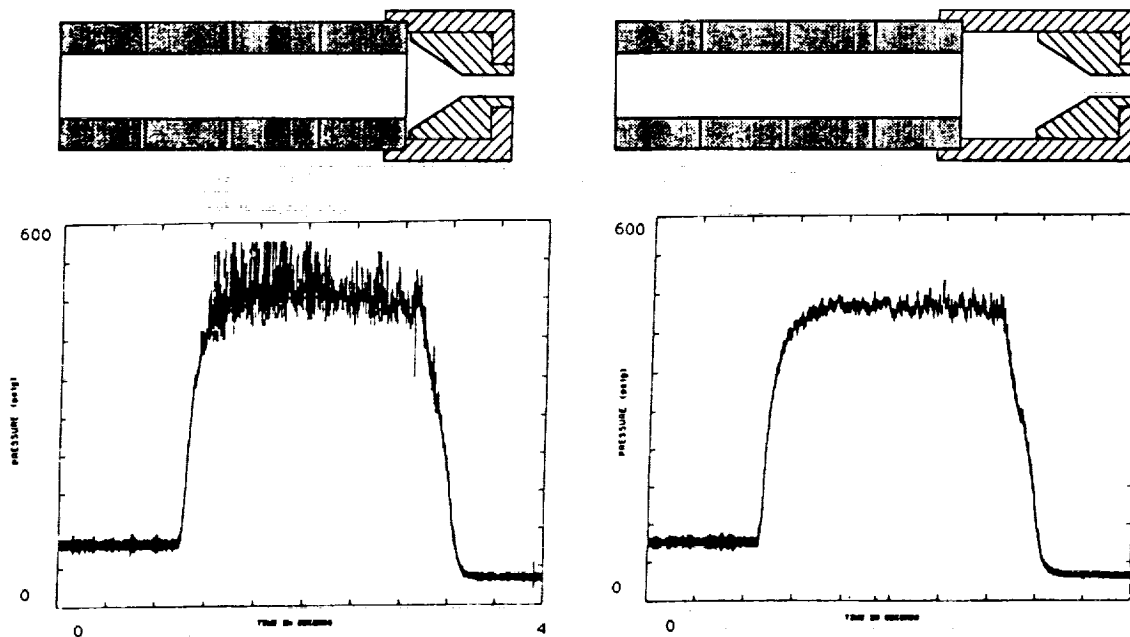Short mixing section   Long mixing section

Figure 3. HTPB Mixing Chamber Test Results

K-4

1991

NASA/ASEE SUMMER FACULTY FELLOWSHIP PROGRAM

MARSHALL SPACE FLIGHT CENTER
THE UNIVERSITY OF ALABAMA

USE OF PHOTOSTRESS TECHNIQUES TO CHARACTERIZE THE
MECHANICAL BEHAVIOR OF WELDMENTS

Prepared by: Samuel C. Gambrell, Jr. Ph.D.

Academic Rank: Professor

Institution: The University of Alabama
                                      Tuscaloosa, Department of
                                      Engineering Mechanics

NASA/MSFC:

    Office: Materials and Processes

    Division: Metallic Materials

    Branch: Metallurgy Research

MSFC Colleague: Thomas F. Morris
                                      Dennis R. Moore

Contract No.:   NGT-01-008- 021

L

INTRODUCTION

Photoelastic coatings are useful to view strains in a large field and to examine strain gradients in the field. Contrary to strain gages which average strains along their length, photoelastic coatings provide measurements of strain over a gage length of essentially zero (at a point).

When testing is done using specimens having welds between parent material, there are, in general, four zones in which strains may be significantly different. These zones are (a) the weld material, (b) the fusion boundary, (c) the heat affected zone, and (d) the parent material. To date, most all strain measurement on welded specimens has been done using strain gages to measure strain in the various zones, thereby averaging across the strain gradient and across zone boundaries in some cases.

BASIC TECHNIQUE

In an effort to eliminate strain averaging, photoelastic coatings were used to characterize the mechanical behavior of weldments when tested in uniaxial tension. Data were taken at various points along the specimen and were used to construct stress-strain curves. The basic strain-optic law states that

$$\gamma_{max} = \epsilon_1 - \epsilon_2 = \frac{N\lambda}{2t_p K} = Nf \qquad [1]$$

where N = fringe order,
λ = wavelength of light $= 22.7 \times 10^{-6}$ inches,
t_p = thickness of coating, and
K = calibration constant of coating.

Since $\epsilon_2 = -\mu\epsilon_1$ for uniaxial tension, equation [1] may be written for the elastic range as

$$\epsilon_1 = \frac{Nf}{(1+\mu)} \qquad [2]$$

where μ = Poisson's ratio. For the inelastic range, Poisson's ratio must be replaced by the contraction ratio, α, which Chakrabarty (1) approximates as

$$\alpha = 0.5 + (0.5 - \mu)(\frac{E_t}{E}) \qquad [3]$$

where E_t = the tangent modulus and
E = the modulus of elasticity.

Thus, equation [2] becomes

$$\epsilon_1 = \frac{Nf}{(1+\alpha)} \qquad\qquad [4]$$

for the inelastic range. The contraction ratio may be calculated for each value of uniaxial stress using a tangent modulus curve constructed from a regular stress- strain curve. Contraction ratios for the weld material and parent material were calculated, and were approximated for the fusion boundary and heat affected zones.

Since strains exceeding the 0.2 percent offset are seldom allowed in design, data collection was limited to maximum strains of from one to two percent where the engineering and true stress-strain curves are essentially the same. Figure 1 shows an example of the stress-strain curves obtained for the various zones using photoelastic coatings. Color photographs of the fringe patterns in the coatings clearly showed the strain gradients and the four zones previously mentioned.

CONCLUSION

In comparison to use of strain gages, more technical expertise, calculations, and care are required to successfully use the photoelastic coating technique. However, strain averaging is eliminated and, up to a maximum strain of from one to two percent, photoelastic coatings provide a useful method to characterize material behavior.

References

1. Chakrabarty, J., Theory of Plasticity, McGraw Hill Book Co., Inc., New York, 1987.

2. "Operating Instructions and Technical Manual-Strain Measurement with the 030-Series Reflection Polariscope," Measurements Group, Inc., Raleigh, NC.
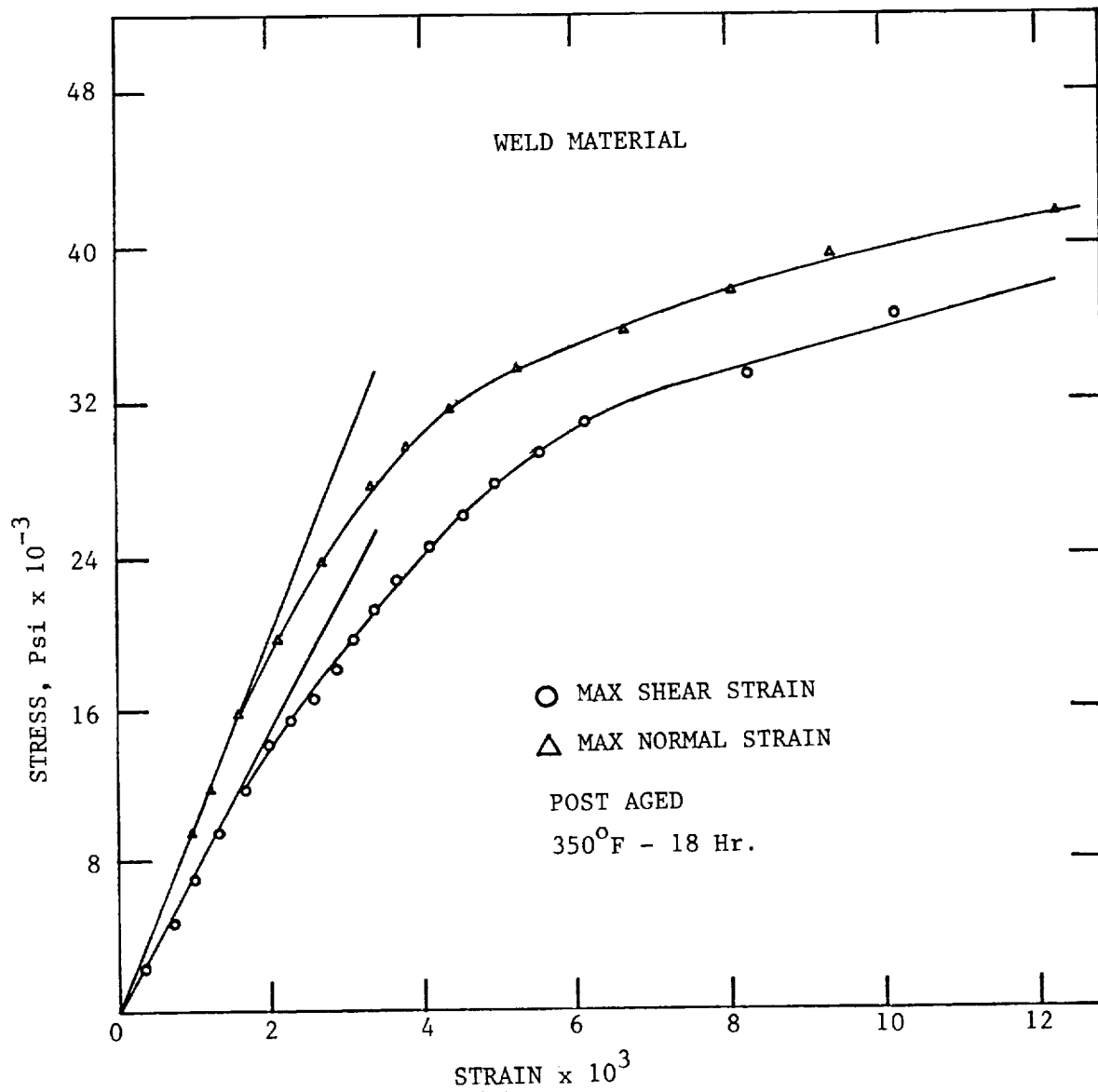
FIGURE 1

L- 3

1991

NASA/ASEE SUMMER FACULTY FELLOWSHIP PROGRAM

MARSHALL SPACE FLIGHT CENTER
THE UNIVERSITY OF ALABAMA IN HUNTSVILLE

RECOMMENDATIONS FOR AN EXECUTIVE
INFORMATION SYSTEM (EIS)
FOR THE NASA ACCOUNTING AND FINANCIAL
INFORMATION SYSTEM (NAFIS)

Prepared by: Ernest Preston Goss

Academic Rank: Associate Professor

Institution: University of Southern Mississippi &
                      Dept. of Management Information Systems

NASA/MSFC:

        Laboratory: Institutional and Program Support
        Division: Information Systems
        Branch: Data Systems

MSFC Colleagues: Mr. Alan Forney & Mr. Neil Rodgers

Contract No: NGT-01-008-021
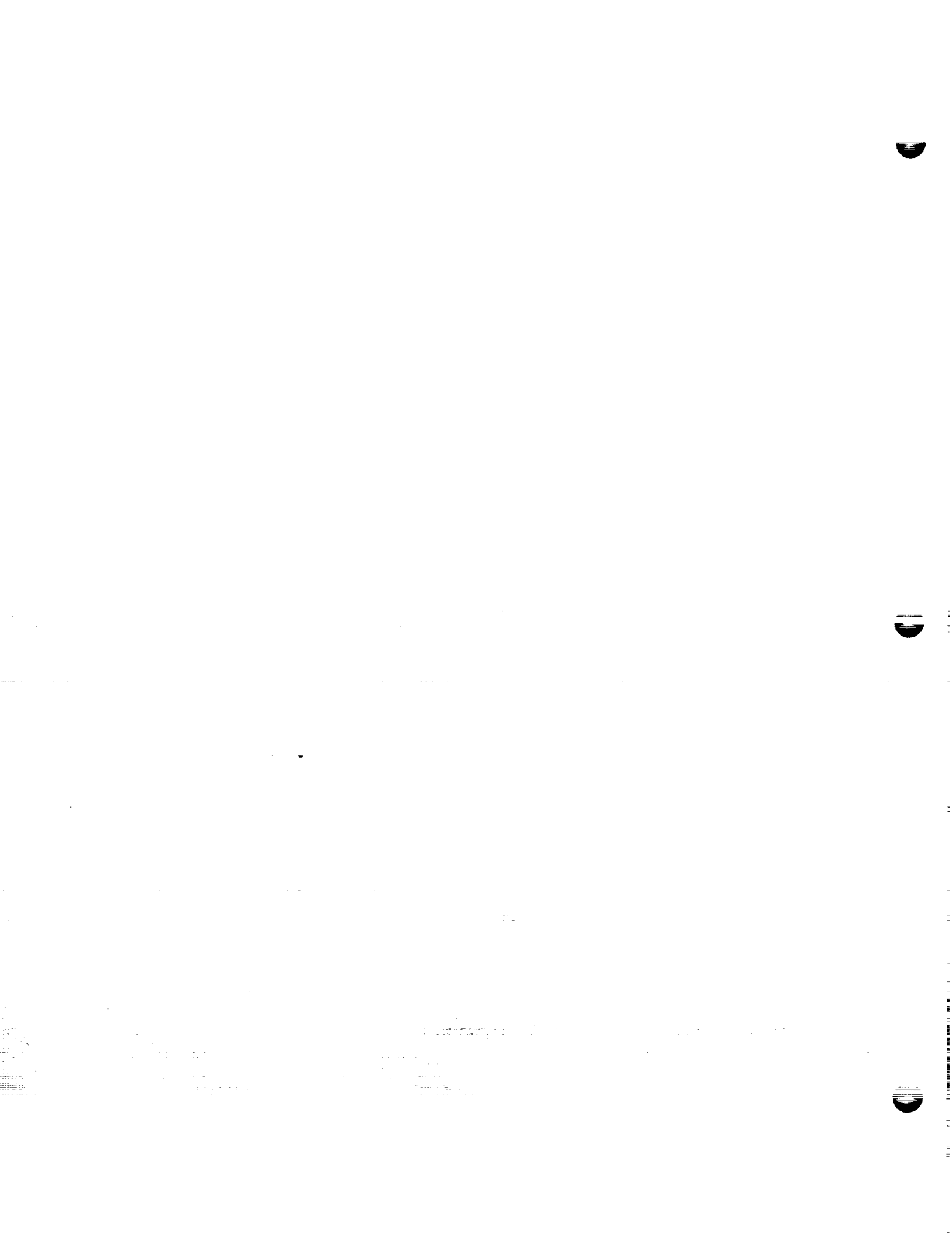
RECOMMENDATIONS FOR AN EXECUTIVE INFORMATION SYSTEM (EIS) FOR THE NASA ACCOUNTING AND FINANCIAL INFORMATION SYSTEM (NAFIS)

In partial fulfillment of my Summer Faculty Fellowship contractual obligation, Mr. Alan Forney and Mr. Neil Rodgers provided me with a "statement of work" which in summary required me to:

I.   Survey state-of-the-art computing architectures, tools and technologies for implementing an EIS.

II.   Review MSFC capabilities and efforts to-date in developing an EIS for Shuttle Projects Office and the Payloads Project Office.

III.   Review management reporting requirements for the NAFIS project in the areas of cost, schedule, and technical performance. Insure that the EIS fully supports these requirements.

IV.   Develop and implement a pilot concept for a NAFIS EIS.

The following represents a summary of my findings in fulfillment of this contractual obligation. In addition to the following EXECUTIVE SUMMARY, a separate study was completed and available under a separate cover.

EXECUTIVE SUMMARY

In order for managers to use the NASA Accounting and Financial Information System (NAFIS) more effectively, an EIS component must be added which supplies data specific to the manager's needs through a simple, intuitive graphical interface.[3] This EIS module will deliver mission critical information to the manager in a format which enhances decision making.

The following recommendations represent the summary findings of this initial survey regarding the implementation of a NAFIS EIS:

1. Due to the difficulty of specifying EIS requirements in advance, prototyping is recommended.

---

[3]The MITRE Study, examining the MSFC MIS, concludes that a GUI would greatly enhance the MSFC MIS.

a. Prototype should support multiple platforms.
b. Prototype should not be a "throw away" development but should instead be a first step in a production EIS.
c. Prototype should be modular in design and be able to download data from the NAFIS database residing either on the IBM 3090 or the VAX 4000.

2. EIS must provide access to the current E-Mail system and to other Data General (DG) applications used by managers.

3. No new databases should be created to support the EIS. The EIS should, instead, extract data from the NAFIS database as demanded by the decision maker. The EIS should not run in "real" time in terms of the NAFIS database residing on the IBM 3090 host.

4. Due to the existence of multiple environments, multiple locations, and long time horizon, a commercial off-the-shelf (COTS) EIS development tool is recommended. Based upon initial reviews, the ComShare EIS product is recommended in combination with "data pipelines."

5. In order to enhance interoperability between the IBM host and other hardware devices, Hewlett-Packard's NewWave, VAX's Pathworks or ComShare's EasyTrieve should be implemented on personal computers. In addition to adding access across heterogenous devices, these products would reduce overall cost by negating the need for mainframe EIS products.

6. Several recommendations contained in the MITRE Study impinge directly on the EIS and are adopted for the NAFIS EIS:

a. Initial prototype should be in a client/server environment with the travel module.

1) The MITRE Study recommends migration of applications to the client/server environment.
2) The movement to a client/server architecture is necessary to support the EIS capabilities currently in the market and to insure adequate response time.

b. The MITRE Study recommends the movement away from menus to a graphical user interface (GUI). This study likewise recommends an EIS development methodology that makes maximum use of a graphical user interface. For many managers, this will necessitate the replacement of the DG nodes, which cannot support this interface. However, users of NAFIS who do not demand a GUI, such as clerical personnel, may continue to use the DG nodes until they are inconsistent with overall NAFIS goals.

1991

NASA/ASEE SUMMER FACULTY FELLOWSHIP PROGRAM

MARSHALL SPACE FLIGHT CENTER
THE UNIVERSITY OF ALABAMA IN HUNTSVILLE

IGNITION TRANSIENT ANALYSIS OF SOLID ROCKET MOTOR

Prepared By: Samuel S. Han, Ph.D.

Academic Rank: Associate Professor

Institution: Tennessee Technological
                                      University, Department of
                                      Mechanical Engineering

NASA/MSFC:

        Laboratory: Propulsion
        Division: Propulsion Systems
        Branch: Performance Analysis

MSFC Colleague: S. Don Bai, Ph.D.
                                      Charles F. Schafer, Ph.D.

Contract No.:   NGT-01-008-021
                                      The University of Alabama
                                      in Huntsville

INTRODUCTION

Measurement data on the performance of space shuttle solid rocket motors show wide variations in the head-end pressure changes and the total thrust build-up during the ignition transient periods. To analyse the flow and thermal behavior in the tested solid rocket motors, a 1-dimensional, ideal gas flow model via SIMPLE algorithm was developed [4]. Numerical results showed that burning patterns in the star-shaped head-end segment of the propellent and the erosive burning rate are two important factors controlling the ignition transients.

The objective of the present study is to extend the model to include the effects of aluminum particle commonly used in solid propellents. To treat the effects of aluminum-oxide particles in the combustion gas, conservation of mass, momentum and energy equations for the particles are added in the numerical formulation and integrated by following IPSA [5] approach.

METHOD OF ANALYSIS

Governing Equations

Conservation of mass is

$$\frac{\partial}{\partial t}(r_i \rho_i A) + \frac{\partial}{\partial x}(r_i \rho_i u_i A) = (\omega_i \rho_{PR} - r_i \rho_i) r b + \dot{m}_{ig} , \tag{1}$$

where subscript i indicates i component, A is the cross-sectional area of the port, r_i is the volume fraction , ρ_i is the material density, u_i is the velocity, ω_i is the mass fraction in the propellent, ρ_{PR} is the density of the propellent, b is the perimeter of the burning cross-section, $\dot{m}_{ig}$ is the igniter gas flow rate. Burning rate of the propellent is given by [2]

$$r = r_{ref} (P/P_{ref})^n + \alpha_e G^{0.8} D_n^{-0.2} exp(-\beta_e r \rho_{PR} / G) . \tag{2}$$

The first part in the RHS of eqn (2) is the standard burning rate and the second part the erosive burning rate. Conservation of mass also requires that

$$\sum r_i = 1.0 \quad ; \quad \sum \omega_i = 1.0 . \tag{3}$$

Conservation of linear momentum is

$$\frac{\partial}{\partial t}(r_i \rho_i u_i A) + \frac{\partial}{\partial x}\left[A\left(r_i \rho_i u_i^2 - r_i \mu_i \frac{\partial u_i}{\partial x}\right)\right] = -r_i A \frac{\partial P}{\partial x} \tag{4}$$

$$- \tau_{w_i} \ell_w - r_i \rho_i r b u_i + A F_{-j} .$$

Thermodynamic pressure of the system is due to gas phase only and is given by

$$P = \rho_i R_i T_i f(\rho_i) , \tag{5}$$

where f(ρ_i) is a correction needed for high pressure gas [3]. The wall shear stress is given by

$$\tau_{w_1} = \tfrac{1}{3} f \rho_1 u_1^2 , \tag{6}$$

where f is the friction factor obtained by measurement.
The inter-phase friction force is given by [1]

$$F_{2i} = \left(18 \, r_2 / d_2^2 \right) \mu_1 \left(u_2 - u_1 \right) \left(1 + R_e^{2/3} / 6 \right) , \tag{7}$$

where d_2 is the particle diameter and the Reynolds number is
defined by

$$R_e = \rho_1 | u_2 - u_1 | d_2 / \mu_1 . \tag{8}$$

Energy conservation is , in terms of internal energy,

$$\frac{\partial}{\partial t} \left(r_i \rho_i e_i A \right) + \frac{\partial}{\partial x} \left[A \left(r_i \rho_i e_i u_i - r_i \frac{k_i}{c_{v_i}} \frac{\partial e_i}{\partial x} \right) \right] =$$

$$- r_i \rho \frac{\partial (u_i A)}{\partial x} + u_i \tau_{w_i} P_w + \Phi_i - q_i P_w + A Q_{ij} \tag{9}$$

$$+ A F_{ij} u_{ij} + \omega_i \rho_{PR} r b h_{f_i} + \dot{m}_{ij} h_{ij} ,$$

where k_i is thermal conductivity, h_{f_i} is the enthalpy of formation,
h_{ij} is the enthalpy of igniter gas, and Φ_i is the dissipation.
    Heat transfer from the gas to the solid propellant when the
propellant surface temperature is lower than a preset auto-ignition
temperature is determined by

$$q_1 = h_c \left(T_1 - T_s \right), \tag{10}$$

where h_c is a convective heat transfer coefficient determined by
measurement. Inter-phase heat transfer is calculated by [1]

$$Q_{2i} = \left(6 \, k_1 \, r_2 / d_2^2 \right) \left(T_2 - T_1 \right) \left(0.58 \, R_e^{0.7} P_r^{0.3} \right), \tag{11}$$

where

$$P_r = \mu_1 \, c_{p_1} / k_1 . \tag{12}$$

    Heat transfer from the gas to the solid propellant is assumed
to be one dimensional transient conduction [4].

Initial and Boundary Conditions
    Initially stagnant atmospheric air is filled in the chamber
and the nozzle. Transient process begins with the introduction of
igniter gas into the chamber at the head-end section. Heat transfer
from the gas to the solid propellant raises temperature of the
propellant resulting in auto-ignition. Mass and energy released
from the burning solid propellant rapidly increase momentum and
energy of the flow in the system and the total thrust. Open
boundary conditions are maintained at the exit of the nozzle and
solid wall conditions are used at the head-end.

Numerical Method

IPSA (Inter-Phase-Slip-Algorithm) originated by Spalding [5] is used to approximate the solution of governing equations. IPSA is an extension of SIMPLE method and consequently follows a similar computational procedures. Equation (1) is solved for the volume fraction of particle phase and equation (3) is used to find volume fraction of the gas phase. With known volume fractions and a guessed pressure field, momentum equations are solved for velocities. Corrections on density, velocity and pressure are made by solving pressure correction equation. Energy equation is solved to update temperature change. These steps are repeated until convergence is satisfied within a given time step.

RESULTS AND CONCLUSIONS

Geometry of the motor, igniter gas flow rate and other physical and numerical parameters are those used in a previous analysis based on a single fluid model [4].

Numerical results obtaind by the single fluid option of the present model are shown in Figure 1 in comparison with measurement data. Numerically predicted pressure increase after the flame spreding (0.12 sec) is higher than the measured data. Higher pressure increase is due to higher burning rate which is caused by higher flow speed in the chamber. Predicted total thrust is much higher than the measured value (about 46 % higher at 0.6 sec).

Numerical results using two-fluid option of the model are shown in Figure 2. Particle diameter is assumed to be 10 m and the density of the particle is 1500 kg/m . Particle loading of the aluminum in the solid propellant is 10 %. Due to increased mixture density, flow speed in the chamber is much slower and subsequently slower increases in pressure gradient and total thrust. Numerical results are in agreement with physical expectations.

REFERENCES

1. Baum, J. D., and J. N. Levine,"Modeling of Nonlinear Longitudinal Instability in Solid Rocket Motors," Acta Astronomica, Vol. 13,1986, 339-348.
2. Caveny, L. H, and K. K. Kuo,"Ignition Transients of Large Segmented Solid Rocket Boosters," NASA CR-150162, NASA/MSFC, April 1976.
3. Gokhale, S. S., and H. Krier,"Modeling of Unsteady Two-Phase Reactive Flow in Porous Beds of Propellant," Prog. Energy Combust. Sci., Vol. 8, 1982, 1-39.
4. Han, S. S., "Ignition Transient Analysis of Solid Rocket Motor," Final Report, Summer Faculty Program, ASEE/MSFC, 1990.
5. Spalding, D. B., "Numerical Computation of Multi-Phase Flows," Von Karman Institute for Fluid Dynamics, Lecture Series 1981-1982, Jan. 1981.
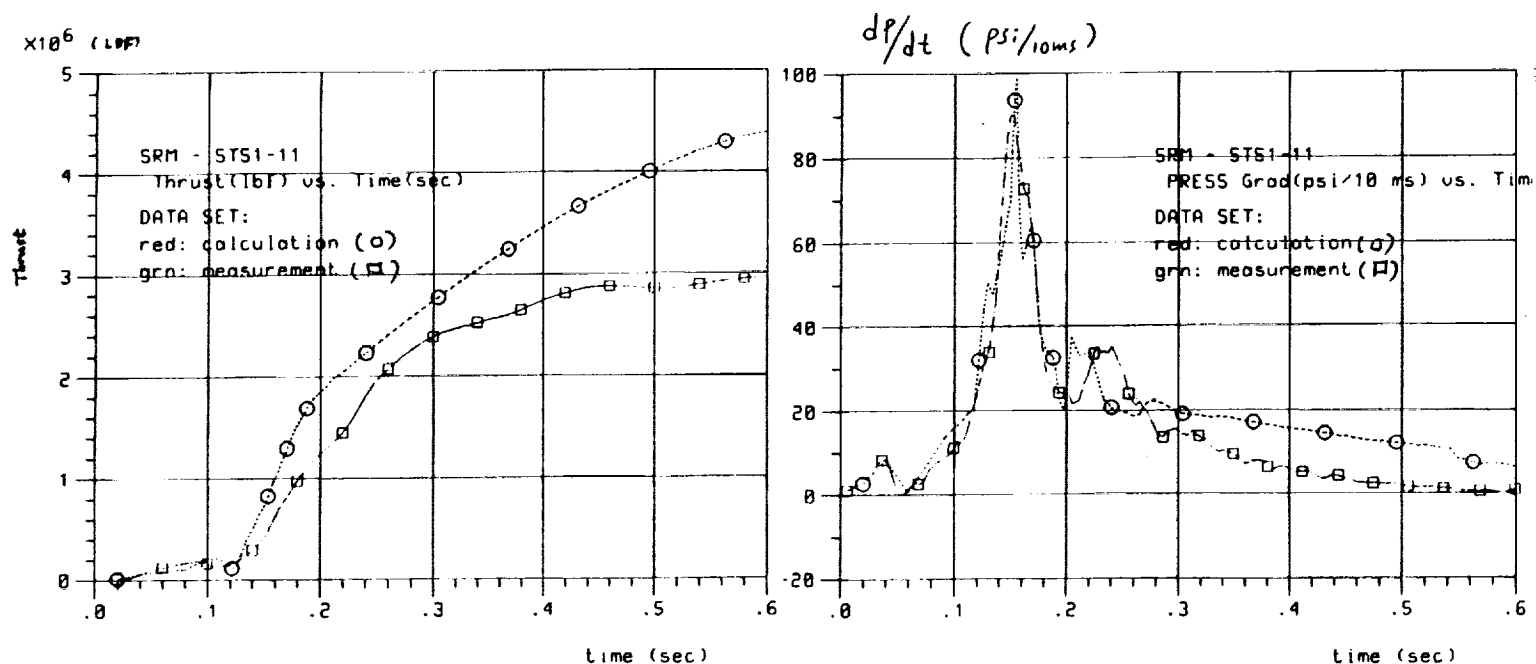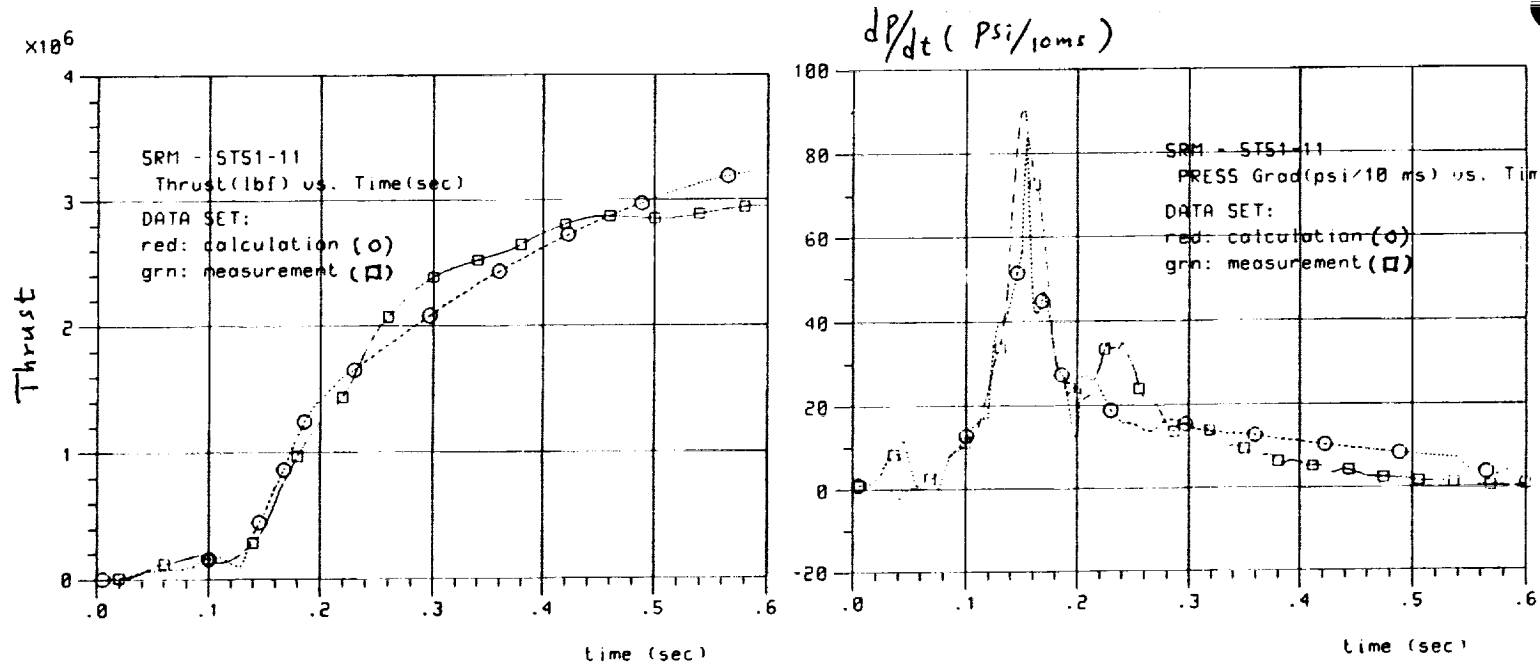
Fig. 1

Fig. 2

1991

NASA/ASEE SUMMER FACULTY FELLOWSHIP PROGRAM

MARSHALL SPACE FLIGHT CENTER
THE UNIVERSITY OF ALABAMA IN HUNTSVILLE

FAILURE ANALYSIS OF THE LITHIUM BATTERY: A STUDY OF THE
HEADER DEPOSIT ON THE CELL TOP AND DIFFUSION WITHIN
THE ELECTRODE GLASS SEAL USING NUCLEAR MICROANALYSIS AND
FTIR SPECTROSCOPY

Prepared By: Razi A. Hassan

Academic Rank: Assistant Professor

Institution: Alabama A&M University
                           Department of Chemistry

NASA/MSFC:

        Laboratory: Information   &   Electronic
                           Systems
        Division: Electrical
        Branch: Electrical/Electronics Parts

MSFC Colleague: Michael Martin

Contract No.:   NGT-01-008-021
                           The University of Alabama in
                           Huntsville

O

INTRODUCTION

The Solid Rocket Booster Range Safety System (SRBRSS) uses a lithium/poly-carbon monofluoride primary battery as a source of electrical power. The battery is manufactured by the Eagle Picher Industries. After cell fabrication and activation some battery cells have shown self discharge. One possible source of this cell discharge has been suggested to be the formation and growth of a conducting crystallized chemical compound across the glass bead insulator, electrically shorting the glass bead to the casing. This laboratory has begun an analysis of this compound, the glass seal holding the cathode into place, and the cell electrolyte, using Fast Fourier Transform Infrared (FFTIR) Analysis, Rutherford Backscattering Spectroscopy (RBS), and Nuclear Reaction Microanalysis. Preliminary measurements have confirmed the existence of lithium, nitrogen, fluorine, and oxygen on a reddish-brown deposit covering parts of the glass seal holding the positive electrode in place.

Cells usng Li metal electrodes, have many advantages over conventional primary batteries (5). One principal disadvantage of using Li batteries on a commercial basis would be the environmental impact of the florocarbon material. Another would be the relatively high expense of (CF)n.

The overall cell reaction and the electrolyte chemicals are described in (1) and (6).

EXPERIMENTS

Fast Fourier Infrared Spectroscopy (FFTIR) was used to analyze the organics present on the glass seal surface and the electrolyte material. These experiments were performed in the laboratory of Dr. James Thompson of Alabama A&M University. The Rutherford Backscattering Spectroscopy (RBS) and Nuclear Reaction Microanalysis were used to semiquantitativbely analyze the atomic compositions of the glass surface and within the glass seal. These experiments were performed in an accelarator in the James Foster Radiation Center, directed by Dr. Daryush Ila, of Alabama A&M University.

This problem has been previously studied extensively by NASA scientists (3). Scattering Electron Microscopy (SEM) was done on the electrodes, glass seals, and headers, to study the higher atomic weight elements (Z >19). These results suggested the presence of the following elements: magnesium, silicon, sulfur, potassium, barium, iron, nickel, arsenic, and chlorine. They also suggested that the problem of cell discharge/shorting is in the manufacturing design. It was suggested that if the company manufacturing the batteries would take more cautionary measures that this problem would probably be eliminated:
(A) isolate the NASA batteries from impurities during the manufacturing process. NASA batteries, apparently, are prepared in an environment which does not exclude impurities such as Cl⁻.
(B) changing the glass seal. Some have suggested using a "Zeigler-Type" seal, to replace the present glass seal.

Others at NASA (2a) have suggested that because of the many chemicals present in the cell system (electrodes, casings, electrolytes, separators, etc.), it will be extremely dificult to analyze all of the possible chemical reactions that take place. This is especially true for LDEF batteries, due to the extended contact of the cells' chemicals with one another.

NUCLEAR MICROANALYSIS

Nuclear microanalyses were performed on the cell header deposit and the glass seal. (see figs. 1&2). Fluorine was detected in the glass. There is little doubt that it came from the cathode material. Lithium was also detected. It is uncertain if the Li present was from the electrode or simply from the glass itself, since one of the components of the glass is Li. More quantitative studies need to be performed. A "significant amount" of lithium and fluorine were present in the reddish-brown deposit on the glass surface.

As previously mentioned, there are many possible chemical reactions that could take place within the LDEF cells, given the composition of the cell components and the length of time (6 years) they have been in close contact with each other.

FFTIR

These spectra have not given conclusive information. Preliminary tests do not confirm the presence of DMSO in the electrolyte through the reduction of DMSI, as this investigator suspects. More work needs to be done. It has been suggested that Nuclear Magnetic Studies (NMR) could give the kind of information that is needed to support the author's hypothesis concerning the electrolyte.

DISCUSSION

It is interesting that the reddish-brown material on the surface of the glass seal has the same physical appearance as Li_3N (4). The source of the Li could have been the electrode or the electrolyte. Nitrogen appears to be a natural contaminant of Li metal. "The solid solubility of nitrogen in lithium at the eutectic temperature is 0.024 mol percent at $180.24°C$. This high solubility of nitrogen suggests that in lithium batteries, some nitrogen is expected to be evolved during discharge, unless the gas is scrupuously excluded from the lithium. Attempts to remove nitrogen from Li by filtration have suggested that once this metal has been saturated with nitrogen, impurity levels below 0.08 mol percent would be diffiuclt to achieve" (4). Studies on polycrystalline Li_3N showed it to be a good conductor of Li^+ at moderate temperatures.

Nitrogen gas, N_2 has been observed when Li cells discharge (4). It is likely that it occurs through one or both of the pssible mechanisms:
(1) dissolution of dissolved or trapped nitrogen
$$2N \text{ (Solution)} \longrightarrow N_2(g) \qquad [1]$$

(2) electrochemical oxidation of lithium nitride, a known surface contaminant
$$Li_3N \longrightarrow 3Li^+ + 1/2\ N_2(gas) + 3e^- \qquad [2]$$
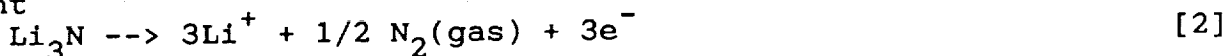
This latter reaction is catlyzed by moisture.

It has already been suggested by members of this laboratory that the discharge/ shorting problem somehow involves the glass seal. Preliminary RBS results confirm the presence of Li in the glass. Since Li is also one of the ions already present in the glass, it cannot be stated at this point whether it came from "somewhere outside of the glass" or not. More quantitative studies need to be made ot confirm this point.

There are, however, many possible paths for electrochemical reactions to occur between the Li electrode and the glass.

In a damp environment, the Li electrode develops a grayish-black tarnish which progresses to a white powder of LiOH:

$$2Li + 2H_2O --> 2LiOH + H_2 \qquad\qquad [3]$$
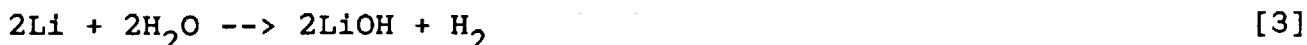
Visual observations suggest that some of this material is also found on the header.

The organic solvent in the electrolyte is DMSI, dimethyl sulfite. It is speculated that some of this substance is reduced to DMSO, dimethyl sulfoxide. There are reports which suggest that Li is more soluble in DMSO than in DMSI. It is suspected that some of the DMSI is being converted into DMSO through the following possible mechanism:

$$(CH_3O)SO + 4H^+ + 4e- --> (CH_3)SO + 2H_2. \qquad\qquad [4]$$
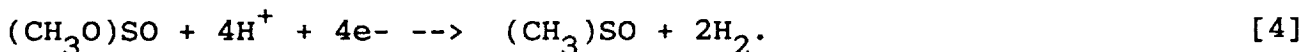
The DMSO would then dissolve some of the Li metal. One possible mechanism for this process is as follow:

$$1.)\quad (CH_3)_2SO + H_2O = H_2SO_3 + CH_3OH \qquad\qquad [5]$$

$$2.)\quad H_2SO_3 + 2Li --> Li_2SO_3 + H_2 \qquad\qquad [6]$$
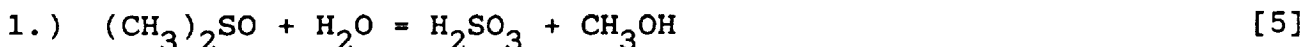
There is also speculation that the following reaction takes place between DMSI and the Li electrode:

$$2Li + 2(CH_3O)_2SO --> Li_2SO_3 + SO_2 + H_2 + CH_2 = CH_2$$
$$+ CH_3 - O = CH_3 \qquad\qquad [7]$$
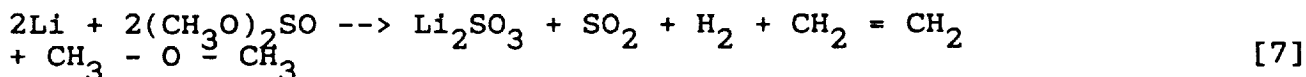
All of these hypothese should be further tested using NMR studies on the electrolyte mixture.

PROJECTED RESEARCH

It is clear why one NASA researcher was moved to suggest that the problem of chemically analyzing the Li cells is at best an extremely difficult one. At Alabama A&M, work has began to successfully identify the chemical components of the glass seal and the header deposit. Some of the findings support their initial hypothese concerning a discharge mechanism for the lithium batteries. This analysis, however, needs

quantitative research in order to completely characterize the cell
chemistry, thus, to find the reason behind the shorting.

BIBLIOGRAPHY
1. Bagotzky, V. S, and Skundin, A. M.: "Chemical Power Sources" (Academic
Press, New York, 1980)
2. Congo, Richard, NASA internal memorandum, Dec. 1990
2a. Dalins, Ilmars, NASA internal memorandum, Oct. 30, 1990
3. Linden, D.: "Lithium Batteries-An Emerging Technology", "Batteries
Today", (Feb. - Mar. 1980)
4. McDonald, Robert, "Sources of Pressure in Lithium Thionyl Chloride
Batteries", J. Electrochem. Soc.: Electrochemical Science and Technology,
129 (11) (1982)
5. Venkatasetty, H. V.: "Lithium Battery Technoloy" (John Wiley, New
York, 1984)
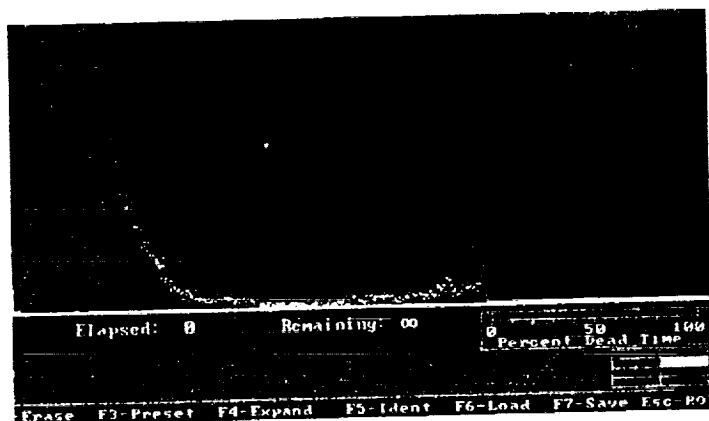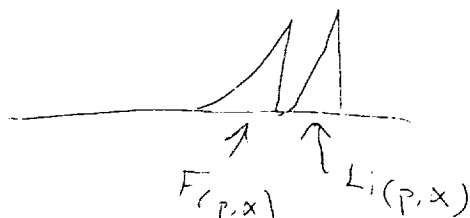
Figure 1: ALPHA Particles Spectrum
Header Material Indicates the
presence of Lithium and Fluorine.
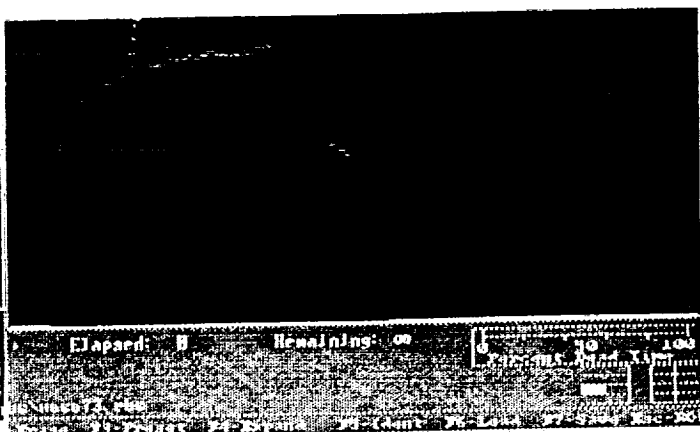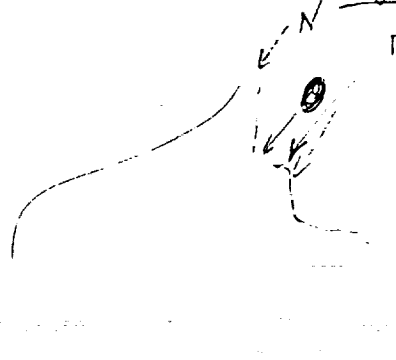
Figure 2: RBS Spectrum (1.614 MEV Protons)
Header Deposit indicates the presence of
Nitrogen, Oxygen, Fluorine.

1991

NASA/ASEE Summer Faculty Fellowship

Marshall Space Flight Center
University of Alabama, Huntsville

On the Development of System–Theoretic Tools for the Design of Integrated Health Monitoring and Controls for Rocket Propulsion Systems

Prepared By:	Arthur J. Helmicki
Academic Rank:	Assistant Professor
Institution:	University of Cincinnati Department of Electrical and Computer Engineering

NASA/MSFC:

Office:	Structures and Dynamics Laboratory
Division:	Control Systems Division
Branch:	Mechanical Control Systems Branch

MSFC Colleagues:	D. Pat Vallely Tom Fox
Contract Number:	NGT–01–008–021 University of Alabama, Huntsville

P

As NASA continues to develop various advanced propulsion technologies for space exploration two factors are becoming increasingly dominant in design specifications: increase operational reliability and decrease operational cost. One approach that has been proposed to meet these challenges is to incorporate into current and future rocket propulsion systems some sort of diagnostic/monitoring capability in the form of a Health Monitoring System (HMS). HMS technology offers the promise of increased operational reliability through its ability to assess system performance, detect and isolate degradations and/or failures, and modify system operation so as to minimize effects on performance. Decreased operational costs are accrued by the use of the HMS technology to help automate inspection and checkout procedures and to help minimize maintenance activities by transitioning from a maintenance-on-routine basis to a maintenance-on-condition basis.

The block diagram shown in Figure 1(a) illustrates a generic interconnection of a rocket engine (E), together with its sensors (S), actuators (A), and controller (C), and a generic HMS. The main functional components of the HMS can be classified according to their level of sophistication as follows [6]:

Safety Monitoring: Assure completion of mission. Simplest level of HMS function. Typically takes the form of a red-line checking algorithm which can initiate engine shutdown. Currently in use on SSME in the form of FASCOS system.

Health Monitoring: Determine condition of engine components during operation and identify any anomalous behaviors. Next higher level of HMS function. Possessing some form of failure/degradation isolation and accomodation capabilities. Currently under development for use on SSME in the form of SAFD [2] and on STME in the form of RECOMS [1].

Condition Monitoring: Determine readiness of engine to perform required mission. Most sophiticated level of HMS Function. May involve use of trending analysis, artificial intelligence, etc. Currently an open research area.

As the descriptions above indicate, the sate-of-the-art in HMS technology is still relatively unsophisticated. Several interesting issues remain as yet unresolved. The purpose of the research reported here is to study, from a systems engineering perspective, the particular issues of analysis and synthesis for generic HMS's such as the one depicted in Figure 1(a). Specific system-theoretic questions of interest include: Can one develop analytical methods for the analysis and synthesis of HMS specifications? Given a set of HMS specifications, can one develop analytical methods for deciding on the selection and placement of sensors to achieve the given specifications? Given a set of HMS specifications and an HMS sensor suite, can one develop analytical methods for characterizing the algorithms needed to process the sensor data in order to achieve the given specifications? To what extent do the design objectives of a HMS conflict/interact with design objectives of a control system?

The research presented here proposes a system-theoretic framework within which questions like those posed above can be studied in a unified manner. In addition, partial answers to the last question posed, i.e., the question of control/HMS conflict/interaction, are given as an indication of the potential utility of the proposed framework. Finally, it is indicated how the proposed framework can be extended to handle some of the other questions raised above.

The specific issue of the impact of control system design objectives on HMS design objectives and vice versa is particularly interesting in that a fundamental objective of control systems is that they be relatively insensitive to small changes in the system being controlled (i.e., the so-called robustness issue) whereas it is precisely the objective of HMS's that they be able to sense changes in system behavior. This conflict can be more concretely illustrated by considering the block diagram given in Figure 2. It shows a plant

$$\left[\begin{array}{c} y_1 \\ y_2 \end{array} \right] = Pu = \left[\begin{array}{c} P_1 \\ P_2 \end{array} \right] u \; .$$

together with a compensator K and diagnostic module D. Subsystem P_1 defines those plant sensors selected for diagnostic purposes, and subsystem P_2 defines those plant sensors selected for control purposes. The exogenous signal f is representative of a sensor failure, i.e., $f = 0$ corresponds to nominal sensor behavior and $f \neq 0$ corresponds to an off-nominal condition in one or more of the sensors defined by P_2. The goal here is to design K to achieve good control performance and to design D so that failures at f can be monitored at

d, the diagnostic module output. Straightforward manipulations yield that the transfer function M_{fd} from f to d is given by:

$$M_{fd} = DP_1K(I - P_2K)^{-1} .$$

This expression clearly indicates that the extent to which the loop gain P_2K is shaped to achieve control objectives has an impact on our ability to monitor failures f at d. Moreover it is clear that K and D cannot be designed independently without possible adverse effects to either control performance or diagnostic performance.

The discussion above indicates that an integrated analysis of HMS and control system design is necessary. For this purpose the configuration shown in Figure 1(b), discussed in [4], will be considered. Here T and T' represent, respectively, the engine system together with its sensors and actuators, and an integrated health monitoring and control system (IHMC). They are partitioned conformably with respect to their inputs/outputs as follows:

$$\begin{bmatrix} z \\ y \end{bmatrix} = T \begin{bmatrix} w \\ u \end{bmatrix} = \begin{bmatrix} T_{11} & T_{12} \\ T_{21} & T_{22} \end{bmatrix} \begin{bmatrix} w \\ u \end{bmatrix}, \quad \begin{bmatrix} z' \\ y' \end{bmatrix} = T' \begin{bmatrix} w' \\ u' \end{bmatrix} = \begin{bmatrix} T'_{11} & T'_{12} \\ T'_{21} & T'_{22} \end{bmatrix} \begin{bmatrix} w' \\ u' \end{bmatrix} .$$

Definitions and interpretations of the various signals shown in Figure 1(b) are listed in Table 1. Off-nominal conditions are handled in a manner similar to that shown in Figure 2. Specifically, off-nominal conditions are represented by injecting fictitious input signals at

$$n = \eta + f , \; n' = \eta' + f' , \; w .$$

Here f, f' denote, respectively, sensor and actuator failures/degradations, η, η' denote, respectively, sensor and actuator noise, and w denotes internal failures/degradations. Both control and HMS design objectives can be stated in terms of these interpretations as indicated in Table 2.

The motivation for this choice of framework stems from the direct similarity between the generic architecture depicted in Figure 1(a) and the structure of the interconnection shown in Figure 1(b). We note that this similarity has already been suggested in the literature [5] for the case where the block T has the restricted form shown in Figure 1(c). However, this restriction has two severe limitations which make it inadequate for use in the present context: First, the fact that y is directly tied to the plant P output implies that no distinction is made between those sensors used for control and those used for diagnostics. In actual propulsion systems such as the SSME there are always many more sensors available for health monitoring than are used for control. Second, the fact that the exogenous plant input w is restricted to enter at the plant output corresponds reflecting respresentative failure inputs to the plant output, thus adding some degree of conservatism to this configuration. The results given below are extended to encompass the general T block.

Using straightforward transfer function analysis methods the interaction effects between the health monitoring module and the control module can be characterized and quantified. Table 3 summarizes some of the key tradeoffs uncovered using this analysis. For example, the first entry illustrates that sensor noise cannot be simultaneously rejected at the diagnostic output over the same frequency range that sensor faults are to be detected. This, in turn, means that there is a direct tradeoff to be made between sensor noise rejection and achievable diagnostic specifications. Similar arguments can be given for the other entries of Table 3, and although space constraints do not permit their inclusion here they are fully documented in [3] together with a more detailed analysis of the IHMC structure of Figure 1(b).

In addition to directly addressing issues related to interaction of health monitoring and controls modules the framework associated with Figure 1(b) can be used indirectly to obtain information on the problems pertinent to the design of IHMC. As one example, consider the problem of sensor suite selection, i.e., the problem of how to select a group of sensors to achieve a given level of health monitoring and control performance. Based on physical reasoning a candidate set of sensors can be selected thereby defining the entires of T. Once this is accomplished, analysis similar to that above can be used to see how eliminating certain sensors effects the overall IHMC performance. In this way trade studies can be formulated to analyze optimal sensor suite selection.
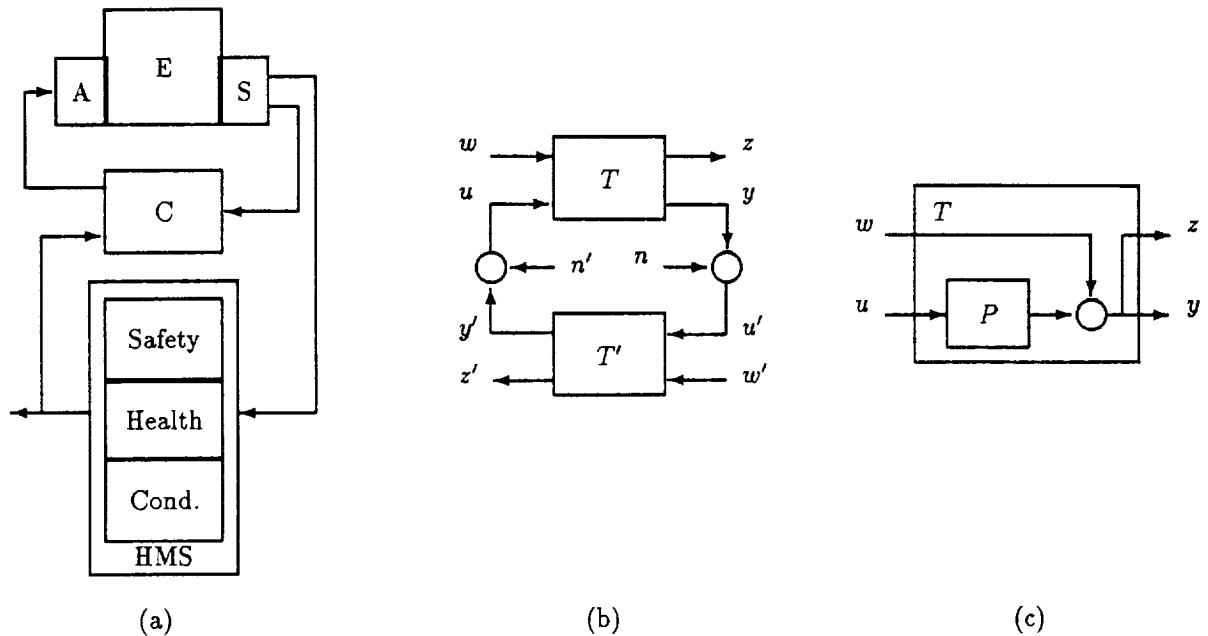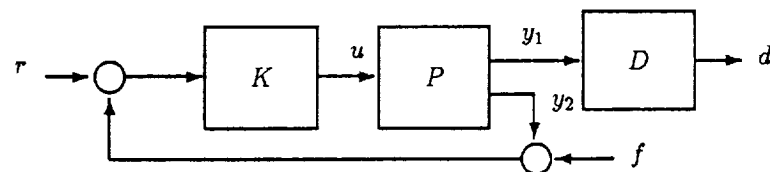
(a) (b) (c)

Figure 1: Generic Architecture.

Figure 2: "Unintegrated" Health Monitoring and Control?

Signal	Interpretation	Examples
z	Engine output variables not sensed for IHMC	Thrust, etc.
y	Engine output variables sensed for IHMC	Pressures, Temperatures, etc.
w	Exogenous engine input variables	Disturbances, internal component failures, etc.
u	Engine input variables actuated by IHMC	Actual valve settings, etc.
z'	IHMC diagnostic output variables	Pressures, Temperatures, etc.
y'	IHMC output variables fed to Engine	Ideal valve settings, etc.
w'	Exogenous IHMC input variables	Controller commands, etc.
u'	IHMC input variables from Engine sensors	Actual sensor values, etc.
n, n'	Exogenous interconnection inputs	Noise, sensor failures, actuator failures, etc.

Table 1: Signal Interpretations for Figure 1(b).

References

[1] S. K. Hagar and J. F. Alcock. Rocket engine condition monitoring system. In *Proc. 25th J. Prop. Conf.*, Monterey, CA, July 1989. AIAA Paper 90-2852.

[2] M. W. Hawman. Health monitoring system for the SSME – program overview. In *Proc. 26th J. Prop. Conf.*, Orlando, FL, July 1990. AIAA Paper 90-1987.

[3] A. J. Helmicki. On the Development of System–Theoretic Tools for the Design of Integrated Health Monitoring and Controls for Rocket Propulsion Systems. Technical report, NASA Marshall Space Flight Center, August 1991. Detailed report for NASA/ASEE Summer Faculty Fellowship Program.

[4] C. N. Nett. Algebraic aspects of linear control system stability. *IEEE Trans. on Auto. Contr.*, AC-31:941–949, 1986.

[5] C. N. Nett, C. A. Jacobson, and A. T. Miller. An integrated approach to controls and diagnostics: The 4–parameter controller. In *Proc. Amer. Cont. Conf.*, June 1988.

[6] A. Norman and M. Taniguchi. Development of an advanced failure detection algorithm for the SSME. In *Proc. 24th Joint Prop. Conf.*, Boston, MA, July 1988.

Control Objectives:

Interconnection should be stable.

Noise/Disturbance Rejection $\Rightarrow$ $M_{\eta y}, M_{\eta' y}, M_{wy} \approx 0$.

Command Tracking $\Rightarrow$ $M_{w'y} \approx I$.

Control Effort $\Rightarrow$ $M_{w'u}, M_{\eta u}, M_{\eta' u}$ sized reasonably.

Satisfy above robustly in the face of modeling errors.

Health Monitoring Objectives:

Noise Rejection $\Rightarrow$ $M_{\eta z'}, M_{\eta' z'} \approx 0$.

Command Rejection $\Rightarrow$ $M_{w' z'} \approx 0$.

Failure/Degradation Tracking $\Rightarrow$ $M_{f z'}, M_{f' z'} \approx I$.

Satisfy above robustly in the face of modeling errors.

Table 2: Control and Health Monitoring Objectives.

Sensor Noise Rejection vs. Sensor Fault Detection:
$$M_{\eta z'} = M_{f z'}$$
Actuator Noise Rejection vs. Actuator Fault Detection:
$$M_{\eta' z'} = M_{f' z'}$$
Sensor Fault Detection vs. Actuator Fault Detection vs. Internal Fault Detection:
$$M_{f' z'} = M_{f z'} T_{22} \ , \ M_{w z'} = M_{f z'} T_{21}$$

Table 3: Control/Health Monitoring Objective Conflicts/Interactions.

1991

NASA/ASEE SUMMER FACULTY FELLOWSHIP PROGRAM

Numerical Methods for the Analysis of Sampled-Data Systems and for the Computation of System Zeros

Prepared by:	A. Scottedward Hodel, Ph. D.
Academic Rank:	Assistant Professor
Institution	Department of Electrical Engineering
	Auburn University
NASA/MSFC:	
Office:	Structures and Dynamics Laboratory
Division:	Control System Division
Branch:	Mechanical Systems Control Branch
MSFC Colleague:	D. P. Vallely
Contract No:	NGT-01-008-021
	The University of Alabama at Huntsville
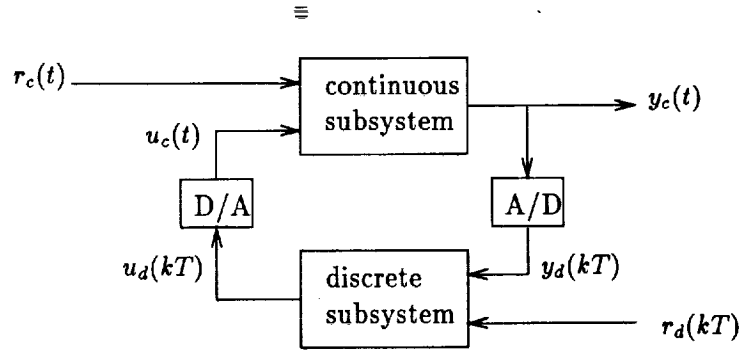
Figure 1: General sampled data system

1 MARSYAS Overview

MARSYAS is a computer-aided control system design package for the simulation and analysis of open loop and closed loop dynamic systems. Prior to the summer of 1991, MARSYAS functios provided simulation of sampled data (mixed discrete-time and continuous-time) systems; however, sampled-data system analysis of stability, frequency response and transfer function coefficients was not implemented. Analysis of purely continuous-time systems was available, but the underlying computational procedures did not employ several recent advances in numerical techniques.

This report outlines the numerical and theoretical basis behind the MARSYAS functions developed during the summer of 1991. In particular, the numerical computation of the matrix exponential $e^A = I + A + \frac{A^2}{2!} + \frac{A^3}{3!} + \cdots$ as described in [11] and the numerical computation of the finite system zeros of a dynamic system (continuous-time or discrete-time) as discussed in [4], [6], and [8] are presented. These two numerical functions and their associated numerical tests comprise the bulk of the work done by the author while working in tandem with John Tiller (BCSS) and D. Pat Vallely (NASA-MSFC). The analysis of sampled-data systems is discussed in Section 2; the numerical computation of system zeros is discussed in Section 3.

2 Discretization of LTI Continuous Systems

A general sampled-data system is shown in Figure 1. The system has an external continuous-time input $r_c(t)$ and an external discrete-time input $r_d(t)$, and maps these signals to continuous-time outputs $y_c(t)$ and to discrete-time ouputs $u_c(t)$. Due to the use of A/D and D/A converters, sampled-data systems are nonlinear and time-varying in general. That is, there is no transfer function from $r_c(t)$ to $y_c(t)$, even if the constituent subsystems are linear and time-invariant (LTI)! However if the subsystems are LTI, the behavior of the A/D and D/A converters ($u_c(t) = u_d(kT)$, $t \in [kT, kT + T)$) implies that one may obtain discrete-time transfer functions $Y_d(z)/R_d(z)$ and $U_d(z)/R_d(z)$. This is accomplished by computing matrices F and G such that a continuous time system $\dot{x} = Ax + Bu$ may be equivalently represented at sampling times $0, T, \ldots, kT, \ldots$ as $x(kT + T) = Fx(kT) + Gu(kT)$. This conversion is obtained via the relations $F = e^{AT}$, $G = \left(\int_{0^T} e^{A(T-t)} dt \right) B$, where the matrix exponential e^{AT} is defined as $e^{AT} \triangleq I + AT + (AT)^2/2! + \cdots$.

Van Loan [10] observes that F and G may be simultaneously computed as $\begin{bmatrix} F & G \\ 0 & I \end{bmatrix} = exp \left(\begin{bmatrix} A & B \\ 0 & 0 \end{bmatrix} \right)$; that is, only a single matrix exponential is required.

Computation of the matrix exponential is not a trivial task. (See, for example, [7].) However, Ward [11] has proposed the use of Padé approximations with preconditioning for this purpose. The algorithm is shown in Figure 2. This procedure was tested at MSFC during the summer of 1991 in several numerical experiments; computed eigenvalues of $F = e^A$ were compared with the exponentials of the eigenvalues of

1	Avg eig. shift	$A := A - \phi I$	reduce dynamic range of $\lambda's$
2	balance	$A := D^{-1}AD$	reduce non-normality powers of 2, no roundoff
3	scale	$A := A * 2^{-j}$	reduce so $\|A\| < 1$; no roundoff
4	Padé:	$F := D_3(A)^{-1} N_3(A)$	experiments: D_8, N_8 don't help much
5	Square	$F := F^{(2^j)}$	$F := F^2$ j times, $\log(a^n) = n \log(a)$
6	inverse balance	$F := DFD^{-1}$	no (new) roundoff
7	inverse shift	$F := e^\phi F$	$e^{A-bI} = e^A e^{-b}$

Figure 2: Computation of the matrix exponential

A, with good agreement. Similarly, matrices $A = V\Lambda V^{-1}$ were constructed so that computed values of F could be compared with exact (known) solution values, again with good agreement. Experiment models had up to 109 states with wide variation in coefficients. Little difference was found between using 3rd order Padé approximations and eigth order Padé approximations; hence, for the sake of computational speed, MARSYAS presently uses 3rd order approximations.

3 Factored Transfer Functions

Numerical experiments involving discretized sampled-data systems with fast modes revealed that existing MARSYAS software was not adequate for the computation of associated system zeros. Prior to the summer of 1991, MARSYAS computed the zeros of $H(s) = C(sI - A)^{-1}B + D$ as

$$z_i = \lambda_i^{-1} \left(\begin{bmatrix} -A & -B \\ C & D \end{bmatrix}^{-1} \begin{bmatrix} I & 0 \\ 0 & 0 \end{bmatrix} \right).$$

Unfortunately, discretized systems obtained from continuous time systems with fast modes (relative to the sampling interval) are nearly uncontrollable; that is, the matrix $\begin{bmatrix} -A & -B \\ C & D \end{bmatrix}$ is nearly singular.

EISPACK routine `balanc` [9] and Ward's GEP balancing procedure [12] attempt to *reduce* the dynamic range of the coefficients in the algebraic eigenvalue problem (AEP) and the generalized eigenvalue problem (GEP), respectively, *without* introducing any roundoff error. Both of these procedures may be divided into two steps: (1) permutation and (2) scaling.

For example, the permutation step `gep_perm` of Ward's balancing procedure computes permutation matrices P_1 and P_2 such that the transformed matrix pencil

$$(\hat{M} - \lambda\hat{N}) = P_1(M - \lambda N)P_2$$

may be conformably partitioned as $\hat{M} = \begin{bmatrix} \hat{M}_{11} & \hat{M}_{12} & \hat{M}_{13} \\ 0 & \hat{M}_{22} & \hat{M}_{23} \\ 0 & 0 & \hat{M}_{33} \end{bmatrix}$ and $\hat{N} = \begin{bmatrix} \hat{N}_{11} & \hat{N}_{12} & \hat{N}_{13} \\ 0 & \hat{N}_{22} & \hat{N}_{23} \\ 0 & 0 & \hat{N}_{33} \end{bmatrix}$ where $\hat{M}_{11}$,
$\hat{N}_{11}$, $\hat{M}_{33}$ and $\hat{N}_{33}$ are upper triangular and $\hat{M}_{22}$ and $\hat{N}_{22}$ form a reduced order permutation-irreducible GEP. Following `gep_perm`, the scaling step `gep_scale` of Ward's balancing procedure computes diagonal matrices $D_i = \text{diag}(r^{k_1^{(i)}}, \dots, r^{k_n^{(i)}})$, $i = 1, 2$, where r is the machine radix. D_1 and D_2 are selected so that the elements of the matrix products $D_1\hat{M}D_2$ and $D_1\hat{N}D_2$ are of approximately the same magnitude. (The use of powers of the machine radix r allows these matrix products to be computed without roundoff.)

The AEP balancing procedure `balanc` may be similarly divided into a permutation step `aep_perm` and scaling step `aep_scale`. However, `balanc` requires that $P_1 = P_2^{-1} = P_2^T$ and $D_2 = D_1^{-1} = \text{diag}(r^{-k_1^{(1)}}, \dots, r^{-k_n^{(1)}})$. The use of similarity transforms P_1 and D_1 preserves the $N = I$ structure of the AEP.

Algorithm	Preconditioning	Computed Zeros
ENVD	none	$-1904, (-1500 \pm j8.744 \cdot 10^4), -336.2,0,0$
EISPACK	none	$-5.468 \cdot 10^5, (2.688 \pm j4.720) \cdot 10^5,$ $(9.913 \pm j9.359) \cdot 10^7, -1500, -1500$
ENVD	`zgep_scale`	$-1500,-1500$
EISPACK	`gep_perm, gep_scale`	$1500 \pm j2.7847 \cdot 10^{-5}$

Figure 3: Numerical results for Example 3.1.

Since Ward has developed an effective preconditioner for the generalized eigenvalue problem [12], it was decided to modify MARSYAS to use this balancing procedure in tandem with the QZ iteration [8] as implemented in EISPACK. This procedure resulted in great improvement in the accuracy of MARSYAS computed results. Ward's balancing procedure may be applied without roundoff error and will usually provide improvement in the computed results. However, the QZ iteration fails to isolate zeros at infinity, and so these zeros may be perturbed in the Riemann sphere to large (but finite) zeros of arbitrary phase.

Emami-Naeini and Van Dooren [4] propose a procedure for the solution of the zero-computation generalized eigenvalue problem that reduces the original problem to one of lower degree that has the same finite zeros as the original system but with no zeros at infinity. This code has been tested on several industrial system models with great success. However, implementation of this algorithm (as available from `netlib` at Oak Ridge National Labs) proved disastrous when applied to a model of the oxidzer-preburner valve dynamics of the SSME. This failure was due to widely varying magnitudes in the coefficients in the system model. As a part of the 1991 summer faculty program, a new balancing procedure for the zero-computation generalized eigenvalue problem

$$\begin{bmatrix} -A & -B \\ C & D \end{bmatrix} x = \lambda \begin{bmatrix} I & 0 \\ 0 & 0 \end{bmatrix} x$$

was developed as a preconditioner to the Emami-Naeini/Van Dooren algorithm; see [6] for details. Use of this procedure in tandem with modified procedures from [12] and EISPACK provides improved numerical robustness as shown in the following example.

Example 3.1 Consider the following seventh order single-input, single-output dynamic system based upon the space shuttle main engine oxidizer-preburner valve dynamics. The system coefficients are $a_{11} = -7000$, $a_{12} = -2.5 \times 10^7$, $a_{17} = -1.82943 \times 10^9$, $a_{21} = 1$, $a_{32} = 6.4 \times 10^5$, $a_{33} = -2,240$, $a_{34} = -a_{32}$, $a_{43} = 1$, $a_{54} = 9.03934$, $a_{65} = 225,449$, $a_{66} = -3,000, a_{67} = -2.25 \times 10^6$, $a_{76} = 1$, $b_{11} = 1.44813 \times 10^8$, $c_{15} = 1.26582$, and all other matrix entries are zero. The EISPACK implementation of the QZ algorithm and the Emami-Naeini/Van Dooren (ENVD) algorithm were applied to this system with either no preconditioning, Ward's balancing procedure `gep_perm`, `gep_scale`, or the zero-computation generalized eigenvalue balancing procedure `zgep_scale`. A summary of the numerical results is in Figure 3. (Ward's balancing procedure [12] correctly isolates six generalized eigenvalues at infinity; the correct finite system zeros are $s = 1500 \pm j2.7847 \times 10^{-5}$. The `zgep_scale` scaled system coefficients are $a_{11} = -7000$, $a_{12} = -762.9$, $a_{17} = -1744.7$, $a_{21} = 32,768$, $a_{32} = 78.125$, $a_{33} = -2240$, $a_{34} = -156.25$, $a_{43} = 4096$, $a_{54} = 72.31472$, $a_{65} = 27.52$, $a_{66} = -3000$, $a_{67} = -34.33$, $a_{76} = 65,536$, $b_{11} = 1.0789$ and $c_{15} = 0.6329$.

References

[1] William L. Brogan. *Modern Control Theory*. Prentice-Hall, Englewood Cliffs, N. J., 3rd edition, 1991.

[2] Paul Concus, Gene H. Golub, and Dianne P. O'Leary. A generalized conjugate gradient method for the numerical solution of elliptic partial differential equations. In J. R. Bunch and D. J. Rose, editors, *Sparse Matrix Computations*, pages 309–332. Academic Press, 1976.

[3] A. R. Curtis and J. K. Reid. On the automatic scaling of matrices for Gaussian elimination. *J. Inst. Maths. Applics.*, 10:118–124, 1972.

[4] A. Emami-Naeini and P. Van Dooren. Computation of zeros of linear multivariable systems. *Automatica*, 18(4):415–430, 1982.

[5] G. H. Golub and C. Van Loan. *Matrix Computations*. Johns Hopkins University Press, Baltimore, MD, 2nd edition, 1989.

[6] A. Scottedward Hodel and John Tiller. Computation of system zeros with balancing. Submitted to the *1991 Allerton Conference*, Monticello, Illinois, October 1991.

[7] C. Moler and C. Van Loan. Nineteen dubious ways to compute the exponential of a matrix. *SIAM Review*, 20(4):801–836, October 1978.

[8] C. B. Moler and G. W. Stewart. An algorithm for generalized matrix eigenvalue problems. *SIAM J. Numer. Anal*, 10(2):241–256, April 1973.

[9] B. N. Parlett and C. Reinsch. Balancing a matrix for calculation of eigenvalues and eigenvectors. *Numer. Math.*, 13:293–304, 1969.

[10] C. F. Van Loan. Computing integrals involving the matrix exponential. *IEEE Transactions on Automatic Control*, AC-23(3):395–404, June 1978.

[11] Robert C. Ward. Numerical computation of the matrix exponential with accuracy estimate. *SIAM J. Numer. Anal.*, 14(4):600–610, 1977.

[12] Robert C. Ward. Balancing the generalized eigenvalue problem. *Siam J. Sci. Stat. Comput.*, 2(2):141–152, June 1981.

1991

NASA/ASEE SUMMER FACULTY FELLOWSHIP PROGRAM

MARSHALL SPACE FLIGHT CENTER
THE UNIVERSITY OF ALABAMA

BIOLOGICAL PATTERNS: NOVEL INDICATORS FOR PHARMACOLOGICAL ASSAYS

Prepared By: Jacqueline U. Johnson, V.M.D., M.S.

Academic Rank: Assistant Professor

Institution: Alabama A & M University, Food Science &
                        Animal Industries

NASA/MSFC:
        Laboratory: Space Science
        Division: Microgravity Sciences and Application
        Branch: Biophysics ES-76

MSFC Colleague: Helen C. Matsos
                        Dr. David A. Noever

Contract No.:   NGT-01-002-099
                        The University of Alabama

R

INTRODUCTION

Algae, protozoa, and spermatozoa form macroscopic patterns while mobile, analagous to thermally driven convection cells. Interest within the fluid dynamics arena has increased to demonstrate theories of gravity-related mechanisms. The appearance of these bioconvective patterns is the result of fluid dynamic instability (protozoa and algae) and wave-forming hydrostatic mechanisms (spermatozoa). Definitive KC-135 aircraft studies have clearly demonstrated the existence of several mechanisms governing cell viability and movement.

The research focus of ground experiments has been to 1) further characterize these mechanisms driving bioconvective pattern formation in simple cellular organisms; 2)study the relationship between variable gravity and the streaming patterns observed in dense cultures of free-swimming organisms; 3) to devise simple ground tests to determine future bioprocessing needs; and 4) to devise and patent toxicity assays for detecting metallic ions and pharmacological products.

CONTENT

As part of Marshall Space Flight Centers' summer faculty fellowship program (SFFP) within the biophysics branch, development of bioassays for detecting metallic ions and pharmacological products has been devised utilizing the pattern forming abilities of these organisms as a macroscopic detector of chemicals and biologically active agents. The addition of cadmium at varying concentrations to these biological cultures has been shown to effect the mobile function, and hence the macroscopic patterns of the protozoa, Tetrahymena Pyriformis.

Sperm motility is essential for the penetration and genetic investments of the oocyte (1). Conceivably, every ejaculate contains some minute percentage of abnormal spermatozoa (motile or immotile), but absolute criteria for variations in sperm normality due to microgravity influences have yet to be established. It is therefore of interest to monitor pattern formation as a sensitive indicator of cell viability and function. In addition to these ground tests, the SFFP project has persued initial activities of cryopreservation and storage of spermatozoa and other single cells. In preliminary findings of post-thaw survival of spermatozoa, the rate of thaw (30 seconds versus 65 seconds in water-bath maintained at $36^{o}C$) and medium type used to preserve cells greatly affects the percent survival rates. Herein, these and other factors influencing cryopreservation will need to be closely evaluated prior to reliance on low gravity test designs.

CONCLUSIONS

Variable gravity testing using the KC-135 demonstrated clearly that biological pattern formation was definitively shown to result from gravity alone (protozoa), and not from oxygen gradients in solution. Motile pattern formation of spermatozoa are driven by alternate mechanisms, and apparently are not affected by short-term changes in gravity. The chemical effects found appear to be secondary to the primary effect of gravity. Cryopreservation may be the remedy to the problem of 'spare' or 'standing order' biological samples for testing of space lab investigations, but further studies are necessary.

REFERENCES

Roberts, A.M. Nature. 228, 375-376 (1990)

Noever, D.A. International Biotechnology Science Conference, San Francisco, CA. October 23-28, 1990

1991

NASA/summer faculty fellowship program

Marshall Space Flight Center
The University of Alabama

Disordering and H-embrittlement of
Pb(110)* surface using Embedded Atom Method and
Molecular Dynamics

Prepared by: Majid Karimi, PhD

Academic Rank: Associate Professor

Institution: Alabama A&M University
                                Physics Department

NASA/MSFC:
    Office: EH22

    Division: Metallic Materials

    Branch: Metallurgical & Failure
                                Analysis

MSFC Colleague: Ilmars Dalins, PhD

Contract No.:   NGT-01-008-021
                                The University of Alabama

S

Problem statement

The dynamics and structure of crystal- melt interface are of great importance in crystal growth, melting, and other properties of solid liquid interface. The EAM, a semiempirical method developed by Daw and Baskes(1-3), for determining the energetics of atoms in a bulk enviroment , is a useful method for use in the computer simulation. The EAM functions of Pb in conjunction with the MD code are employed to study melting and disordering of Pb(100) surface. The EAM functions are fitted to the bulk experimental data at zero temperature and it is not clear if it will behave correctly at higher temperatures. In fact, it was shown(4) that use of a similar type of potential at higher temperatures might result in a negative coefficient of thermal expansion. The primary purpose of this report is to perform MD simulation combined with the EAM functions of lead to study melting of Pb(110) surface. This provide an accurate test of the EAM functions at higher temperatures. In particular, we calculate two dimensional structure factor, two dimensional pair distribution function, and density profile as a function of temperature up to the melting point of lead.

Methodology

Empirical pair potentials are suffering from two major problems, zero Cauchy pressure, i.e., $P_c \neq 0$ and equality of the vacancy formation energy E_v with the cohesive energy E_c. In fact, in most of the metals $P_c = 0$ and $E_v < E_c$. To overcome these shortcomings the EAM functions were developed. In the EAM, the energy of an assembly of atoms is calculated as a function of their atomic coordinates. The major contribution to the energy of each atom comes from the embedding term F which can be interpretted as the energy that is gained when an atom is embedded into the charge density created by all the other atoms. Embedding function is supplemented by a two body potential Φ mimicing the core-core repulsion,

$$E_i = F_i + .5 \sum_{j \neq i} \Phi_{ij}(r_{ij}) \ , \tag{1}$$

where E_i is the energy of atom i, F_i is the embedding energy of atom i, ρ is the charge density at site i, Φ_{ij} is the electrostatic interaction between cores of atoms i and j, and r_{ij} is the interatomic distance between atoms i and j. ρ is approximated by the superposition of atomic charge densities of all the other sites except site i,

$$\rho_i = \sum_{j \neq i} \rho_j^a \ , \tag{2}$$

where   is the atomic charge density.

F and Φ are determined by considering functional forms for them and fitting them to the bulk properties of solid. The exponential forms were considered for ρ and $\Phi(2)$. Parameters of the EAM functions of lead are tabulated in Ref.(3). Conditions under which simulations were performed are reported in table (1), where T is the temperature, and t_E and t_T are equilibrium and total simulation times.

In the MD simulation, one simply integrates the classical equations of motion from which velocity and position of the N particles in the system of volume V are calculated. Energy E remains constant in a microcanonical ensemble, so the time average of any property is equal to the time average over a microcanonical ensemble of configurations each having that same E, V, and N(ergodicity)(5). Averages over a canonical ensemble, where V, T, and N are constant or over an isothermal-isobaric ensemble, where T, P, and N are constant are more easily compared with the experimental results than averages over a microcanonical ensemble. Algorithms for T and P control have already been developed. Calculation of interparticle forces usually accounts for about 85% of the total simulation time. If all particles interact, calculation of the forces require $N(N-1)/2$ calls to the force routine. However, calls to the force routine can be reduced to $N*N_n$ if force is cut off beyond N_n neighbor of each atom.

We now briefly discuss the effects of hydrogen on metal-metal bonding using pair potential as well as the EAM and then compare our results. The interaction of the two metal atoms using the pair potential approach is,

$$E_1 = \Phi_{M-M}(r_{M-M}),\tag{3}$$

where r_{M-M} is the interatomic distance. The force experienced by each atom is given by,

$$F_1 = \Phi'_{M-M}(r_{M-M}).\tag{4}$$

We now put a hydrogen atom near to one of the metal atoms and calculate the potential and force between the two metal atoms;

$$E_2 = \Phi_{M-M}(r_{M-M}) + \Phi_{H-M}(r_{H-M}),\tag{5}$$

$$F_2 = \Phi'_{M-M}(r_{M-M}).\tag{6}$$

Therefore, in the pair potential approach, presence of the hydrogen does not change the force between the metal atoms. We now repeat the same calculation using the EAM formalism.

$$E_1 = 2F_M(\rho_M(r_{M-M})) + \Phi_{M-M}(r_{M-M}),\tag{7}$$

$$F_1 = 2F'_M(\rho_M)\rho'_M(r_{M-M}) + \Phi'_{M-M}(r_{M-M}),\tag{8}$$

$$E_2 = F_M(\rho_M(r_{M\text{-}M}) + \rho_H(r_{H\text{-}M})) + F_M(\rho_M(r_{M\text{-}M})) + F_H(\rho_H(r_{H\text{-}M})) +$$

$$\Phi_{M\text{-}M}(r_{M\text{-}M}) + \Phi_{H\text{-}M}(r_{H\text{-}M}), \tag{9}$$

$$F_2 = F_M'(\rho_M + \rho_H)\,\rho_M'(r_{M\text{-}M}) + F_M'(\rho_M)\,\rho_M'(r_{M\text{-}M}) + \Phi_{M\text{-}M}'(r_{M\text{-}M}), \tag{10}$$

$$F_2 - F_1 = F_M'(\rho_M + \rho_H)\,\rho_M'(r_{M\text{-}M}) - F_M'(\rho_M)\,\rho_M'(r_{M\text{-}M}). \tag{11}$$

Assuming $\rho_H \ll \rho_M$ (which is a reasonable approximation), we can Taylor expand $F_2 - F_1$,

$$F_2 - F_1 = F_M''(\rho_M)\,\rho_H \rho_M(r_{M\text{-}M}), \tag{12}$$

where $F_M'' > 0$, $\rho_H > 0$, and $\rho_M' < 0$. This means that presence of the hydrogen will weaken the metal-metal bonding.

Results

a) Density profile $\rho(z)$

The atom density per unit length is:

$$\rho(z) = (1/\sqrt{2\pi}\sigma) \sum_i \exp[-(z - z_i)^2 / 2\sigma^2]$$

where $\sigma = .1\, d_{110}$ is the width parameter of the distribution, $d_{110} = a/2\sqrt{2}$, and $a = 4.91$ Å. Result of the density profiles as a function of temperature is shown in Fig.(1).

b) Structure factor $S_1(T)$

The time-averaged squared modulus of the two dimensional structure factor for layer 1 at temperature T is:

$$\langle |S_1|^2 \rangle = \langle 1/n_1 | \sum_i \exp[-i g \cdot r_i |^2 \rangle,$$

where $\langle \rangle$ denotes the time averaging, n_1 is the number of atoms in layer 1, and the sum is over the atoms of layer 1. $\langle |S_1|^2 \rangle$ is calculated for $g = 2\pi/a(1,0)$. Our result for $\langle |S_1|^2 \rangle$ as a function of temperature T for the top nine layers are shown in Fig.(2)

Conclusions

The maximum in $\rho(z)$ for layer L2 is lower than for L1 at temperatures 300 K and 400 K. A transfer of atoms between L2 to L1 occurs between 400 K to 500 K. Above 500 K an adatom is formed above L1 and leaves vacancies in L1 and L2. $\langle |S_1|^2 \rangle$ versus T curves show disordering of the top two layers begins near 400 K. The number of adatoms increases with the temperature and is maximum near the bulk melting temperature.

Hydrogen embrittles the metal provided that the EAM approach is used for the energetics of the atoms. More work is needed to quantify the embrittlement near the grain boundaries in metals with and without the presence of hydrogen.

References

*. Because of the limited time available during the summer faculty program, we decided to first test our model predictions against a system with known experimental data. Pb was chosen partly because of availability of the EAM functions from our previous work and a rich collection of experimental data. Reference (6) has clearly shown that this type of calculation can easily be extended to the materials more relevant to the aerospace industry. Unfortunately, we did not have time to develope the EAM functions for that system.

1. M. S. Daw and M. I. Baskes, **Phys. Rev. B29**, 6443 (1984).
2. R. A. Johnson and D. J. Oh, **J. Mater. Res.4**, 1195 (1989).
3. M. Karimi, Z. Yang, P. Tibbits, D. Ila, I. Dalins, and G. Vidali, MRS Proceeding, **vol.193**, 83 (1990).
4. J. B. Adams and S. M. Foiles, **Phys. Rev. B41**, 3316(1990).
5. D. W. Heerman, **Computer Simulation Methods, Springer Series**, 2nd ed., (1990).
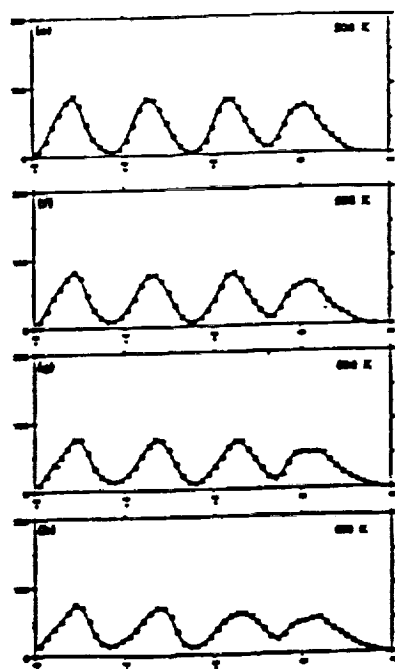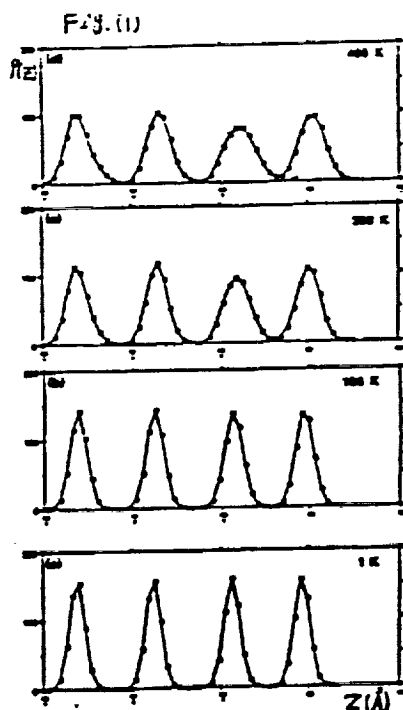6. E. T. Chen, R. N. Barnett, and U. Landman, **Phys. Rev. B41**, 439(1990).

Fig. (1)

Fig. (2)

Table (1)

1991

NASA/ASEE SUMMER FACULTY FELLOWSHIP PROGRAM

MARSHALL SPACE FLIGHT CENTER
THE UNIVERSITY OF ALABAMA

DEVELOPMENT OF A CALIBRATED SOFTWARE RELIABILITY MODEL
FOR
FLIGHT AND SUPPORTING GROUND SOFTWARE
FOR
AVIONIC SYSTEMS

Prepared By: Stella Lawrence

Academic Rank: Professor

Institution: Bronx Community
                        College,
                        Department of
                        Engineering
                        Technologies

NASA/MSFC:

        Office: Information &
                                Electronic
                                Systems Laboratory

        Division: Software & Data
                                 Management

        Branch: Systems Software

        MSFC Colleague: Kenneth Williamson

        Contract No.:   NGT-01-008-021
                                The University of
                                 Alabama

T

The object of this project was to develop and calibrate quantitative models for predicting the quality of software. Reliable flight and supporting ground software is a highly important factor in the successful operation of the space shuttle program. Reliability is probably the most important of the characteristics inherent in the concept of "software quality." It is the probability of failure free operation of a computer program for a specified time and environment.[1]

A software reliability model specifies the general form of the dependence of the failure process on the principal factors that affect it: fault introduction, fault removal, and the environment.

Since some of the factors involved in the preceding are probabilistic in nature and operate over time, software reliability models are generally formulated in terms of random processes. Analytic expressions can be derived for the average number of failures experienced at any point in time, the average number of failures in a time interval, the failure intensity at any point in time, the probability distribution of failure intervals.

A good software reliability model gives good predictions of future failure behavior, computes useful quantities, is simple, widely applicable, and based on sound assumptions. Prediction of future failure behavior assumes that the values of model parameters will not change for the period of prediction.

The models use the Poisson process to model software occurrence, either the HPP (Homogeneous Poisson Process) or NHPP (Nonhomogeneous Poisson Process).

The models used in the present study consisted of: 1. SMERFS (Statistical Modeling and Estimation of Reliability Functions for Software).[2] There are ten models in SMERFS: error count models (generalized Poisson model, NHPP model, Brooks and Motley, Schneidenwind model, S-shaped reliability growth model) and time-between-error models (Littlewood and Verrall Bayesian model, Musa execution time model, geometric model, NHPP model for time between error occurrence, Musa logarithmic Poisson execution time model), 2. Kenneth[3] Williamson's NHPP Binomial type software reliability model, 3. Goel-Okumoto NHPP model.[4]

The software utilized consisted of the IMCE (Image Motion Compensation Electronics) software flight data, BATSE (Burst Transient Source Experiment, Gamma Ray Observatory) software, and a further program will also utilize POCC (Payload Operations Control Center for the Space Shuttle), Payload Checkout Unit Software for the Space Shuttle and HIT software (space shuttle telemetry systems).

Before discussing the results obtained with the models used in the present study, it must be kept in mind that software reliability modeling is just one of many tools. It cannot provide all the answers to the problems managers must face.

It must be taken as a bit of information, which along with others, is helpful in making a realistic judgement concerning a program's status.

For a first run, the results obtained in modeling the cumulative number of failures versus execution time showed fairly good results for our data. Plots of cumulative software failures versus calendar weeks were made and the model results were compared with the historical data on the same graph. If the model agrees with actual historical behavior for a set of data then there is confidence in future predictions for this data.

Considering the quality of the data, the models have given some significant results, even at this early stage. With better care in data collection, data analysis, recording of the fixing of failures and CPU execution times, the models should prove extremely helpful in making predictions regarding the future pattern of failures, including an estimate of the number of errors remaining in the software and the additional testing time required for the software quality to reach acceptable levels.

It appears that there is no one "best" model for all cases. It is for this reason that the aim of this project was to test several models. One of the recommendations resulting from this study is that great care must be taken in the collection of data. When using a model, the data should satisfy the model assumptions.

As previously stated, the data has to have the ability to correctly identify and measure what is desired. The data provided must satisfy the following: 1. It should be correctly recorded. 2. It should consist of samples that are random in nature. 3. It should be stated in CPU hours per failure, i.e. state CPU time as well as the date of the error. 4. All errors should be accurate.

Reliability should improve if the field software is corrected as failures occur. What about repeated failures due to the same fault? Fixing of faults leading to failures has to be properly recorded and properly attended to. The record of failures must be obtained for a sufficient length of time. Recent theory indicates that the failure intensity function probably decreases exponentially with time, i.e. a plot of the rate of occurrence of failures versus the number of faults found decreased asymptotically to zero.

There are also several recommendations regarding the use of the models: 1. The models require the insertion of various parameters. The models should be run with various values of these parameters, which should be carefully chosen for optimum results. 2. The data should be modeled piecewise, in addition to running the models for the total data. 3. Various forms of data input are provided including time between failure data and error count data and the model may yield different results for different types of data input.

4. The length of the trial should be a proportion of the expected life of the system; predictions made from a very small set of data tend to be poor. 5. The rate of manifestation of errors varies greatly from fault to fault, models which treat all faults as having the same rate may lead to optimistic bias estimates. Perhaps, some type of analysis should be performed to classify failures by severity, what kind of failure is it and is it critical or not?

To sum up the preliminary trials indicate that the models tested show much promise and that with their proper use and tailoring they are expected to yield an accurate reliability prediction for the flight and supporting ground software of embedded avionic systems.

REFERENCES
1. Musa, John S., Iannino, A., and Okumoto, Kazuhira, Software Reliability Measurement, Prediction, Application, McGraw-Hill Book Company, New York, 1987.
2. Farr, William H., Strategic Systems Department, Naval Systems Warfare Center, Dahlgren, VA 22448-5000, Smith, Oliver D., EG & G Washington Analytical Service Center, Inc., 1900 Dahlgren Road, Dahlgren, VA 22448, Sponsored by Strategic Systems Programs, Washington, DC 20376-5002, Statistical Modeling and Estimation of Reliability Functions for Software (SMERFS), Report No. NSWC TR 84-373, Revision No. 2, March, 1991.
3. Williamson, Kenneth, Non-Homogeneous Poisson Process Binomial Type Software Reliability Model, Preliminary Edition, EB41/Software & Data Management Division, EB42/Systems Software Branch, Marshall Space Flight Centeó, Huntsville, AL 35811, July, 1991.
4. Vienneau, Robert, Computerized Implementation of the Goel-Okumoto NHPP Software Reliability Model, ITT Research Institute, Beeches Technical Campus, Route 26N, Rome, N.Y. 13440, November, 1987.

1991

NASA/ASEE SUMMER FACULTY FELLOWSHIP PROGRAM

MARSHALL SPACE FLIGHT CENTER

THE UNIVERSITY OF ALABAMA IN HUNTSVILLE

DEVELOPMENT OF A MOON-BASED MAGNETOSPHERIC AND CORONAL IMAGER USING A LARGE BROADBAND ARRAY

PREPARED BY: GEORGE LEBO, Ph.D.

ACADEMIC RANK   ASSOCIATE PROFESSOR

INSTITUTION: UNIVERSITY OF FLORIDA
                        DEPARTMENT OF ASTRONOMY

NASA/MSFC

OFFICE: OFFICE OF THE ASSOCIATE DIRECTOR
                        FOR SCIENCE

MSFC COLLEAGUE: N.F. SIX, Ph.D.

CONTRACT NO: NGT 01-008-021
                        THE UNIVERSITY OF ALABAMA IN
                        HUNTSVILLE

I.   THE LUNAR BASED SOUNDER AND RADIO TELESCOPE

        The "Missions to and from Planet Earth" mandated by President
Bush in 1989 provide a unique opportunity for magnetospheric and
coronal plasma physicists to cooperate with low frequency radio
astronomers in the development of an advanced experiment designed
for the lunar surface. A large active lunar based array would
sound the Earth's magnetosphere at VLF frequencies and the solar
corona at decametric wavelengths allowing plasma physicists to map
both the Earth's magnetosphere and those regions in the solar
corona that trigger precursors to solar flares. With the
transmitter silent, the array would become the ideal low frequency
radio telescope, examining both geospace emissions such as auroral
kilometric radiation and extraterrestrial signals from the
planets, pulsars, supernova remnants, and active galactic nuclei.
Both experiments satisfy requirements mandated in both "Mission to
Planet Earth" and in "Mission from Planet Earth." By proposing a
cooperative effort both communities (plasma physicists and radio
astronomers) stand to benefit.

        Jim Green, Director of the NASA Space Science Data Center
(NSSDC) at GSFC; Tony Phillips, Research Fellow at California
Institute of Technology; T.D. Carr, Director of the University of
Florida Radio Observatory (UFRO) and the author are enlisting the
cooperation of the scientific community in defining the system
specifications. Some components, such as the receivers, will be
standard "off-the shelf" items, hence will require little
developmental research. However, others, such as the individual
antenna elements, and the phasing and matching networks, will
require some R&D to satisfy the frequency requirements (20 KHZ-40
MHZ).

        By flying the experiment in Earth orbit first, Dr. Green
proposes to gather valuable magnetospheric data as well as to
prove the principle of the large moon based experiment. He claims
that funding for the preliminary ground based studies at the UFRO
may be available as early as FY 92. The author will co-write with
Dr. Green and others a proposal to NASA to this effect.

II.   ARCHIVING THE UNIVERSITY OF FLORIDA'S RADIO DATA AT THE NSSDC

        Astronomers at the UFRO have synoptically monitored
Jupiter's radio emission since 1957. They have the world's most
extensive collection of such data. Starting in about 1975 they
have also occasionally recorded Io-related decametric storms using
a high-speed broadband recording system. They now desire to make
these data available to the entire scientific community by
archiving them with the NSSDC. When the author visited GSFC and
NASA Headquarters on July 17, 1991, he discussed with Dr. Green
how these data would be transferred to the NSSDC. Work to this
end is now proceeding with an initial transfer expected by 9/1/92.
They also discussed how the acoustooptic spectrograph currently

used at the UFRO could be upgraded to make future data more easily available to the NSSDC and how acoustooptic techniques could be used in the proposed lunar based magnetospheric sounder. Through contacts at the UAH the author had learned of Dr. Anthony Vanderlugt currently a professor at North Carolina State University who spearheaded the first acoustooptic research in the early 1970's. Dr. Vanderlugt offered to help in the design of a spacecraft acoustooptic spectrograph. An investigation of a broadband phasing technique known as a Rottman Lens was initiated.

III. THE NASA VISITING LECTURERS PROGRAM

The author and his colleague, Frank Six have both given many popular level talks on NASA's missions and the related science to public audiences. To expand this activity they have designed a "NASA Lecturer's Program" in which it is proposed that NASA will fund the travel of select NASA appointed lecturers to address university groups, schools, and public audiences. The plan is to make the lecturer's program available to JOVE institutions and public audiences in their areas on a 1-year trial basis. A JOVE university receiving a visiting lecturer would arrange for him/her to address a mix of college students, alumni, public school students, and service clubs in two or three lectures spanning two days and would agree to pay all local expenses.

The lecturers would be chosen for their ability to speak knowledgeably about NASA's missions and experiments and to excite audiences at all levels. The visiting lecturers program will not only educate but will inspire students to pursue scientific and technical careers and will awaken in the adults the awe and excitement of NASA's missions.

Dr. Ed Wells, professor, and Dr. Paul Smeyak, Chairman of the Telecommunications Department at the UF have both indicated enthusiastic interest in developing a series of five to seven minute NASA promotional video tapes for the visiting lecturer's program as class projects for their students. The UF's Telecommunication Department is one of the largest in the United States. The author will coordinate the preparation of these tapes.

IV. INTRODCUING MINORITY SCHOOLS TO SPACE GRANT CONSORTIA
USING   THE JOVE PROGRAM

In a recent visit to the UF, the author met with Dr. Harry Shaw, UF's Director of Minority Affairs, and Dr. Martin Eisenberg, Chairman for Aeronautical Engineering at the UF and Director of the Florida Space Grant Consortium. Each is interested in involving the UF with JOVE institutions. Dr. Eisenberg sees JOVE as a natural way to introduce Florida's smaller institutions to NASA research making them eligible as members in Florida's Space Grant Consortium and offering an opportunity for the major consortium members to serve as mentors in the JOVE program.

Should the UF serve as a mentor institution, through the JOVE program, it may collaborate with minority institutions thereby attracting good minority students into the UF's graduate programs. To that end, Dr. Shaw is putting together a list of minority school administrators who, with his guidance, may be convinced to apply for JOVE participation.

Dr. Charles MacGruder, a physics professor at Fisk University (a JOVE member institution in Nashville) and the author have discussed a joint research effort in which Dr. MacGruder's MS graduates could attend the UF to do their Ph.D. work in astrophysics. The author and others in the UF's Department of Astronomy share Dr. MacGruder's research interests (VLF radio propagation, astrophysics, radio astronomy). The author has also contacted faculty and administrators at Embry Riddle University in Daytona Beach, FL, and South Carolina State College in Orangeburg, SC and he plans to cultivate the interest of other institutions in the JOVE program with the UF potentially acting as the mentor institution.

V. METEOR/SHUTTLE PROGRAM

During his summer at MSFC, the author finished a paper entitled, "The First Multi-Frequency Observation of Decametric Radio Emission by a Meteor" which will be submitted to Icarus. He intends to propose a follow-on experiment to NASA in which appropriately placed radio receivers would monitor radio emissions from the re-entering shuttle as it penetrates the earth's atmosphere.

1991

NASA/ASEE SUMMER FACULTY FELLOWSHIP PROGRAM

MARSHALL SPACE FLIGHT CENTER
THE UNIVERSITY OF ALABAMA AT HUNTSVILLE

ADAPTIVE OPTICS IN COHERENT LIDAR WIND MEASUREMENTS:
A FEASIBILITY STUDY

Prepared By: Robert P. Leland, Ph.D.

Academic Rank: Assistant Professor

Institution: The University of Alabama
                        Department of Electrical Engineering
NASA/MSFC:

        Division: Guidance, Control, and Optical
                        Systems
        Branch: Optical Systems

MSFC Colleague: James Bilbro

Contract No.:   NGT-01-008-021
                        The University of Alabama at
                        Huntsville

Laser Doppler radar, or Lidar, is widely used for remote sensing of wind velocities. Usable wavelengths for the laser are limited by the effects of atmospheric turbulence. An adaptive optical system is proposed to compensate for turbulence effects on signal power. The feasibility of an adaptive system is considered in light of the effects of speckle from the aerosol target.

Lidar wind measurements are made by sending a laser beam into the atmosphere, and measuring the Doppler shift in the frequency of the radiation reflected by small particles, or aerosols, which are moving with the wind. The frequency shift is proportional to the wind velocity along the beam. (see Drain (2)). Pulsed lidar systems, transmit short pulses and use the time-of-flight of the pulse to determine the range of the reflecting aerosols (see Bilbro (1)). At shorter wavelengths, greater range resolution is achieved, however turbulence effects are increased. Atmospheric turbulence reduces the signal power from a heterodyning receiver in two ways. First the beam width at the target is increased, which increases speckle. Second, the wavefront at the receiver is distorted, resulting in destructive interference of different areas of the beam crossection. The effects of turbulence on lidar signal to noise ratios are described in Frehlich and Kavaya (3).

Adaptive optical systems have been used to compensate for the effect of turbulence on telescope imaging, laser radars, beamed energy and other applications (see Pearson et al (7)). The principal components are a wavefront sensor to measure phase distortion, and a deformable or segmented mirror to impose a phase correction on the transmitted beam or received signal. The wavefront measurements determine the commands to the actuators controlling the mirror shape, making the system adaptive.

Most adaptive optical systems require a point source, such as a star or a glint on a solid target to obtain a useful signal. In the lidar problem, the target is a distributed aerosol, which introduces speckle effects. Zirkind and Shapiro (8), and Kokorowski et al (5) studied speckle in adaptive systems with hard targets, but assumed long decorrelation times. Murty (6) studied speckle effects from distributed aerosols, and found the decorrelation times to be about $1 - 3 \mu s$.

The proposed adaptive optical system and lidar are shown in Figure 1 below. The primary mirror of a Cassegrainian beam expander is made up of identical hexagonal segments with spherical curvature. Each segment is attached to a common rigid base by three piezoelectric actuators to allow a piston motion of the segment, and a two axis tilt. The mirror materials are chosen for high stiffness and resistance to deformation due to heating. A figure sensor measures the position and orientation of each segment for accuracy. The primary mirror is 20 cm in diameter. The combined optical path for both the transmitted and reflected beam helps increases signal power and reduces the effects of turbulence. An hexagonal array of Hartmann sensors is used to measure local slopes of the wavefront. The wavefront is reconstructed from these measurements. Hexagonal arrays are 13 % more efficient than rectangular ones for 2-D signal reconstruction. Due to the weak reflected signal, the wavefront sensor must use coherent detection, and will also be used to sense the

Doppler shift. This requires the design of a new type of sensor. The primary laser transmits bursts of 10 pulses of 100ns duration spaced about 2 μs apart at a wavelength of 2 microns. The bursts are spaced about 1 - 2 ms apart. The local oscillator laser operates at a frequency separated from the primary laser by 100 MHz to obtain wind direction as well as speed. A target range of 1 km is assumed.
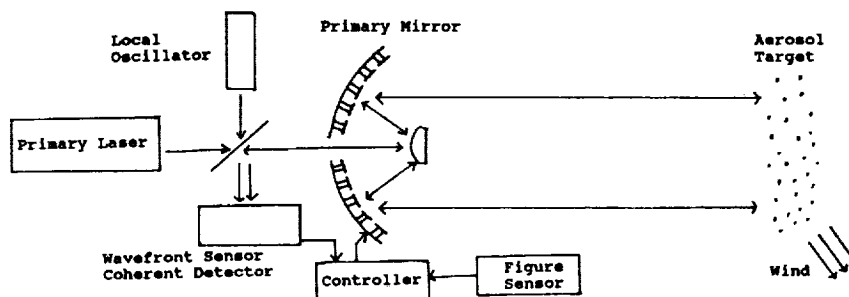

Figure 1.

The spatial and temporal bandwidth are the critical design issues of the system. The spatial bandwidth is determined by the numbers of mirror segments and wavefront sensor cells. The mirror segment size must be comparable to the Airy disk and the Fried coherence length. The mirror segment size is limited by the size of the actuators. A primary mirror with 60 hexagonal segments, 1.28 cm on each side is proposed. A 61 element Hartmann sensor array to measure the wavefront is proposed.

The response times of the mirror segments are .1 - 1 ms, which gives the adaptive system a maximum bandwidth of 1 kHz, which is too slow to compensate for target speckle. Thus the wavefront measurements from one burst of pulses must be used to determine the mirror shape for the next burst of pulses, when the speckle will no longer be correlated. The effect of speckle on wavefront measurement is reduced by averaging over the pulses in a single burst, leaving only the turbulence effects. Greenwood (4) found that systems with bandwidths of 100 to 200 Hz were able to compensate for turbulence effects, and this can be achieved if the laser can produce the necessary pulse repetition rate.

Since the system cannot compensate for speckle, the objective will be to maximize the signal power averaged over the target speckle. Let $E_T(\rho,z)$, $E_R(\rho,z)$, and $E_{LO}(\rho,z)$ be the complex phasors of the transmitted beam, the reflected beam, and the local oscillator beam, assuming a sinusoidal time dependence. Note that each of these beams has a different frequency, but this is not relevant to signal power effects. The signal power is given by

$$ |i_s|^2 = K_D |\int_A E_R(\rho,0)\overline{E_{LO}(\rho,0)}\,d\rho|^2 $$

where K_D is a constant describing the detector gain. Signal power is maximized when $E_R\overline{E_{LO}}$ has constant complex phase over the receiver aperture A. It is assumed that E_{LO} has a constant phase across the receiver, so power is maximized by holding the phase of E_R constant over the receiver. The reflected signal is

V-2

$$E_R(\rho,0) = \sigma \sum_{j=1}^{N} e^{i\theta_j} E_T(r_j) G(r_j;\rho,0) e^{i\gamma(\rho)}$$

where r_j is the position of the j'th aerosol, θ_j is a random phase, σ is a reflectivity constant, and G is the Greens function describing propagation in the turbulent atmosphere. If the number of aerosols in the scattering volume is large, the Central Limit Theorem applies, and the reflected signal is a circulo-complex Gaussian random field. $\gamma(\rho)$ is the phase shift induced by the segmented mirror. The transmitted beam $E_T(\rho,z)$ also depends on $\gamma(\rho)$.

If the local oscillator and the transmitted beam are the same in the receiver plane, that is $E_T(\rho,0) = E_{LO}(\rho,0)$, then the speckle averaged signal power can be calculated in the target volume as

$$E[|i_s|^2] = \sigma^2 K_r \int\int_{z_1 R^2}^{z_2} |E_T(\rho,z)|^4 d\rho dz$$

where K_r is a constant describing the reflectivity and density of the aerosol. From this expression, the signal power is maximized when the mirror shape γ is chosen to reduce spreading of the transmitted beam.

The average signal power can be calculated in the receiver plane as

$$E[|i_s|^2] = K_D \int\int_{A\,A} J(\rho,\rho') E_{LO}(\rho,0) \overline{E_{LO}(\rho',0)} \, d\rho d\rho'$$

where J is the speckle averaged coherence function of the reflected beam

$$J(\rho,\rho') = E[E_R(\rho,0) \overline{E_R(\rho',0)}]$$

in the receiver plane, and is given by

$$J(\rho,\rho') = \sigma^2 K_r \int\int_{z_1 R^2}^{z_2} |E_T(\rho^*,z)|^2 G(\rho^*,z;\rho,0) \overline{G(\rho^*,z;\rho',0)} e^{i(\gamma(\rho)-\gamma(\rho'))} dz d\rho^*$$

Assuming the local oscillator phase is constant, the signal power is maximized by choosing $\gamma(\rho)$ to give J a constant phase.

Averaging wavefront measurements from several pulses gives a direct measurement of $\angle J(\rho,\rho')$. Let $\theta(\rho) = \angle E_R(\rho,0)$. The k'th cell of the Hartmann sensor measures the average wavefront slope across the cell

$$S_k = \frac{1}{|A_k|} \int_{A_k} \nabla\theta(\rho) \, d\rho$$

By averaging the slope measurements from several pulses, a good estimate of the expected slope can be obtained. The expected slope is

$$E[S_k] = \frac{1}{|A_k|} \int_{A_k} \nabla \Delta J(\rho, \rho)\, d\rho$$

where the gradient is taken with respect to only the first argument of J. For points sufficiently close together, ΔJ can be approximated by

$$\Delta J(\rho, \rho') = \overline{S_k} \cdot (\rho - \rho')$$

where $\overline{S_k}$ is the averaged value of the slope. It remains to reconstruct the remaining values of ΔJ. If ΔJ has the form

$$\Delta J(\rho, \rho') = \phi(\rho) - \phi(\rho')$$

then ΔJ can be recovered from $\overline{S_k}$, k = 1...60 by standard wavefront reconstruction techniques. The tilt and displacement of the mirror segments $\mathcal{Y}(\rho)$ are then chosen to make $\Delta J(\rho, \rho') = 0$.

In conclusion, adaptive optics is a promising technique for improving the performance of a 2μ lidar wind measurement system. The chief technical challenges are a laser that will give the required output and pulse repetition rate, a combined Hartmann sensor and heterodyne detector, and a suitable wavefront reconstruction algorithm. Further research is required to assess the performance improvement given by the adaptive system under various atmospheric conditions, and an analysis of the convergence and stability of the adaptive system.

References

1. Bilbro, J. W., "Coherent CO2 Lidar Systems for Remote Atmospheric Measurements", <u>Optical and Laser Remote Sensing</u>, D. K. Killinger and A. Mooradian ed, Springer Verlag, Berlin, 1983.
2. Drain, L. E., <u>The Laser Doppler Technique</u>, John Wiley and Sons, New York, 1980.
3. Frehlich, R. G. , Kavaya, M. J., "Coherent Laser Radar Performance for General Atmospheric Refractive Turbulence", to appear in Applied Optics.
4. Greenwood, D. P., "Bandwidth Specification for Adaptive Optics Systems", Journal of the Optical Society of America, Vol 67, No 3, Mar. 1977, p 390-393
5. Kokorowski, S. A., O'Meara, T. R., Lind, R. C., Calderone, T., "Automatic Speckle Cancellation Techniques for Multidither Adaptive Optics", Applied Optics, Vol 19, No 3, Feb. 1980, p 371-381.
6. Murty, S. R., "Aerosol Speckle Effects on Atmospheric Pulsed Lidar Backscattered Signals", Applied Optics, Vol 28, No. 5, Mar. 1989, p 875-878.
7. Pearson, J. E., Freeman, R. H., Reynolds, H. C.,"Adaptive Optical Techniques for Wave-Front Correction", <u>Applied Optics and Optical Engineering</u>, Vol. VII, Academic Press, 1979, p 245-343.
8. Zirkind, N. E., Shapiro, J. H.,"Adaptive Optics for Large Aperture Coherent Laser Radars", <u>Laser Radar III</u>, R. J. Becherer ed, Sept. 6-7, 1988, Boston, Mass., SPIE, Vol 999.

1991

# NASA/ASEE SUMMER FACULTY FELLOWSHIP PROGRAM

MARSHALL SPACE FLIGHT CENTER
The University of Alabama at Huntsville

The BATSE SLED: The Problem and The Correction

Prepared by: John Patrick Lestrade

Academic Rank: Associate Professor

University and Department: Mississippi State University
                                             Department of Physics and
                                             Astronomy

NASA/MSFC:

    Laboratory: Space Science

    Division: Astrophysics

    Branch: High-Energy Astrophysics

MSFC Colleague: G. J. Fishman

Contract No.:   NGT-01-008-021
                                             The University of Alabama
                                             at Huntsville

SPD B6
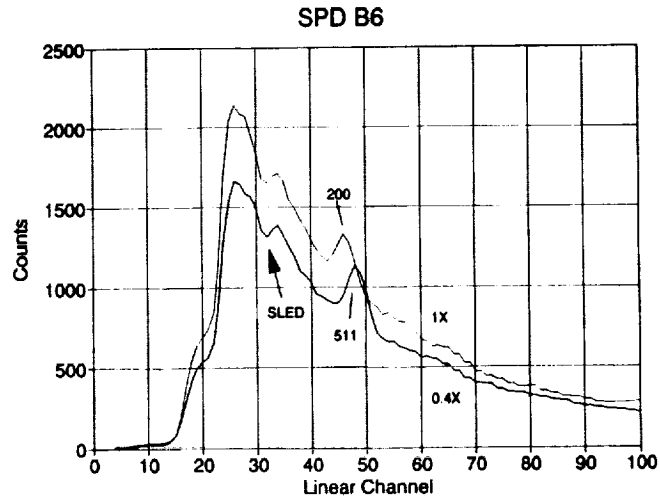
Figure 1. The SLED in the BATSE SPD Spectra.

1. Introduction:

The Burst And Transient Source Experiment (BATSE) has been in space for 4 months and, by anyone's reckoning, is performing better than even the most optimistic pre-flight predictions. That doesn't mean there haven't been some small surprises.

Because of the discreteness of γ-ray energies available to us in pre-flight testing, we could not subject the instrument to the continuous distribution of energies it now sees in space. Therefore, it was not until the beginning of mission operations that a small non-linearity was discovered in the low energy region of the SPD spectra (Band, 1991). The nickname for this depression is the *SLED* (Spectrocopy Low-Energy Depression). Figure 1 presents sample spectra for module 6 at two gains (1X and 0.4X). Note that the position of the sled is gain-independent in channel space.

A further study on a non-flight module discovered the cause lay in the spectroscopy analog electronics. Above a certain energy threshhold, the digital signal from the SPEC-FAST2 discriminator causes, in effect, an extra small amount of charge to be added to the SHER analog input. Figure 2 presents the laboratory measurements of SHER output energy as a function of input energy. The change of slope at the point of the SLED results in narrower bin widths for the channels in that region. The SLED is approximately 5 channels wide. It should be mentioned that below the SLED and for many decades above the SLED (not shown in Figure 2) the response is extremely linear.

The proposed fix was to move the lower straight line up to match the extrapolation of the upper straight line, shown by the dotted line. In effect, this means reassigning channel numbers. All channel edges lower than the SLED are moved a fixed amount to higher channel numbers. Channel edges *in* the SLED are moved a different amount depending on their position. The latter obviously results in narrower channel widths in energy space.

Although the energy at which this effect occurs is lower than the stated design specifications of the BATSE modules, it was felt that we could significantly enlarge the range of our data coverage, if we could fix this depression. Plotting the spectra in energy space provides a guide for fixing the depression. Since the SLED is constant in channel position
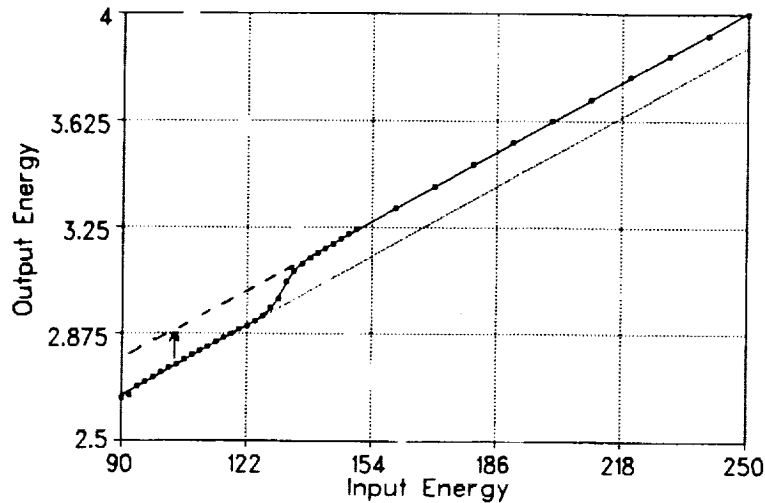
Figure 2. MQT Output vs. Input Energy (both in arbitrary units).
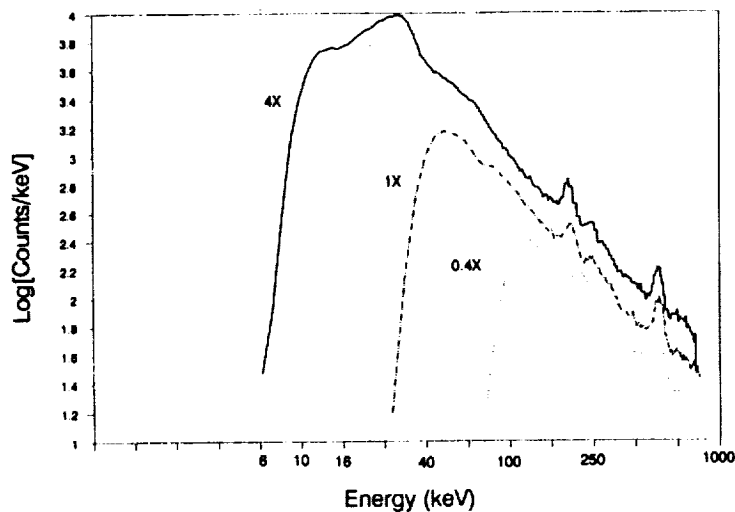
Figure 3. The SLED in Energy Space.

for different gains, it will appear at different energies. This is shown in Figure 3 where the SLED occurs at approximately 15 keV, 60 keV, and 200 keV for gains of 4X, 1X, and 0.4X, respectively.

The background at 60 keV, distorted in the 1X spectrum, is undistorted in the 4X spectrum. Thus the 4X spectrum tells us what the corrected 1X spectrum should look like. In the same way, the 1X and 4X spectra tell us what the 0.4X spectrum should look like at 200 keV. Since there were no spectra that provided a hint as to what the 4X spectrum should look like at 15 keV, we temporarily increased the gain for four in-flight detectors to 5X.

SLED removal from B7
4X gain
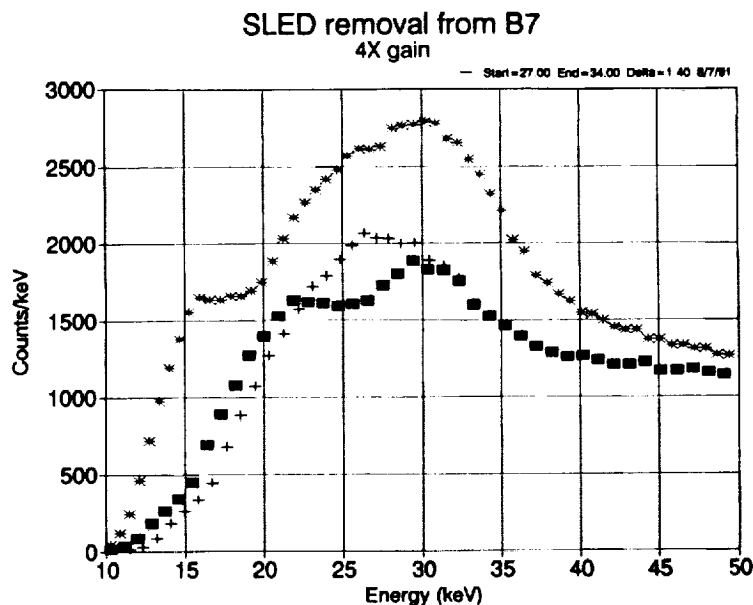
Figure 4. The Corrected Spectrum for SPD 7 at 4X Gain.

2. The Fix

It was determined from Figure 3 that the form of the SLED correction would be a change to the channel number x to $x + \delta$, where

$$\delta = d\left[1 - \frac{1}{1 + e^{-(x-c)/w}}\right],$$

and where d is the maximum value of δ (≈ 1 chan), c is the center of the SLED, and w is the width of the SLED.

Making the correction involved finding the optimum set of SLED parameters for each detector that would fill in the depressions at all three gains to match the expected backgrounds. This was done with an optimization program that was created for spreadsheets on IBM compatibles, *Goal Solutions* by Enfin Software. Figure 4 shows the spectrum of SPD B7 with and without the SLED correction. Note how the channels to the left of the SLED are shifted to the right.

3. Results:

Table 1 presents the results of the analysis for all eight SPD's. Since the position and width of the sled is dependent on the setting of the lower level discriminators (LLD's), the present LLD settings are also included.

The plan since launch has been to keep the LLD's at a constant setting. However, if they are changed, or drift, then the derived SLED parameters must also change. In order to measure the correlation between LLD voltage and SLED parameters, we will soon measure spectra for several different LLD settings. The results of that analysis will be added to Table 1 in the near future.

Table 1. Optimum Parameters for the SLED Correction.

Module number	LLD (Hex Volts)	Center	Width	d: Offset
0	24	27.0	1.20	1.20
1	20	32.1	1.54	0.84
2	20	11.0	1.33	1.40
3	1C	17.4	1.36	0.92
4	14	23.7	1.62	0.73
5	1C	25.0	1.33	1.20
6	24	31.9	1.11	0.86
7	2C	30.5	1.56	1.40

4. Acknowledgements

As in previous summers here at MSFC with the BATSE team, I have benefitted greatly from the camaraderie and spirit of the team members. Their willingness to cooperate is unbounded. For that I am very grateful.

I would also like to acknowledge the BATSE representatives at the University of San Diego, Jim Matteson and David Band and those at the Goddard Space Flight Center, Bonnard Teegaren, Brad Schaeffer, and Jay Norris. They have all been aggresive in pursuing this and other BATSE phenomena. Thanks.

Finally, a special thanks to Jerry Fishman for his continued help and support.

5. References:

1) Austin, R. W., 1991, Letter to BATSE Personnel entitled "Spectroscopy HER Data Notch", June 4, 1991. unpublished.

2) Band, D. L., 1991, Fax to Bill Paciesas entitled: "Of Dips and LLD's: Characterization of an Additional Low Energy Non-Linearity in SD Spectra". May, 29, 1991, unpublished.

NASA/ASEE SUMMER FACULTY FELLOWSHIP PROGRAM

MARSHALL SPACE FLIGHT CENTER
THE UNIVERSITY OF ALABAMA

VISUALIZATION OF DNA MOLECULES IN TIME DURING
ELECTROPHORESIS

Prepared by: Seth Lubega

Academic Rank: Professor

University and   Oakwood College
Department: Dept. of Biological Sciences

NASA/MSFC:

        Laboratory: Space Science Laboratory
        Division: Microgravity Science & Application
        Branch: Biophysics Branch

MSFC Colleagues: Dr. Robert S. Synder
                       Dr. Percy H. Rhodes

.

Visualization of Individual DNA Molecules

For several years individual DNA molecules have been observed and photographed during agarose gel electrophoresis. The DNA molecule is clearly the largest molecule known. Nevertheless, the largest molecule is still too small to be seen using a microscope. A technique developed by Morikawa and Yanagida has made it possible to visualize individual DNA molecules. When these long molecules are labeled with appropriate fluorescence dyes and observed under a fluorescence microscope, although it is not possible to directly visualize the local ultrastructure of the molecules, yet because they are long light emitting chains, their microsocpic dynamical behavior can be observed. This visualization works in the same principle that enables one to observe a star through a telescope because it emits light against a dark background. The dynamics of individual DNA molecules migrating through agarose matrix during electrophoresis have been described by Smith et al. (1989), Schwartz and Koval (1989), and Bustamante et al. (1990). DNA molecules during agarose gel electrophoresis advance lengthwise thorough the gel in an extended configuration. They display an extension-contraction motion and tend to bunch up in their leading ends as the "heads" find new pores through the gel. From time to time they get hooked on obstacles in the gel to form U-shaped configurations before they resume their linear configuration.

Fractionation of DNA by Electrophoresis

The visualization of the conformation dynamics of DNA molecules during electrophoresis has contributed much to the design of improved methods of DNA size fractionation. In particular, efforts to obtain complete physical maps of human chromosomes require techniques capable of separating large DNA fragments whose dimensions differ only in a small percentage of their total length. DNA molecules smaller than 50Kb are easily separated on the basis of their size. Large DNA molecules tend to migrate at the same rate. Schwartz and Cantor (1984) described a method that effectively separates large DNA molecules by agarose gel electrophoresis. The Pulse Field Gel Electrophoresis (PFGE) method is based on the fact that DNA molecules in solution behave like a worm-like coil. The pores in the agarose are smaller than the dimension of the coils formed by molecules larger than 30Kb in size. When a large DNA molecule enters such a gel in response to an electric field, the coils must elongate parallel to the field. When the field is shut off and a new field is applied perpendicular to the long axis of the DNA molecule, it finds itself lying across the openings of several pores. It will have to reorient itself and enter one of them. Bustamante et al. (1990) described and

photographed the beads and kinks that form along the molecule during the orientation process. The key to separation is the fact that larger molecules take longer to reorient than smaller ones. As the cycle is repeated, each molecule will have a characteristic net mobility along the diagonal of the gel.

Considerable progress has been made in our lab in preparation of materials and techniques for fractionation and visualization of chromosomal DNA. Intact yeast chromosomal DNA was prepared, fluorescently labelled with ethidium bromide, and microscopically visualized and photographed (1990). A new Zeiss research microscope has been installed in Dr. Percy Rhodes' lab equipped with a 35mm photographic system and video image system. The design of the electrophoretic chamber and power systems to be used with the microscope is almost complete. Phage lambda DNA has been stained with ethdium bromide and visualized by brownian motion in distilled filtered water using a small black and white video camera and video monitor.

As soon as the above preparations are completed the following will be investigated: 1) fractionation and visualization of T2 chromosomal DNA molecules during agarose gel electrophoresis using constant and pulse field direct currents. 2) Intact yeast chromosomal DNA molecules will be prepared and investigated using the same methods. 3) The feasibility of modifying the techniques used to prepare intact yeast chromosomal DNA and using them to obtain intact chromosomal DNA from animal cells grown in tissue culture, spermatozoa, and protozoa is being investigated.

The experience of working with the MSFC team for two summers has been enlightening and exciting. Special appreciation goes to MSFC colleagues Robert Synder, Percy Rhodes, and Teresa Miller, as well as numerous others who have been so helpful and friendly. It is hoped that colloboration will continue through the Summer Faculty Fellow Research Continuation Grant.

References

1. Bustamante, Carlos; Gurrieri, Sergis and Smith, Steven B. (1990) "Observation of Single DNA Molecules during Pulsed-Field Gel Electrophoresis by Fluorescence Microscopy," Methods: A Comparison to Methods in Enzymology, Vol. 1, No. 2, pp. 151-159.

2. Lubega, Seth (1990) "Visualization of Yeast Chromosomal DNA," Research Report 1990, NASA/ASEE, NASA CR-184044: XXZI-XXZI-5.

3. Schwartz, David C., and Koval, Michael (1989) "Conformational Dynamics of Individual DNA Molecules During Gel Electrophoresis," Nature, Vol. 338, No. G215, pp. 520-522.

4. Morikawa, K., and Yanagida M. (1981) J. Biochem (Tokyo) 89:693.

5. Smith, Steven B., Aldridge, K., and Callis, James B. (1989) "Observation of Individual DNA Molecules Undergoing Gel Electrophoresis," Science, 243:203-206.

1991

NASA/ASEE SUMMER FACULTY RESEARCH PROGRAM

MARSHALL SPACE FLIGHT CENTER
THE UNIVERSITY OF ALABAMA IN HUNTSVILLE

EFFECTS OF VEGETATION ON SOIL MOISTURE DISTRIBUTION & FLUX
WITH IMPLICATIONS FOR THE GLOBAL HYDROLOGIC CYCLE

Prepared by: Emir Jose Macari, Ph.D.

Academic Rank: Assistant Professor

University and Department: University of Puerto Rico
                                      Civil Engineering Dept.

NASA/MSFC:
    Laboratory: Space Science
    Division: Earth Science and
                                      Applications
    Branch: Special Projects

MSFC Colleague: N. C. Costes, Ph.D.

Date: July 19, 1991

Contract No.:   The University of Alabama
                                      in Huntsville
                                      NGT-01-008-021

Y

Abstract

Recent climate modeling experiments have identified the critical need for a better understanding of land surface - atmosphere interactions. An important issues in global climate modeling is to be able to relate land surface and atmospheric processes. In the past this link has been inadequately represented due to the lack of understanding of the interaction between the processes and also due to the large spatial variability of the hydrological and soil properties. A project was initiated at MSFC in FY 90 under the Center's Directorate Discretionary Fund (CDDF) to study small-scale effects of vegetation on the distribution and fluxes of soil moisture. Installation of a large array of instruments was accomplished during that first year (FY 90), during this second year of the project the instrumentation and data collection systems were improved and data has begun to be taken. Preliminary analysis of the data show that the equipment has been functioning properly. This report presents some of the preliminary results that have recently been analyzed.

Introduction

The Mission to Planet Earth has as one of its main objectives the study of the changes that the planet has and is undergoing. Mission to Planet Earth describes a focused effort in satellite remote sensing and the associated ground-based research from a variety of fields that will characterize the global environment as an interacting system. The Earth Observing System (EOS) is an integral part of Mission to Planet Earth and is dedicated to providing the new observations, data and information necessary to understand the way the Earth works as a natural system.

With the development of EOS, scientists will be able to observe and understand many of the key variables and processes of the global-scale cycles of energy and water. Water plays a global role of enormous variety of Earth system processes. Water is considered to be the most powerful agent of topographic change. Water is also necessary for life on Earth, playing a major role in climate regulation. In addition to its role in ocean circulation and precipitation, water can also affect climate in the continents through transpiration within plant and soil ecosystems. Short term hydrological events, such as droughts or large precipitation activity can cause substantial ecological changes on regional scales.

The ability to model the current climate and potential climate changes is intimately connected to our understanding of the hydrologic cycle. The generalized schemes that are used in models are unlikely to be equally applicable to all

areas, which means that the ability to simulate climate and climate changes will vary from area to area. It is necessary to include in models all the characteristics of a particular area which may impact these processes. One of the chief characteristics that varies from area to area and impacts hydrologic processes is the vegetation.

Large scale hydrologic studies are essential to the NASA/MSFC EOS initiative in order to better understand hydrological flux processes that are a main ingredient in global biosphere interactions. One of the most important questions for modeling the global hydrologic cycle includes the interrelationship between land surface and atmospheric processes for variable spatial and temporal scales. Global climate models have shown that proper modeling of the Earth's surface (which is commonly modeled as a boundary layer) is of great importance to the results obtained in such modeling studies.

Scope of Work

During the summer of 1990 a large array of soil moisture and precipitation instruments were installed at a field site within Redstone Arsenal to monitor the ambient atmospheric and soil conditions. Tipping bucket rain gauges monitor sub-canopy throughfall and stemflow and free-field precipitation. In addition an array of 36 manually-read rain gauges has been installed, this year, beneath the tree canopy in a six-by-six grid to evaluate the spatial variability of soil moisture that can be attributed to throughfall. Thirty three sets of tensiometers were also installed in various locations. Each set having three tensiometers installed at 1', 2', and 3' depths. The tensiometers are used to monitor the soil moisture conditions prior to, during, and after rain events. Data acquisition for the system is controlled by three programmable data loggers that sample the instruments at specified times and upload the information to solid state storage modules that are subsequently downloaded to a PC for analysis.

Preliminary results show that the instrumentation is generating good data. These results have enabled us to begin to make comparisons between the soil-vegatation conditions at the site (i.e. bare, grass-covered, and grass and tree-covered soil). Comparisons can also be made of the canopy-covered to the free-field areas. Data from the tipping bucket and manually read rain gauges have shown temporal and volumetric variations in the amounts of precipitation reaching the ground. However a statistically valid data base must be developed in other to make definite conclusions. The soil moisture response to precipitation events is shown in Figure 1 in the form of tensiometer signals at depths of 1'

and 3' with precipitation amounts in time. Figure 1 shows
that the response of the tensiometers prior to a
precipitation event is in the form of drying (i.e. increase
in tension) while after the precipitation the tension begins
to diminish. One can also notice that the response of the 1'
depth tensiometers is quite dramatic and quick while for the
3' depth tensiometers it is greatly attenuated in quantity
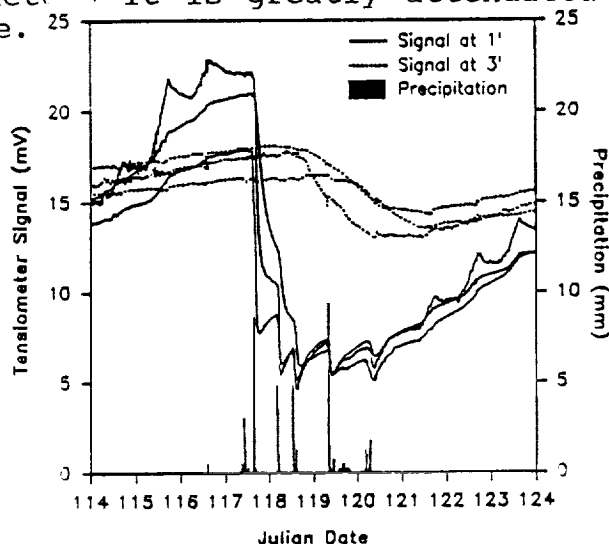and response time.

Figure 1.- Soil moisture response to precipitation events
over a ten day period as a function of depth.

Figure 2 presents the response of the tensiometers
after a precipitation event. This figure shows that a higher
rate of moisture loss is observed for the upper most soil
layers. A higher moisture loss is also observed for soils
with both trees and grass cover, as compared to that of
grass cover or bare soil. This last point illustrates the
importance of the study of the effects of vegetation on soil
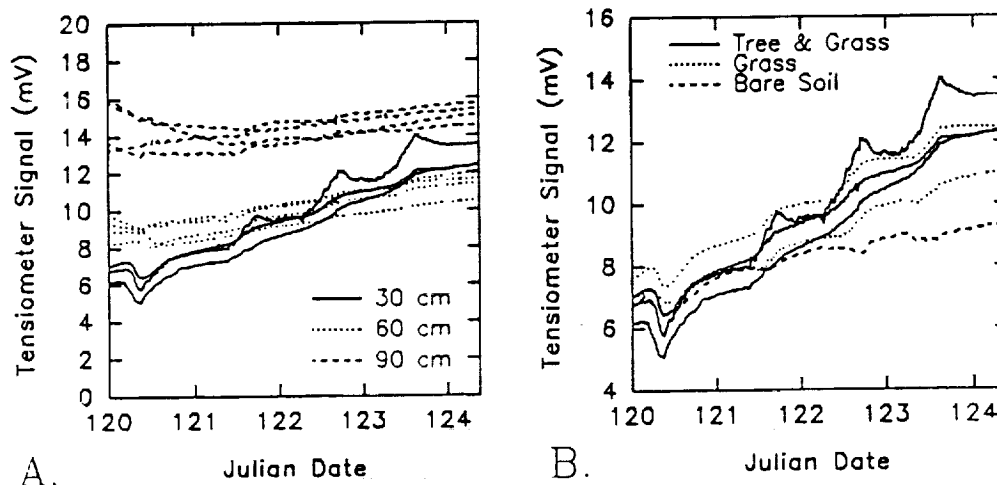moisture conditions.

Figure 2. Rate of soil moisture loss as a function of
(A) depth, and (B) vegetation cover.

Acknowledgements

References

Brutsaert, W., 1989: Committee on large-scale experimentation. OES Trans. AGU, 70:530.

Costes, N.C., McDonnell, J.J., and Macari, E.J., 1990: Experimental techniques for assessing vegetation-induced moisture flux. Fall Meeting, American Geophysical Union, San Francisco, CA.

Eagleson, P.S., 1978: Climate, soil, and vegetation: 2. The distribution of annual precipitation derived from observed storm sequences. Water Resour. Res., 14:713-721.

Gurney, R.J., 1987: The proposed Global Energy and Water Cycle Experiment (GEWEX). EOS Trans. AGU, 68:707.

Laymon, C.A., Macari, E.J., and Costes, N.C., 1992: Small-scale field experiment of land surface-atmosphere interactions with EOS implications. Space 92, ASCE/NASA, Denver, Co. (accepted for publication).

McDonnell, J.J. and Costes, N.C., 1990: Use of remote sensing in process hydrology at varying basin scales. 1st Joint USA/USSR Hydrology and Hydrogeology Meeting, Leningrad, USSR, 1:24.

Mintz, Y., 1984: The sensitivity of numerically simulated climates to land-surface boundary conditions. In J.T. Houghton (ed), The Global Climate, p.79-105.

Ye, D., 1989: Sensitivity of climate model to hydrology. IUGG Geophys. Monogr., 52:101-108.

Yeh, T.C., R.T. Wetherald and S. Manabe, 1884: The effect of soil moisture on the short-term climate and hydrology change - a numerical experiment. Mon. Weather Rev., 112:474-490.

NASA/ASEE Summer Faculty Fellowship Program

Marshall Space Flight Center

"Control of a Flexible Beam Using Fuzzy Logic"

Prepared By: Claire L. McCullough, Ph.D.

Academic Rank: Assistant Professor

Institution: University of Alabama-Huntsville
                        Dept. of Electrical and Computer
                        Engineering

NASA/MSFC:

Laboratory: Structures and Dynamics

Division: Control Systems

Branch: Pointing Control Systems

MSFC Colleague: Ms. Angela P. Bukley

Introduction

The goal of this project, funded under the NASA Summer Faculty Fellowship program, was to evaluate control methods utilizing fuzzy logic for applicability to control of flexible structures. This was done by applying these methods to control of the Control Structures Interaction Suitcase Demonstrator developed at Marshall Space Flight Center. The CSI Suitcase Demonstrator is a flexible beam, mounted at one end with springs and bearing, and with a single actuator capable of rotating the beam about a pin at the fixed end. The control objective is to return the tip of the free end to a zero error position (from a nonzero initial condition). It is neither completely controllable nor completely observable.[1] Fuzzy logic control was demonstrated to successfully control the system and to exhibit desirable robustness properties compared to conventional control.

Fuzzy Logic

"Fuzzy" logic, which was initially developed by Lofti A. Zadeh of Berkeley, is a combination of multi-valued logic, probability theory, and artificial intelligence. It incorporates the imprecision inherent in many real-world systems, including human reasoning, by allowing linguistic variable classifications such as "big," "slow," "near zero," or "too fast." Unlike binary logic, fuzzy systems do not restrict a variable to be a member of a single set, but recognize that a given value may fit, to varying degrees, into several. For example, a speed of 55 mph may be moderately slow, fast, or too fast depending on other factors such as speed limit or road condition.

Fuzzy systems operate by testing variables with IF-THEN rules, which produce appropriate responses. Each rule is then weighted by a "Degree of Fulfillment" of the rule invoked; this is a number between 0 and 1, and may be thought of as a probability that a given number is considered to be included in a particular set. A wide variety of shapes is possible for fulfillment functions, triangles and trapezoids being the most popular.[2] Fulfillment functions for this study were of the form

$$fuzzy(x,m,s,p) = \exp(-(|x-m|/s)^p) \tag{1}$$

where m, s, and p are user-chosen parameters and x is the value to be tested. This function was chosen because of its flexibility; by changing "m," "s," and "p" whole families of different functions can be obtained. A sample of the functions obtained by varying the "p" parameter is shown in Figure 1. The system operates by testing rules of the type

"If error is big and velocity is small,
   then u should be negative and big."

The degree of fulfillment for such a rule is the minimum of the degrees of fulfillment of the antecedent clauses; i.e.,

$$DOF = \min [DOF_{error\ big}, DOF_{velocity\ small}]. \tag{2}$$

The total output of the control system is a weighted sum of the responses to all "n" rules

$$u = (_{i=1}\Sigma^n\ w_i\ (DOF_i)\ B_i^d)/(_{i=1}\Sigma^n\ w_i\ (DOF_i)) \tag{3}$$

where DOF_i is the degree of fulfilment of rule "i," B_i^d is the "defuzzified" output response to rule "i," and w_i is a weight indicating the relative importance of rule "i."[3]

The Basic Fuzzy Control System

A simulation of the CSI Suitcase Demonstrator was implemented on a 386 PC equipped with MATLAB. The two measurable quantities at the system output are line of sight error and angular rate of change. Fuzzy categories assigned to each were positive-big, positive-medium, positive-small, zero, negative-big, negative-medium, and negative-small. In addition, LOS error has a "near-zero" category (see Figure 2 for category examples). A standard fuzzy control system was generated using 14 rules. The rules for the initial system were of two types

Set A: If LOS error is positive-big, then u is negative-big.
            (7 rules, one for each category of LOS error)

Set B: If LOS error is near-zero and velocity is positive-big,
            then u is negative-big.
            (7 rules, one for each category of angular velocity)

The rules in set A approximate a proportional control scheme; set B approximates derivative control, but is only effective when LOS error is small. This strategy is to drive the system to the desired output as quickly as possible, and only apply damping when the system response is close to the desired value. This was demonstrated to be successful in [3]. A wide variety of fuzzy system responses can be generated by changing "s," "p," and the weights of the rules. The optimal choice of system parameters, weights, etc. would depend on the desired performance characteristics for the system to be controlled; criteria used in this study for "good" control were smooth system performance, quick convergence of LOS error to 0, and small overshoot. The unforced response of the system is shown in Figure 3, and a typical fuzzy system response is given as Figure 4. Removing the "near zero" condition on the second set of rules resulted in slightly slower system response with less overshoot, as expected. Various "p" values were tried, with p=2 appearing to be optimal (lower values allowed more overshoot, and higher values resulted in failure to damp out some of the system frequency components). Changing "s" factors demonstrated that acceptable system performance is still obtained when spread is increased by as much as 100% (though overshoot increases as the factor is increased), while a relatively small (25%) decrease again leads to undamped frequency components (as higher "p" values have smaller spread, this is consistent with the results for changing "p"). Thus great overlap between sets is acceptable, while too little overlap gives less optimal results. A slightly smoother response, with no appreciable change in settling time, was obtained by averaging the control over 2, 3, or 4 time steps. The system was found to behave adequately when randomly chosen plant matrix parameters were altered by + or - 50%, and when Gaussian noise was added to system states.

Anticipatory Fuzzy Control

A new control strategy, called anticipatory fuzzy control, was developed under this program. This differs from traditional fuzzy control in that once fuzzy rules have been used to generate a control (as in equation (3)), a predictive routine built into the controller is called to anticipate the effect of the proposed control on the system output. If using the current control value will result in system behavior which is in some way unacceptable, additional rules are called. This method may be used to nest as many sets of rules as the designer desires. Advantages of this approach compared to standard fuzzy controllers are
1.   Nesting rules allows use of only as many rules as are necessary to achieve desired system performance, resulting in savings in computer run time.
2.   By predicting system performance, controls which would result in unstable or unacceptable system performance can be eliminated.

Z-2

Standard predictive fuzzy control, which uses only predictive rules, requires more calls to the predictive routine than this scheme, and fails to take advantage of all system knowledge.[4] The simplest type of anticipatory system control has a single additional rule of the form

"If the current value of the control (u_0) will cause the difference between the current and anticipated values of velocity to be 'big,' then

$$u = u_0(1 - \beta \cdot \text{bigt})," \tag{4}$$

where β is a user-chosen parameter between 0 and 1, and "bigt" is the fulfillment function for the anticipated difference in velocity values (which is proportional to the predicted acceleration of the system.) A typical response with $\beta = .7$ is shown in Figure 5. Higher values of β result in smoother responses with slightly more overshoot; lower values resemble the nonanticipatory response (Figure 4). In every case, the anticipatory fuzzy system results in smoother system response than the traditional fuzzy control. Conclusions on the effects of changing "p" and "s" hold for the anticipatory system as well. Averaging control over two or more steps had a more marked effect on the anticipatory system, with the best response (shown in Figure 6) resulting when control was averaged over two time steps. When plant parameters were perturbed, as discussed earlier, the system exhibited a larger overshoot, but still settled to 0 within 3 seconds. In contrast, a standard linear quadratic regulator had considerably less overshoot, but failed to drive the system to 0 within 5 seconds. The anticipatory fuzzy system tolerated added state noise much better than the LQR, in which the noise caused a wide excursion from the desired LOS error value of 0.

Similar system responses can be achieved using a more complex, but more intuitively satisfying, anticipatory system with several additional rules of the form

"If u_0 is positive big and a positive big u will make the change between current and anticipated values for velocity "big," then u is positive medium."

Effects of these rules are added in to the sums in equation (3). However, this method offers no improvement in performance over the simpler anticipatory system, while requiring more calls to the predictive routine, and therefore more computer run time.

Conclusions

Fuzzy control methods have been demonstrated to adequately control the CSI Suitcase Demonstrator. A new type of anticipatory fuzzy controller has been developed, and has been demonstrated to exhibit desirable output properties. The fuzzy controllers have been shown to be robust in the fact of added noise and perturbations in plant parameters. It is my conclusion that fuzzy contollers show great promise for use in contol of flexible structures and should be further evaluated.

References

[1] Sharkey, J., Private Communications, MSFC, July 1991.
[2] Self, K., "Designing with Fuzzy Logic," IEEE Spectrum, November 1990.
[3] Chiu, S., Chand, S., Moore, D., and Chaudhary, A., "Fuzzy Logic for Control of Roll and Moment for a Flexible Wing Aircraft," IEEE Control Systems, June 1991.
[4] Miyamoto, S., Yasunobu, S., and Ihara, H., "Predictive Fuzzy Control and Its Application to Automatic Train Operation Systems," Analysis of Fuzzy Information, J. C. Bezdek, ed., CRC Press Inc., Boca Raton, FL, 1986.
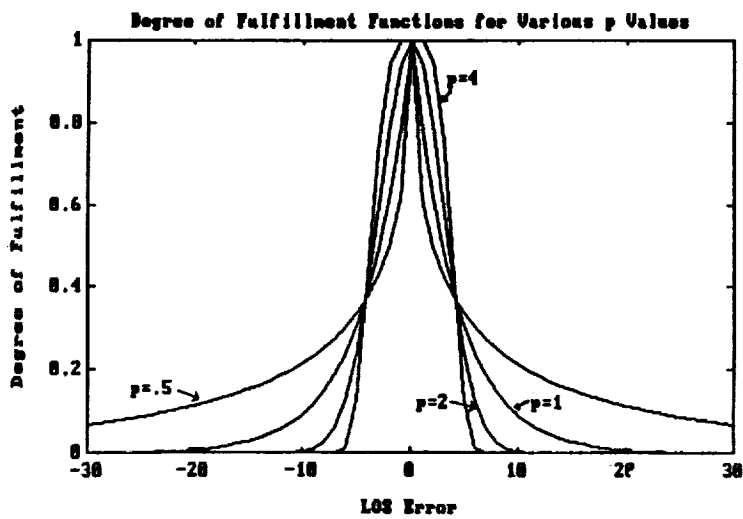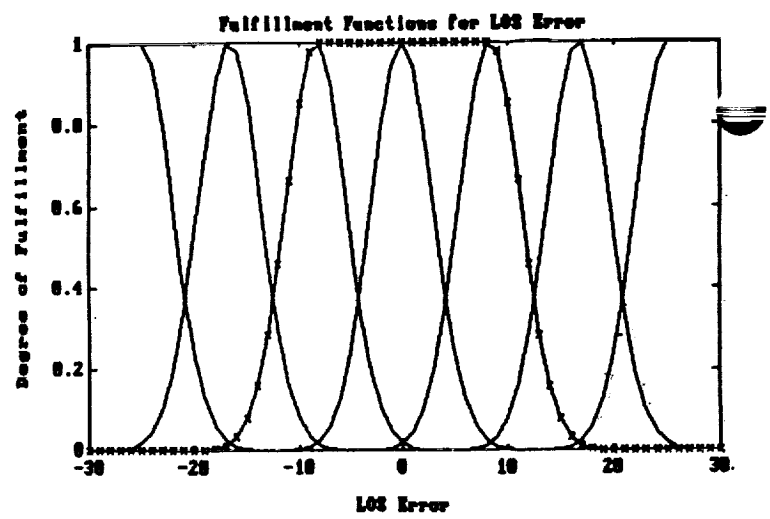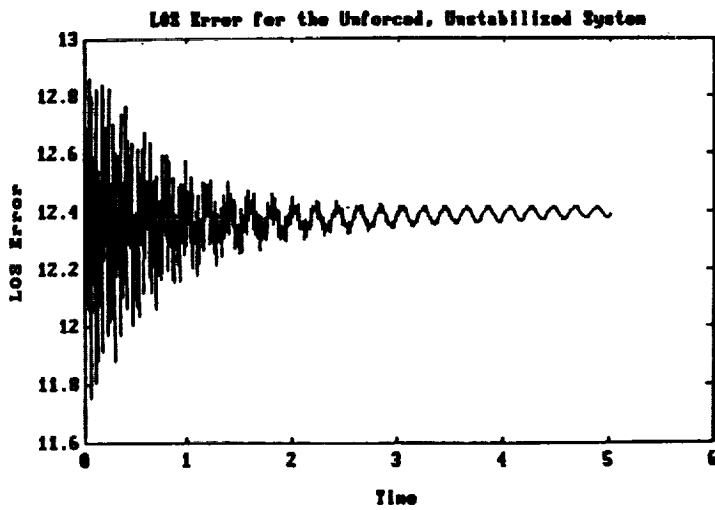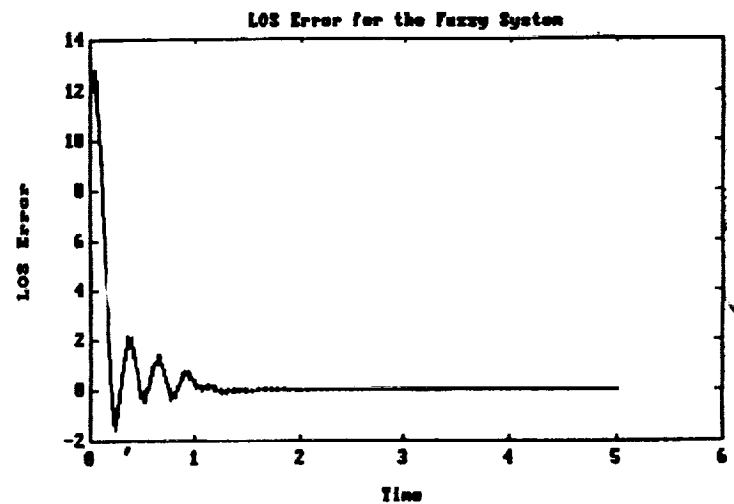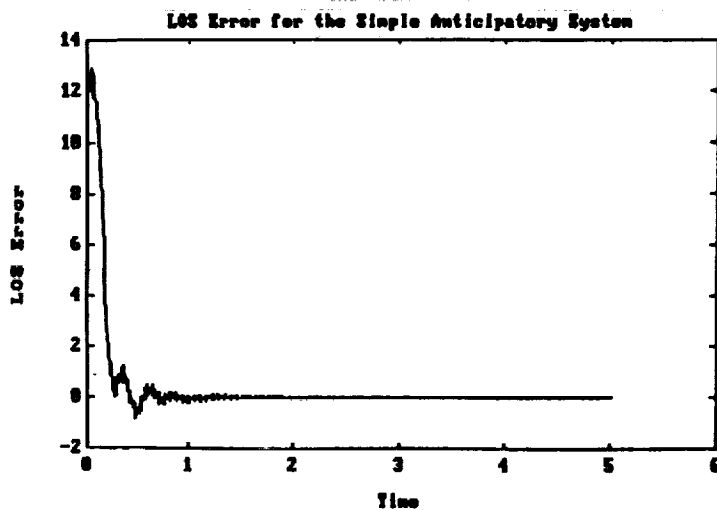
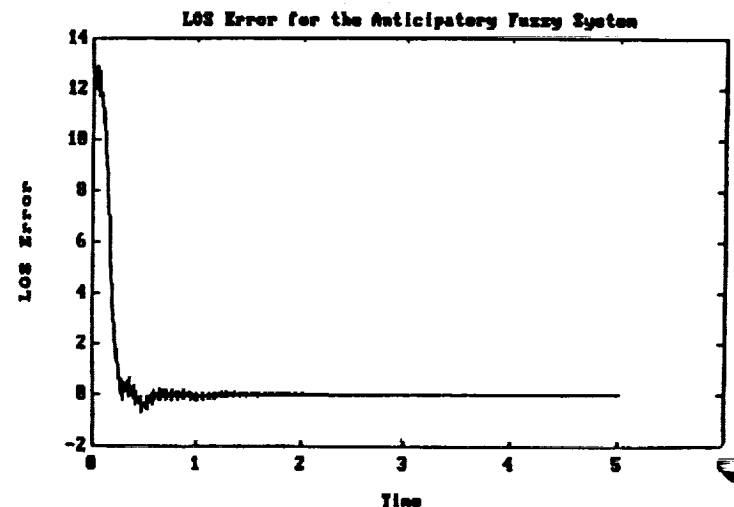Figure 1

Figure 2

Figure 3

Figure 4

Figure 5

Figure 6

Z-4

1991

NASA/ASEE SUMMER FACULTY RESEARCH FELLOWSHIP PROGRAM

MARSHALL SPACE FLIGHT CENTER
THE UNIVERSITY OF ALABAMA IN HUNTSVILLE

REDESIGN OF FLIGHT SPACE SHUTTLE MAIN ENGINE NOZZLE G-15
SEAL AREA BASED ON THE THERMAL ANALYSIS AND FLOW MODELS

Prepared: Gary H. McDonald, Ph.D., P.E.

Academic Rank: Assistant Professor

University and   The University of Tennessee
Department: at Chattanooga
                             Mechanical Engineering-Mechanics

NASA/MSFC:

 Laboratory: Propulsion

 Division: Component Development

 Branch: Turbomachinery and
                             Combustion Devices

NASA colleague: Joan G. Trolinger

Date: August 15, 1991

Contract No.:   NGT 01-008-021
                             The University of Alabama
                              in Huntsville

INTRODUCTION

In the Space Shuttle Main Engine (SSME), the main combustion chamber (MCC) and nozzle are combustion devices used for transporting the supersonic turbulent combustion gases from the injector plate to the exit nozzle plane where the thrust is produced to help propel the shuttle orbiter. The liquid hydrogen fuel and liquid oxygen oxidizer are pumped by low and high pressure turbopumps to the injectors. Then, the fuel mixture is ignited through the converging-diverging MCC to an expansion ratio of 5:1 to the MCC exit plane from the MCC throat. The nozzle which is mated to the MCC using a circumferential ring of bolts further expands the supersonic combustion gas to an area ratio of 77.5:1 to the nozzle exit plane from the MCC throat to produce the required thrust. At the interface between the MCC and nozzle, there exists a G-15 seal area to prevent hot gases from escaping the MCC/nozzle into the aft end of the shuttle orbiter. A problem has evolved with the INCO-718 metal bellows seal in the G-15 seal area. After post-engine and post-flight inspections, a discoloration or bluing of the bellows seal and in one case, a stress rupture crack in the bellows seal has occurred.

In this study, the main objective is to understand the present sealing area response to environmental conditions of the supersonic turbulent combustion gases which has led to both stress rupture cracks and hot gas leakage. A review of the existing thermal analysis and flow modelling has been performed of the present design and seal alternatives have been suggested to possibly reduce or eliminate the hot gas flow recirculation problem and the associated seal cracking.

THERMAL ANALYSIS and FLOW MODELLING

Several thermal analysis and flow modelling studies have been performed to identify the causes of the G-15 bellows seal discoloration and stress rupture problem. McConnaughey [1] and others performed a computational fluid mechanics study motivated by SSME post-flight and post-test inspections identifying the G-15 seal problem. The flow field in the G-15 region was created by a protrusion of the nozzle coolant tubes brazed on the interior of the nozzle shell. Too much protrusion of the coolant tubes created a forward face step preceeded by a narrow G-15 cavity existing between the mating MCC/nozzle interface. The forward step caused a supersonic shock to form at the leading edge of the MCC lip while another shock formed when the main flow stream reattached with the nozzle tubes downstream of the G-15 cavity. This protrusion and gap distance have been

identified as the prime causes for hot gas ingestion in the G-15 cavity, thus, causing an extreme temperature increase of the bellows seal. The reason for coolant tube protrusion is due to an inherent out-of-roundness of the nozzle when mating with the MCC. So, areas of maximum coolant nozzle protrusion into the hot gas free stream is strongly correlated to bellows seal discoloration. However, it should be noted that some cases exist of no protrusion of the coolant tubes into the nozzle free stream did cause some bellow seal damage, but, was minor when compared to the protrusion and gap cases.

A study by Sharma, Dang, and Kassner [2] used the Korst theory to model a forward facing protrusion. Based on the interaction between dissipative shear flow and the adjacent free stream along with the conservation of mass in the wake, there were four flow components analyzed. These components were flow approaching trailing edge of the MCC, expansion around the trailing edge, mixing with the free-jet boundary over the cavity and recompression at the end of the wake at the protruding nozzle coolant tubes. This approach allowed for a unique stable solution for base pressures used to calculate cavity pressure, injection flow rate in the cavity, and gas temperature of the injected flow. This method agreed with the CFD approach concerning the creation of hot gas recirculation within the cavity causing high bellows seal temperatures.

A study by Roman [3] created a thermal-flow model using the SINDA computer program to predict cavity and seal temperatures. This approach also included the FRI (Flow Recirculation Inhibitor) which was a material inserted into the G-15 seal cavity to reduce or prevent hot gas recirculation creating the high seal temperatures. The FRI is made of Nextel material sewed around the nozzle tubes before the tubes enter the outlet coolant manifold. Also, the FRI is glued with uralite to the nozzle lip. The FRI has experienced some burning in testing due to the protrusion and gap dimensions being too large allowing for more hot gas ingestion.

SEALING ALTERNATIVES

Based on the thermal and flow models, a review of the literature on sealing was performed to identify possible replacements of the bellows seal. Seals are classified into two basic categories which are static and dynamic. Static seals are used when the sealing surfaces experience no relative motion between the parts except due to load and thermal expansions. Dynamic seals are used to seal a stationary surface with a

rotating or reciprocating surface. After reviewing various seal texts [4] & [5], some recommended changes are shown in Figures 1 through 4. These recommended seals are static-type. In all of these figures, a recommendation of the MCC lip extension and possible nozzle lip extension were made to help diminish the protrusion and gap effect. It should be noted that the current INCO 718 bellows seal is a load assisted seal with Teflon covered ends loaded in compression due to the bolts and engine thrust. In Figure 1, the usage of a metallic U,C,K,E,V, or X seal can be used to replace the bellows seal in a shortened cavity next to the bolt circle. It is recommended that a secondary seal be used like a metallic gasket around the bolt circle. In Figures 2 & 3, a piston ring and labyrinth seal were used as a primary seal whereas a shortened bellows seal would be a secondary seal. In Figure 4, a recommendation was made to not change the type of seal, but, to tap into an adjacent MCC coolant passage to lower the bellows seal temperature since stress rupture cracks occur due to the loss of ductility of the Inconel 718 material at excessive high temperatures.

RECOMMENDATIONS

Several recommendations were made based on this study.

1. Use a different type of metal seal in the G-15 seal area and use a type of secondary seal in the bolt circle area.

2. Evaluate other high temperature materials for possible replacement of INCO 718. (other metals or bimetallic composite combinations)

3. Investigate the feasibility of reconstructing the MCC lip to block the cavity and possible redesign of the nozzle lip to avoid usage of the FRI.

4. Establish criteria for the improvement of stack and brazing nozzle tubes to avoid a protrusion circumferentially at the MCC/nozzle interface.

5. Investigate the possibility of tapping into the MCC coolant passage adjacent to the bellows seal to keep the temperature from reaching the stress rupture temperature for Inconel 718.

REFERENCES

1. McConnaughey, H.V., J.M. Farrell, T.A. Olive, G.B. Brown, & J.B. Holt, "Aerothermal Environment Induced

by Mismatch at the SSME Main Combustion Chamber - Nozzle Joint," (to be published)

2. Sharma, L., T. Dang, & R. Kassner, "Application of Korst Theory to SSME MCC/Nozzle Mismatch Problem," Rocketdyne - Rockwell International report, August 7, 1989.

3. Roman, J.M., "Space Shuttle Main Engine (SSME) E0213 G-15 Thermal Analysis," internal memo ED64 (91-19), NASA/MSFC, Huntsville, AL.

4. Buchter, H.H., Industrial Sealing Technology, John Wiley & Sons, Inc., New York, NY, 1979.

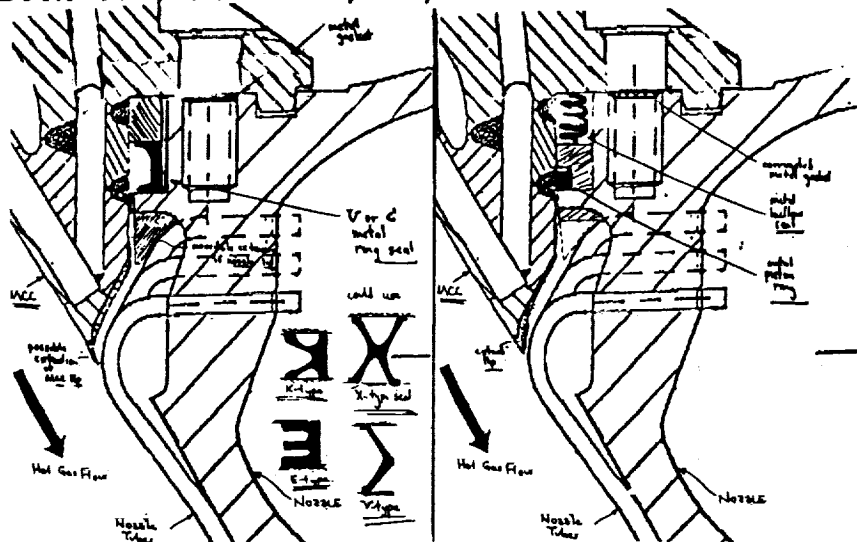5. Parmley, R.O., Mechanical Component Handbook, McGraw Hill Book Co., New York, NY, 1985.

Figure 1: U,C,K,V,E,& X Seals   Figure 2: Piston Ring - Bellows Seal
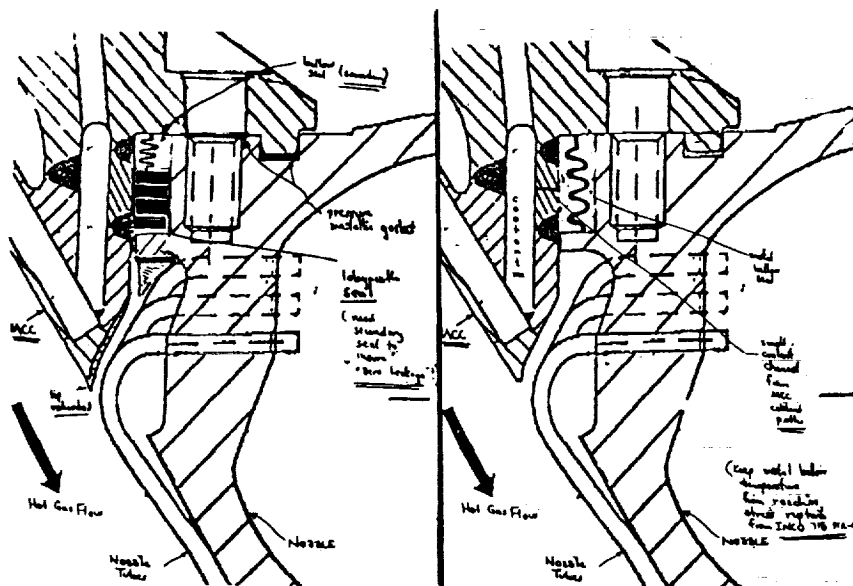
Figure 3: Labyrinth Seal - Bellow Seal   Figure 4: Coolant Passage to Bellows Seal

1991

NASA/ASEE SUMMER FACULTY RESEARCH FELLOWSHIP PROGRAM

MARSHALL SPACE FLIGHT CENTER

THE UNIVERSITY OF ALABAMA AT HUNTSVILLE

**AN INVESTIGATION OF PRE-LAUNCH AND IN-FLIGHT STS RANGE SAFETY
RADIO SIGNAL DEGRADATION AND DROPOUT**

Prepared by:	Malcolm W. McDonald, Ph.D.
Academic Rank:	Associate Professor
Institution:	Berry College Department of Physics
NASA/MSFC: (Laboratory) (Division) (Branch)	Information & Electronic Systems Computers and Communications Communications Systems
MSFC Colleagues:	David P. Harris, EB33 William W. Hopkins, EB33
Date:	July 19, 1991
Contract Number	NGT-01-008-021 The Univ. of Alabama at Huntsville

AN INVESTIGATION OF PRE-LAUNCH AND IN-FLIGHT STS RANGE SAFETY RADIO SIGNAL DEGRADATION AND DROPOUT

I. Introduction to the Shuttle Range Safety System (SRSS).

The term, "Range Safety", in this report refers to the need and responsibility to assure protection of the population and property in the environs of the launch areas of the Air Force Eastern Test Range (AFETR) and along the trajectory of the vehicles in flight. Included in the AFETR are the two launch complexes, pads 39A and 39B, at the Kennedy Space Center (KSC) from which shuttle launches occur. The term, "Shuttle Range Safety", refers specifically to range safety concerns surrounding the launches of the Space Transportation System (STS) vehicle, or "Shuttle" as it is commonly identified.

An individual at the AFETR charged with the responsibility of assuring range safety is the Range Safety Officer (RSO). The RSO is employed by the AFETR and is thus not an employee of the National Aeronautics and Space Administration (NASA). The RSO has the important responsibility of sending a command to destroy any launched vehicle which errs sufficiently from a planned flight trajectory as to present a hazard to population or property. The destruct command is sent in the form of an encoded radio signal from one of several range safety transmitters included in the AFETR to receiving antennas onboard the vehicle.

The range safety system (RSS) transmitters operate at a frequency of 416.500 MHz. The transmitting antennas transmit left circularly polarized waves, and the shuttle range safety system (SRSS) receiving antennas onboard the shuttle vehicle receive left circular polarization.

The shuttle vehicle consists of the orbiter, which carries the crew and payload, two solid rocket boosters (SRB's), and the external tank (ET) which contains the hydrogen and oxygen fuel burned by the orbiter's three main engines. A total of six range safety receiving antennas are positioned on the shuttle vehicle. This includes two on the left SRB, two on the right SRB, and two on the ET.

In addition to the Cape range safety transmitter facility, other tracking and range safety transmitter systems currently used by the AFETR are based at (a) the Jonathan Dickson site, approximately 100 miles south and 30 miles east of the Cape site, (b) the Bermuda island site, and (c) a site at Wallops Island, Virginia. Particular characteristics of the four currently-used transmitter facilities are summarized in Table I.

TABLE I. Characteristics of AFETR Range Safety Transmitter Facilities.				
	Cape	Jonathan Dickson	Wallops	Bermuda
Power	*	69 dBm (8 kw)	60 dBm (1 kw)	69 dBm (8 kw)
Ant. Gain	*	22 dB	18 dB	18 dB
Altitude	21.8 meters	12.3 meters	14.9 meters	19.8 meters
Latitude	28.4394° N	26.6550° N	37.8665° N	32.3480° N
Longitude	80.5983° W	80.1080° W	75.5050° W	64.6535° W

The asterisk appearing in Table I under the Cape transmitter site is to indicate that a combination of transmitting capabilities exists at that site. The Cape transmitter site has two omni antennas and two 18-dB gain steerable antennas. It also has a low-power transmitter (about 600-700 watts, nominal) and another for high-power transmission (8 kw, nominal). Normal procedures for shuttle launches are for the Cape site to transmit on high-power from an omni antenna.

Range safety depends upon maintaining a sufficiently high power input to the integrated receiver-decoders (IRDs) onboard the two SRBs and the ET. This study focused on observed fades or dropouts of signal levels to some of the IRDs on some flights both while the vehicle was on the launchpad and during flight. This study is limited to those shuttle flights that have occurred from STS-26 through STS-40.

II. Analysis of Signal Level Fluctuations

Any analysis of range safety signal behavior begins at the launchpads. Table II illustrates the history of background signal levels on the launchpads at the various IRDs mounted on the vehicle. The power levels are expressed in units of dBm (decibels relative to one milliwatt). An observed anomaly observed in this data is that the power level at the pad 39A is persistently lower than at pad 39B, despite being somewhat closer to the transmitter. This is being interpreted as due to a destructive interference contribution in the transmitter illumination of the pad by reflections from reflecting surfaces in the vicinity, a condition which does prevail at pad 39B because of a different geometry.

Table II. **Background Signal Levels at T-600 Seconds**

STS	Launch Date	Pad	LHA (dBm)	LHB (dBm)	RHA (dBm)	RHB (dBm)	ET (dBm)
26	9/29/89	B	-47	-46	-48	-45	-61
27	12/02/88	B	-48	-42	-49	-47	-58
29	3/13/89	B	-47	-45	-48	-47	-56
30	5/04/89	B	-46	-40	-46	-45	-55
28	8/08/89	B	-45	-40	-46	-44	-56
34	10/18/89	B	-46	-45	-47	-49	-60
33*	11/22/89	B	-60	-56	-59	-60	-68
32	1/10/90	(A)	(-58)	(-62)	(-55)	(-56)	(-58)
36	2/28/90	(A)	(-58)	(-60)	(-52)	(-53)	(-53)
31	4/24/90	B	-50	-50	-49	-50	-59
41	10/06/90	B	-46	-44	-47	-47	-60
38	11/15/90	(A)	(-55)	(-64)	(-52)	(-52)	(-55)
35	12/02/90	B	-42	-44	-47	-45	-62
37	4/05/91	B	-48	-46	-48	-49	-63
39	4/28/91	(A)	(-58)	(-58)	(-51)	(-52)	(-56)
40	6/05/91	B	-48	-46	-48	-45	-60

Fluctuations of IRD power levels during the countdown before launch are attributable to the retraction motions of two major launch tower appendages, the orbiter access arm and the vent gas recovery system arm (the "beanie cap"). Reflections from the moving surfaces into the SRSS antennas cause signal fluctuations during the motions. Also the stowage positioning of the appendages at the conclusion of their motion can be the cause for a shifting up or down in the background power levels into the IRDs.

During the flights of the shuttle, several types of IRD signal fluctuations have been noted in the flight data and treated. These include: (a) a very rapid fluctuation observed in the ET data during the roll-pitch maneuver which the shuttle undergoes from about 7 to 20 seconds after liftoff, (b) a drop in the signal level to both right SRB receivers of about 20 to 30 dB during the roll-pitch maneuver, (c) a marked further degradation of the right SRB receiver signal levels starting at about 80 seconds into the flight (most noticeable on launches into high-inclination orbits), (d) a general pattern of longer-period fluctuations in both the SRB and ET receiver data after the roll-pitch maneuver, and (e) after SRB separation, ET signal variations of slow modulated variation superimposed on a motonically decreasing background.

The rapid ET signal fluctuations (a) are directly attributable to two causes. The first is the rapid phasing interference to be expected by the motions of the two ET antennas as the vehicle rolls through an angle in excess of 90 degrees in less than 15 seconds. During most of the roll the A antenna is moving away from the transmitting antenna while the B antenna is rolling around in the direction toward the transmitting antenna. Thus, the wave path to the A antenna is increasing while the wave path to the B antenna is decreasing , hence the rapid phasing interference. A second contribution to the rapid ET signal fluctuations during the roll is attributable to the structure in the roll-axis ET antenna pattern.

The signal level drop (b) comes about because the two right SRB antennas rotate around into the "shadow" of the shuttle, thus experiencing a diminished input power. The right SRB receiver signal fading (c) is due to increasing attenuation by the SRB plume as the vehicle's aspect, as viewed from the transmitter, becomes a tail-end view.

The general pattern of longer-period fluctuations (d) after the roll-pitch maneuver in both the ET and SRB receiver data before SRB separation are probably due to (1) slow phasing interference effects caused by changes in total wave propagation paths into the pair of antennas on an SRB or the ET as the vehicle moves along its trajectory, slowly changing its aspect with respect to the Cape transmitter, and (2) SRSS antenna pattern variations.

The slow modulated fluctuations in the ET data after SRB separation (e) can be explained. The monotonically decreasing background is a natural space loss drop due to increasing distance from transmitter to ET antennas, while the modulated variations are almost certainly due to SRSS antenna pattern fluctuations.

Preliminary explanations have been proposed for many of the observed fluctuations in signal levels. It is being recommended that experiments and further investigation be performed to test the validity of certain of the explanations offered in the analysis section. Such will be pursued as a continuation of this summer's investigation.

1991

NASA/ASEE SUMMER FACULTY FELLOWSHIP PROGRAM

MARSHALL SPACE FLIGHT CENTER
THE UNIVERSITY OF ALABAMA

GROUND-BASED HIGH ENERGY ASTRONOMY

Prepared by:	Charles H. McGruder III, Ph.D.
Academic Rank:	Full Professor
Institution:	Fisk University Physics Department
NASA/MSFC:	

Office:
    Division:
    Branch:
	Space Science Laboratory
	Astrophysics
	High Energy Astrophysics

MSFC Colleague:	Jerry Fishman, Ph.D.
Contract No.:	NGT-01-008-021 The University of Alabama

CC

I. Introduction

The electromagnetic spectrum is divided into six parts. Astronomical observations of half of these parts, namely the long wave parts, are ground-based. "Ground-based" means the measuring instruments are located on the earth's surface. The short wave or high energy parts of the electromagnetic spectrum are not ground-based. Instruments for measuring these celestial radiations are carried aloft by balloons or rockets. The reason why there is no ground-based high energy astronomy is because these radiations do not reach the earth's surface. They are absorbed in the earth's atmosphere. So it appears that ground-based high energy observational astronomy is impossible. Nevertheless, my basic aim is to develop a ground-based high energy astronomy.

To see how this just may be possible we ask: What happens to the high energy photons when they interact with the earth's atmosphere? The answer is: they ionize the atoms of the earth's atmosphere. Thus, celestial high energy radiation - that is the far ultraviolet, X-Ray and Gamma Rays - lead to the production of free electrons. How can we detect these electrons? Free electrons in general influence the propagation of electromagnetic radiation. So, if we send radio waves of an appropriate frequency (VLF - very low frequency) into the region of the atmosphere (the ionosphere), where the free electrons are produced, then by studying the received radio waves we can hope to ascertain the electron density in these regions and draw conclusions about the celestial radiation which caused them.

Why develop a ground-based high energy astronomy? After all we have short wave detectors on board satellites, which lie outside the earth's atmosphere. There are two major advantages that our technique possesses. They are:
1. financial - compared to any other technique this method is cheap. The Gamma-Ray Observatory (GRO) for example cost about $560 million, whereas a VLF radio monitoring facility in the thousands.
2. The possibility of all sky observations on a 24 hour continuous around the clock basis. Satellites like GRO can not see at any given time about 30% of the sky. This is because the earth blocks the satellite's view. A world wide VLF radio monitoring network would be capable of all sky observations.

The specific aim of the project at hand is to study the changes in amplitude and phase of VLF radio waves to see if we can detect the ionospheric disturbance (that is the change in electron density) caused by a Gamma-Ray burst[1].

The possible advantages of observing gamma-ray bursts through ionospheric disturbances are[1]:

1. better localization of burst directions through a large network of VLF receiving points.
2. Measurement of total ionizing fluence of gamma-ray bursts.
3. comparison with satellite data (GOES and GRO) to derive properties of the ionosphere

There is a major problem here: The ionospheric disturbance caused by a Gamma-Ray burst is at best extremely difficult and at worse impossible to detect. So far only one event has been detected via this method. Therefore, it was decided to study the ionospheric disturbance caused by solar flares first with the hope that they will teach us how to detect the elusive Gamma-Ray bursts. Much is to be learned about the ionosphere and its reaction to impulsive ionization.

II. VLF Radio Monitoring Facility

My basic aim this summer was: To secure VLF data so that it could be analyzed at Fisk University in Nashville. This proved to be a major task. Huntsville does have a VLF monitoring facility, but it had three major problems

(1) it was only operating 67% of the time.
(2) The number of 9 track tapes was too cumbersome. Two tapes a day or 730 tapes a year if operation time were 100%. Just copying the tapes takes a lot of time. All tapes had to be copied because the originals must go to Stanford University, the owners of the Huntsville VLF-receiving equipment.
(3) Many tapes contained numerous parity errors. Some tapes were almost completely unusable.

All of the above problems have been solved by introducing the Exobyte tape drive. It employs 8mm tapes which have a capacity of 2.239 Gigabytes. We now:
(1) operate 90% of the time
(2) have only two small cassette tapes per week and
(3) no more parity errors.

The Huntsville facility received during the period of observation (May-July 1991) VLF radio waves from the following transmitters:

Area	City	frequency
Australia	Perth	22.3 kHz
Hawaii	Lualualei	23.4 kHz
Maine	Cutler	24.0 kHz
Nebraska	Silver Creek	24.8 kHz
Washington	Jim Creek	48.5 kHz
Puerto Rico	Aquadilla	28.5 kHz

III. Results

   As a first step to developing this method, ground-based
observations of solar flares were correlated with satellite
observations from the Gamma-Ray Observatory and the GOES satellite.
The results are summarized as follows:

Total number of VLF - solar flares:	75
Comparison with GOES-West Satellite:	
Percent of VLF found in GOES:	96%
Number of VLF not found in GOES:	3
Comparison with Gamma Ray Observatory(GRO)	
Percent of VLF found in GRO:	55%
Percent of VLF not found in GRO:	45%
Percent not found due to occultation:	28%
Percent of VLF missed in GRO:	17%

   Firstly, we discuss the comparison of ionospheric disturbances
attributed to solar flares with the GOES-West satellite. We see
that 96% were actually solar flares according to the GOES-West
satellite. These results clearly demonstrate the ability of the
method to differentiate between ionospheric disturbances caused by
a celestial source and those due to ionospheric and magnetospheric
effects. All three of the VLF-solar flares that were not considered
solar flares by GOES did show significant flux increases in the
hard X-Ray region (0.5-4Å) according to GOES but were too weak in
the soft X-Ray region (1-8Å) to be classified as solar flares.
Thus, all of the ionospheric disturbances which were interrupted to
be solar flares actually corresponded to flux increases in the
solar hard X-Ray emission.

   Secondly, we discuss the comparison of VLF-found solar flares
with the solar flares found by the BATSE detectors of the Gamma-Ray
Observatory (GRO). A large percentage (45%) were not classified as
solar flares according to BATSE. However, 28% of the total or 62%
of those that could not be found by BATSE were due to the fact that
GRO could not see the sun because the earth was in between the
spacecraft and the sun (occultation).

IV. Research Plan

A. The Search for Gamma-Ray Bursts
1. So far not a single Gamma-Ray Burst is readily apparent in the low time resolution data used for detection of the above mentioned solar flares. To find Gamma-Ray Bursts the following approach will be used: Low intensity solar flares are to be located in the VLF data using the GOES and BATSE flares as a guide. Hopefully, this will teach us how Gamma-Ray Bursts will look like in the VLF-data since they are in general of low intensity in the spectral region, which above VLF frequencies seem to be capable of detecting.
2. Search along different propagation paths – variation of both transmitter and receiver points.
3. Search at other frequencies.
B. Comparison with GOES and BATSE
1. Starting from GOES and BATSE to see how many flares are not contained in the VLF data and to understand why they are missing.
2. Derivation of the threshold value for solar flares by comparing VLF with GOES and BATSE.
3. Comparison of (a) onset, rise, maximum and decay times of VLF with the corresponding values for GOES and BATSE to derive the properties of the ionosphere.
C. VLF-solar flares
The study of solar flares in the VLF data in reference to: (a) changes in amplitude and phase of the VLF (b) zenith angle dependency (c) frequency dependency and (d) dependency on the propagation path of the VLF signal.
D. Theoretical
1. Detailed calculations of electron density distributions during solar flares from the known irradiation according to GOES-West and during gamma-ray bursts from the known irradiation according to BATSE are to be carried out. Specifically, the time dependency of the irradiation will be incorporated, which is generally not done.
2. Dropping the assumption of a simple exponential electron density distribution and the concept of "reflection height" in the standard model for VLF wave propagation in the terrestrial waveguide[2], the temporal behavior of the VLF amplitude is to be reconciled with observations.

References:
1. Fishman, G.J. & Inan, U.S. Nature 331, 418-420 (1988)
2. Wait, J.R. & Spies, K.P. NBS TN 300 (1964)

1991

NASA/ASEE SUMMER FACULTY FELLOWSHIP PROGRAM

MARSHALL SPACE FLIGHT CENTER

LUNAR TRANSIT TELESCOPE LANDER DESIGN

Prepared By: **Husam A. Omar, Ph.D.**

Academic Rank: Assistant Professor

Institution: University of South Alabama
Department of Civil Engineering
Mobile, Alabama 36688

NASA/MSFC:

       Office: Space Explorations PS02

       Division: Program Development

       Colleague: Max Nein

Lunar telescopes provide several advantages over earth based and space telescopes. The absence of atmosphere around the moon provides a much clearer view than earth based telescopes. Furthermore, the lunar surface can provide anchorage and support for the telescope thus eliminating a lot of vibrations associated with free flying space telescopes. The precise movements of the moon can serve as a platform for telescopes that can be used to scan the skies both efficiently and economically. The Program Development group at NASA's Marshall Space Flight Center has been involved in studying the feasibility of placing a 16 meter telescope on the lunar surface to scan the skies using visible/ Ultraviolet/ Infrared light frequencies. It became apparent that many of the technologies needed to achieve this objective are not currently available and will not be available in the near future. Therefore, the astronomical science community, realizing the many advantages of Lunar Telescopes, decided to go for a precursor telescope that is simple to build, transport and deploy on the lunar surface. This telescope will provide the science community with basic science in the near future and the engineering community with badly needed information about the influence of the Lunar environment on the telescope's mirrors, support systems and structure. The precursor telescope is now called the TRANSIT LUNAR TELESCOPE (LTT). The Program Development Group at Marshall Space Flight Center has been given the task of developing the basic concepts and providing a feasibility study on building such a telescope. The telescope should be simple with minimum weight and volume to fit into one of the available launch vehicles. The preliminary launch date is set for 2005.

A study was done to determine the launch vehicle to be used to deliver the telescope to the lunar surface. The TITAN IV/Centaur system was chosen. The engineering challenge was to design the largest possible telescope to fit into the TITAN IV/Centaur launch system. The telescope will be comprised of the primary, secondary and tertiary mirrors and their supporting system in addition to the lander that will land the telescope on the lunar surface and will also serve as the telescope's base. The lunar lander should be designed integrally with the telescope in order to minimize its weight thus allowing more weight for the telescope and its support components.

The objective of this study were to design a lander that meets all the constraints of the launching system. The basic constraints of the TITAN IV/Centaur system are as follows
- Max. dry weight of telescope and lander is 3075 Kg
- Max. shroud size of the Centaur is 4.52 meters
- Lateral frequencies must be above 2.5 Hz
- Avoid axial frequencies between 17 and 24 Hz
- Avoid lateral frequencies between 6 and 10 Hz

TELESCOPE/LANDER CONFIGURATION

Several telescope/lander configurations have been considered in this study. Figure 1 shows a typical lander configuration. A three mirror telescope will be used. The mirrors and supporting equipment will be surrounded with a solar shield as shown in the figure. The lander will have four legs for added stability. The diameter of the telescope and the lander in the stowed position will be 4.26 meters thus leaving a 0.13 meter clearance on all sides of the Centaur. Four H_2 and four O_2 propellent tanks will be used. Four side beams are used to connect the four tanks together. The O_2 tanks are supported on the side arms. The telescope components are supported on the O_2 tanks.
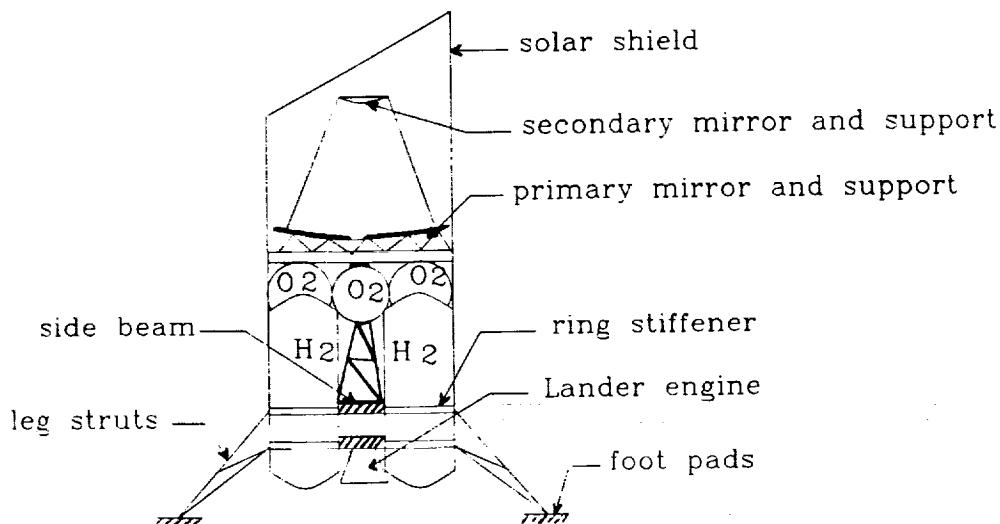
Figure 1: Telescope/Lander configuration

MODELING THE LANDER

The lander shown in Figure 1 has been modeled using a finite element program called SAP 90. The program used is capable of modeling both static and dynamic loading. It has plate/shell elements that can model the in-plane and out-of-plane stiffness of the propellent tanks where the legs connect. The lander legs were modeled using frame elements. Because of symmetry in the lander about two axis only one-fourth of the lander has been modeled.

The foot pads were designed assuming a lunar soil bearing pressure of 6.9 kPa (equivalent to 1 psi). Using the initial weight estimates for all subsystems the diameter of a single foot pad was found to be 0.61 meters. The initial size of the foot pads were used in the finite element model to generate stresses and deformations.

Since the telescope is scheduled to be launched in the near future the material used in the lander design should one whose properties and behavior are well known and available. In this study the material of choice was Al Li Weldalite^{TM} 049 produced by Martin Merietta. This Aluminum alloy is light weight (Density is 2.7 g/cc), weldable, has high ultimate tensile strength (UTS is 620 MPa), and has high modulus of elasticity (E is 76.5 GPa).

Two types of loads were applied to the model. The first is static loads which represent the weights of the telescope's mirrors, support systems and support structure. The second is dynamic impact loads resulting from landing the telescope on the Lunar surface. In the literature, the impact loads have been traditionally modeled using a spike of the accelerations in a short period of time. Therefore, in this study the same procedure was followed and a spike of 3g were applied in the vertical direction and 0.5g in the horizontal direction in a time period of 0.6 seconds.

A preliminary study was conducted to determine the feasibility of supporting the lander legs using the H_2 tanks. The objective was to determine the tank thickness required to support the lander legs without excessive stresses. The analysis showed that the thickness needed was not less than 0.02 meters which will yield extremely heavy tanks (weight of four tanks 1728 Kg). Therefore, the tanks were then stiffened in the horizontal direction using ring stiffeners located at the level where the leg struts join into the tank. The ring stiffeners will support all lateral loads coming from the legs upon impact. This allows significant reduction in the thickness of the tank's walls. Currently the analysis shows that when using two ring stiffeners that are 0.03 meters by 0.06 meters allows the tank walls to be reduced to 0.008 meters in thickness which makes the total weight of the four H_2 tanks 693 Kg. Figure 2 shows the maximum moment distribution in the tank.

The SAP 90 analysis program also calculates stresses in the leg struts, foot pad and side beams connecting the tanks together. Based on the analysis the following sizes seem to be appropriate. The leg struts are assumed to be thin shell tubes 0.08 meters in diameter and 0.005 meters in thickness. The struts are filled with honeycomb crushable Aluminum to provide appropriate attenuation for the vibrations resulting from landing on the lunar surface. The total estimated weight for the leg struts is 169 Kg. A foot pad thickness of 0.005 meters has been shown to be appropriate thus resulting in total mass of 75 Kg. The side beams used were 0.1 meters high, 0.03 meters deep and 0.553 meters long. The total mass for the connecting beams was found to be 72 Kg. Therefore,

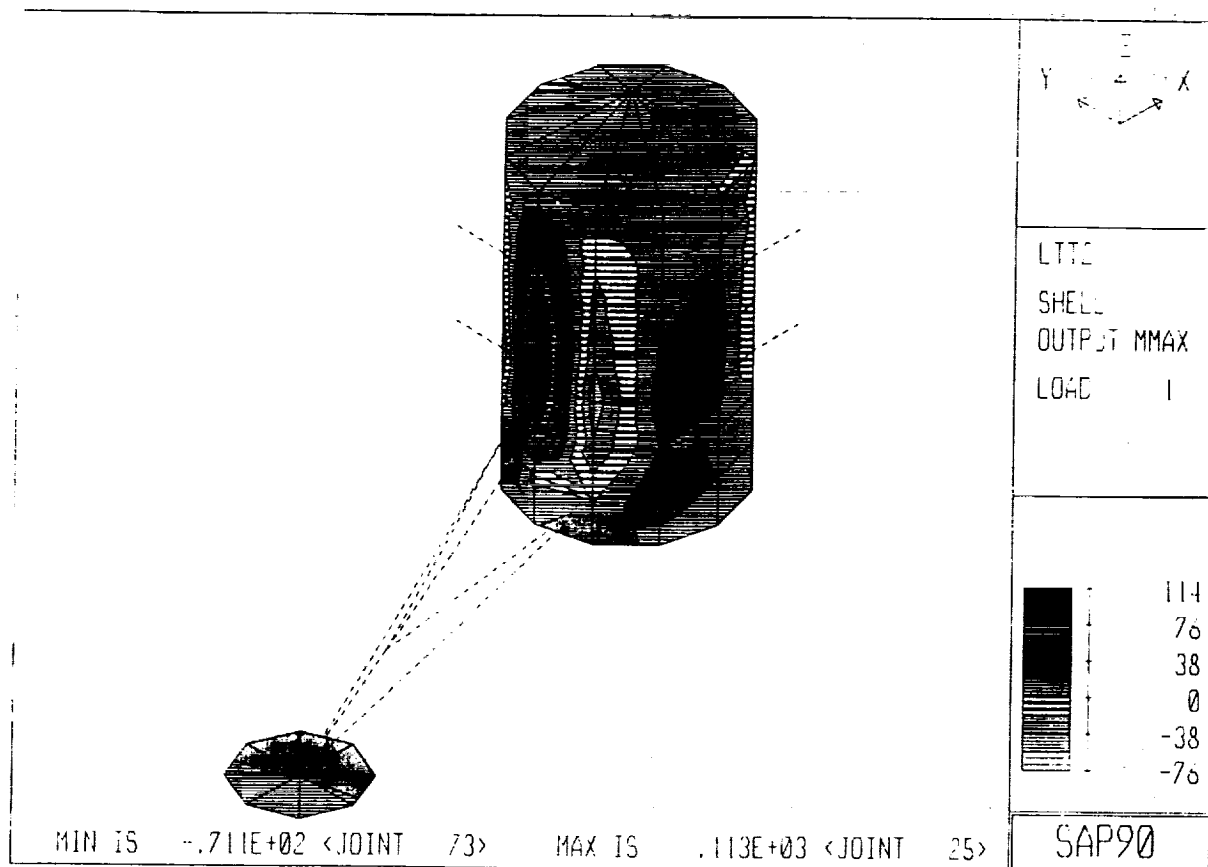the total current estimate of the lander components is 1009 Kg.

Figure 2: Maximum moment distribution in tank

SUMMERY AND RECOMMENDATIONS

The LUNAR TRANSIT TELESCOPE (LTT) will serve as a precursor for other bigger and better lunar telescopes in the future. It is a great challenge to design a Telescope/Lander system that can be launched using existing vehicles such as the TITAN IV/Centaur system. All the work done so far is preliminary and many changes will take place before the final version of this telescope will be built and deployed.

Although the objectives of this study of producing a preliminary design for the LTT has been achieved there is still several aspects that need to be investigated. The influence of lunar regolith properties on the dynamics of landing should be studied. In addition, the stability of landing on a slope or in a crater should be investigate. Furthermore, the location of the lander leg struts should be optimized to reduce stresses in the tanks and increase stability of landing.

1991

NASA/ASEE SUMMER FACULTY FELLOWSHIP PROGRAM

MARSHALL SPACE FLIGHT CENTER
THE UNIVERSITY OF ALABAMA

THE MAGNITUDE OF THE MAGNETIC FIELD NEAR THE SURFACE
OF A HIGH-T_C SUPERCONDUCTOR WITH A TRAPPED FLUX

Prepared By: Dan R. Overcash, Ph.D.

Academic Rank: Associate Professor

Institution: Lenoir-Rhyne College
                         Department of Physics and Earth Sciences

NASA/MSFC:

        Laboratory: Space Science Laboratory
        Division: Astrophysics Division
        Branch: Infrared and Cryogenic Physics Branch

MSFC Colleague: Palmer N. Peters, Ph.D.

Contract No.:   NGT-01-008-021
                         The University of Alabama
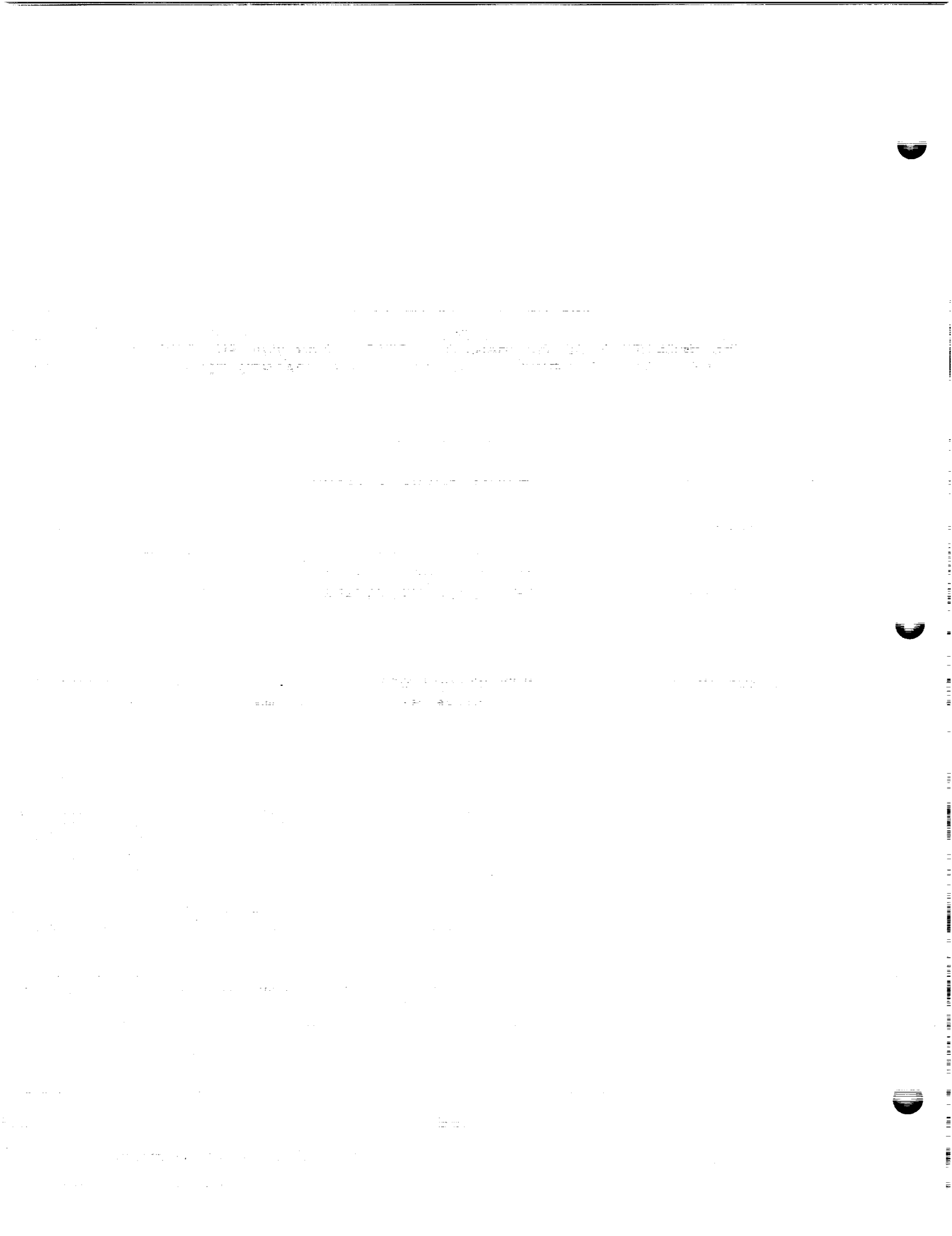
EE

THE MAGNITUDE OF THE MAGNETIC FIELD NEAR THE SURFACE OF A HIGH-T_c SUPERCONDUCTOR WITH A TRAPPED FLUX

In 1986, much excitement was caused by the discovery of a class of materials that conducted electricity with zero resistance at temperatures above the boiling temperature of liquid nitrogen. This excitement was checked with the difficulties of manufacturing ceramics and the usefulness of these high temperature superconductors restricted by their becoming high resistive conductors at small current densities. A lack of pinning of the magnetic field flux caused the return of high resistance as the current was increased in these materials. A study of the magnetic field near the surface of a high temperature superconductor is a first step in the search for a means of pinning the flux lines and increasing their critical current densities.

A review of magnetic field sensor technology[1,2] list the following magnetic sensor technology: Search coil magnetometer, flux gate magnetometer, Optically pumped magnetometer, nuclear precession magnetometer, SQUID magnetometer, Hall effect sensor, magnetoresistive magnetometer, magnetodiode, magnetotransistor, fiber optic magnetometer, and magneto-optic sensor.

To obtain high resolution of the magnetic fields near a 77 Kelvin surface placed constraints on the technology that could be used. A search coil was built with a 10-turn loop that was 1 mm in diameter and on the end of a ceramic shaft. Electrical contact was made by grinding notches in the ceramic shaft and winding the ends of the coil leads around the shaft. Gold brushes were needed and a dentist drill technique was to be used to spin the coil 100,000 rpms to detect magnetic fields of 1 gauss. This technique was abandoned as the ceramic shaft shattered even at modest rpms.

Charles Sisk scanned the surface of the superconductor with a small magnet attached to a rod which was connected to a strain gauge. He measured the force on a 0.01 mm^2 magnet near the surface. This force was proportional to the gradient of the magnetic field. He also scanned with a loop of wire and measured the induction. He may scan again with increased resolution with a loop that is wound on an easily magnetized material. Photograph #1 is the computer generated 3D image of the magnetic force.

A Hall probe is usually used to determine magnetic field strength but they are extremely sensitive to temperature change and have a lower temperature limit of -40 $^{\circ}$F. I used an RFL industries model 912015 flat hall probe with an active area of

0.040 inch by 0.090 inches. The claimed temperature sensitivity of 0.05%/$^\circ$C was checked and found to be -10%/$^\circ$C. To keep the temperature above -40 $^\circ$F, a heater of 14 ohms was would on a ceramic shaft and a thermocouple was embedded in the probe mount to monitor the temperature of the probe. Several layers of super insulation and a nylon sheath cover was used to prevent liquid nitrogen from touching and cooling the probe. A current of 250 ma kept the probe at a temperature within 1 $^\circ$C or 5 $^\circ$C during the surface scan. The magnetic field was a maximum of 300 gauss which the computer generated 3-D image in photograph #2 and -100 gauss imaged off the edge of the superconductor.

A comparison between the defects in the surface of the superconductor and the magnetic field showed only a change in the field near a notch and the edge. No correlation was found between the surface grain or structure and the oscillations in the magnetic field. The observed changes in the magnetic field show resonances which may give an indication into the non-flux pinning in these superconductors. A flux pinning mechanism will increase the critical current densities, therefore, other methods of determining this field should be tried.

With a trapped flux of several hundred gauss and nanovolt sensitivity, a search coil could be used rotating at hundreds of rpms.

A flux-gate magnetometer was designed with a detector wound on a ferrite core obtained from an early computer core memory. Orthogonal windings around the ferrite core will give magnitude and direction of the magnetic field. I would like to spend this academic year building the detection circuitry and winding a 1 mm flux-gate detector and return to Marshall to scan the surface on a high temperature superconductor and obtain the magnitude and direction of the magnetic field near a high temperature superconductor.

I could also build a flux-gate magnetometer with a high-T_c superconductor pickup coil operated near H_{c2}.

REFERENCES

1. Lenz, James, E., "A Review of Magnetic Sensors", Proceedings of the IEE, Vol. 78, No. 6, June 1990.

2. Wiksow, John P., Jr., Jan van Egeraat, Yu Pei Ma, Nestor G. Sepulveda, Daniel J. Staton, Shaofen Tan, and Ranjith S. Wijesinghe, "Instrumentation and Techniques for High-Resolution Magnetic Imaging", To appear in Digital Image Synthesis and Inverse Optics A.F. Gmitro, P.S. Idell, and I.J. LaHaie, Eds. SPIE Proceedings Vol. 1351.
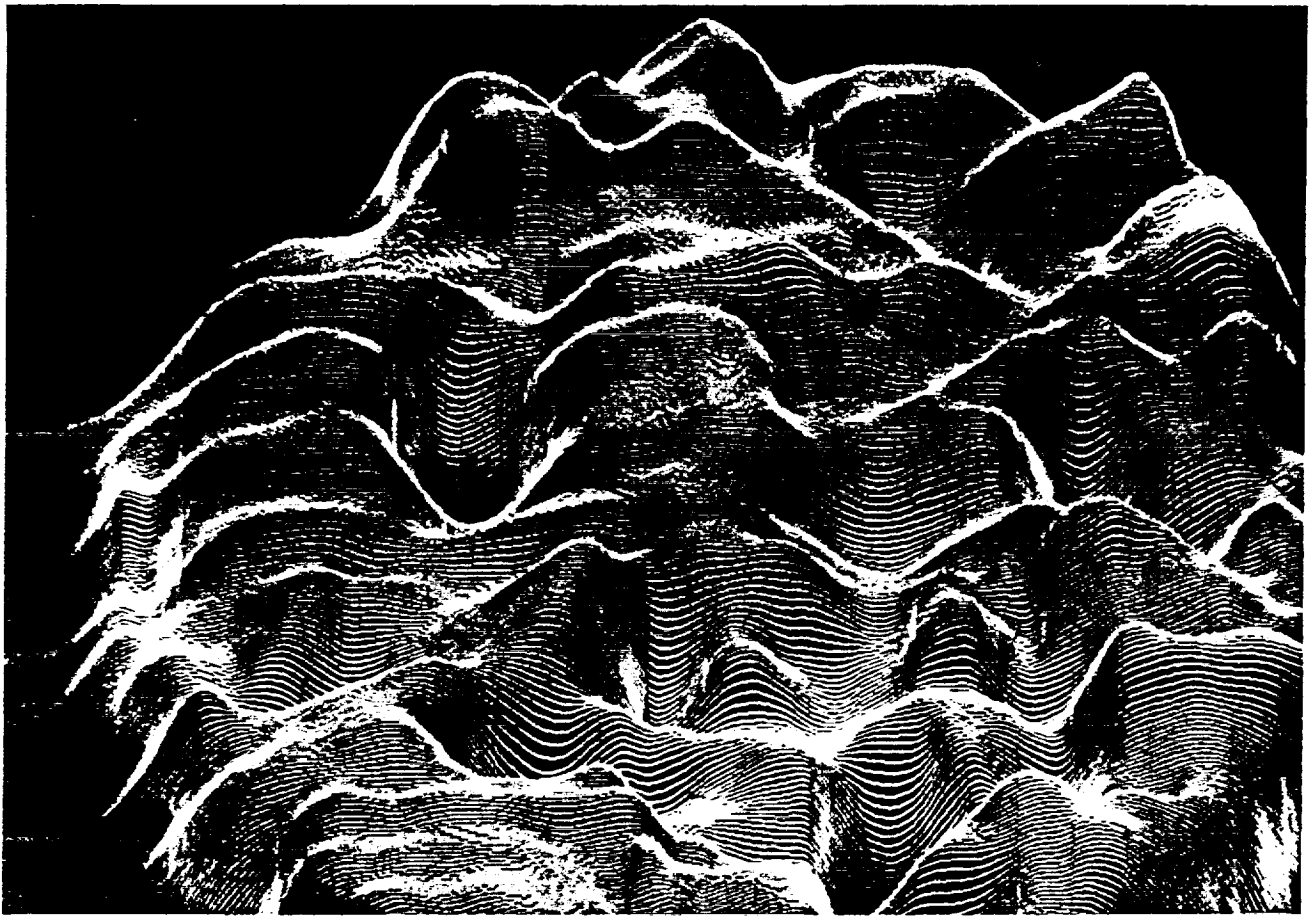
Photo #1   Computer generated 3D image of the magnetic force.
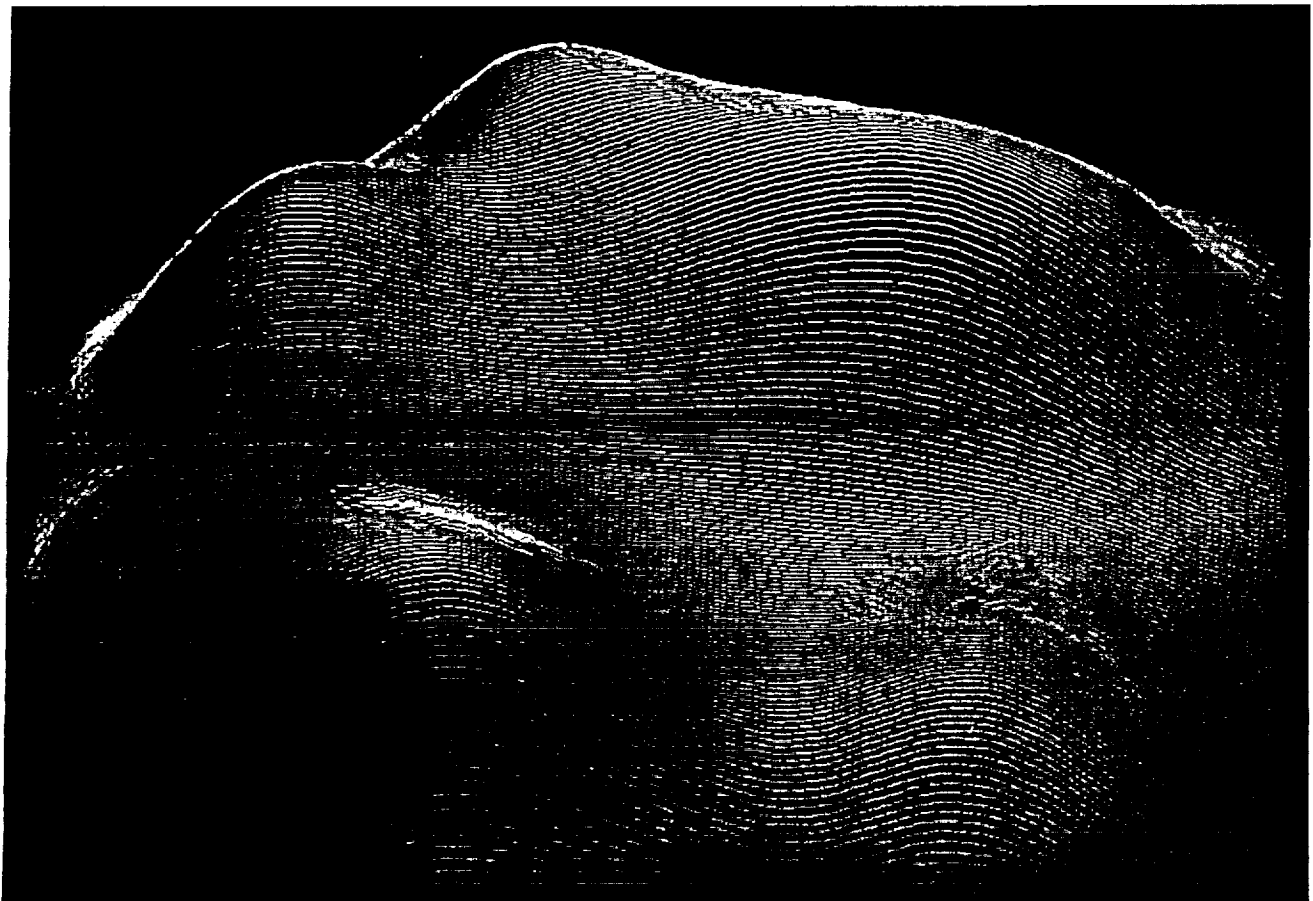
Photo #2   Computer generated 3D image of magnetic field (300 gauss)

1991
NASA/ASEE SUMMER FACULTY FELLOWSHIP PROGRAM

MARSHALL SPACE FLIGHT CENTER
THE UNIVERSITY OF ALABAMA

LINEARIZED FORCE REPRESENTATIONS FOR
TURBOPUMP LIQUID ANNULAR SEALS

Prepared By: Alan B. Palazzolo, Ph.D.

Academic Rank: Associate Professor

Institution: Texas A&M University
                         Department Mechanical Engineering

NASA/MSFC:

Office: Structures & Dynamics Laboratory
Division: Control Systems Division
Branch: Mechanical Systems Control Branch

MSFC Colleague: Mr. Donald Vallely

Contract No: NGT-01-008-021

The mechanical integrity and performance of the SSME and ATD turbopumps are a constant concern at NASA. These two factors are in turn significantly influenced by mechanical vibrations. These vibrations arise from imbalance of the rotating shafts, from broadband random excitation and from internal sources of self excitation (instability). Liquid, annular interstage seals are known to influence vibrations within the turbopump. The de-stabilizing and stabilizing forces within the seal are quantified by the cross coupled stiffness and damping coefficients, respectively. Mr. George L. von Pragenau of MSFC initially postulated, and later rigorously proved by simulation, that cross coupled stiffness could be reduced by roughening the stationary part of the seal. Mr. von Pragenau employed a Moody type friction model in his analysis for leakage and dynamic coefficients in these seals. Henry Black first recognized that the inlet tangential velocity (pre-swirl) of the seal can significantly effect its cross-coupled stiffness coefficient. Although von Pragenau did not include this in his simulation his work did have a constant swirl modeled along the length of the seal. Turbomachinery designers have installed axial taper in seals as a means to alter their stiffnesses. An effect of the taper is that the axial velocity component varies along the length of the seal. The varying axial velocity significantly complicates the governing flow equations, requiring numerical integration for their solution.

The summer faculty fellow has developed the analysis and an accompanying Fortran code SEALPAL1 to simulate liquid annular seals with axial taper, Moody friction factors and pre-swirl. The output of the code includes all dynamic coefficients (stiffness, dampings, and inertias), leakage rate, torque and horsepower loss. In addition to the software the faculty fellow has prepared the two following 200 page (plus) theoretical manuals;

Palazzolo, A.B., 1991, "A Theoretical Manual
for G. L. von Pragenau's Liquid Seal
Simulation Program," May-June

Palazzolo, A.B., 1991, "Dynamic Coefficients
for Incompressible, Liquid Annular
Seals Including Moody Friction Factor,
Taper and Pre-Swirl," June-July

The leakage, torque and horsepower are determined by simultaneously solving the axial momentum, circumferential momentum and continuity equations for a shaft-centered (non-vibrating) configuration. The fluid is simulated with a bulk flow model with shear tractions described by Moody's equations. The dynamic coefficients are obtained by performing a perturbation analysis about the shaft-centered state. This step requires linearization of the momenta and continuity equations. The resulting perturbation pressure is integrated to obtain forces on the shaft that are parallel and perpendicular to the whirl vector. The stiffness, dampings, and inertias are obtained by least square curve fitting these forces to the spring-mass-damper ideal model.

The computer code results were compared with five (5) cases from the literature. The agreement was very good in almost all instances except several predicted cross coupled stiffnesses were significantly lower than those appearing in the literature. This disagreement could reflect a theoretical or programming error by the faculty fellow or in the literature, or could be a result of the difference in friction factor models on other assumptions employed.

The following table shows a comparison between the current code results and those given by Scharrer for a high pressure, high speed seal;

	Scharrer	SEALPAL1
Direct Stiffness	1.4×10^6 lb/in	1.33×10^6 lb/in
Direct Damping	148. lb.s./in	149. lb.s./in
Direct Mass	3.8×10^{-3} lb.s./in^2	3.8×10^{-3} lb.s./in^2
Cross Stiffness	3.8×10^5	3.3×10^5

Figure 1 shows the steady state solution variables (velocities, pressure, whirl ratio) for this test case.

Future work proposed in this area includes expansion of SEALPAL1 to simulate;

       O   seal housing expansion,

       O   Hir's friction factors,

       O   thermal effects,

       O   arbitrarily shaped clearance profile, and

       O   compressibility and variable property effects.

REFERENCES

1. Scharrer, J., and Nelson C., "Rotor Dynamic Coefficients for Pertially Tapered Annular Seals, "ASME Paper No. 90-Trib-25.

SCHARRER

1-1⊖——⊖5-1✕——✕7-1△——△11-1

axial velocity (in/s)

circumferential

velocity (in/s)

pressure (psi)

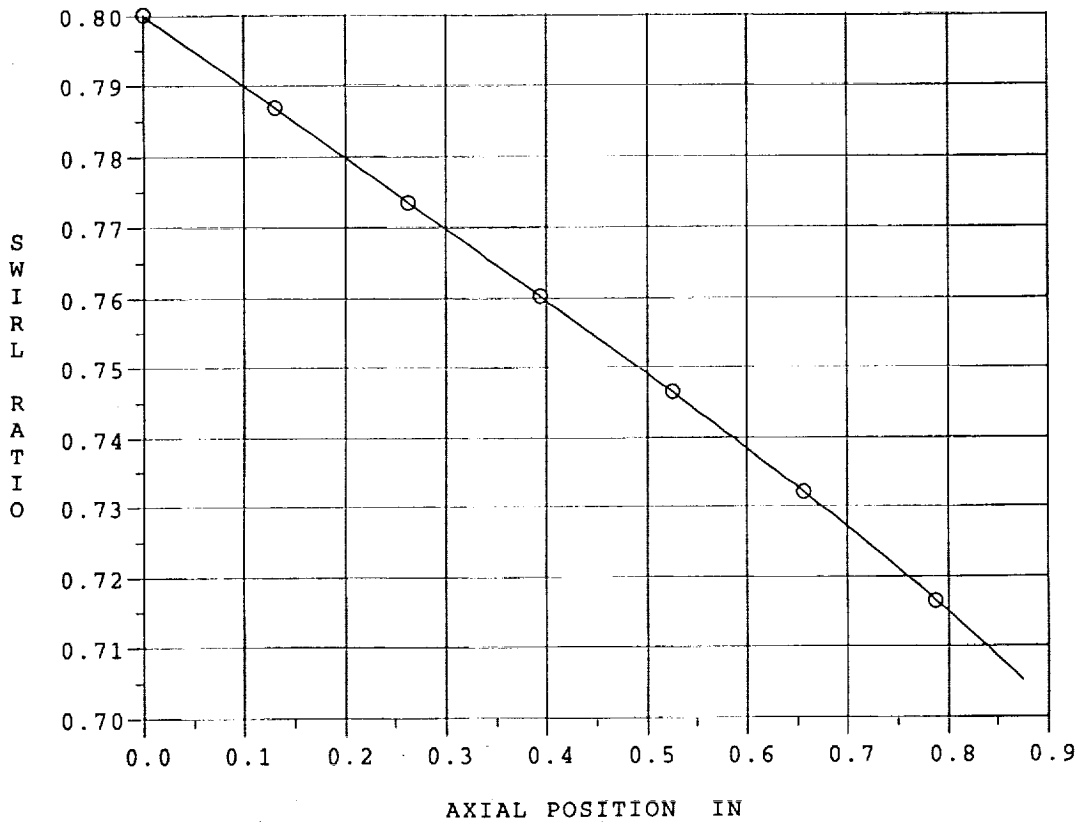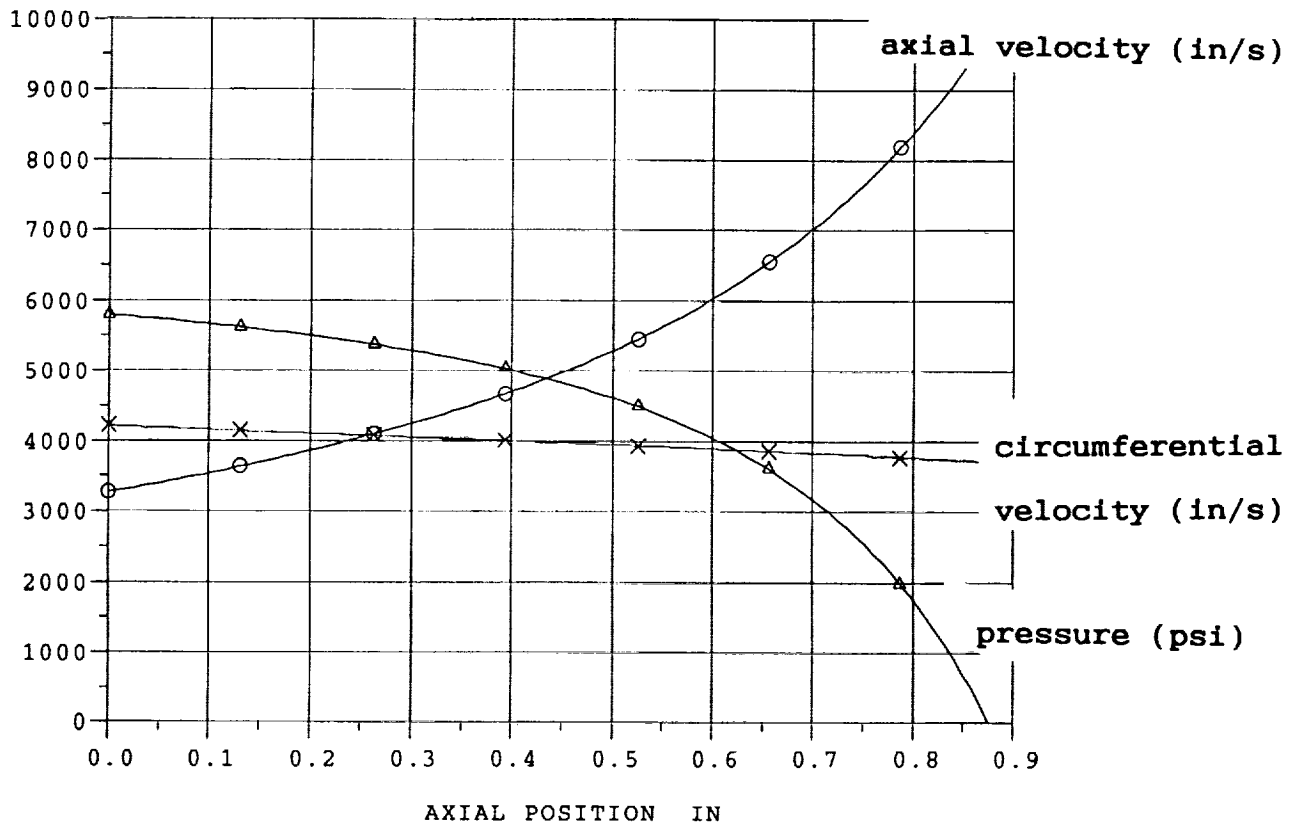AXIAL POSITION   IN

S
W
I
R
L

R
A
T
I
O

AXIAL POSITION   IN

Fig. 1   Steady State Solution Variables

FF-4

1991

NASA/ASEE SUMMER FACULTY FELLOWSHIP PROGRAM

MARSHALL SPACE FLIGHT CENTER
THE UNIVERSITY OF ALABAMA

A THEORETICAL STUDY OF THE STEADY STATE OF A SPACE PLASMA

Prepared By: Michael J. Pangia, Ph.D.

Academic Rank: Assistant Professor

Institution: LaGrange College
                                      Department of Physics

NASA/MSFC:

        Office: Space Science Laboratory
        Division: Solar-Terrestrial Physics
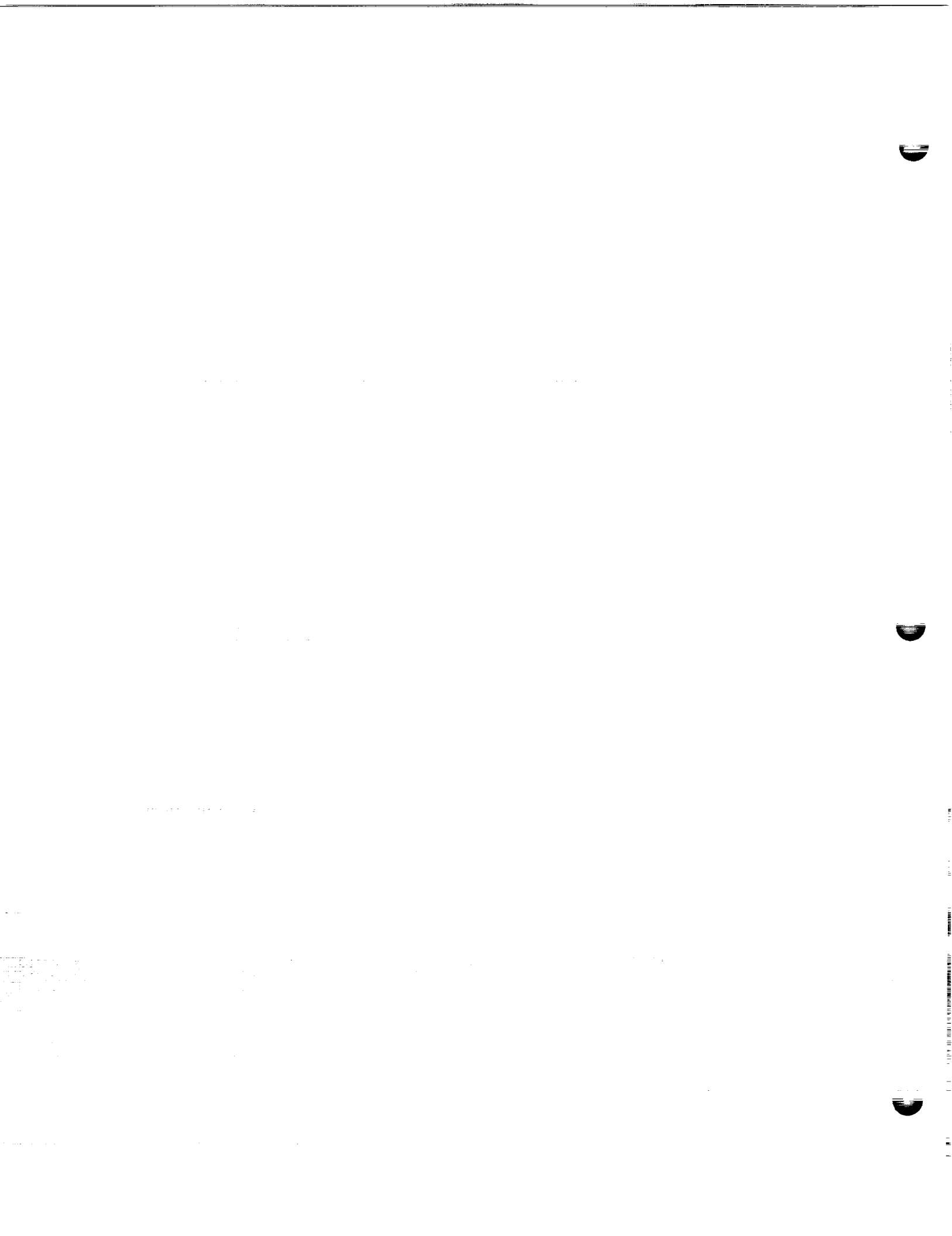   Branch: Magnetospheric Physics

MSFC Colleagues: Thomas E. Moore, Ph.D.
                                      Craig J. Pollock, Ph.D.
                                      Dennis L. Gallagher, Ph.D.

Contract No.:   NGT-01-008-021
                                      The University of Alabama

An important and outstanding problem in Space Plasma Physics is accounting for the velocity distributions observed in the solar wind and the Earth's magnetosphere. This translates to seeking the steady-state configuration of the plasma, the properties of which are strongly related to the wave activity in the plasma. In many regions, particle distributions are well approximated by a single hump distribution known as the κ (Kappa) distribution (see for example, *Lui and Krimigis*, 1981). *Hasegawa et al.* (1985) have derived the κ distribution as a steady-state plasma distribution using a Fokker-Planck description of the plasma. However, from the study, it is difficult to actually determine the value for κ for comparing to fits of the data. This study restricts itself to the situation of electrostatic wave activity in a plasma with zero magnetic field and where the (positive) ion motion can be neglected. The end result of the study is a simple criterion for determining the shape of the distribution, or, more specifically, κ.

The fundamental equations for a plasma are the Vlasov equation for the dynamics of the electron distribution function f(t,x,v) and Gauss's law for the electrostatic electric field E(t,x). Written in Gaussian units, they are, respectively,

$$\partial_t f + v \partial_x f - \frac{e}{m} E \partial_v f = 0 \tag{1}$$

$$\partial_x E = 4\pi e\, n_o - 4\pi e \int_{-\infty}^{\infty} dv\, f \tag{2}$$

The independent variables are time (t), space (x) and particle velocity (v) in the x direction. A partial derivative with respect to one of the variables is denoted by subscripting the partial derivative symbol ∂. The electric field vector, and the positive x and v axes all point in the same direction. The electron has mass m and charge $-e$. The ions have charge e and are uniformly distributed over space with number density n_o. The normalization for the electron distribution is that the number of electrons between (x,v) and (x+dx,v+dv) is f(t,x,v)dx dv.

Observed particle distributions represent a type of spatial average. For comparison with observations and to get a simpler equation to analyze, the electron distribution is written as the sum of two distributions, $f(t,x,v) = f(t,v) + f'(t,x,v)$. As seen from the arguments of functions, f(t,v) is the spatially uniform part of the distribution and f'(t,x,v) is the part which can vary with x. In practice, f(t,v) would be the observable part of the distribution. It will be assumed that the plasma is infinite in extent. This means that one way to determine f(t,v) is to take the limit of f(t,x,v) as $|x| \to \infty$, and extract the uniform part of the distribution. Another way to determine f(t,v), which will be applied here, is to define the following averaging process

$$<A> = \lim_{L \to \infty} \int_{-L}^{L} \frac{dx}{2L} A(x) \tag{3}$$

At infinity f' will at most oscillate with finite amplitude (i.e., wave amplitude is bounded), so that $<f'> = 0$. Applying (3) to the total distribution function gives

$$\lim_{L \to \infty} \int_{-L}^{L} \frac{dx}{2L} f(t,x,v) = f(t,v) \tag{4}$$

Applying (3) to (2) gives

$$\lim_{L \to \infty} \frac{E(t,L) - E(t,-L)}{2L} = 4\pi e\, n_o - 4\pi e \int_{-\infty}^{\infty} dv\, f(t,v) \tag{5}$$

It is unrealistic to have a large scale, uniform electric field, therefore, the condition $<E> = 0$ is imposed. This amounts to using the boundary condition that E at most oscillates with a finite amplitude at infinite distances. Equation (5) then says that the quasi-neutrality condition is enforced; namely, that

$$\int_{-\infty}^{\infty} dv\, f(t,v) = n_o \tag{6}$$

In place of (2), one has

$$\partial_x E = -4\pi e \int_{-\infty}^{\infty} dv\, f' \tag{7}$$

Applying (3) to (1) gives

$$\partial_t f(t,v) - \frac{e}{m} <E \partial_v f'> = 0 \qquad (8)$$

As a check of consistency, it will now be verified that (6) is true for all time, along with determining some other important properties of the first and second velocity moments of f(t,v). Integrating (8) over all velocity values gives that the zeroth velocity moment of f(t,v) is constant in time, which is consistent with (6). The first velocity moment of (8) involves the zeroth moment of f', which is eliminated using (7). This gives that the first velocity moment of f(t,v) is also constant, and its value is taken to be zero by choice of reference frame. Recalling that no large scale electric field is allowed, there can be no uniform current flowing in the plasma. Therefore, the Maxwell-Ampere equation for electrostatic waves simplifies to

$$\partial_t E = 4\pi e \int_{-\infty}^{\infty} dv \, v \, f' \qquad (9)$$

Making use of (9), the second moment of (8) is a statement of energy conservation. In summary, the first three moments of (8) give

$$\frac{d}{dt} \int_{-\infty}^{\infty} dv \, f(t,v) = 0 \; ; \; \frac{d}{dt} \int_{-\infty}^{\infty} dv \, v \, f(t,v) = 0 \; ; \; \frac{d}{dt} \left\{ \frac{1}{2} m \int_{-\infty}^{\infty} dv \, v^2 f(t,v) + \frac{1}{8\pi} <E^2> \right\} = 0 \qquad (10)$$

Equation (8) is just one of the equations required to solve for f(t,v). Since f(t,v) depends on f' and E, both (1) and (7) are also needed. Substituting (8) into (1) gives

$$\partial_t f' + v \partial_x f' - \frac{e}{m} E \partial_v f(t,v) - \frac{e}{m} \left\{ E \partial_v f' - <E \partial_v f'> \right\} = 0 \qquad (11)$$

The full set of equations for the present study are (7), (8) and (11). Since observations show that the κ distribution is a persistent feature in many regions of the space plasma environment, an analysis of the steady-state properties of the plasma is desired. The existing set of equations require that f(t,v) and f' be specified at some time, call it the "initial" time t=0 (E at each time is uniquely specified by (7) subject to the boundary condition that the spatial dependence of E at most oscillates with a finite amplitude at infinity).

Consider the following initial condition

$$f'(0,x,v) = A \, g(v) \sin(kx) \quad \text{and} \quad E(0,x) = E_o \cos(kx) \qquad (12)$$

where A, E_o and k are related constants. The averaging process encountered in evaluating the dynamics in (8) and (11) can be performed using the trigonometric identities

$$2 \sin(kx) \cos(kx) = \sin(2kx) \quad \text{and} \quad \cos^2(kx) = \frac{1}{2} + \frac{1}{2} \cos(2kx) \qquad (13)$$

Application of (3) to (13) gives

$$<\sin(kx) \cos(kx)> = 0 \quad \text{and} \quad <\cos^2(kx)> = \frac{1}{2} \qquad (14)$$

Substitution of (12) into (8) gives that the first partial time derivative of f(t,v) is initially zero. Evaluation of the second partial derivative requires using (9) and (11) to determine the initial values of the first partial time derivatives of E and f', respectively. The result is that second partial time derivative of f(t,v) is not zero for any f(0,v), which means that the uniform part of the distribution will always change as a result of the initial condition. Therefore, at least for initial conditions of the same type as (12), there can be no steady-state of the plasma, for after the plasma has evolved to a final state, the system can be caused to change again by externally reinitiating a spatial perturbation. In respect to the Vlasov description of the plasma, external means of causing spatial variation would be due to particle effects, such as discreteness and collisions. For later reference, both of the terms in (11) enclosed within { · · · } give zero contribution to the second derivative of f(t,v).

A second possibility to a steady-state equilibrium is that the plasma eventually resides in a state of minimal change. In other words, as a result of the plasma response to perturbations, it eventually attains a state for which the net change in f(t,v) is a minimum, but not zero. This will be referred to as a quasi-steady state, since the state could still be changed if perturbed. To proceed, the following assumptions are made:

1) Waves are initiated by something external to the Vlasov theory of a plasma.

2) Waves are repeatedly being initiated.

3) The rate at which energy is delivered to the plasma through repeated wave initiations is much slower than the rate at which the quasi-steady state is attained.

It should be emphasized that, in the present context, "external" means external to the Vlasov theory. Ultimately, the source of energy comes from the plasma particles either from kinetic (particle) or potential (electrical) energy, but through a mechanism unaccounted for by the present theory. However, any more encompassing theory would be correspondingly more difficult to handle. Assumptions (1) and (2) provide an operational means of attaining quasi-steady state. Together they imply that it is insufficient to simply solve the initial-value problem one time through, as the final state obtained could readily be change by repeating the perturbation. Assumption (3) is made in light of energy conservation. As seen from the second moment equation in (10), the energy brought into the system from a given perturbation goes into plasma thermal energy. Consistency of Assumptions (1) and (2) together with the fact that plasma temperatures are finite, leads one to the assumption that the energy from the perturbations is slowly supplied to the plasma.

Further work is necessary to specify a precise meaning of the statement that the net change in $f(t,v)$ must be minimized in a quasi-steady state. Clearly, the statement should in some way apply to the whole distribution, rather than some particular velocity or even some particular velocity moment. Consider the κ distribution,

$$f_\kappa = \frac{A_\kappa}{(1+\frac{v^2}{2\kappa v_e^2})^\kappa} \tag{15}$$

where A_κ is a normalization constant and v_e is the thermal speed. The only parameter that should be affected by minimizing the change in the whole distribution is κ, since it determines the shape of the function. The other parameters, A_κ and v_e, are subject to the constraints on the moments of the distribution, the number density and thermal energy of the plasma, respectively.

An analytical expression for the change in $f(t,v)$ is now sought subject to simplifying assumptions. Firstly, as the system approaches quasi-steady state, it is reasonable to assume that f' is small compared to $f(t,v)$. Consistency with (7) implies that the electric field is also small. Consequently, the terms within $\{ \cdots \}$ in (11), which contain products of small quantities, will be neglected. The resulting equation is the linearized Vlasov equation with a time varying uniform distribution. Solving this equation for $f'(t,x,v)$ with $f'(0,x,v)$ as its initial condition gives

$$f'(t,x,v) = \frac{e}{m}\int_0^t dt' E(t',x-v(t-t'))\partial_v f(t',v) + f'(0,x-vt,v) \tag{16}$$

(This expression can be verified by direct substitution into the linearized form of (11).) Substitution of (16) into (8) gives

$$\partial_t f(t,v) = \frac{e^2}{m^2}\int_0^t dt' <E(t,x) E(t',x-v(t-t'))> + \frac{e}{m}<E(t,x) f'(0,x-vt,v)> \tag{17}$$

The right-hand side of this equation is quadratic in small quantities, which means that $f(t,v)$ changes slowly. These terms must be included to account for the leading order changes in $f(t,v)$. Even though (17) is an approximation, the main conclusions of the analysis thus far still apply. In particular, (10) still holds as well as the conclusion that $f(t,v)$ does change subject to the perturbation in (12), since the negligible terms in (11) do not contribute to the initial value of the second partial time derivative of $f(t,v)$.

Consistent with quasi-steady state being defined as a state of minimal change in $f(t,v)$ is the assumption that the change in $f(t,v)$ is small for this state. Therefore, in determining the change in $f(t,v)$ at or near quasi-steady state, $f(t,v)$ can be treated as constant in (16) and on the right-hand side of (17), where the function $f(0,v)$ will be used in its place. Note that the starting time $t=0$ here refers to the start time of one of the perturbations that occurs when the system is close to quasi-steady state. Under this assumption, f' and E obey the standard linearized Vlasov and Gauss equations. In particular, the temporal behavior of the electrostatic field can in many situations be approximated by a product of a monotonic and an oscillatory function corresponding to damping with rate γ (damping when $\gamma>0$) and a oscillation of angular frequency ω_0, respectively (see for example, *Nicholson*, 1983). The rates γ and ω_0 are determined from the root of the dielectric function, which itself

depends on f(0,v). Therefore, the following explicit form for the electrostatic field will be used to calculate the change in f(t,v) near quasi-steady state

$$E(t,x) = E_o e^{-\gamma t} \cos(\omega_o t) \cos(kx) \qquad (18)$$

The same initial condition of (12) is in use. Substitution of (12) and (18) into (17) enables one to calculate the net change in f(t,v) due to this perturbation. As an intermediate step, the time integral in (17) is evaluated to give

$$\int_0^t dt' <E(t,x)\,E(t',x-v(t-t'))> = \sum_{\sigma=\pm1} \frac{E_o^2}{2} e^{-\gamma t} \cos(\omega_o t) \left\{ \frac{e^{-\gamma t}\{-\gamma\cos(\omega_o t) + (\omega_o-\sigma kv)\sin(\omega_o t)\} + \gamma\cos(kvt) - \sigma(\omega_o-\sigma kv)\sin(kvt)}{\gamma^2 + (\omega_o-\sigma kv)^2} \right\}$$

The final expression for the net change in f(t,v) is

$$f(\infty,v) - f(0,v) = \int_0^\infty dt\,\partial_t f(t,v) = \sum_{\sigma=\pm1}\sum_{\mu=\pm1} \frac{e^2}{4m^2} \frac{E_o^2 \partial_v f(0,v)}{\gamma^2+(\omega_o-\sigma kv)^2} \left\{ \frac{-1}{4\gamma} + \frac{-\gamma^2+\omega_o-\sigma kv}{2(\gamma^2+\omega_o^2)} + \frac{\gamma^2-\sigma\mu(\omega_o-\sigma kv)(\omega_o-\mu kv)}{\gamma^2+(\omega_o-\mu kv)^2} \right\}$$
$$+ \sum_{\sigma=\pm1} \frac{e}{4m} A E_o \partial_v \left\{ g\,\frac{\omega_o-\sigma kv}{\gamma^2+(\omega_o-\sigma kv)^2} \right\} \qquad (19)$$

From this expression, the damping rate γ is the only factor that can be used to minimize the change in f(t,v) without singling out any one of the terms in (19). Therefore, it is concluded that the criterion for attaining quasi-steady-state is that f((t,v) will be such that it maximizes the damping rate, or, in reference to (15), κ attains a value such that γ is maximized. Physically, greater damping means that the waves dissipate faster and exist for shorter times. That this leads to a smaller change in f(t,v) is reasonable on the basis that it is the waves that change f(t,v) and waves which exist for shorter times with smaller amplitudes will produce less overall effect.

It is necessary to discuss the special case of $\gamma=0$. If such a mode exists, (19) shows that f(t,v) changes infinitely fast at all velocities. This is a clear breakdown of the approximations that lead to (19), chiefly the assumption that f(t,v) changes slowly. In such a situation, one expects that the energy oscillates back and forth between the particles and field without any loss. The criterion of minimal change in f(t,v) in some sense still applies, but now in reference to the time average, with there being no net change on the average. However, in reference to the κ distribution, a $\gamma=0$ mode exists only for infinite wavelength waves ($k\to0$); namely, a uniform electric field that varies in time. For a uniform field, f(t,v) would have to be changing as fast as the oscillation to produce the required charge separation at infinity. Such a possibility was ruled out from the onset of this study on the grounds that a uniform electric field infinite in extent is physically unlikely to exist.

As a preliminary evaluation of the theory, compare the damping rates γ_1 and γ_∞ for the $\kappa=1$ and $\kappa\to\infty$ distributions, respectively, the latter being a Maxwellian distribution.

$$\frac{\gamma_1}{\omega_o} = k\lambda_D \;\; ; \;\; \frac{\gamma_\infty}{\omega_o} \approx \left[\frac{\pi}{8}\right]^{\frac{1}{2}} e^{-3/2} \frac{e^{-1/(2k^2\lambda_D^2)}}{k^3\lambda_D^3} \qquad (20)$$

The parameter λ_D is the Debye length for the plasma. The expression for γ_∞ applies only for $k\lambda_D \ll 1$. Of these two values, $\kappa=1$ would be the quasi-steady state distribution, since it gives a larger damping rate, at least for long wavelength perturbations. This is consistent with fits to observed particle distributions, which show that κ is not very large. The complete range of allowable κ must be analyzed for a better comparison with observations.

In summary, examination of the Vlasov theory of a plasma lead to the hypothesis that a plasma may reside in a state of minimal change of the uniform distribution. This statement was made definite by determining that the change in the whole distribution can be minimized if the damping rate were maximized. A preliminary test of the theory shows that one would expect a plasma well fit by a κ distribution to have a low κ value.

References

Hasegawa A., K. Mima, and M. Duong-van, "Plasma distribution function in a superthermal radiation field," *Phys. Rev. Let.* **54**, 2608, 1985.

Lui, A. T. Y., and S. M. Krimigis, "Energetic ion beam in the earth's magnetic lobe," *Geophys. Res. Lett.* **10**, 13, 1983.

Nicholson, D. R., *Introduction to Plasma Theory*, John Wiley & Sons, New York, 1983.

C-3

1991

NASA/ASEE SUMMER FACULTY FELLOWSHIP PROGRAM

MARSHAL SPACE FLIGHT CENTER
THE UNIVERSITY OF ALABAMA

STUDIES OF THE CHARGING OF A THIN
DUST LAYER IN A PLASMA

Prepared By: Lennart R. Peterson, Ph.D.

Academic Rank: Professor

Institution: University of Florida
                                      Department of Physics

NASA/MSFC:

        Laboratory: Space Science Laboratory

        Division: Solar-Terrestrial Physics

        Branch: Magnetospheric Physics

MSFC Colleague: Craig J. Pollock, Ph.D.

Contract No.   NGT-01-008-021

HH

INTRODUCTION

Unlike the normal forms of matter (solid, liquid and gas) usually experienced on Earth, the usual form of matter in most of the universe is that of a plasma, or at least that of a partially or fully ionized gas. Often coexisting with the plasma are dust clouds containing grains varying in size from the submicrometer to the centimeter range or larger, grains which are in general charged by collisions with plasma ions and electrons or by photoionization. In most cases, the dust grains are widely enough separated in comparison with plasma particles that these relatively isolated grains follow orbits controlled mainly by external gravitational and electromagnetic fields, including radiation pressure. In other cases, the dust grains are of sufficient density that their presence has a significant effect on the plasma itself, as well as on each other, resulting in collective motions. In a complete calculation, then, the dust particles have a charge state and undergo motion, both of which are dependent on the plasma parameters as well as on the location of other charged grains. The charged particle trajectories themselves create fields that are superimposed on any external fields, and the resulting fields in turn exert partial control over the trajectories that create these same fields. In other words, a complete analysis requires a self-consistent calculation. Two examples of these latter types of cases within the solar system include cometary tails immersed in the solar wind and the dust rings of Saturn, Uranus and Jupiter embedded in each planet's magnetosphere.

DISCUSSION

One of the fundamental properties of any plasma is its Debye length, defined in MKS units by the expression

$$ D = \left(\frac{\epsilon_0 K \, T_e}{n \, e^2} \right)^{1/2} \tag{1} $$

Here, T_e is the electron temperature and n is the plasma particle density. The Debye length is a measure of the distance over which a charge embedded in the plasma is effectively shielded by plasma charges of opposite sign. Collective effects are expected whenever a large number of dust grains are present within a sphere of a Debye radius. Otherwise, if grains are widely separated the dust grains are effectively shielded from each other and are able to act independently. One of the important collective effects

pointed out first by Goertz and Ip (1984) is that under the condition that interparticle grain separations are small with respect to the Debye length, the amount of charge on single dust grains in a dusty plasma is much reduced from its value expected when other dust grains are not present. The reduction can be as much as two or three orders of magnitude. Additional refinements to the charging model were made by Whipple et al. (1985) and by Houpis and Whipple (1987). These efforts all made use of the solution to a linearized form of the Poisson equation. The study by Houpis and Whipple also included a power-law particle-size distribution. The charge-to-mass ratio for grains is an important determining factor in assessing the significance of electromagnetic forces over other factors, such as gravity. In Saturnian rings, gravitational force on a typical grain is much larger than electromagnetic forces. Yet, even weak electromagnetic forces are capable of causing substantial variations in the normal Kepler orbits expected from gravity alone and must often be included because of their subtle effects.

Analytic solutions are of great value in understanding important aspects of the dust-plasma system but are by nature limited because of the approximations needed to make the problem tractable in practice. In order to overcome some of the limits imposed by an analytic solution, Wilson (1987, 1988) used a particle simulation technique to study the charge structure and electric field in a thin dust layer, one which has a thickness of the order of the plasma Debye length. In addition to the charge structure and the electric fields present as a function of position in the layer, the results also give the phase space distribution of plasma particles within the layer, as discussed in the next paragraph.

The assumptions of Wilson's study are as follows. First, the dust layer is considered a plane sheet of either a Gaussian or a square number-density profile fixed in space and is subjected to an ambient electron and proton plasma that feeds simulation charges from a reservoir outside the boundaries of the dust layer. Secondly, the only source of plasma particles is photoionization, resulting in Maxwellian photo electrons from the dust grains. Thirdly, collisions between plasma particles and dust grains are, of course, included, but plasma-plasma collisions are neglected since they involve mean free paths much larger than the dimensions of the dust layer. Fourthly, the only factor controlling particle trajectories within the dust layer are local electric fields. Finally, the dust grains all have the same radius. The equation set that is effectively satisfied are the Boltzmann equation, Poisson's equation and the dust charging equation,

$$\frac{\partial f_s}{\partial t} + v_z \frac{\partial f_s}{\partial z} + \frac{q_s}{m_s} E_z \frac{\partial f_s}{\partial v_z} = \left(\frac{\delta f_s}{\delta t}\right)_1 + \left(\frac{\delta f_s}{\delta t}\right)_g \qquad (2)$$

$$\frac{\partial E_z}{\partial z} = \frac{1}{\epsilon_0} [\, e(n_i - n_e) + q_d n_d \,] \qquad (3)$$

$$n_d \frac{\partial q_d}{\partial t} = \int_{-\alpha}^{\alpha} \sum_s q_s \left\{ \left(\frac{\delta f_s}{\delta t}\right)_g - \left(\frac{\delta f_s}{\delta t}\right)_{1} \right\} dv_z \qquad (4)$$

In equations (2) through (4), f_s is a one-dimensional distribution function for species s (electrons or protons) in t, z and v_z space and n_e, n_p and n_d are electron, proton and dust grain number densities. Subscripts 1 and g in equations (2) and (4) denote loss terms and gain terms, respectively, for particles of species s. The distribution functions for electrons and protons are found by injecting simulation particles from the bordering plasma into the dust layer, each particle representing a certain number of electrons or protons. The dust density distribution stays constant, but of course becomes charged as time progresses toward some equilibrium state of the system.

WORK IN PROGRESS

Wilson's results indicate the presence of significant and systematic structure in the electric field as a function of location within the dust layer. Since the plasma and dust parameters assumed are in the range of the values that describe the rings of Saturn, this structure, if real, has implications for the dynamical features of the rings. Of prime importance, therefore, is a detailed look at the results to see if any mechanisms exist that can mute the fields.

The present study, in collaboration with C. J. Pollock from MSFC and G. R. Wilson from UAH, is designed to extend Wilson's model to include refinements in the actual operational design of the simulation code itself and to include additional physics in order to assess the resulting electric field structure and grain charges. Most of the initial phases of the work have focussed on the fact that the code, though in principle reliable, suffers from severe time constraints, requiring as much as 10-50 hours of CPU time for typical runs on a VAX computer. It is likely that by staging the code into steps in which early steps are carried out crudely and later steps successively fine tune the results, stage-by-stage, the total CPU time can be cut

significantly. Preliminary results indicate the possibility
to cut CPU time to as much as 1/3 or 1/5 the former time.
The original Wilson code has been carefully examined, tested
and documented. Shortcuts and staging systems have been
introduced and tested which should make the code produce
more accurate results with a finer grid system than would
have been feasible heretofor. Continued testing and
implementation of these refinements will be carried out at
the author's home institution in the near future.

In addition to the effort at reducing CPU time to a
manageable amount, work is in progress to include a dust-
size distribution instead of assuming all dust grains have
the same size. Competition between dust grains of different
sizes may well lead to interesting and important differences
in charging that lead to differences in small grain versus
large grain particle dynamics. For example, one possible
effect is for electric repulsion to spread out smaller
particles more than larger particles in the dust layer.
These differences, as well as the E-field structure are of
special interest to research on Saturnian rings with their
unusual spoked and beaded appearance, as well as on rings
about Uranus and Jupiter.

in the longer term, there are additional processes that
may need to be included. One is the possibility of charging
by the knocking off of secondary electrons as a result of
energetic electron or ion collisions. Another effect may be
field emission of electrons by grains of very small radius.
Finally, the generation of ion cyclotron or ion acoustic
plasma waves may serve as a damping mechanism for
thermalizing the plasma distribution and muting the interior
electric field variations.

REFERENCES

1. Goertz, C. K. and W.-H. IP, Limitation of electrostatic
   charging of dust particles in a plasma, J. Geophys. Res.
   Lett., 11, No. 4, 349-352, April, 1984.
2. Houpis, H. L. F. and E. C. Whipple, Electrostatic charge
   on a dust size distribution in a plasma, J. Geophys.
   Res., 92, No. A11, 12,057-12,068, Nov., 1987.
3. Whipple, E. C., T. G. Northrop, and D. A. Mendis, The
   electrostatics of a dusty plasma, J. Geophys. Res., 90,
   No. A8, 7405-7413, Aug., 1985.
4. Wilson, G. R., Simulation of the plasma interaction with
   thin dust clouds, Ph.D Dissertation, Brigham Young Univ.,
   Dec., 1987.
5. Wilson, G. R., The electrostatic charging of thin dust
   clouds, J. Geophys. Res., 93, No. A11, 12,771-12,781,
   Nov., 1988.

1991

NASA/ASEE SUMMER FACULTY FELLOWSHIP PROGRAM

MARSHALL SPACE FLIGHT CENTER
THE UNIVERSITY OF ALABAMA IN HUNTSVILLE

SEDS1 MISSION SOFTWARE VERIFICATION
USING A SIGNAL SIMULATOR

Prepared By: William E. Pierson

Academic Rank: Professor

Institution: West Virginia Institute of
                          Technology, Department of
                          Electrical Engineering

NASA/MSFC:

        Laboratory: Program Development
        Division: Payload and Orbital Systems
        Branch: Orbital Support Systems Group

MSFC Colleague: Chris Rupp

Contract No: NGT-01-008-021
                          The University of Alabama
                          in Huntsville

SEDS1 MISSION SOFTWARE VERIFICATION
USING A SIGNAL SIMULATOR

August, 1991

BACKGROUND

The first flight of the Small Expendable Deployer System (SEDS1) is scheduled as the secondary payload of a Delta II in late 1992. The objective of the SEDS1 mission is to collect data to validate the concept of tethered satellite systems and to verify computer simulations used to predict their behavior. SEDS1 will deploy a 50 lb. instrumented satellite as an end mass using a 20 km tether. Langley Research Center is providing the end mass instrumentation, while the Marshall Space Flight Center is designing and building the deployer. The objective of the experiment is to test the SEDS design concept by demonstrating that the system will satisfactorily deploy the full 20 km tether without stopping prematurely, come to a smooth stop on the application of a brake, and cut the tether at the proper time after it swings to the local vertical. Also, SEDS1 will collect data which will be used to test the accuracy of tether dynamics models used to simulate this type of deployment. The experiment will last about 1.5 hours and complete approximately 1.5 orbits.

Radar tracking of the Delta II and end mass is planned. In addition, the SEDS1 on-board computer will continuously record, store, and transmit mission data over the Delta II S-Band telemetry system. The Data System will count tether windings as the tether unwinds, log the times of each turn and other mission events, monitor tether tension, and record the temperature of system components. A summary of the measurements taken during the SEDS1 shown in Table 1. The Data System will also control the tether brake and cutter mechanisms.

Two major sections of the flight software, the data telemetry modules and the data collection modules, were developed and tested under the 1990 NASA/ASEE Summer Faculty Fellowship Program. To facilitate the debugging of these software modules, a prototype SEDS Data System was programmed to simulate turn count signals. During the 1991 summer program, the concept of simulating signals produced by the SEDS electronics systems and circuits has been expanded and more precisely defined. This signal simulator will be used to debug and test the entire SEDS1 Mission Software.

SEDS MISSION SOFTWARE VERIFICATION TEST SPECIFICATION

A series of tests will be performed to exercise the software modules which make up the Mission Software of the SEDS Data System. These tests will be performed by using a SEDS Signal Simulator to generate signals which will simulate the inputs normally produced by sensors and circuits in the SEDS system. The test configuration is depicted in Figure 1. A SEDS Data System CPU Card will be modified to construct the SEDS Signal Simulator.

Signals will be generated which simulate both nominal flight conditions and all anticipated anomalies. In addition, the tests provide a means for monitoring and analyzing outputs produced by the SEDS Mission Software for controlling the tether brake and cutter mechanisms.

Table 1. SEDS Measurements

MEASUREMENT	RANGE	SAMPLE RATE
T1 - Tether Temperature	-30° to +80° F	1 per 10 seconds
T2 - Brake Temperature	-30° to +80° F	1 per 10 seconds
T3 - Cannister Temperature	-30° to +80° F	1 per 10 seconds
T4 - Electronics Temperature	-30° to +80° F	1 per 10 seconds
B1 - Turn Counter Beam #1	Discrete	Asynchronous
B2 - Turn Counter Beam #2	Discrete	Asynchronous
B3 - Turn Counter Beam #3	Discrete	Asynchronous
F1 - Tether Tension #1	-0.25 to +0.25 N.	500 per second
F2 - Tether Tension #2	-2.5 to +7.5 N.	500 per second
IN1/IN2- Satellite Deployment	Discrete	Asynchronous

FIGURE 1. SEDS MISSION SOFTWARE TESTING USING A SIGNAL SIMULATOR
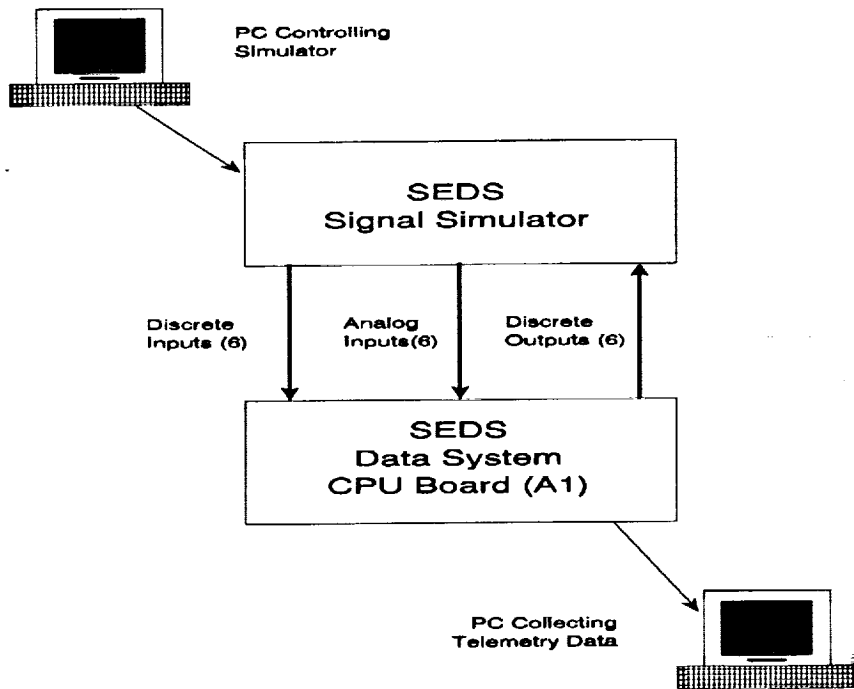
With the exception of control signals for the tether brake and cutter, correct operation of the Mission Software can be verified by examining the data collected and transmitted by the Mission Software over the serial port of the SEDS Data System. An IBM-compatible PC will be connected to this serial port to collect the

mission data. The PC will execute software to display summary data contained in the Master Frames sent by the SEDS Data System. In addition, this software will store the serial data in a disk file to be used in post-test analysis and documentation. The signals generated by the SEDS Data System to control the tether brake and the tether cutter cannot be analyzed by monitoring the serial data stream. Therefore, the PC controlling the SEDS Signal Simulator will monitor, display and store these control signals levels.

There will be two groups of tests performed on the SEDS Mission Software using simulated input signals: Turn Counter Tests and Mission Simulation Tests. The Turn Counter Tests will focus on modules which execute the turn count functions of the Mission Software and exercise these modules under both normal and anticipated anomalous conditions. The Mission Simulation Tests will emulate the complete SEDS experiment cycle and will be designed to represent both normal and anticipated anomalous conditions. The Turn Counter Tests are described in Table 2, and the Mission Simulation Tests are described in Table 3.

TABLE 2. TURN COUNTER TESTS

TEST	CHANNEL-A	CHANNEL-B	OTHER
1	No failure, no flutter	No failure, no flutter	No pre-deployment turn count activity
2	No failure, no flutter	No failure, no flutter	2 sec. of pre-deployment activity on Channel-A
3	No failure, flutter present	No failure, no flutter	No pre-deployment turn count activity
4	No failure, no flutter	No failure, flutter present	No pre-deployment activity
5	Failed at 0.5s	No failure	No pre-deployment turn counts or flutter
6	No failure	Failed at 0.5s	No pre-deployment turn counts or flutter
7	Failed at 0.5s, normal at 2.5s	No failure	No pre-deployment turn counts or flutter
8	No failure	Failed at 0.5s, normal at 2.5s	No pre-deployment turn counts or flutter
9	No failure, occurs before Ch.-B	Overlaps Ch.-A in same 2ms interval	No pre-deployment turn counts or flutter
10	Overlaps Ch.-B in same 2ms interval	No failure, occurs before Ch.-A	No pre-deployment turn counts or flutter

During each of the SEDS Mission Simulation Tests, the SEDS Simulator will generate independent signals to each analog input of the SEDS unit under test. The analog signals provided by the simulator will be one of three levels: 0v (0.2v, max), half-scale (2.5v ±10%), or full-scale (5.0v ±10%) and will be applied in regular

cycles. The purpose of applying simulated analog inputs to the SEDS Data System is not to gauge the accuracy of the A/D converter circuitry but to assure that the data collection modules in the Mission Software is correctly collecting and transmitting temperature and tension information.

TABLE 3. MISSION SIMULATION TESTS

	CHANNEL-A	CHANNEL-B	BRAKE ENABLE SWITCH
1	No failure	No failure	Asserted after 40,000 counts on Channel-A
2	No failure	Fails after 10,000 counts	Asserted after 40,000 counts on Channel-A
3	Fails after 10,000 counts	No failure	Asserted after 40,000 counts on Channel-B
4	No failure	Fails after 10,000 counts	Not asserted
5	Fails after 10,000 counts	No failure	Not asserted

CONCLUSION

The SEDS Signal Simulator will be used in the debugging and in the formal verification of the SEDS1 Mission Software. The Simulator will not only emulate normal flight conditions but also exercise all modules written to handle anticipated anomalous flight conditions, conditions that would be difficult to reproduce and control with actual SEDS hardware. The simulator will help to expedite software development and to increase the confidence of the users of the Mission Software. With little modification, the Simulator should be useful in the software development of future SEDS flights.

REFERENCES

1. "SEDS Data System Functional Requirements", Energy Sciences Laboratories, Inc. and Program Development, MSFC, May 1988.

2. "SEDS Data System Data Collection and Telemetry Software", Final Report, NASA/ASEE 1990 Summer Faculty Fellowship Program, Contract No. NGT-01-002-099, MSFC, Huntsville, AL.

3. "SEDS Mission Software Verification Test Procedures, NASA/ASEE 1991 Summer Faculty Fellowship Program, Contract No. NGT-01-008-021, MSFC, Huntsville, AL.

4. "MSFC Software Management and Development Requirements Manual", Software and Data Management Division, January, 1991, MSFC, Huntsville, AL.

1991

NASA/ASEE SUMMER FACULTY FELLOWSHIP PROGRAM

MARSHALL SPACE FLIGHT CENTER
THE UNIVERSITY OF ALABAMA

**EMERGENCY EGRESS REQUIREMENTS
FOR
SPACE STATION FREEDOM**

Prepared By: Paul S. Ray

Academic Rank: Assistant Professor

University and   The University of Alabama
Department: Industrial Engineering
                                      Tuscaloosa, Alabama

NASA/MSFC:

        Division   Systems Safety Engineering
        Branch: Project Safety Engineering

MSFC Colleague: Richard Siler
                                      Mark D'Agostino

Contract No: NGT-01-008-021
                                      The University of Alabama

Introduction

There has been concern regarding the survival of the Space Station Freedom and its crewmembers during an emergency. An emergency can arise from the following: (a) Depressurization due to breach of the station's hull by space debris or meteoroids, seal failure, vent failure, or inadvertent activation of a vent by a crewmember; (b) toxicity created by released chemicals; and (c) a large fire resulting from an electrical short or explosion.

Previous considerations, including nodes at the ends of international modules, egress aids, zoning of equipment, clear aisles, and, most recently, the racetrack configuration, have been discarded. In addition, the issue of crew and station survivability has become more urgent for evaluation due to restructuring of the station. A number of components are to be analyzed for updating the requirements for emergency egress.

Objectives

The objectives of the study were to determine if the pressurized elements and hatchways of the Space Station Freedom support the emergency egress of crewmembers during operation of the station at the stage of Permanently Manned Capacity (PMC).

Emergency Egress

Emergency egress has been defined as the exit from a pressurized element when an event occurs which makes that element uninhabitable.

Assumptions

1. The latest Restructured Space Station Configuration as given in Figure 1.

2. All hatches will remain open during normal operation within the station, between the orbiter and the station, and between the ACRV and the station.

3. Hatches will be operated manually from both sides.

4. The orbiter will always be manned with two crewmembers while docked at the SSF.

5. Crewmembers can maintain a transition speed of 1 ft/sec when moving an injured person and 5 ft/sec when moving through an induced airflow caused by a 4 inch diameter hole in the station's hull. The time values are based on the Skylab experience, tests conducted in KC135, and empirical data obtained from the astronauts.

Emergency Egress Tasks

The emergency egress tasks for the restructured station consist of:

1. Perceiving the emergency alarm siren.
2. Translating to the IMPACT workstation, switching off the alarm, use trackball, and learn the emergency action needed from display.
3. Don mask, help the injured crewmember to don mask, and translate to the safe area.
4. Close hatch and switch off the inter-module ventilation to isolate the affected element.

Structural Design of Egress Translation Path

The pressurized elements studied consist of: Pressurized Docking Adapter (PDA), hatch, redesigned modules (Laboratory and Habitation), birthing mechanism, and resource node. The elements were considered assembled in the restructured configuration as shown in Figure 1.

The rack locations were also considered with respect to the egress path .

Emergency Egress Scenarios and Estimated Times

The possible egress paths for four emergency scenarios considered were: (I) Accident occurs in a module and crewmembers translate to the attached node, (II) accident occurs at a node and crewmembers translate through it to the safe node (half station concept), (III) accident occurs at a module close to a node and crewmembers are not able to translate through the affected area, and (IV) accident occurs at a node and crewmembers cannot translate through it.
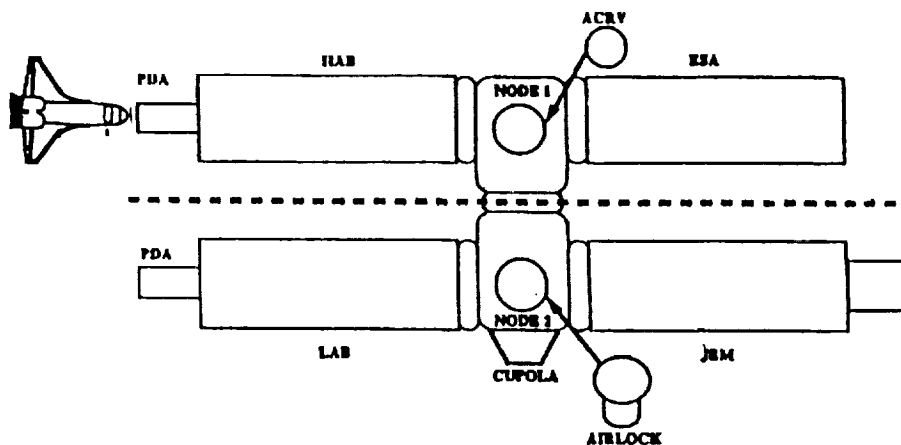
POTENTIAL DISTRIBUTION SCHEMES

Figure 1

Sketch of Restructured Space Station Configuration

The estimated egress times are:

Case	Egress time (sec)
I	2.44
II	2.96
III	2.62
IV	1.37

In the case of cases III and IV, there is the possibility that the crewmembers may become trapped in the attached module in case of a severe accident occurring at or close to a resource node.

Translation Aids

It has been found that mobility aids, such as handrails, handholds, or footloops, are essential for safe egress during emergencies at free-flight terminal points, while changing direction, for control of body orientation, or for initiation of translation.

Summary

The observations are summarized as follows:

1. The structural design of the pressurized elements and the hatches studied is adequate for the emergency egress translation requirement. However, passage through the PDA may present a problem during the movement of an injured crewmember to the orbiter.

2. The current locations of a few racks, close to the hatches, may cause some obstruction for translation to the orbiter.

3. The egress time required in the worst situation, excluding entrapment, is estimated to be about three minutes.

4. There is a chance of getting crewmembers trapped in a module in case of a sever accident occurring at or close to a resource node.

5. Handholds and footloops around the hatches and kick surfaces along the translation path are required to aid emergency egress translation.

Suggested Additional Studies

o   Evaluation of descriptive vs. graphic display of Emergency Action Information.

o   Stowage locations of emergency equipment (PBA, Handrails, Egress Lighting) and their identification.

o   Evaluation of emergency egress requirements during the build-up of the station through its various stages starting from MB-6.

Recommendations

1. The requirement of a minimum clear egress path of 43 inches in diameter should be modified for non-circular paths (egress through PDA).

2. Locations of racks requiring more frequent maintenance should be away from the hatch to ensure better chance of a clear path for emergency egress.

3. The ACRV should be made capable of docking at the PDA of Laboratory and Habitation modules, including hatch commonalty and move capability. This will provide duel escape paths comparable to that provided by the racetrack configuration.

4. The estimated maximum time of emergency egress is about three minutes. However, the time values used should be verified by appropriate tests under microgravity conditions.

5. Handrails and foot restraints around the hatches and kick surfaces along the egress translation paths should be provided to act as translation aids during emergencies.

6. Suggested additional studies should be conducted prior to finalization of the space station design.

1990

NASA/ASEE SUMMER FACULTY FELLOWSHIP PROGRAM

MARSHALL SPACE FLIGHT CENTER
THE UNIVERSITY OF ALABAMA

Using Probabilistic Analysis to Assess the Reliability of Predicted SRB Aft-Skirt Stresses

Prepared by: James A. Richardson, Ph.D.

Academic Rank: Assistant Professor

Institution: University of Alabama,
                                          Tuscaloosa, Civil
                                          Engineering Department

NASA/MSFC:

    Office: Structures and Dynamics Lab
    Division: Structural Analysis
    Branch: Systems Response

MSFC Colleague: John Townsend, Ph.D.

Contract No.:   NGT-01-008-021
                                          The University of Alabama

Introduction

Probabilistic failure analysis is a tool to predict the reliability of a part or system. In situations where a part can be designed to carry loads well below its strength, probabilistic failure analysis is not necessary. When a part must be designed to carry loads almost equal to its strength, however, the variability in the loads and strength should be considered in order to ensure acceptable reliability. Probabilistic analysis methods were applied to an example problem as a step toward evaluating the usefulness of the method for MSFC engineers. For this project, probalistic techniques were used to predict critical stresses which occur in the solid rocket booster aft-skirt during main-engine buildup, immediately prior to lift-off.

Background

During a structural test of the skirt, the skirt failed at a load corresponding to a factor of safety of 1.28. Because this was less than the desired factor of safety of 1.40, the skirt attracted a lot of attention. One of the outcomes was the skirt supports, called hold down posts (HDP), were instrumented with strain gages in order to determine the actual peak loads on the skirt. These loads occur during the approximately seven-second period immediately prior to lift-off, when the main engines are building up maximum thrust.

Unfortunately, the measured loads (specifically the Z component) do not agree with the calculated loads nor with equilibrium! As a result, the predicted aft-skirt stresses have been unreliable. The goal of my summer project was to investigate the deviations in the predicted skirt stresses due to deviations in the measured HDP strains. The effects of deviations of other parameters affecting the predicted skirt stresses were also studied.

Analysis Procedure

The procedure of calculating skirt stresses based on measured HDP strains is illustrated in the diagram in Figure 1. The procedure begins with peak HDP strains measured during the main-engine build-up phase, immediately prior to lift-off. Next, the strains are multiplied by calibration constants to yield the forces at the top of the hold down posts (HDP loads). (The HDP loads are equal and opposite to the loads on the skirt, as shown in Figure 1.) In the last step, the HDP loads are multiplied by the skirt stress-indicator equations to yield the skirt stresses in the vicinity of the weld region.
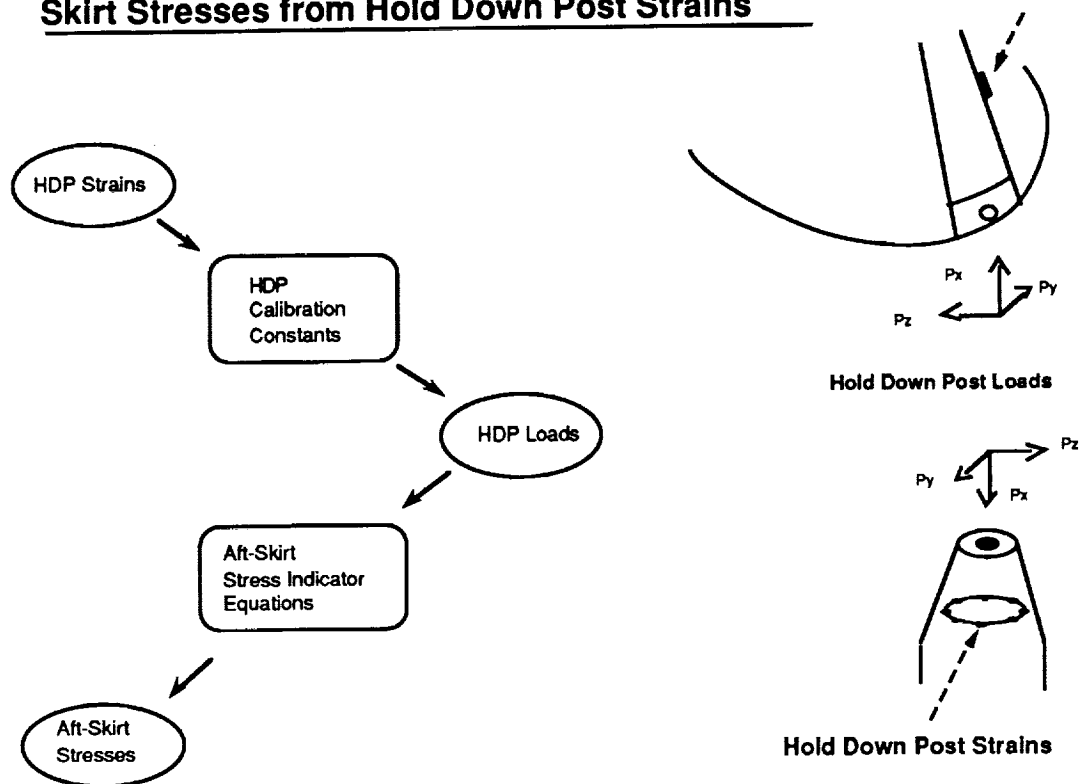
Skirt Stresses from Hold Down Post Strains

Figure 1. Diagram and flow chart of predicting skirt stresses from hold down post (HDP) strain measurements.

A distribution of predicted skirt stresses was generated using Monte Carlo simulation. Using this technique, HDP strains were drawn at random from assumed distributions and multiplied by the calibration constants to yield HDP loads. The procedure was repeated 300 times, each time drawing a new set of strains at random from the strain distributions. The result was a distribution of HDP loads. The HDP load distributions were then used as input in another Monte Carlo simulation to produce distributions of skirt stresses.

The results from two of the most significant analyses are discussed below. In these analyses, actual peak strains and calibration constants from shuttle flight STS-27 were used as the means of the distributions. The peak strains ranged from 40 to 277 microstrains and the calibration constants ranged from 0.008 to 0.322. The strains were assumed to vary uniformly about their means +/- 2 microstrains and the HDP calibration constants were assumed to vary uniformly about their means by +/- .01.

Results

The resulting load distributions had coefficients of variation (standard deviation divided by the mean) of 2%, 3%, and 8% for the X, Y, and Z loads. The Z load distribution has a much larger deviation than either the X or Y load distributions. The recorded HDP loads from numerous shuttle launches show this same trend. This study determined that the higher deviation of the Z loads was due to the way the strain gages are oriented in the hold down posts and the small magnitude of the HDP strains (less than 200 microstrain).

Aft-Skirt Stress at HDP #4 for Two HDP Load Distribtions

Mean = -58.3
S. Dev = 5.22 (9.0%)

Mean = -58.3
S. Dev. = 17.6 (30%)

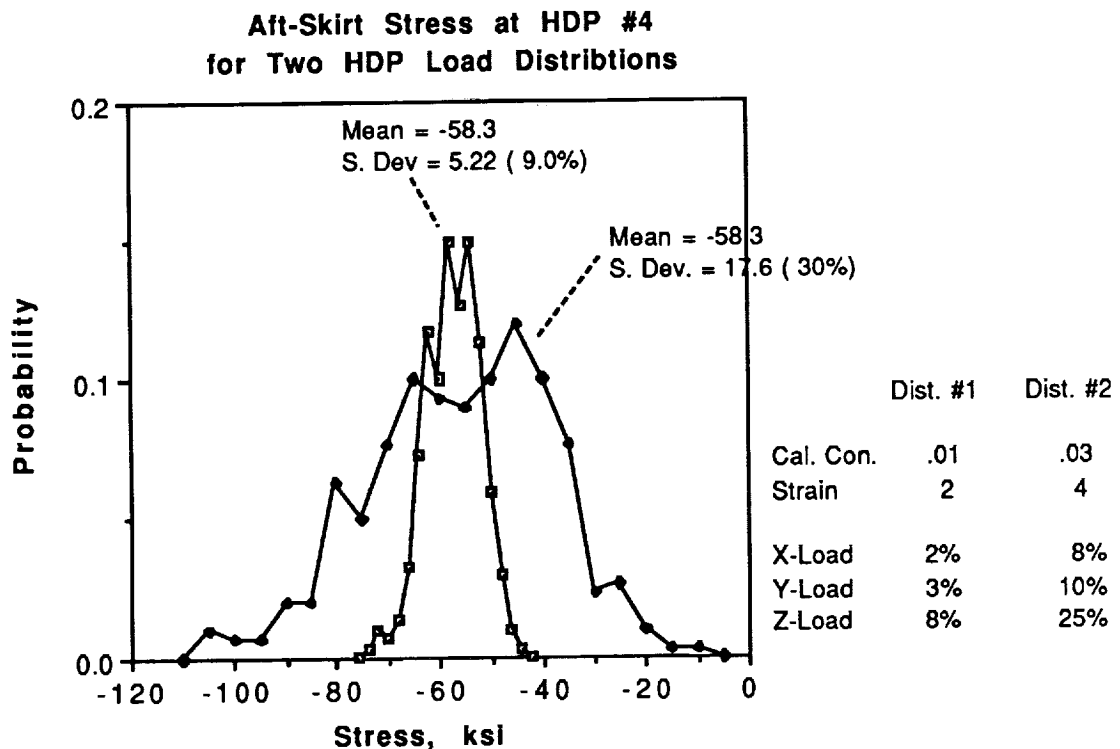|	Dist. #1	Dist. #2
Cal. Con.	.01	.03
Strain	2	4
X-Load	2%	8%
Y-Load	3%	10%
Z-Load	8%	25%

Figure 2.   Predicted aft-skirt stress distributions.

The load distributions were used in turn for another Monte Carlo simulation to generate skirt stress distributions. The distribution of stresses near HDP #4 is shown in Figure 2 as the narrower distribution. A second analysis, using a more conservative strain variation of +/- 4 microstrains and a calibration constant variation of +/- .03, is also plotted in Figure 2.

The stress distribution plotted in Figure 2 shows that even for very optimistic (unconservative) strain and calibration constant

deviations (2 microstrain and .03 calibration constant), the predicted stresses range from 45 ksi to 70 ksi. Because the actual skirt stresses are not separated from the failure stress by a comfortably large margin, this is considered to be too large of a deviation.

Summary and Conclusions

More than any other HDP load component, the Z-loads are sensitive to variations in strains and calibration constants. Also, predicted aft-skirt stresses are strongly affected by HDP load variations. Therefore, the instrumented hold down posts are not effective load transducers for Z-loads, and, when used with aft-skirt stress indicator equations, yield estimates with large uncertainty.

Monte Carlo simulation proved to be a straight-forward way of studying the overlapping effects of multiple parameters on predicted equipment performance. An advantage of probabilistic analysis is the degree of uncertainty of each parameter is stated explicitly by its probability distribution, allowing it to be communicated among engineers.

It was noted, however, that the choice of parameter distribution had a large effect on the simulation results. Many times these distributions must be assumed. In my opinion, the engineer who is actually designing or analyzing the part should be responsible for the choice of parameter distributions. Therefore, it is important for the designer or analyst to understand probabilistic analysis so that he can make valid assumptions when using it.

1991

NASA/ASEE SUMMER FACULTY FELLOWSHIP PROGRAM

MARSHALL SPACE FLIGHT CENTER
THE UNIVERSITY OF ALABAMA

SPACE STATION INTERNAL PROPAGATION

Prepared by: J. E. Richie, Ph. D.

Academic Rank: Assistant Professor

Institution: Marquette University,
                                Department of Electrical
                                and Computer Engineering

NASA/MSFC:

    Division: Computers and
                                Communications

    Branch: EB33/Communications and
                                Systems

MSFC Colleague: J. Leon Bell
                                David P. Harris, Jr.

Contract No.:   NGT-01-008-021
                                University of Alabama in
                                Huntsville

I. Introduction

The Space Station Freedom (SSF) is planned with a wireless communication system in place for the transmission of information between crew members on board. The clarity of transmission is paramount to an effective system of communication. This report contains a short overview of the system including the requirements of interest, and a statement of the problem that was concentrated upon. The theory used to solve the problem is explored. The results given are for the experiments performed on a mockup of the proposed structure at the Marshall Space Flight Center.

The requirements on the signal level are that there is a 45 dB signal to noise ratio (SNR) from end to end, and that coverage over 99% of the volume be maintained. It is this last, 99% requirement that is addressed in the report.

II. Theory

The SSF wireless unit is operated inside a large cavity or waveguide that causes reflections. Because the number of modes is very large, it is not easily modeled using modal techniques. It is also filled with equipment that will increase the reflections. This is a formidable problem.

The point of attack will be to randomly sample the field strength inside the volume and estimate a probability distribution function (pdf) for the field strengths inside. Once a pdf is found, the requirement that 99% of the volume be covered can be re-designed and verified. The method for finding the 99% point shall be to find the location that insures that 99% of the area under the pdf is to the left. This is the power level obtained. The system power can be scaled to provide a 45 dB SNR.

The Rice-Nakagami or Rice distribution is a simple extension of the Rayleigh distribution where there is a significant line-of-sight path from the transmitter to the receiver (1). The line-of-sight path is a coherent component to the statistical distribution of the field strength inside the volume. For SSF, this distribution will correspond to the summation of a coherent line-of-sight path between the transmitter and the receiver and an incoherent portion. The incoherent portion is the sum of reflections from the walls and the equipment inside of the SSF. The distribution is given by:

$$p_R(A) = \frac{A}{\sigma_s^2} e^{-\left(\frac{A^2 + A_0^2}{2\sigma_s^2}\right)} I_0\left(\frac{A_0 A}{\sigma_s^2}\right) \qquad [1]$$

where σ_s^2 is the variance (the subscript s is to differentiate this with the Rayleigh variance), A_0 is the strength of the coherent component, I_0 is the modified Bessel function of the first kind of order 0, and the subscript R on the pdf name is to denote a Rice distribution.

The Rice distribution, $p_R(A)$, has two estimated parameters to fit the data. The variance describes the spread of amplitudes similar to the Rayleigh variance. The value A_0 is proportional to the field strength of the line-of-sight component. It is important to note in passing that this distribution is ideal in cases of transmission over a rough surface.

The χ^2 test (2) has been used with much success to obtain the Rice distribution. A simple search routine was implemented to find the appropriate pdf parameters.

IV. Results

The experiments are detailed in (3,4). The experiments were performed on a 43 foot mockup with a diameter of 14 feet that was filled with demonstration equipment, and an empty mockup of the same diameter that was empty. The values of the parameters for each test were found and tabulated. A typical distribution with the Rice fit is shown in figure 1.

Conclusions reached from the results of the two tests are the shown in figure 2. The A_0 value is relatively independent of frequency. This was expected. The variance found should decrease slightly as the frequency increases. The results are ambiguous within this small frequency range. The average value of A_0 at 450 MHz was found to be 9.6 and the average variance was 18.2. If we compare the experiment 1 results (12.6 and 18.9), we see that the variance is much lower in the empty 27 foot mockup. It is believed the major contributor to this drop is the absence of the randomly placed scatterers in the second experiment.

V. Conclusions

The Rice pdf has been found to be the optimal distribution from theoretical and experimental results. This can been demonstrated quite convincingly.

VI. References

(1) Beckmann, P., and A. Spizzichino, <u>The Scattering of Electromagnetic Waves from Rough Surfaces</u>, Norwood, MA: Artech House, 1987.

(2) Guttman, I., <u>et al</u>, <u>Introductory Engineering Statistics</u>, 3rd Ed., New York: John Wiley, 1982, pp. 174-176.

(3) Bell, J.L., "Space Station Propagation Tests", internal memo, Lab. EB33, MSFC, Huntsville AL, Feb. 7, 1991.

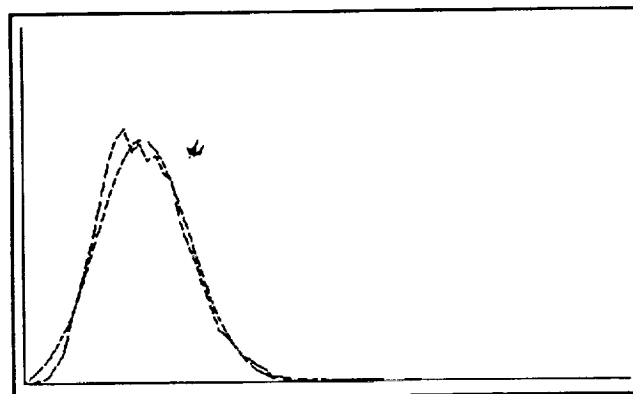(4) Bell, J.L., "Space Station Propagation Tests", internal memo, Lab. EB33, MSFC, Huntsville, AL, July 30, 1991.

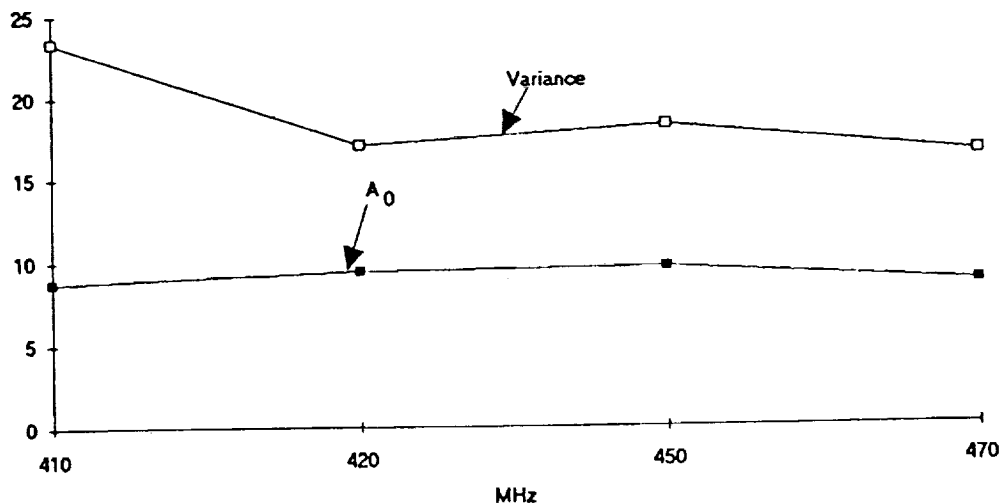**Figure 1.** Rice fit of data set 1, experiment 1.

**Figure 2.** A_0, σ_s^2 vs. frequency over averaged test cases.

1991

NASA/ASEE Summer Faculty Fellowship Program

Marshall Space Flight Center
The University of Alabama in Huntsville

Space System Production Cost Benefits From
Contemporary Philosophies in Management and Manufacturing

Prepared By: Russell L. Rosmait

Academic Rank: Assistant Professor

Institution: Pittsburg State University,
                                      Dept. of Engineering Tech
                                      Pittsburg, Kansas 66762

NASA/MSFC:

    Office :   Program Planning Office
    Division: Engineering Cost Group

MSFC Colleague: Joseph W. Hamaker

Contract No.:   NGT-01-008-021
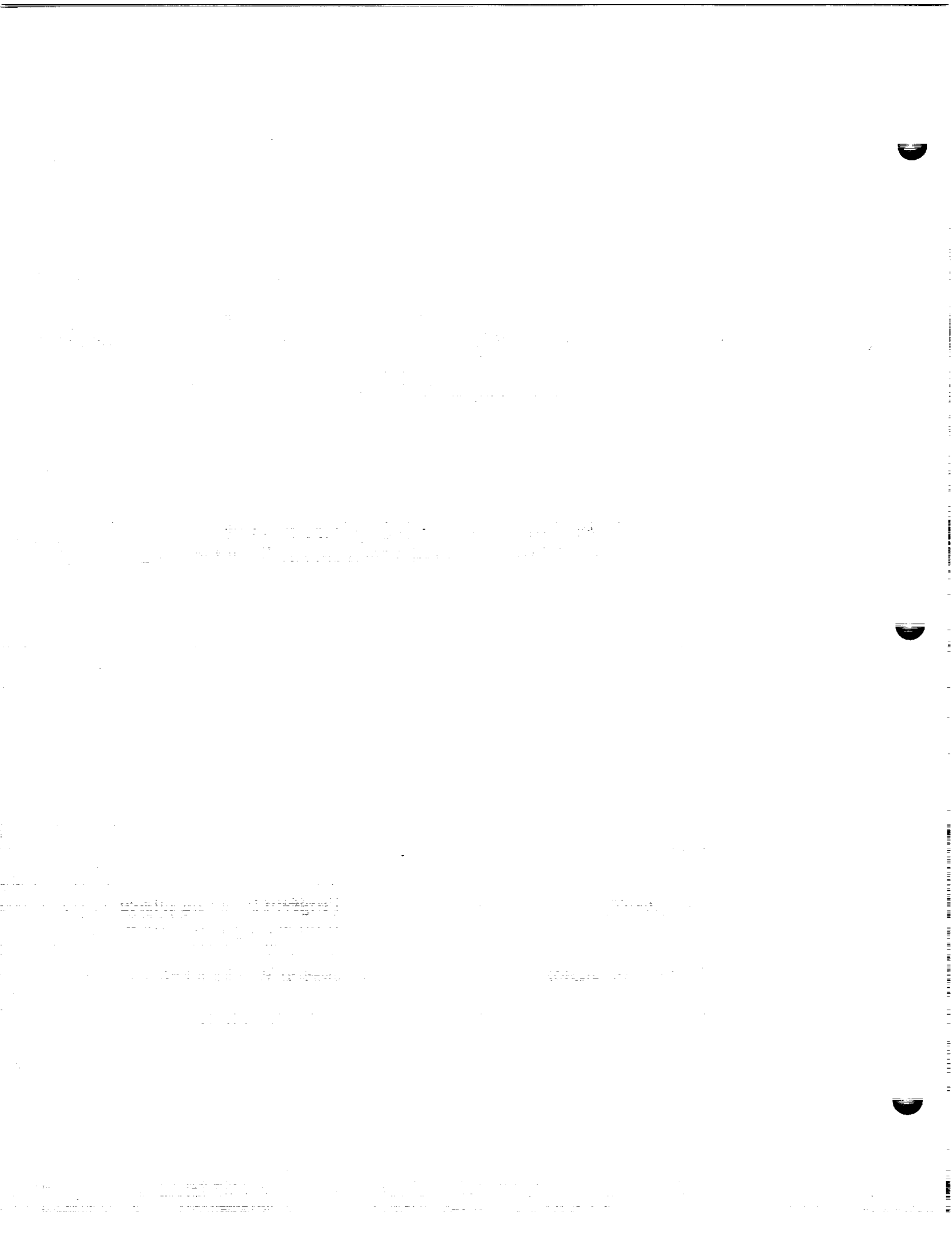
The cost of manufacturing space system hardware has always been expensive. Coupled with funding cutbacks, tight budgets and NASA's shrinking share of the federal monies, the need to find space system manufacturing cost savings is ever present.

The Engineering Cost Group of the Program Planning office at the Marshall Space Flight Center is attempting to account for cost savings that result from new technologies in manufacturing and management. Currently, historical programs are used as data points in parametric estimates of future space system programs. The concern of the Engineering Cost Group is that the historical analogs reflect costs of space system hardware produced with the use of old technology. These systems may have cost less if current technologies would have been available when they were manufactured. Because the implementation of new technology changes are not being represented in the historical programs, the cost of future space system programs could be overstated.

The objective of the Engineering Cost Group is to identify and define contemporary philosophies in manufacturing and management. Through interviews, literature searches, and direct discussions with NASA engineers and contractors, a list of seven management and manufacturing categories were identified: Design, Testing, Materials Processing, Factory Automation, Quality Systems, Production Management Systems and Materials Selection.

The scope of this project is to collect information which would assist in quantifying the reduction in cost of space system hardware and launch vehicles due to current philosophies within contemporary management and manufacturing. Figure 1 illustrates the seven broad categories that make up the areas where technological advances can assist in reducing space system costs. Included within these broad categories in figure 1 is a list of the processes or techniques that specifically provide the cost savings within todays design, test, production and operations environments. The processes and techniques listed all provide some cost saving. They achieve their savings in the following manner:

1. Increased Productivity
2. Reduced Down Time
3. Reduced Scrap
4. Reduced Rework
5. Reduced Man Hours
6. Reduced Material Costs

In addition, it should be noted that cost savings from production and processing improvements effect 20% to 40% of production costs whereas savings from management improvements effect 60% to 80% of production cost. This is important to note because most efforts in reducing cost are spent trying to reduce cost in the production.

It should also be noted that a panel assembled by the Director of Science and Technology Policy, Executive office of the President was given the task of identifying similar technologies. These technologies were deemed critical to the national economic prosperity and to national security. The panel's list of technologies fell into six broad categories. Two of the panel's six broad categories (Materials and Manufacturing) represent a majority of the technologies identified by the Engineering Cost Group.

The Engineering Cost Group is planning to continue the work started during the summer of 1991. Future plans for the continuation of this project are as follows:

1. Continue to compile information on new technologies and document areas of savings.

2. Use National Critical Technologies Panel report to the president as a guide for classification and documentation of new technologies.

3. Investigate savings achieved by prime contractors through the installation of new technologies within management and manufacturing .

4. Use the above information to develop cost factors for the new technologies

Item number one will discuss current philosophies within contemporary management and manufacturing and include specific areas of cost savings associated with them. Using the National Critical Technologies Panel report as a guide for the materials and manufacturing section will insure continuity and credibility with current national reports. Item three will investigate past and present cost savings from new management and manufacturing advances on current space system hardware. Prime government contractors as well as leading corporations will be served to collect information on the successful implementation of the new technologies. Specifically, cost saving documentation will be gathered. Finally, item four will conclude with possible cost factors associated with each new management and manufacturing technology. The developed cost factors associated with the new management and manufacturing innovation could then be applied to cost estimates developed from historical cost data to reflect the use of new technologies. Collected data could also be evaluated to determine production quantities required to amortize the cost of implementation.

References

Garrett, R. W. : "Eight Steps to Simultaneous Engineering" Manufacturing Engineering, November 1990, Page 41-47

Niebel, B. W., Draper, A.B. Wysk, R.A. : <u>Modern Manufacturing Process Engineering</u>, McGraw-Hill First edition 1989.

Heine, H. J. : Casting to Near Net Shape. Foundry Management and Technology, Penton Publishing. Cleveland, OH, April 1987, P. 22-27

Kutcher, R.E., Schwelkert, P.G., Bailey, P.G. : Manufacturing Methods for Production of Premium Quality Castings at a Lower Cost, Wright-Pattern Air Force Base, OH, Final Report for Period 1 April 1976 - 31 August 1980.

Philips, W.D. : Report of the National Critical Technologies Panel, U.S. Goverment, Office of the Science and Technology, Executive office of the President, March 1991.

NASA George C. Marshall Space Flight Center
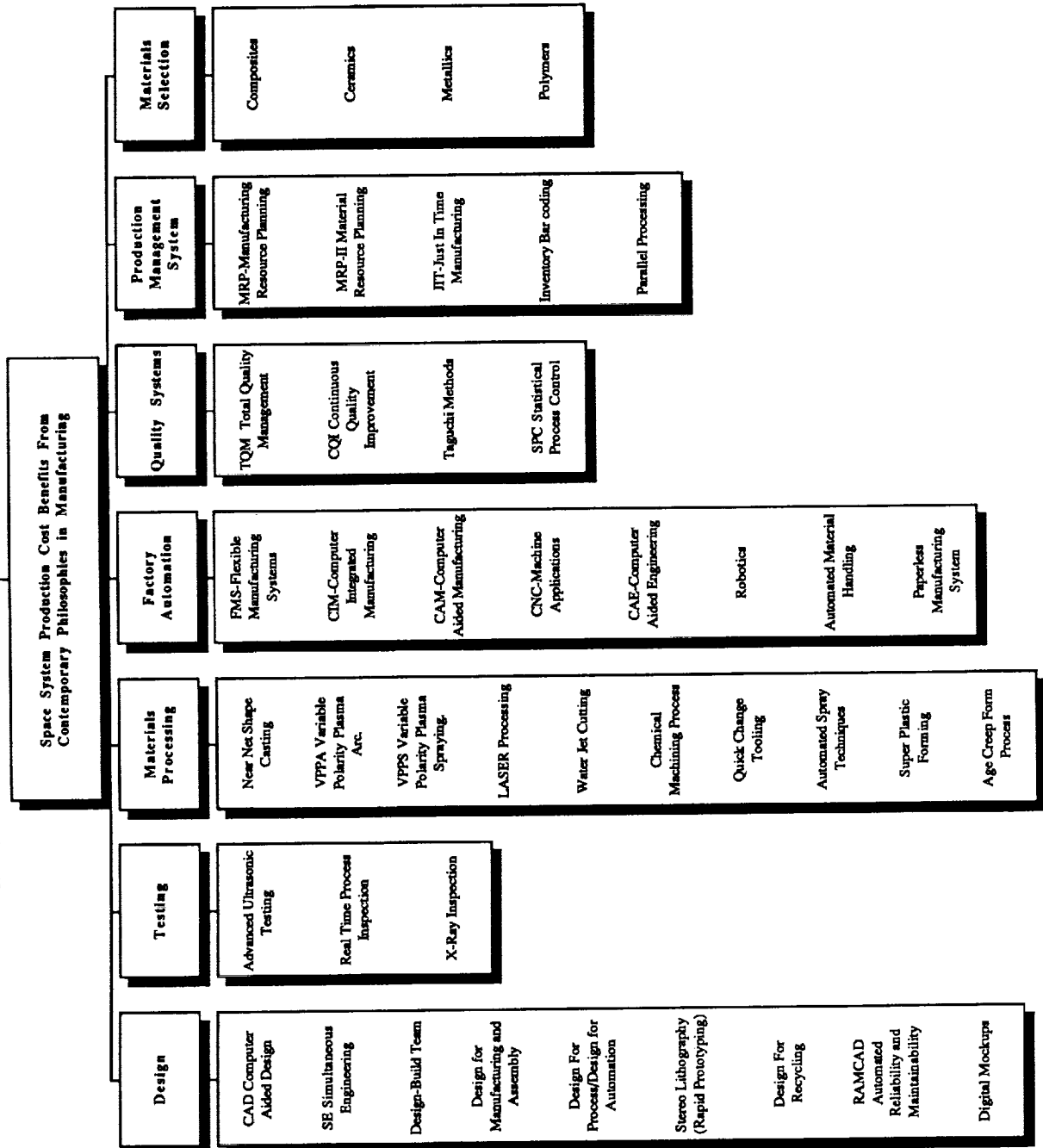Program Planning Office · Engineering Cost Group · Proposal

Space System Production Cost Benefits From Contemporary Philosophies in Manufacturing

Materials Selection
- Composites
- Ceramics
- Metallics
- Polymers

Production Management System
- MRP-Manufacturing Resource Planning
- MRP-II Material Resource Planning
- JIT-Just In Time Manufacturing
- Inventory Bar coding
- Parallel Processing

Quality Systems
- TQM Total Quality Management
- CQI Continuous Quality Improvement
- Taguchi Methods
- SPC Statistical Process Control

Factory Automation
- FMS-Flexible Manufacturing Systems
- CIM-Computer Integrated Manufacturing
- CAM-Computer Aided Manufacturing
- CNC-Machine Applications
- CAE-Computer Aided Engineering
- Robotics
- Automated Material Handling
- Paperless Manufacturing System

Materials Processing
- Near Net Shape Casting
- VPPA Variable Polarity Plasma Arc.
- VPPS Variable Polarity Plasma Spraying
- LASER Processing
- Water Jet Cutting
- Chemical Machining Process
- Quick Change Tooling
- Automated Spray Techniques
- Super Plastic Forming
- Age Creep Form Process

Testing
- Advanced Ultrasonic Testing
- Real Time Process Inspection
- X-Ray Inspection

Design
- CAD Computer Aided Design
- SE Simultaneous Engineering
- Design-Build Team
- Design for Manufacturing and Assembly
- Design For Process/Design for Automation
- Stereo Lithography (Rapid Prototyping)
- Design For Recycling
- RAMCAD Automated Reliability and Maintainability
- Digital Mockups

Figure 1

1991
NASA/ASEE SUMMER FACULTY FELLOWSHIP PROGRAM

MARSHALL SPACE FLIGHT CENTER
THE UNIVERSITY OF ALABAMA

HIGH VOLTAGE PLASMA SHEATH ANALYSIS
RELATED TO TSS-1

Prepared By: John W. Sheldon, Ph.D.

Academic Rank: Professor

University and   Florida International University
Department: Physics Department

NASA/MSFC:

    Laboratory: Space Science Laboratory
    Division: Solar-Terrestrial Physics Division
    Branch: Magnetospheric Physics Branch

MSFC Colleague: Nobie H. Stone, Ph.D.

Contract No.:   NGT-01-008-021
                                      The University of Alabama

Introduction

On the first mission of the Tethered Satellite System (TSS-1), a 1.8m diameter spherical satellite will be deployed a distance of 20 km above the space shuttle Orbiter on an isulated conducting tether. The satellite will be held at electric potentials up to 5000 volts positive with respect to the ambient plasma. Due to the passage of the conducting tether through the earth's magnetic field, an emf will be created, driving electrons down the tether to the orbiter, out through an electron gun into the ionosphere and back into the positive-biased satellite. Instrumentation on the satellite will measure electron flow to the surface at several locations, but these detectors have a limited range of acceptance angle. The problem addressed herein is the determination of the electron current distribution over the satellite surface and the angle of incidence of the incoming electrons relative to the surface normal.

The Mathematical Model

In the ionosphere at the altitude of the planned orbit, the average thermal velocity of electrons 1.9×10^5 m/s, the average thermal velocity of the ions is 1.1×10^3 m/s and the velocity of the satellite is 8×10^3 m/s. Furthermore, the electrons spiral about the earth's magnetic field lines (0.4 Gauss) with a radius of 3 cm, while the ions spiral with a radius of 5m. Under these conditions, the electron thermal energy, $kT = 0.17$ eV and the satellite radius $R_p = 163$ Debye lengths.

In the present calculation, it is assumed that there will be a sheath region around the satellite devold of ions due to the high positive potential and that electrons approach this sheath along the magnetic field lines neglecting their initial velocity due to the ambient spirals. The governing equations in this sheath are taken to be (1) the Steady-state Taylor-Vlasov equations which relate the components of the electron velocity to the local electric potential, (2) the continuity equation for electrons which relates their velocity components to the electron density and, (3) the Poisson equation which relates the electron density to the electric potential. The boundary conditions at the outer edge of the sheath are that the electron velocity is equal to the ambient electron drift velocity, the electron density is the ambient value.

Symmetry conditions which apply at the magnetic pole and equator are used in equations (1)-(3) to obtain a single ordinary differential equation. This equation is solved in each region by backward differencing and the potential distributions and location of the space charge minima for the pole and equator are determined. The angular weighted average of these solutions at the radius of the equatorial space charge minimum is used as the outer boundry condition for the potential.

The Solution

Finite difference equations, using backward differencing for equations (1)-(2) are solved simultaneously. Equation (3) is solved by the successive over-relaxation method. The computer program begins by using a guessed potential distribution and solving equations (1)-(2) to obtain the electron density. Using this

electron density a new potential distribution is obtained and used in equations (1)-(2), repeating the cycle. The above process is repeated until potential, electron density, and electron velocity spacial distributions have converged. Then the angles of incidence of the current to the satellite surface are obtained from the electron velocity components.

Results

The computational program has been carried out for satellite potentials from 100 to 100,000 (in units of kT). The sheath radius R_s at the magnetic equator (the lcoation of the space charge minimum) is compared to the satellite radius R_p in the table below.

Sheath Radius

Satellite potential, Vp (kT)	Rs/Rp
100	1.125
1,000	1.566
10,000	2.922
30,000	4.131
100,000	6.418

The sum of the radial and polar velocity vector components are shown in Figure 1 and a contour plot of the magnitude of the corresponding azimuthal velocity components is presented in Figure 2. As the satellite potential is increased from 100 to 100,000 kT this azimuthal velocity component increased especially in the equatorial region. Above 30,000 kT electrons no longer make contact with the surface at the equator.

Acknowledgment

The author is grateful to Dr. Nobie Stone for his hospitality, his suggestion of this problem and for many helpful and stimulating discussions during which the mathematical model was formulated. I also wish to thank Dr. Kenneth Wright and Dr. Scott Boardsen for their assistance with computer coding.
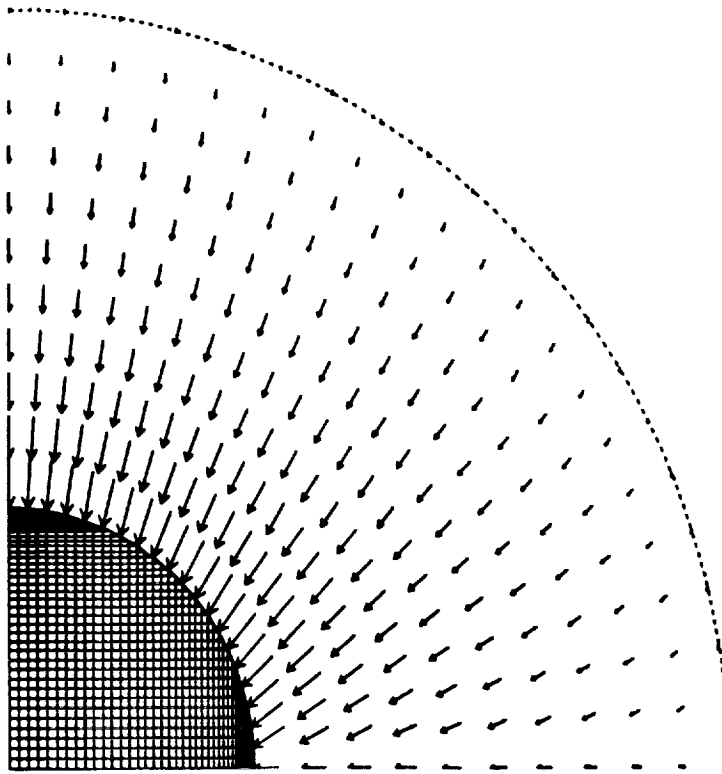
Figure 1. Electron velocity vectors (radial + polar components). V_p = 10,000
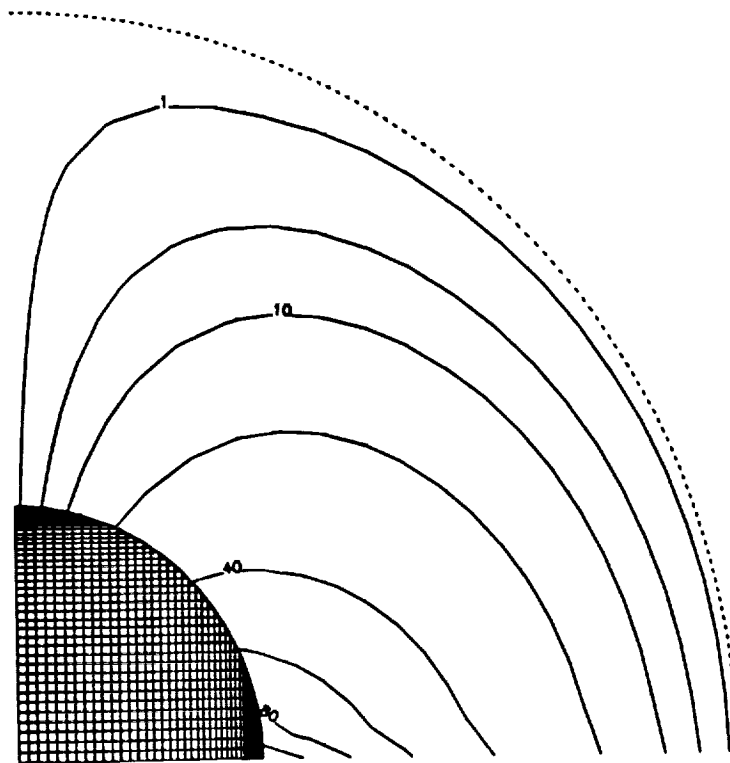

Figure 2. Magnitude of the electron Azimuthal velocity component (in units of

ambient electron thermal velocity). Vp = 10,000

1991

NASA/ASEE SUMMER FACULTY FELLOWSHIP PROGRAM

MARSHALL SPACE FLIGHT CENTER
THE UNIVERSITY OF ALABAMA

GROUP EVAPORATION

Prepared By: Hayley H. Shen, Ph.D.

Academic Rank: Associate Professor

Institution: Clarkson University
                                      Department of Civil and
                                      Environmental Engineering

NASA/MSFC:

       Office: Propulsion Laboratory
       Division: Propulsion Systems
       Branch: Performance Analysis

MSFC Colleague: Charles F. Schafer, Ph.D.

Contract No: NGT-01-008-021
                                      The University of Alabama

Liquid fuel combustion process is greatly affected by the rate of droplet evaporation. The heat and mass exchanges between gas and liquid couple the dynamics of both phases in all aspects: mass, momentum, and energy. Correct prediction of the evaporation rate is therefore a key issue in engineering design of liquid combustion devices. Current analytical tools for characterizing the behavior of these devices are based on results from a single isolated droplet. Numerous experimental studies have challenged the applicability of these results in a dense spray.

To account for the droplets' interaction in a dense spray, a number of theories have been developed in the past decade. These theories were reviewed last summer by the author under the summer faculty fellowship program. Predictions from these theories show significant deviation of the evaporation rate from the single droplet result. Although the applicability of these theoretical results awaits experimental verification, their implementation into CFD codes can already be carried out to assess the magnitude of their effect.

This summer's study was concentrated on two tasks. One was to investigate how to implement the existing theoretical results, the other one was to explore the possibility of experimental verifications.

The current theoretical results of group evaporation are given for a mono-dispersed cluster subject to adiabatic conditions. The time evolution of the fluid mechanic and thermodynamic behavior in this cluster is derived. An example is given in the following figure (Bellan and Cuffel 1983, Fig.5).
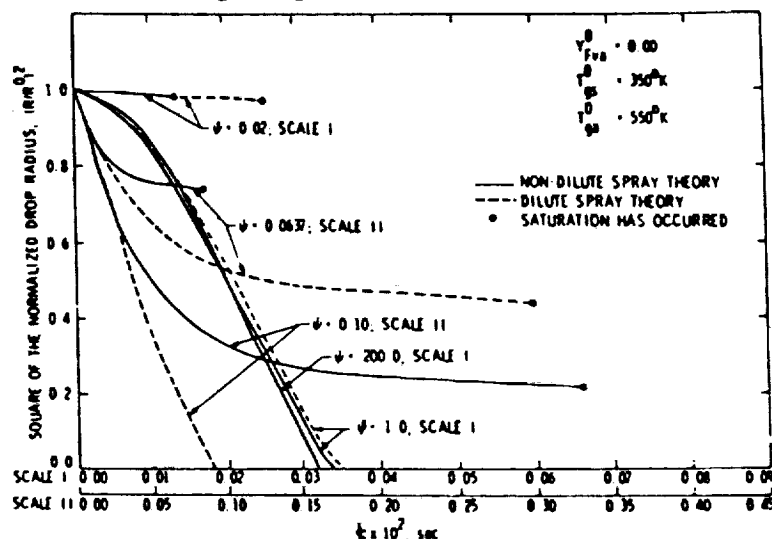

where $Y_{F_g}^0$ is the initial mass fraction of fuel in the gas phase, T_{gs}^0 and T_{ga}^0 are the initial droplet and gas temperatures respectively, and R/R^0 is the ratio of current to initial droplet radius, = air-fuel mass ratio/stoichiometric air-fuel mass ratio.

The above results are not in the form of a subscale model for CFD codes. In CFD codes, the concept requires that in each time step, the evaporation in each computational cell is

determined by the conditions in the cell. However, the conditions in each cell are solved from conservation laws that include the transport of properties among neighboring cells. Therefore, results from the adiabatic conditions in the current theories must be modified to obtain the necessary subscale model. Moreover, the given theoretical results have been obtained from numerical integrations which covered only a small range of parameters as shown in the previous figure. A much broader range of parameters must be derived for application.

Extension of the current theories to cover a wide range of parameters and deriving a subscale model for CFD codes require a longer period of study than a ten-week's work. An approximate solution has thus been derived and utilized in one of the CFD codes. This approach is discussed below.

In the derivation, the superposition principle is utilized. At first, a single droplet evaporation is modeled by setting the boundary conditions at the droplet surface and at the average midpoint between two droplets. The boundary conditions at the droplet surface are from the usual mass and energy balance law, together with the Clausius-Clapeyron relation. The boundary condition at the midpoint is approximated as the superposition of the condition at that location from two non-interacting droplets. This is illustrated in the following figure.
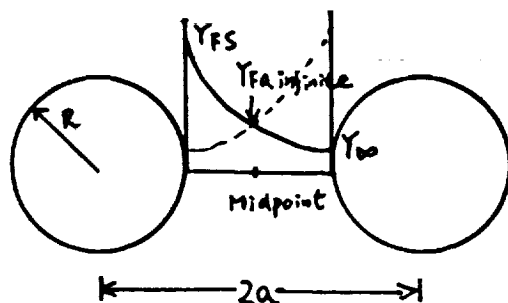
$$Y_{FA\,finite} \simeq 2(Y_{FA\,infinite} - Y_\infty) + Y_\infty$$

$$Y_\infty \simeq Y_{ambient}$$

The result of this approximate solution yields $m/m_0 = 1 - Y_{ambient}R/a$, where m and m_0 are the evaporation rates for a droplet in a cluster and for a single isolated droplet respectively. This result is a first order approximation in terms of $Y_{ambient}$ and R/a.

Since the above formula only depends on the current local information, it can be used as a subscale model to test the effect of group evaporation. However, the average distance "a" between neighboring droplets is not available from current experimental data. Therefore, this formula cannot be utilized at the moment. An estimated distance between droplets is obtained by spreading all droplets equally in the computational cell. Using the mass flow rate and drop size distribution from a pressure-atomized spray, reported by Drallmeier and Peters (1991), the estimated distance between droplets yields $Y_{ambient}R/a = 0.1\%$. Which is too low to produce any effect. This shows that it is very important to obtain the correct constitution of the clusters to evaluate the group evaporation effect.

In order to demonstrate the potential significance of the group effect in spray calculations, a parametric study was carried out utilizing the MAST code, developed by C.P. Chen at UAH. Three different evaporation rates have been used. The spray data given in Drallmeier and Peters (1991) is simulated. The total mass flux downstream from the injector is plotted in the following figure. The evaporation rate utilized to calculated the three curves are assumed to be constant fractions of the evaporation rate for a single isolated droplet. Three different fractions: 1, 0.8, and 0.5 are used.
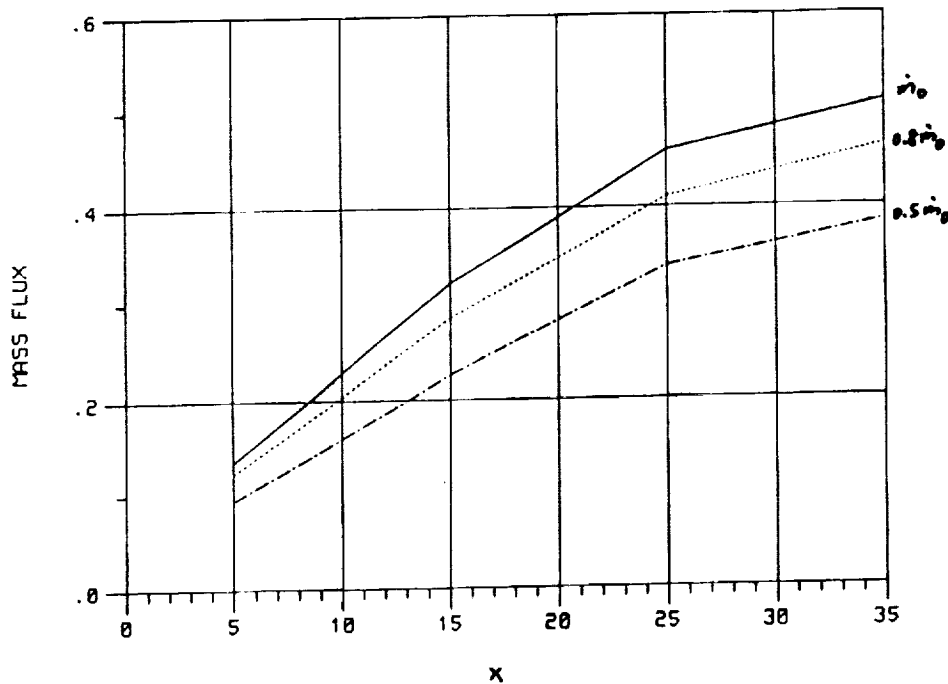
In reality, the farther from the injector, the smaller the drop size, and the smaller the value R/a, while the value $Y_{ambient}$ increases. These characteristics result from the evaporation process. Therefore, the modification of the evaporation rate should not be constant as assumed above. The curves however are valuable for assessing the potential effect of group evaporation. As shown in the above figure, from no group effect to 50% of group effect, the mass flux can deviate by about 30%. Therefore correct account for evaporation in a cluster is important for liquid fuel engine designs. Further analytical work must be initiated to investigate this important mechanism.

Many theoreticians have strongly suggested the need for experimental work to verify their results. However, true spray evaporation is a very difficult phenomenon for accurate measurements. The idealized conditions used in theories, such as uniform, spherical droplets homogeneously distributed in space, are impossible to realize in the laboratory. Thus, even if measurements can be accurately made, the data may be ambiguous for verifying theories.

An alternative technique is proposed. Large crystal growth is a diffusion controlled process, similar to droplet evaporation. The mathematical structure of the two processes are identical in the growth/decay for the case of a single isolated particle. The D^2-t law (D is the particle diameter and t is time), for the rate of growth/decay, has been verified in numerous experimental works for both phenomena. The observation and measurement of crystal growth is comparably much easier than droplet evaporation. Idealized conditions such as uniform, spherical, and homogeneously distributed particles are possible to create for crystal growth. A setup utilizing salt, distilled water, and ice as a temperature controlling material for boundary condition, with a nucleation controlled ice growth in a distilled water bath, is a candidate for such experiment. Comparison of growth rates between a single ice particle and a lattice of ice particles can be used to verify the theoretical prediction of the group evaporation effect.

One difficulty in the proposed experiment is the natural convection effect associated with temperature variation in the material. Such effect is not included in the idealized theoretical model and must be eliminated. From the product $GrPr^2$ (Gr is the Grashof number and Pr is the Prandtl number), which represents the time scale for diffusion vs that of natural convection, it is estimated that the natural convection can be neglected for small temperature gradients and small ice particles. For instance, a temperature difference of $0.01^{\circ}C$ between the distilled water bath and the boundary, and an ice particle growing in the size range of 1mm, yield $GrPr^2 < 1$. Such condition is barely achievable in the laboratory. However, if successful, the potential of such experiment for verifying the convective group evaporation is great. Since in forced convection, the natural convection effect becomes negligible, the above limitation can be relaxed considerably. In spray combustion, forced convection is probably much more dominant. Experimental work in such case is therefore of more practical value.

In conclusion, more analytical work is required to extend the current group evaporation theories for a subscale model to be used in CFD codes. In view of the difficulty in idealized evaporation experiments, large crystal growth is a promising alternative for experimentally studying the group effect. Due to the similarity between droplet evaporation and large crystal growth, results from the group crystal growth may be usable for verifying the theories in group evaporation.

REFERENCES

Bellan, J. and Cuffel, R., Combustion and Flame, 51, 55-67(1983).
Drallmeier, J.A. and Peters, J.E., Atomization and Sprays, 1, 63-88(1991).
Shang, H.M., Chen, C.P., and Jiang, Y., AIAA/SAE/ASME/ASEE 26th Joint Propulsion Conf., paper #90-2422.

1991

NASA/ASEE SUMMER FACULTY FELLOWSHIP PROGRAM

MARSHALL SPACE FLIGHT CENTER

THE UNIVERSITY OF ALABAMA

NICKEL HYDROGEN BATTERY EXPERT SYSTEM

Prepared By: Sajjan G. Shiva

Academic Rank: Professor

Institution: University of Alabama in Huntsville
                       Computer Science Department

NASA/MSFC:

    Laboratory: Information and Electronic Systems
    Division: Electrical
    Branch: Electrical Power

MSFC Colleague: Yvette Johnson

Contract No: NGT-01-008-021
                       The University of Alabama

INTRODUCTION

The Hubble Telescope Battery Testbed at MSFC employes the Nickel Cadmium (NiCd) Battery Expert system (NICBES-2) which supports the evaluation of performance of Hubble Telescope space-craft batteries and provides alarm diagnosis and action advice. NICBES-2 provides a reasoning system along with a battery domain knowledge base to achieve this battery health management function. This report summarizes an effort to modify NICBES-2 to accomodate Nickel Hydrogen (NiH2) battery environment now in MSFC testbed.

The prototype version of NICBES (NICBES-1) was developed by Martin Marietta Corporation. It was implemented in Intel 8086 assembly language, C and Prolog and runs on an IBM PC/AT under the DOS. The current version of NICBES (NICBES-2) is implemented on a Sun Microsystem's 386i running SunOS4.0 (UNIX) and is written in SunOS C and Quintus Prolog. The system now operates in a multitasking environment along with a mouse and window based user interface.

A Digital Equipment Corporation LSI-11 based system sends the battery data to the Sun 386i via an RS-232 connection running at 9600 baud using XON/XOFF control. One telemetry burst is received every 30 seconds. NICBES-2 spawns three child processes: serial port process (SPP), data handler process (DHP) and the expert system process (ESP) in order to process the telemetry data and provide the status and action advise.

When data appears on the serial port, SPP collects it character by character and feeds it into a data pipe. The DHP reads the data pipe and converts the character data into numeric values and reduces the raw telemetry data (by calculating averages and means of various battery parameters) in preparation for use by ESP. ESP is awakened by the user's request for a consult/advice function. Each of the three processes is awakened only when its service is desired and they go to sleep when the function is completed. The SPP has the highest priority among the processes.

In short, NICBES-2 performs orbit data gathering, data evaluation, alarm diagnosis and action advice and status and history display functions.

MODIFICATIONS NEEDED

The adaptation of NICBES-2 to work with Nickel Hydrogen (NiH2) battery environment required modifications to all the three component processes. Although the general format of the telemetry input was retained, the components of the telemetry data are different in the case of NiH2 batteries. As such, the data input routines of SPP needed extensive changes. Because of

the differences in the data collected between the NiCd and NiH2 batteries, all DHP routines required changes. The structure and the reasoning mechanism of ESP remain the same. But the rule base needs to be changed to accomodate the NiH2 battery domain.

STATUS

The modifications to SPP and DHP were completed earlier (4). Some data items in the telemetry (Ampere-hour Out, Time-to-Trickle, Telemetry temperatures and Main and Redundant heater flags) were not utilized earlier. The DHP is now modified to utilize these data.

Modifications to ESP required consultations with NiH2 battery experts to collect the rules appropriate to that domain. Several journal articles reporting on battery test environments were consulted along with the current rules in the NiCd case, to arrive at the rules for NiH2 batteries. An initial rule set is now in the knowledge base.

The rules are utilized by the ESP to provide status and action advise during consultations with it. These functions are based on the data over the last 12 orbits. The alarm conditions are generated by the ESP at every telemetry burst, if the ranges of the data do not conform to the established limits. Thirteen alarm conditions were incuded into the ESP, in addition to the ones that were in the system earlier.

WORK NEEDED

An extensive experimentation is needed to refine the current rule set into an optimum one for the NiH2 batteries.

The data files generated by the system seem to be unnecessarily elaborate, and create disk space shortage in the current system. File structures need to be examined to reduce their size if possible. If not, some of the files may need to be archived on the tape storage.

Several means and averages are now computed at 2 minute intervals (i.e. every 4 samples) rather than every other sample as in NiCad environment. Adequacy of these computation needs to be examined.

Battery health management in general depends on the data collected over a long period of time (years in some cases). As such, the data reduction routines in NICBES-2 should be generalized to expand the range from the current last 12 orbits mode.

The current structure of the system is dependent on 6 batteries and 22 cells per battery. The system need to be generalized to accomodate more general battery environments.

The system at present provides battery management advise only when consulted. The ultimate aim should be to place the system in closed control loop such that the management actions are automatically done.

REFERENCES

1) Bykat, A. "User's Manual for NICBES-2," NAG8-105, NASA/MSFC, Aug.89.
2) Bykat, A. "Program Maintenance Manuals for SPP, DHP and ESP'" NAG8-105, NASA/MSFC, August 89.
3) Bykat, A. "SIRE Manual'" NAG8-105, NASA/MSFC, August 89.
4) Shiva, S. G. "Development of Nickle Hydrogen Battery Expert System," NGT-01-002-099, NASA/MSFC, August 90.

1991

NASA/ASEE SUMMER FACULTY FELLOWSHIP PROGRAM

MARSHALL SPACE FLIGHT CENTER
THE UNIVERSITY OF ALABAMA

Development of a Pressure Based Multigrid
Solution Method for Complex Fluid Flows

Prepared By: Wei Shyy
Academic Rank: Associate Professor
Institution: University of Florida
                       Department of Aerospace Engineering,
                       Mechanics and Engineering Science

NASA/MSFC:

        Office: Structures and Dynamics Laboratory
        Division: Aerophysics
        Branch: Computational Fluid Dynamics

NSFC Colleague: Mr. P. Kevin Tucker

Contract No.:   NGT-01-008-021
                       The University of Alabalma

In spite of the rapid advent of computer technology over the past several decades, in order to be able to deal accurately with the complex flow problems, there is a need for continuous improvement of computational efficiency. With the large number of grid points normally required for practically relevant flows, iterative methods are often used. However, it is well known that for a SOR type of method performed on a single-grid (SG) system, the number of iterations required typically increases in proportion to the number of grid points. Since the CPU time on a per iteration basis scales with the number of grid points, the grid resolution typically required for satisfactorily solving an incompressible recirculating flow problem would need substantial computational time even on supercomputers. In order to reduce this difficulty associated with the SG solution procedure, the multigrid (MG) technique has been identified as a very useful means for improving the convergence rate of iterative methods.

The multigrid technique, originally developed for the efficient solution of linear, elliptic differential equations, has been used in the field of computational fluid dynamics with increasing popularity. Successes have been reported for both compressible and incompressible flows. However, it is not until more recently that attempts have been reported, with varying degrees of success, on the application to incompressible recirculating flows with primitive variables. Substantial differences exist between the basic numerical algorithms embodied in those studies, notably the way the pressure field is obtained, the choice of the convection scheme, and the design of the grid layout for the velocity and pressure variables. Generally speaking, two methods have been developed for obtaining the solution field, namely, the decoupled method, and the coupled method. In the decoupled method, a two-level iterative procedure is usually employed; one is the outer iteration needed to progressively update different partial differential equations , and the other is the inner iteration devised to solve the system of linear algebraic equations resulting from the discretization procedures of each partial differential equation with other variables remaining unchanged. Within the outer iteration, for a two-dimensional flow with u, v, and p as the dependent variables for example, a cyclic outer iterative procedure is designed to sequentially solve, say, the linearized x-momentum equation first, the linearized y-momentum equation next, and the pressure (correction) equation last. After sweeping through all three equations to obtain partially converged solutions, the x-momentum equation is again invoked to initiate a new cycle, until all three equations are satisfactorily solved. Within the inner iteration, say, the x-momentum equation is discretized and linearized, and the resulting set of linear equations is then solved by an iterative procedure such as the LSOR method till the prescribed number of iterations or the convergence criterion has been reached. For a decoupled algorithm, the treatment of coupling among the dependent variables, such as velocity and pressure, is critical to the overall convergence. Hence, the performance of this type of method depends on such factors as the Reynolds number and the distribution and skewness of the grid in sensitive manners.

In contrast, a coupled method, which solves the velocity vector and the scalar variables at a point, line, or plane simultaneously, usually shows robust performance with respect to parameters such as the Reynolds number. In the context of Cartesian coordinates, the

coupled method is also found to be relatively insensitive to the number of the grid points employed. With the use of curvilinear coordinates, however, the situation is not as favorable, since, depending on the characteristics of the grid skewness, one either has to treat the cross-derivative terms explicitly as source term or solve equations whose coefficient matrix is no longer sparse. Furthermore, from the viewpoint of developing generic computational capabilities for flows involving different physical mechanisms such as turbulence, heat transfer, combustion, and phase change, it is preferable that one does not have to redo the algorithm for a different number of partial differential equations. In this regard, the decoupled method has a clear advantage since it can handle a different number of equations in more a flexible manner. It is with this motivation that in the present work a multigrid method in curvilinear coordinates is developed in conjunction with a basic flow solver reported in Refs [1,2], which utilizes a decoupled algorithm to solve incompressible recirculating flow problems.

A full multigrid /full approximation storage (FMG/FAS) algorithm is utilized to solve the incompressible recirculating flow problems in complex geometries. The algorithm is implemented in conjunction with a pressure-correction/staggered-grid type of technique using the curvilinear coordinates. In order to illustrate the performance of the method, two flow configurations, one a square cavity driven by a sliding top wall and the other a channel with multiple bumps are used as the test problems. Comparisons are made between the performances of the multigrid and single-grid methods, measured by the number of fine grid iterations, equivalent work units, and CPU time. Besides demonstrating that the multigrid method can yield substantial speed-up with wide variations in Reynolds number, grid distributions, and geometry, issues such as the convergence characteristics at different grid levels, the choice of convection schemes, and the effectiveness of the basic iterative smoothers are studied. An adaptive grid scheme is also combined with the multigrid procedure to explore the effects of grid resolution on the multigrid convergence rate as well as the numerical accuracy. A full account of the technique developed along with illustrative results can be found in Ref [3]. Two figures shown here give a depiction of the grid cycle adopted and a sample of the comparison of the relative performance of the method developed.

References

[1]   W. Shyy, S.S. Tong and S.M. Correa, "Numerical Recirculating Flow Calculation Using Body-Fitted Coordinate System," Numer. Heat Transf., vol. 8, 1985, pp. 99-113.

[2]   M.E. Braaten and W. Shyy, "A Study of Recirculating Flow Computation Using Body-Fitted Coordinates:Consistency Aspects and Mesh Skewness," Numer. Heat Transf., Vol. 9, 1986, pp. 559-574.

[3]   W. Shyy and C.-S. Sun, "Development of a Pressure-Correction/Staggered-Grid Based Multigrid Solver for Computing Incompressible Recirculating Flows," AeMES Technical Report, University of Florida, Dept. of Aerospace Engineering, Mechanics and Engineering Science, 1991.
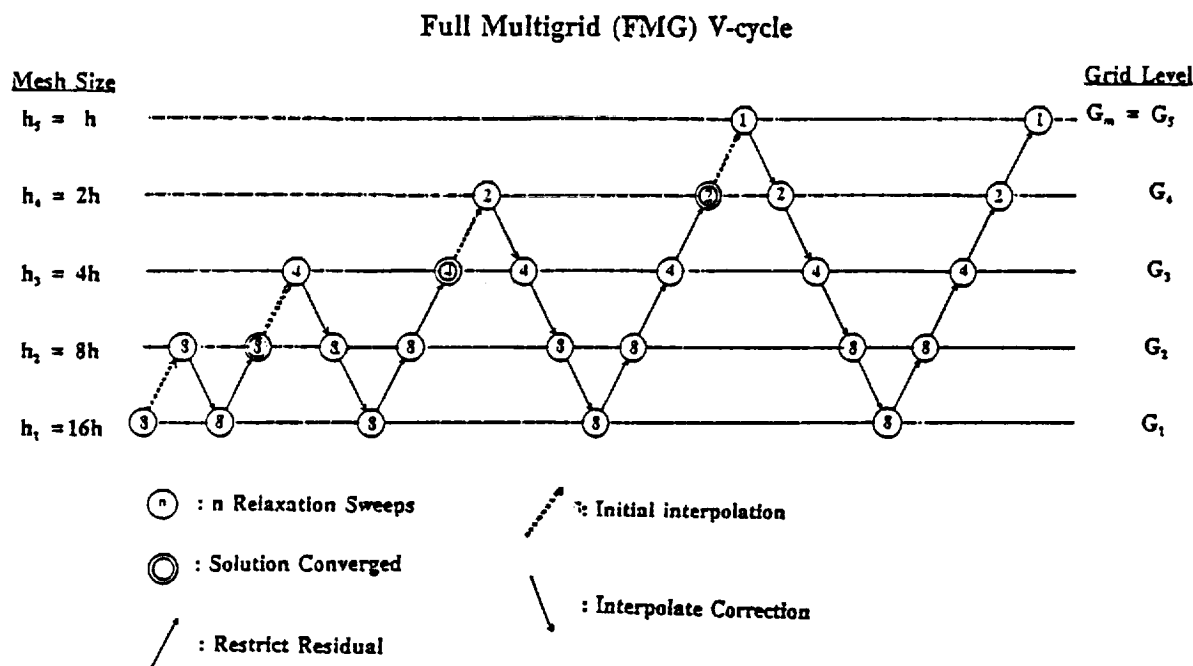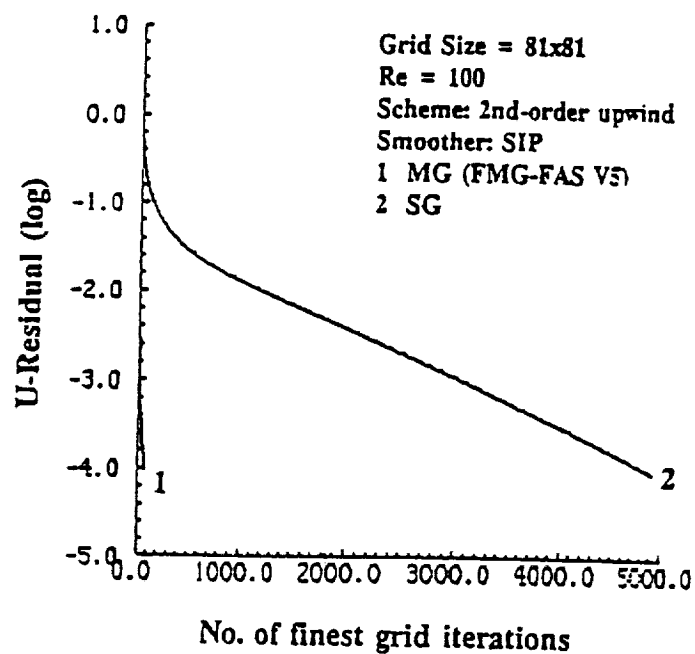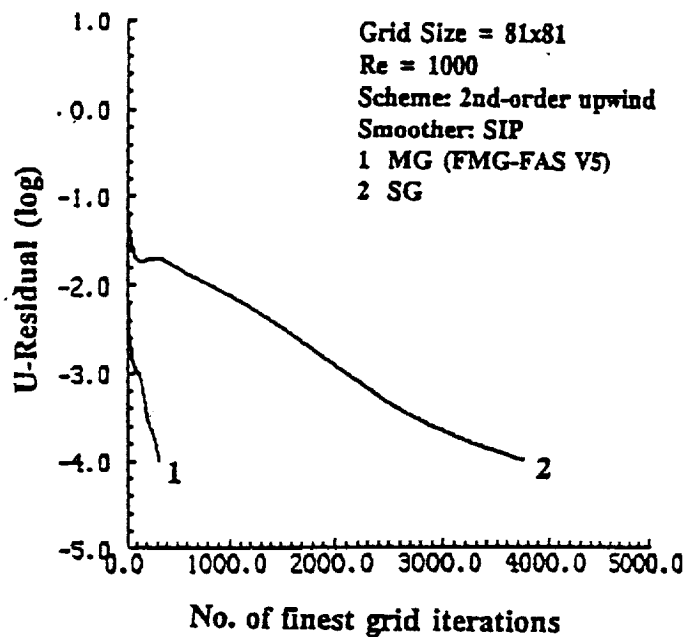
Full Multigrid (FMG) V-cycle

Fig. 1   A full multigrid (FMG) procedure with fixed V-cycles
         M = 5 grid levels.

(a) Re = 100

(b) Re = 1000

Fig. 2 Comparison of convergence rates between multigrid and single-grid solvers on 81x81 grid with SIP as smoother for cavity flow with (a) Re =100, (b) Re = 1000, and second-order upwind convection scheme.

QQ-4

1991

NASA/ASEE SUMMER FACULTY FELLOWSHIP PROGRAM

MARSHALL SPACE FLIGHT CENTER
THE UNIVERSITY OF ALABAMA IN HUNTSVILLE

A HIGH-FIDELITY N-BODY EPHEMERIS GENERATOR
FOR SATELLITES IN EARTH ORBIT

Prepared By: David R. Simmons, Ph.D.

Academic Rank: Professor

Institution: Louisiana College
                                 Department of Mathematics
                                 and Computer Science

NASA/MSFC:
        Office: Systems Analysis and
                                 Integration Laboratory
        Division: Mission Analysis
        Branch: Flight Mechanics

MSFC Colleague: Larry Mullins, Ph.D.

Contract No.:   NGT-01-008-021
                                 The University Of Alabama
                                 In Huntsville

Description of the Project

The Flight Mechanics Branch is currently using a program for mission planning called the Analytic Satellite Ephemeris Program (ASEP). This program, written by Jim McCarter, produces projected data for orbits that remain fairly close to the Earth; ASEP does not take into account lunar and solar perturbations. These perturbations are accounted for in another program called GRAVE, written several years ago by Roger Burrows. This project is a revision of GRAVE which incorporates more flexible means of input for initial data, provides additional kinds of output information, and makes use of structured programming techniques to make the program more understandable and reliable.

Work Done during Summer 1990

David Simmons wrote the FORTRAN program ORBIT during the first summer; the SAIL1 VAX system was used to develop the program. In keeping with structured programming concepts, the program is divided into numerous sub-programs, each with a well-defined task to perform. The text of the source code for one sub-program can usually be printed on a page or less. Most of the variable names are whole words or short phrases which clearly identify the nature of the variable and its role in the program.

ORBIT is divided into three major phases: initialization, integration, and output. During the linking process, the block data subprogram, Load_Common, gives initial values to the key variables in COMMON. Later during the initialization phase, the Get_Parameter subroutine uses tree-structured menus to give users an opportunity to change the starting and ending times, output defaults and state vectors. Get_Parameter can change any of the three forms of state vector (cartesian, spherical-polar, and osculating orbital elements) that are used in the program; the other forms are always re-calculated to conform to the new one. Get_Parameter also provides for the selection of the kind of output to be provided.

The integration phase of the program calculates new values for the elapsed time and the cartesian state vector describing the motion of the satellite. This section of the program follows the GRAVE program very closely. The Encke method is used; subroutine COAST calculates a position along the osculating ellipse from the current position; this position is used by the subroutine DEQG for the calculation of both gravitational and atmospheric forces. DEQG is called by RKG, a general routine for solving first-order differential equations; RKG uses Fehlberg's 13-step version of the Runge-Kutta method. RKG is used in ORBIT with no change from its previous form. COAST has a very tangled structure; Simmons found it necessary to split it into subroutines based on its syntax rather than on its meaning. On the other hand, DEQG has been split into sub-programs in a natural and well-structured way.

ORBIT produces a complete set of output data before the beginning of the integration, and after the end. The user of the program can select an option to generate time and state-vector information on each step of the integration. The integration phase of the program uses the Cartesian form of the state vector, which is assumed to be relative to an inertial reference system. A spherical-polar state vector and a set of osculating elements are calculated for the output phase by a set of routines organized through a master routine called UpDate_Common. These subroutines also adjust various lunar, solar, and time-related variables that are maintained in COMMON. A set of routines controlled by a subroutine called Report_State then display those values and calculate other values which are also displayed. Another user option is to have the displayed values stored in a file.

ORBIT makes either direct or indirect use of about a score of special-purpose routines already available in the MSFC computer systems, along with modified versions of the DEQG and COAST routines from the GRAVE program. It would not have been possible to complete this project in ten weeks if all these routines had not been available. The use of these routines should also make it easier for MSFC personnel who are already familiar with them to understand this program.

Work Done during Summer 1991

The CRRES satellite was launched in July 1990; its orbit has an eccentricity of about 0.71 which made it a very suitable choice for testing the ORBIT program against real data. By summer 1991 there was data available from NORAD for 313 days. Some problems became evident when the program output was compared with this data.

On each output cycle a subroutine calculated a value for the radius of the earth in kilometers; this was stored in a variable named EarthRadius. The same variable name was used in COMMON for the radius of the earth in meters; one of the integration routines used this radius to compute the perturbations due to the oblateness of the earth. Since the radius was too small by a factor of a thousand, the oblateness effects were reduced to insignificance.

The subroutine used to calculate atmospheric effects had one formal argument, the vector acceleration to be modified. The routine which called it, however, used two actual arguments, the cartesian state vector and the acceleration. The result was that the cartesian state was very slightly modified and the vector acceleration was not modified at all; the orbit did not decay as it should.

The 1990 version of the program had an option to print (or save in a file) basic state vector information after every integration step. This was usually too often, so it was modified to produce output on the next integration step after a specified length of time had passed. Since the step size is not likely to be a rational fraction of the orbital period, and since the RKG routine changes the time increment as the integration proceeds, the orbital position at which output occurred had a slight and apparently random variation. This effect was more irritating than serious, but it was eliminated by restructuring the main program. The integration process inherited from GRAVE.FOR adjusts the step size at the end to reach the specified final time. This process is now encapsulated in a subroutine which has a goal time as its only argument. This subroutine is called in a loop in which the goal time is successively set to desired output times.

Since the orbit is not a simple two-body orbit, the values of the osculating elements depend slightly on the position in the orbit at which they are calculated. In particular, there is a relatively sharp increase in the semi-major axis at perigee. If the data are reported at equal time intervals, the mean anomaly drifts around the orbit. Each time the mean anomaly passes through perigee, the output values of the semi-major axis rise and then fall. This effect also appears in the NORAD data, since they are calculated at the ascending node, and the perigee moves slowly around the orbit. Two options to report results at specified times were added to the program in reaction to these problems: at the ascending node, and at a specified value of the mean anomaly.

The program now employs an exponential atmospheric model, which gives good results when compared with the tracking data. The source program has now been incorporated into three files: ORBIT.FOR, ORBIT.INCL, and a file for the block data subprogram, which will vary from mission to mission.

Conclusion

ORBIT has now been tested against tracking data for the first 313 days of operation of the CRRES satellite. A sample graph is given comparing the semi-major axis calculated by the program with the values supplied by NORAD. When calculated for points at which CRRES passes through the ascending node, the argument of perigee, the right ascension of the ascending node, and the mean anomaly all stay within about a degree of the corresponding values from NORAD; the inclination of the orbital plane is much closer. The program value of the eccentricity is in error by no more than 0.0002.

It is characteristic of computer programmers never to be completely satisfied with their productions; some improvements are possible. However, both Mullins and Simmons are convinced that ORBIT is accurate and that it is ready for operational use.
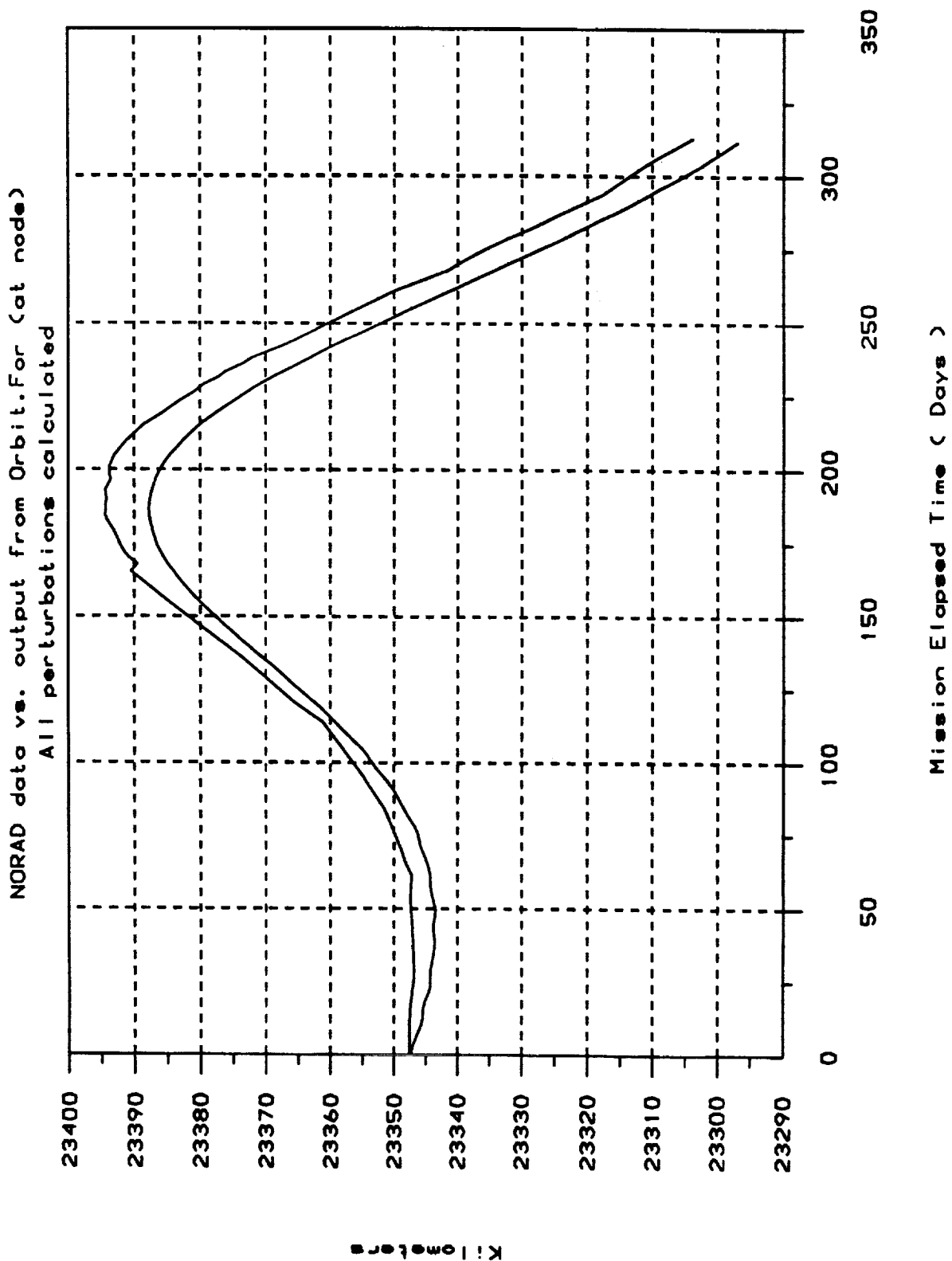
References

Roger Burrows, MSFC: GRAVE.FOR (1985-1988)

J. M. A. Danby: Fundamentals of Celestial Mechanics, 2nd ed.

Larry Mullins, MSFC Course 4181: General Description of Orbits

Accompanying Figure: CRESS Semi-Major Axis

CRRES Semi-Major Axis 2 August 1991 15:45

NORAD data vs. output from Orbit.For (at node)
All perturbations calculated

Mission Elapsed Time (Days)

Kilometers

RR-5

1991

NASA/ASEE SUMMER FACULTY FELLOWSHIP PROGRAM

MARSHALL SPACE FLIGHT CENTER
THE UNIVERSITY OF ALABAMA IN HUNTSVILLE

A STATISTICAL MODEL OF CARBON/CARBON COMPOSITE FAILURE

Prepared By:	Kerry T. Slattery, Ph.D.
Academic Rank:	Assistant Professor
Institution:	Washington University in St. Louis, Department of Civil Engineering

NASA/MSFC

Office:	Materials and Processes Laboratory
Division:	Non-Metallic Materials
Branch:	Ceramics & Coatings
MSFC Colleague:	R.G. Clinton, Ph.D. Roy Sullivan, Ph.D.
Contract No.:	NGT-01-008-021 The University of Alabama in Huntsville

The availability of modern filamentary composite materials for engineering design have provided tremendous opportunities for greatly improved performance. The most frequently cited advantage over conventional metallic materials is their high specific strength and stiffness. Unidirectional strengths of graphite/epoxy composites typically exceed those of high-strength steels with similar stiffness at only one-fifth of the weight. Other potential advantages over metals are corrosion resistance, radar transparency, and improved fatigue performance. One of the primary problems with using composites is that there is still little experience with these materials when compared with metals. This problem is compounded by the fact that the response of composites and their failure mechanisms are much more complex that those of metals.

Failure in filamentary composite materials involves a complex damage accumulation process. The material has randomly dispersed initial flaws in all phases: the fiber, the matrix, and the fiber/matrix interface. As load is applied the flaws grow and coalesce until some critical damage state is formed which results in failure. Most popular failure theories [2] frequently depend upon some anisotropic, distortional energy formulation. This type of approach is very useful in predicting yielding in metals but is not consistent with the mechanisms of failure in composites -- they do not yield in the same sense as metals! Of course, reasonable results can be obtained if the parameters of the model are adjusted based upon experimental data, but these approaches give very little insight into the failure mechanisms and are even less useful in understanding the statistical properties of the strength results. A failure model which considers the stochastic nature of the damage accumulation process is essential to assess reliability and to accurately scale the results from standard test specimens to composite structures.

A superior filamentary composite for high temperature applications is composed of carbon fibers in a carbon matrix. Carbon/carbon composites are the strongest known materials at very high temperatures. Three-dimensionally woven carbon/carbon composites have been used in nozzle components in several tactical missile systems because they exhibit lower erosion than carbon/phenolic composites. Carbon/carbon was also considered for the Advanced Solid Rocket Motor (ASRM) for the Space Shuttle. Among the reasons for not selecting this technological advance was that the carbon/carbon ITE was considered to be a structural component which was required to demonstrate a safety factor of 1.4 for a man-rated system. Available strength data and analysis techniques were inadequate to demonstrate this factor. The fact that the carbon/carbon ASRM ITE would have been much larger than any currently used carbon/carbon nozzle component raised additional concerns. More data on carbon/carbon strength and improved analysis techniques are required to properly analyze these designs.

Possibly the best source of data for carbon/carbon strength in circularly woven parts is from the qualification test rings from

billets for the first stage of the Navy D-5 missile program manufactured by Textron Specialty Materials. Two tensile test rings were machined from one end of each billet and pressurized internally to determine the hoop strength of the composite. The magnitude of the strengths of these rings varied over a wide range of values. The rings which passed the qualification test were sent to NASA/MSFC in order to study the failure modes in an attempt to gain a better understanding of the scatter in the data. The first step in the analysis was to determine the effect of defects on the strength of the rings. Photographs were taken of both sides of the damaged region in all tensile rings. X-ray and CT scan investigations were also conducted on some of the rings to determine the utility of these methods in assessing significant defects. There was some correlation between strength and defects which could be reasonably easily detected using available methods, but most of the data scatter could not be explained by the presence of observable flaws.

Since there appears to be a significant randomness in carbon/carbon material strength which cannot be controlled or detected with current technology, a better model of the material failure based upon statistical principles should be employed. Such a model was developed. Simple applications of the model based upon the limited available data provide encouraging results that indicate that better design of test specimens would provide a substantially higher prediction for the design (A-basis) strength of carbon/carbon composites. Future test programs should consider size effects and defects caused by machining.

An A-basis strength for the carbon/carbon tensile rings from the first stage D-5 billets has been estimated. A statistical failure model has been developed for these rings which indicates that this strength may be very conservative for larger carbon/carbon parts. The results of these qualification tests still don't address the fundamental problem of failure in rocket nozzle components since they don't match the actual loading conditions. A better analysis technique which begins with the statistical distribution of fundamental constituent material properties would produce the ability to compare "apples to apples." A possible framework for improving the analysis would be a heterogeneous/non-continuum finite element approach on the mini-mechanical level similar to that used by Slattery and Hackett [1] on the micromechanical level.

PLEASE NOTE: Information on carbon/carbon composite materials is considered to be sensitive technology subject to export restrictions. This report was reviewed by the Research and Technology office at MSFC to preclude the release of sensitive information. A complete report was given to MSFC colleagues.

REFERENCES

1. Slattery, K.T. and R.M. Hackett, "Computational Simulation of the Creep-Rupture Process in Filamentary Composite Materials," Journal of Reinforced Plastics and Composites, 10-2 (1991) 184-197.

2. Soni, S.R., "A New Look at Commonly Used Failure Theories in Composite Laminates," AIAA, 1983, 171-179.

NASA / ASEE SUMMER FACULTY FELLOWSHIP PROGRAM

MARSHALL SPACE FLIGHT CENTER

THE UNIVERSITY OF ALABAMA IN HUNTSVILLE

TRANSPORT OF PHOTONS PRODUCED BY LIGHTNING IN CLOUDS

Prepared by: Richard Solakiewicz
Academic Rank: Assistant Professor

University and Department: Chicago State University
                                   Department of Mathematics
                                   and Computer Science

NASA / MSFC:
    Laboratory: Space Science
    Division: Earth Sciences /Applications
    Branch: Remote Sensing

MSFC Colleagues: William Koshak
                                   Richard Blakeslee
                                   Hugh Christian

Contract Number   NGT-01-008-021

The optical effects of the light produced by lightning are of interest to atmospheric scientists for a number of reasons (4,7,13). We mention two techniques used to explain the nature of these effects: Monte Carlo simulation (13) and an equivalent medium approach (10). In the Monte Carlo approach, paths of individual photons are simulated; a photon is said to be scattered if it escapes the cloud, otherwise it is absorbed. In the equivalent medium approach, the cloud is replaced by a single obstacle whose properties are specified by bulk parameters obtained by methods due to Twersky. See Phanord (10) for references.

In this report, we use Boltzmann transport theory to obtain photon intensities. The photons are treated like a Lorentz gas. We consider only elastic scattering and neglect gravitational effects. Water droplets comprising a cuboidal cloud are assumed to be spherical and homogeneous. Furthermore, we assume that the distribution of droplets in the cloud is uniform and that scattering by air molecules is negligible. The time dependence and five dimensional nature of this problem make it particularly difficult; neither analytic nor numerical solutions are known (3).

We begin with the single speed Boltzmann transport equation (3)

$$\frac{\partial I}{\partial t} = -c\hat{\Omega} \cdot \nabla I + \frac{c}{4\pi} K \omega_0 \int \mathcal{P} I d\Omega' - K c I + c s, \quad I = I\left(\mathbf{r}, \hat{\Omega}, t\right), \quad [1]$$

where I is the photon intensity which depends on position $(\mathbf{r})$, velocity direction $\left(\hat{\Omega}\right)$, and time (t). Inside the integral, I is considered a function of $\hat{\Omega}'$. Here, c is the speed of light, $K = 1/\Lambda$, where Λ is the mean free path, ω_o is the single scattering albedo, $\mathcal{P} = \mathcal{P}\left(\hat{\Omega}' \cdot \hat{\Omega}\right)$ is the scattering phase function, and s is a source term. The intensity in a volume V bounded by a surface S is uniquely determined by the initial intensity in V, the sources in V, and the intensity incident on S (1).

In order to reduce the number of dimensions, we use the P_N approximation (1,3). The intensity, phase function, and source term are all expanded in series of spherical harmonics $Y_n^m\left(\hat{\Omega}\right) = P_n^m(\cos\theta)e^{im\phi}$; $\hat{\Omega} = \hat{\Omega}(\theta, \phi)$;

$$I\left(\mathbf{r}, \hat{\Omega}, t\right) = \sum b_n^m Y_n^m\left(\hat{\Omega}\right), \quad b_n^m = b_n^m(\mathbf{r}, t), \quad \sum \equiv \sum_{n=0}^{\infty} \sum_{m=-n}^{n}; \quad [2]$$

$$s = \sum s_n^m Y_n^m\left(\hat{\Omega}\right).$$

The addition theorem for spherical harmonics (12) allows us to write

$$\mathcal{P}\left(\hat{\Omega}' \cdot \hat{\Omega}\right) = \sum (-1)^m d_n Y_n^{-m}\left(\hat{\Omega}'\right) Y_n^m\left(\hat{\Omega}\right). \quad [3]$$

In particular, if we use the Henyey- Greenstein function (14), $d_n = (2n+1)g^n$, where g is the asymmetry factor. The integral in [1] may be evaluated using orthogonality. The advection term of contains an inner product of $\hat{\Omega}$ and a gradient which we may write as

$$\hat{\Omega} \cdot \nabla \equiv \sin\theta\cos\phi\frac{\partial}{\partial x} + \sin\theta\sin\phi\frac{\partial}{\partial y} + \cos\theta\frac{\partial}{\partial z}. \quad [4]$$

We absorb the trigonometric functions into the spherical harmonics comprising I with the aid of the recurrsion relations for the Legendre functions (9) and orthogonality is used to obtain the coupled set of partial differential equations,

$$-\frac{1}{c}\frac{\partial b_n^m}{\partial t} = \frac{1}{2(2n-1)}\Delta^* b_{n-1}^{m-1} + \left(\frac{n-m}{2n-1}\right)\frac{\partial}{\partial z}b_{n-1}^m - \frac{(n-m+1)(n-m)}{2(2n-1)}\Delta b_{n-1}^{m+1}$$

$$-\frac{1}{2(2n+3)}\Delta^* b_{n+1}^{m-1} + \frac{(n+m+1)}{2(2n+3)}\frac{\partial}{\partial z}b_{n+1}^m + \frac{(n+m+1)(n+m+2)}{2(2n+3)}\Delta b_{n+1}^{m+1} \qquad [5]$$

$$+K\left(1 - \frac{\omega_0 d_n}{2n+1}\right)b_n^m - s_n^m; \quad \Delta \equiv \frac{\partial}{\partial x}+i\frac{\partial}{\partial y}, \quad \Delta^* \equiv \frac{\partial}{\partial x}-i\frac{\partial}{\partial y},$$

where any function b_n^m with $m > n$ or $n < 0$ is identically zero.

We work with a truncated version of [5] motivated by the Eddington approximation (2), $b_n^m = 0$ for $n \geq 2$. Using the notation $b_0^0 = f_1$, $b_1^1 - \frac{b_1^{-1}}{2} = f_2$, $i\left(b_1^1 + \frac{b_1^{-1}}{2}\right) = f_3$, $b_1^0 = f_4$, we have

$$\frac{1}{c}\frac{\partial f_1}{\partial t} + \beta_0 K f_1 = -\frac{1}{3}\left(\frac{\partial f_2}{\partial x}+\frac{\partial f_3}{\partial y}+\frac{\partial f_3}{\partial z}\right)+s,$$

$$\frac{1}{c}\frac{\partial f_2}{\partial t}+\beta_1 K f_2 = -\frac{\partial f_1}{\partial x}, \quad \frac{1}{c}\frac{\partial f_3}{\partial t}+\beta_1 K f_3 = -\frac{\partial f_1}{\partial y}, \quad \frac{1}{c}\frac{\partial f_4}{\partial t}+\beta_1 K f_4 = -\frac{\partial f_1}{\partial z}, \qquad [6]$$

$$\beta_n = 1 - \frac{\omega_0 d_n}{2n+1}, \quad s = s_0^0,$$

where we have assumed that $s_n^m = 0$, $n \geq 1$. This truncation does not constitute a consistent solution to the transport equation, a fact implicit in (2,5,6) and explicit in (1). Orthogonality may be used to produce an additional five equations which are neglected.

The conditions at an interface between a convex cloud and a vacuum are given by (1,3)

$$I\left(\vec{\rho}, \hat{\Omega}, t\right) = 0, \quad \hat{\Omega}\cdot\hat{n} < 0, \qquad [7]$$

where $\vec{\rho}$ is a position vector on the cloud's boundary and $\hat{n}$ is the outward normal. Physically, this condition corresponds to the requirement that for convex cloud geometries, photons which escape the cloud cannot reenter. With the simplified representation given by the Eddington approximation, it is generally impossible to satisfy [7] exactly. The condition usually used is the Marshak boundary condition (1,2,3,5,6),

$$F_n = -\int_{\hat{\Omega}\cdot\hat{n}<0} \hat{\Omega}\cdot\hat{n}I\left(\vec{\rho}, \hat{\Omega}, t\right)d\Omega = 0, \qquad [8]$$

where F_n is the irradiance in the direction $\hat{n}$. The integral of F_n over a portion of the interface yields the number of photons reentering the cloud through that portion.

Consider a plane surface separating the cloud and the region outside with normal $\hat{n}$. Since we may take the area to be vanishingly small and still require that no photons reenter through this surface, [8] may be rewritten as

$$\int\limits_{0}^{2\pi} d\phi_n \int\limits_{\frac{\pi}{2}}^{\pi} d\theta_n \sin\theta_n \cos\theta_n I[\theta,\phi] d\Omega = 0, \qquad [9]$$

where $I[\theta,\phi]$ is evaluated on the cloud boundary and θ_n is measured from $\hat{n}$ considered as a polar axis. An appropriate rotation of coordinates yields the condition

$$f_1 = \frac{2}{3}(n_x f_2 + n_y f_3 + n_z f_4), \quad \hat{n} = n_x \hat{x} + n_x \hat{y} + n_x \hat{z} \qquad [10]$$

on an interface. This form is valid for any convex shape and is a generalization of a similar condition given by Davies (3).

We use Laplace transforms in [6] and obtain

$$k^2 F_1 = \nabla^2 F_1 + T, \quad k^2 \equiv 3\left(\beta_0 K + \frac{s}{c}\right)\left(\beta_1 K + \frac{s}{c}\right), \quad T \equiv 3\left(\beta_1 K + \frac{s}{c}\right)\left(\frac{f_1(0)}{c} + S\right), \qquad [11]$$

where s is the transform variable, F_1 and S are the Laplace transforms of f_1 and s respectively, $f_1(0)$ is the initial value of f_1, and we have assumed that $f_2 = f_3 = f_4 = 0$ at $t = 0$. The boundary condition becomes

$$\frac{\partial F_1}{\partial n} + h F_1 = 0, \quad h = \frac{3}{2}\left(\frac{s}{c} + \beta_1 K\right). \qquad [12]$$

We consider a cuboidal cloud centered at the origin with boundaries coinciding with $x = \pm\frac{\alpha}{2}$, $y = \pm\frac{\beta}{2}$, $z = \pm\frac{\gamma}{2}$. Equations [11,12] are solved using finite Fourier transforms (14) to obtain

$$F_1 = \sum_{p,q,r} \frac{8h^3 T \cos\xi_p x \cos\eta_q y \cos\nu_r z}{\left(\alpha h + 2\sin^2\frac{\alpha}{2}\xi_p\right)\left(\beta h + 2\sin^2\frac{\beta}{2}\eta_q\right)\left(\gamma h + 2\sin^2\frac{\gamma}{2}\nu_r\right)\left(k^2 + \xi_p^2 + \eta_q^2 + \nu_r^2\right)}, \qquad [13]$$

where T is the finite Fourier transform of T and ξ_p, η_q, ν_r are the roots of

$$\tan\frac{\alpha}{2}\xi_p = \frac{h}{\xi_p}, \quad \tan\frac{\beta}{2}\eta_q = \frac{h}{\eta_q}, \quad \tan\frac{\gamma}{2}\nu_r = \frac{h}{\nu_r} \qquad [14]$$

with positive real parts.

Due to the transcendental nature of the functions defined by [14], it is necessary to resort to numerical methods. Fortunately, it is possible to approximately invert Laplace transforms with a knowledge of $F_1(s)$, $s = 1,2,3,\ldots$. Complete details are provided in Lanczos (8).

Once f_1 is known, f_2, f_3, f_4 may be found using [6]. The photon intensity at a point outside of the cloud in a direction $\hat{\Omega}$ may be traced back to its value on the cloud's surface at an earlier time t' (1), i.e., $I\left(\mathbf{r}, \hat{\Omega}, t\right) = I\left(\mathbf{r} - c\hat{\Omega}(t - t'), \hat{\Omega}, t'\right)$, where t' is chosen so that $\mathbf{r} - c\hat{\Omega}(t - t') = \vec{\rho}$.

We are presently working on implementing the algorithms described above and on a numerical procedure which is not limited to the Eddington approximation. We intend to generalize the results to other cloud shapes and compare results with existing Monte Carlo simulations as well as with results using an equivalent medium approach.

ACKNOWLEDGMENT

REFERENCES

1. Case, K.M. and Zweifel, R.E., *Linear Transport Theory*, Addison Wesley, Mass. (1967).
2. Davies, R., "The effect of finite geometry on the three-dimensional transfer of solar radiation in clouds", *J. Atmos. Sci.*, 35 (1978) 1712–1725.
3. Duderstadt, J. J. and Martin, W.R., *Transport Theory*, Wiley, NY (1979).
4. Ebel, D. M. and McKee, T.B., "Diurnal radiance patterns of finite and semi-infinite clouds in observations of cloud fields", *J. Clim. Appl. Met.*, 22 (1983) 1056–1064.
5. Harshvardhan and Weinman, J. A., "Infrared radiative transfer through a rectangular array of cuboidal clouds", *J. Atmos. Sci.*, 39 (1982) 431–439.
6. Harshvardhan, Weinman, J. A., and Davies, R., "Transport of infrared radiation in cuboidal clouds", *J. Atmos. Sci.*, 38 (1982) 2500–2513.
7. Koshak, W., "Analysis of lightning field changes produced by florida thunderstorms", NASA Technical Memorandum, NASA TM-103539 (1991).
8. Lanczos, C., *Applied Analysis*, Prentice-Hall, NJ (1956).
9. Morse, P. M. and Feshbach, H., *Methods of Theoretical Physics*, McGraw Hill, NY (1953).
10. Phanord, D. D., "Analytical optical scattering in clouds", NASA Report NASA CR-184044, (xxxvi) (1990).
11. Sneddon, I. N., *Fourier Transforms*, McGraw Hill, NY (1951).
12. Stratton, J., *Electromagnetic Theory*, McGraw Hill, NY (1941).
13. Thomason, L. W. and Krider, E. P., "The effect of clouds on the light produced by lightning", *J. Atmos. Sci.*, 39 (1982) 2051–2065.
14. van de Hulst, H. C., *Multiple Light Scattering, Tables, Formulas, and Applications*, Academic Press, NY (1980).

1991

NASA/ASEE SUMMER FACULTY FELLOWSHIP PROGRAM
MARSHALL SPACE FLIGHT CENTER
THE UNIVERSITY OF ALABAMA

RELIABILITY GROWTH MODELS FOR NASA APPLICATIONS

Prepared By: Vidya S. Taneja, Ph.D.
Academic Rank: Professor
Institution: Western Illinois University
                               Department of Mathematics

NASA/MSFC:
Office: System Safety & Reliability
Division: Reliability & Maintain-
                               ability Engineering
Branch: Analysis

MSFC Colleague: Fayssal M. Safie, Ph.D.
                               William C. Smith
                               Frank Pizzano

Contract No.:   NT-01-008-021
                               The University of Alabama

1. Objective: The first objective of any reliability growth
study is Prediction of Reliability at some future instant. We
are concerned with the current reliability estimate, growth
rate, and whether it is possible to extrapolate the growth
pattern in the future. From this we can estimate ultimate
reliability to determine if future reliability requirements will
be met. Also we might investigate how reliability growth of a
system is related to factors such as: number of tests, cost,
number and type of design changes, design reviews, etc. A
second objective of any reliability growth study is statistical
inference, estimation of reliability for reliability
demonstration.

A cause of concern for the development engineer and management
is that reliability demands an excessive number of tests for
reliability demonstration. For example, the STME program
requirements call for .99 reliability at 90% confidence for
demonstration. This requires running 230 tests with zero
failure if a classical binomial model is used. Therefore, more
innovative techniques need to be used. Reliability growth
models are potential candidates for more efficient testing.

It is therefore the objective of this study to explore the
reliability growth models for reliability demonstration and
tracking and their applicability to NASA programs.

2. Background: Technology has been characterized in the past
two decades by the development of complex systems containing
number of subsystems and components, and parts. At the present
time it is realized that these complex designs carry within them
the possibility of various types of error and malfunctions. The
failure of a single inexpansive component may cause the failure
of the entire system.

In the manufacturing of a complex system, such as Space
Transportation Main Engine (STME), the initial prototypes will
invariably have significant reliability and performance
deficiencies. Consequently, such a system is subjected to a
development testing. When a failure occurs, the cause is
isolated and a corrective action is implemented.

Reliability tracking is a method for quantifying and monitoring
a system reliability during the development phase through the
collection and analysis of relevant data. Reliability tracking,
in general, is not contractually required. However, the
existence of a reliability tracking program during early
development phases increases the likelihood that more problems
will be resolved earlier in the program, thus reducing large
costs later.

Reliability growth is the positive improvement in reliability
due to changes in product design or the manufacturing process.
Reliability growth is not automatic: it results only from
Test-Analyze-And-Fix (TAAF). It is expected that this process
of finding problems (design weakness) and fixing (design change)
will result in increasing Time Between Failures (TBF).

Reliability managers have long been aware of the fact that the reliability of the systems should improve as it progresses through development but this growth will meet a targeted rate is always a concern. A reliability growth management program will furnish the manager with a mean to plan this growth and control its progress. Such a program also enables the manager to:

a. Take advantage of experience gained in previous programs
b. Evaluate different potential test plans and select the appropriate one;
c. Evaluate possible causes of failures and the appropriate corrective actions when an ongoing program is experiencing problems
d. Correctly evaluate the progress made by an ongoing program.

3. Reliability Growth Models: A Reliability Growth Model is an analytical tool used to monitor the reliability progress during the development program and to establish a test plan to demonstrate an acceptable System Reliability. Reliability growth models can be used for:

a. Determining the intensity of TAAF to reach reliability objectives;
b. Predicting whether stated reliability objectives will be achieved;
c. Tracking progress, correlating reliability changes with reliability activities; and
d. Planning for a reliability demonstration test; computing confidence limits.

At present there is no shortage of reliabiity growth models, the current problem is the lack of criteria for selecting the best for a particular application. For NASA applications we classify growth models in two groups, growth models for management and growth models for demonstration. The characteristics of each group is summarized as follows:

A. Characteristics of Growth Model for Management/Tracking:

a. Use of objective and subjective information
   - The model is based on engineering concepts and statistical concepts;

b. Prediction
   - The model can be used to forecast Reliability at Maturity from development data;

c. Asymptotic Value
   - the reliability growth value converges to a limiting value with increased time or sample value;

d. Adaptability
   - the model can be used for developmental and operational data
   - the model can adapt quickly to changes in data trends

e. Control
    - The growth model can be used to evaluate growth management
      strategy. The reliability growth can be traced
      statistically, that is, actual growth follow the predicted
      growth curve.

B. Characteristics of a Growth Model for Demonstration:

a. Use of Objective Data
    - The model uses actual test data to estimate the parameters
      of the reliability growth models;

b. Statistical Confidence
    - Statistical Confidence is part of mathematical formulation
      of the models;

c. Model Goodness of Fit
    - The goodness of fit between the reliability growth model
      and data can be checked statistically;

d. Prediction and Control
    - Same as model used for reliability growth management.

4. Applications of Growth Models to NASA Programs

4.1 Space Shuttle Main Engine (SSME) reliability has been
evaluated by Dr. Fayssal Safie [1] using reliability growth
models. The main aim was to study the growth process for the
SSME reliability growth for crit 1 failures during the
operational phase of the program (1/1/79 to 12/31/90). In this
study the growth parameter was used to check for reliability
improvement and the derived reliability represents the
demonstrated reliability of the SSME.

4.2 Space Transportation Main Engine (STME). A reliability
demonstration test plan for STME can be developed using
reliability growth and is under consideration now. This will
use history of previous programs such as J-2, F-1, RL-10, SSME,
H-1, etc. However, much more work needs to be done.

Also, we plan to develop a STME component/system reliability
growth tracking procedure. The objective is to select the
optimum reliability growth model to monitor reliability during
development and predict growth patterns.

As a first step to accomplish this task Redstone Scientific
Information Center was used to compile a bibliography of 65
references (books and articles) related to reliability growth.
This literature covers the past 25 years of work on reliability
growth modeling, assessment, tracking, prediction, and control.
Due to space restriction, this list is not attached to this
report but is available from MSFC, Analysis Branch, Reliability
and Maintainability Division.

5. Recommendations: Reliability is the science of estimating, controlling, and managing the probability of failure. Thus, any high-tech space system can advantageously use methods of reliability. At present, the Department of Defense is using reliability growth, tracking, management, and demonstration for various military projects. NASA needs to invest more time and expand effort in this area.

At any time, both the achieved reliability and its growth trend must be identifiable quantitatively to permit corrective action to achieve specified reliability goals. There is probably no single best approach to high reliability since each application is likely to have unique requirements. Reliability growth modeling can be useful for diverse kinds of equipment. But, NASA programs are very unique and their systems are complex requiring high reliability. Therefore, applications of growth models to NASA programs need to be developed carefully.

The ability to predict the reliability of a system within reasonably close limits, during development and operations is a significant requisite to achieving the very high reliability goals set forth for various NASA systems. It is therefore recommended that NASA develops a manual in the reliability growth area for NASA applications. Two main aims for this new venture are:

a. To evolve a reliability growth modeling analytical procedure which would provide guidance with which to confidently assess, predict, and control the reliability growth of NASA programs.

b. New statistical methodology for unique NASA programs be explored and developed.

When completed, this manual will serve as a tool for designers and managers to improve reliability through the different phases of a NASA program.

6. Acknowledgements:

I have enjoyed working at the Analysis Branch, Reliability Engineering Division, MSFC during Summer 1991. I would like to thank William Smith, Frank Pizzano, and Dr. Gerald Karr for giving me the opportunity and for their help during my stay. Dr. Fayssal Safie introduced the reliability growth area to me. I am very grateful for his patience and for several stimulating discussions. Also, I am thankful to Ms. Terry Christopher for typing this report.

7. References:

[1] Safie, Fayssal M. "SSME Reliability Growth Study" Presentation, MSFC, Reliability Analysis Branch, August 1990

[2] MIL-HDBK-189: Reliability Growth Management, Available from HQ, U.S. Army Commmunications Research and Development Common, Fort Monmouth, NJ, 1981

N92-15898

CHARACTERIZATION OF THE CORROSION RESISTANCE OF BIOLOGICALLY ACTIVE SOLUTIONS - THE EFFECTS OF ANODIZING AND WELDING

Prepared By: Daniel W. Walsh, Ph.D.

Academic Rank: Professor

University and Department: Cal Poly State University, SLO
                                      Materials Engineering

NASA/MSFC:

        Laboratory: Materials and Processes Laboratory
        Division: Metallic Materials Division
        Branch: Corrosion Research Branch

MSFC Colleague: Merlin D. Danford, Ph.D.

Contract No.:   NGT-01-008-021
                                      The University of Alabama in
                                        Huntsville
                                      Huntsville, Alabama

The study of microbiologically influenced corrosion (MIC) is an inherently interdisciplinary effort. An understanding of fabrication processes, metallurgy, electrochemistry and microbiology is crucial to the resolution of MIC problems. The object of this effort was to use AC impedance spectroscopy to characterize the corrosion resistance of Type II anodized aluminum alloy 2219-T87 in sterile and biologically active media and to examine the corrosion resistance of 316L, alloy 2219-T87 and titanium alloy 6-4 in the welded and unwelded conditions. The latter materials were immersed in sterile and biologically active media and corrosion currents were measured using the polarization resistance (DC) technique.

MIC is recognized as a major problem in many industries. MIC is ubiquitous; all alloy systems exhibit susceptibility to microbiological attack. MIC of water treatment and delivery systems is particularly insidious, MIC can occur during construction, testing, operation or shutdown periods. In fact, extended periods of shutdown can be particularly damaging. Researchers have developed some understanding of environments that promote MIC, materials susceptible to MIC, methods to detect MIC and rudimentary approaches to treat and prevent MIC. However, little understanding of the metallurgical basis for these processes has developed. Furthermore, little "hard data" on corrosion rates of material systems in biologically active environments exists. In even fewer cases have researchers examined the effects of fabrication processes on the MIC susceptibility of metals.

Microbes are living agents of corrosion. Their size provides them access to material inhomogeneities at the microstructural level. Microbes are motile, and able to move away from toxic chemicals and toward food - they have specific chemical receptors for target chemicals in the environment. Surfaces of any kind are attractive to most waterborne bacteria. Surfaces, particularly metal surfaces, concentrate scarce resources. The surface concentration of protein and polysaccharide molecules is much greater than that in the bulk solution. Microbes able to attach and establish themselves on such surfaces will be at a competitive advantage in their environment. Microbes are hardy, different varieties can withstand temperature variations from -10°C to 99°C, pH variations from 0 to 10.5 and oxygen concentrations from 0% to 100%. Microbes are prolific and able to exist in large colonies. Many are able to produce extra-cellular slime layers. The slime layer is used by the microbe to protect it from toxins, collect food and anchor to the surface. It also is critical to the development of complex microbial ecosystems, consortia of many different microbes on the surface. These synergistic consortia are able to accomplish complex chemical reactions at the material surface and create aggressive chemical environments. The slime layer is involved in the formation of oxygen depletion cells, it can sequester metabolic byproducts (bacteria found in ECLSS waters are known to produce organic acids and hydrogenase), it can harbor microbes that depolarize cathodic sites (SRB have been found in large numbers in ECLSS waters), thus it will accelerate corrosion. SRBs flourish in anaerobic environments at the film-metal interface, rendering the environment more chemically aggressive and providing several mechanisms to depolarize the rate limiting cathodic reaction. Furthermore, many bacteria can directly oxidize metal ions. At a minimum this will lead to a passive co-accumulation of negative ions (typically Cl^-). This may produce an acidic ferric chloride, cuprous chloride or magne-

sium chloride solution at flaw tips, producing an _in-vivo_ stress corrosion cracking environment more severe than many _in-vitro_ tests.

Slime layers produce a crevice like anaerobic environment in which passivating films damaged by abrasion or halide ion attack go unrepaired. The biofilm can consume oxygen, and prevent oxygen in the environment from reaching the metal surface and restoring passive films. In addition, the lack of oxygen may also promote cathodic reactions that do not involve oxygen.

Metal surfaces are extremely heterogeneous. Regional (on all scales - from submicron to macroscopic) differences are so well defined that local anodes and cathodes form and corrosion takes place on individual pieces of metal. Surface condition, stress state, microstructure, chemistry and inclusion size and distribution affect local electrochemistry and MIC susceptibility. Welding changes the surface texture, and produces local stress fields. More importantly, it alters the size, shape, distribution and amount of microstructural constituents in the fusion zone and in the heat affected zone. In our study welding accelerated and aggravated corrosive attack.

Corrosion implies the existence of anodic sites on a metal surface, where oxidation of insoluble metal atoms to soluble metal ions takes place. Cathodic regions on the metal surface balance the reaction. In systems where external current is not supplied, anodic and cathodic currents must be equal. Reactions at the anode and the cathode can be treated as "half-reactions" whose sum is the total corrosion reaction. Corrosion potentials are thermodynamic quantities, measured at equilibrium, and as such indicate what reactions are possible. Corrosion currents are kinetic values and reflect dynamic, nonequilibrium processes at electrodes. Typically there is a single anodic reaction, the dissolution of metal ions. However, there may be several cathodic reactions; which is favored depends on the chemistry of the environment. In our systems, the pH is near neutral and the oxygen and water reactions are possible. In biologically active media, other reactions are possible, the chemistry at the metal-film interface is drastically different from the bulk chemistry.

Polarization resistance techniques were used to study the uncoated samples, AC impedance techniques were used to study the anodized materials. These methods have been described by Danford (Ref. 1,2,3). The corrosive media used was mild corrosive water for the bare Al 2219 samples and 3.5% NaCl solutions for all other samples. All media were sterilized in an autoclave. Bioactive solutions were made by inoculating these sterile media with 20 ml of ECLSS water. Samples I_{corr} and E_{corr} were monitored over a four week period. Samples were examined by scanning electron microscopy and optical microscopy. Water chemistry and microbial ecology were monitored.

Figure 1 shows the corrosion current measured in Al 2219 over a three week period. Note that initial measurements do not indicate the average current over longer periods. The Al 2219 (welded and unwelded) corrodes at a much lower rate in the sterile media. Similar results were observed in parallel tests with 316L and Ti 6-4. Figure 2 shows the charge transfer resistance measured for anodized samples over a four week period. This value is inversely proportional to the corrosion current. Note the precipitous drop in the resistance for the bioactive solution after several days exposure. The morphology of corrosive attack for the bioactive solutions was also different, microbes aggregated at weak spots in the coating (Fig. 3) and grossly

enlarged pits. Figure 4 shows microbes located between weld ripple marks on 316L material. Microbes also aggregated at pores and flaws in oxide coatings. The microbial attachment density was lower on the unwelded base material.

The results of this testing indicate that ECLSS waters are microbe rich, it contains large numbers of SRBs, Enterobacter, Pseudomonas and Klebsiella - that the AC impedance technique and the DC polarization resistance techniques are well suited to MIC investigations - that microbes attach to <u>all</u> materials studied - that microbes increase I_{corr} and decrease E_{corr} in all samples for all treatments (in the media studied Al 2219 was most susceptible, Ti 6-4 least susceptible) - that anodized materials in sterile media maintain coating integrity for longer periods than typically measured - that ECLSS rich media aggravate corrosive attack of anodized materials and change the morphology of attack - that microbes localize corrosion and fix anodes at microstructural features - that welding increases I_{corr} - that microbes randomly attach to a surface, proliferate at opportune locations, develop a biofilm and form complex consortia on the material surface that inhibit subsequent colonization by other bacteria - that microbes are at a minimum catalysts for the corrosion reaction, but are often directly involved in the corrosion process - that enhanced corrosion in Al 2219 is caused by the promotion of the more rapid hydrogen evolution reaction at the cathode, anaerobic films and SRBs foster this reaction.

The list of people who have helped me this summer reads like the Huntsville phone directory. Thanks to all in the corrosion, micro, FA and metallography groups. Special thanks to Merlin Danford whose quietly correct and kind approach makes working and learning so easy and to Jeff Sanders for field emission effects. Special thanks to Joe Montano, Barry Moody and Carlla Hooper. Special thanks to Tim Huff for all his help and interest. Finally thanks to Kevin Buford - good luck next year at school.
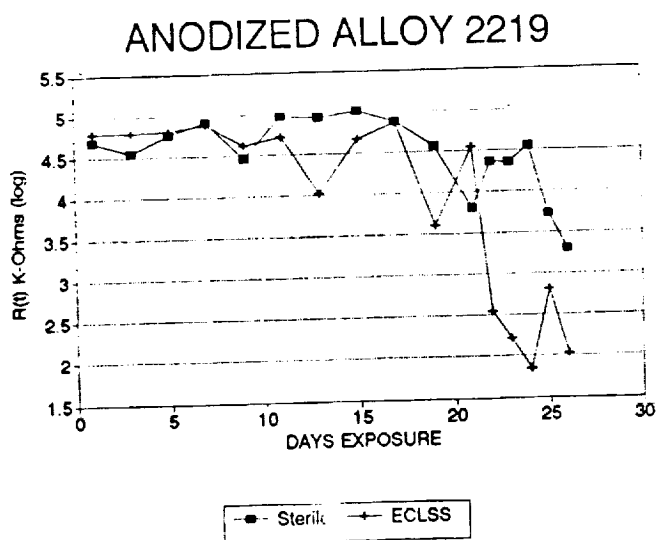
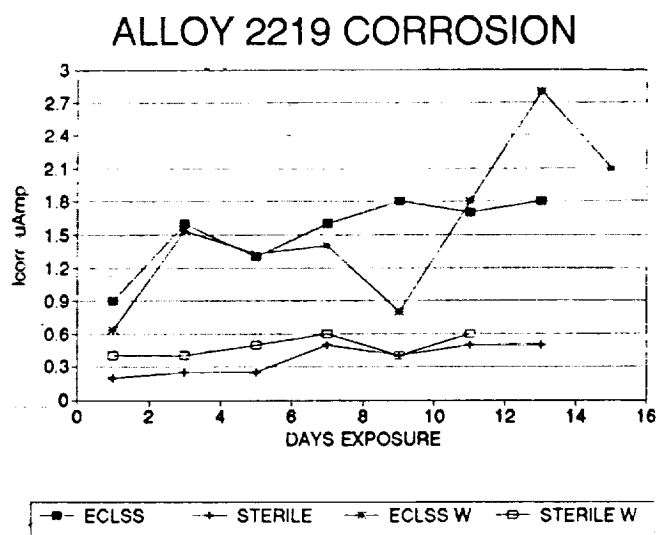## ANODIZED ALLOY 2219
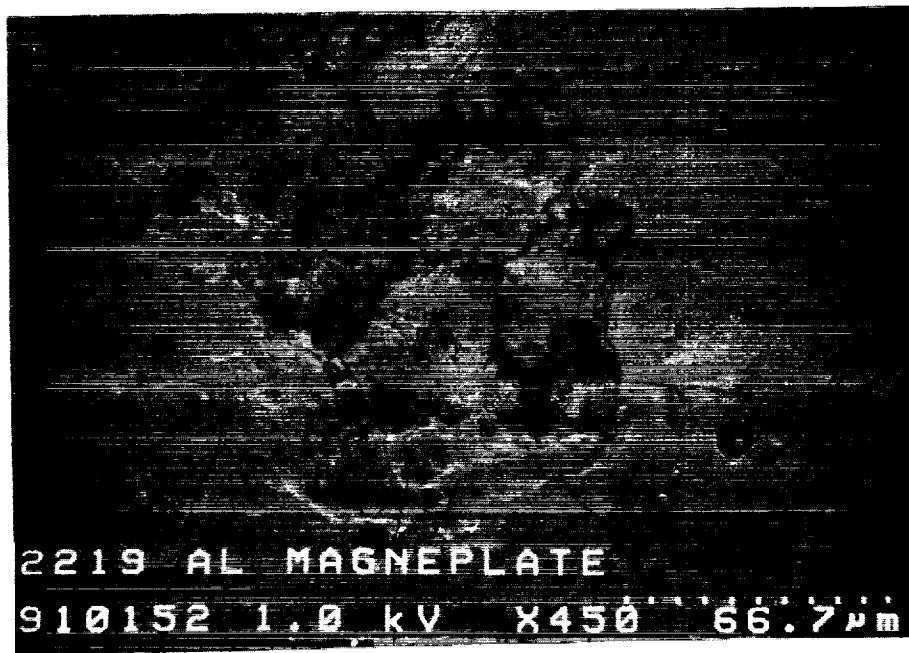
Figure 1.

ALLOY 2219 CORROSION

Figure 2

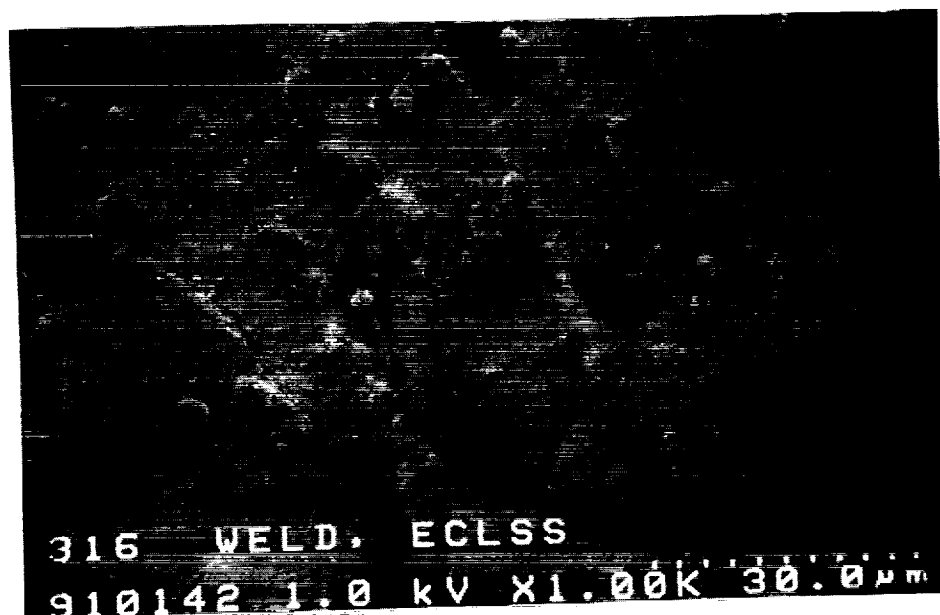Figure 3. Localized MIC attack at weak spot in anodized coating.

Figure 4. Microbes at weld ripple marks on 316L

References

1.   Danford, M. D., Equivalent Circuit Models For AC Impedance Data Analysis, NASA Technical Memorandum TM-100402, June 1990
2.   Danford, M. D., and Knockemus, W. W., The Corrosion Mechanisms For Primer Coated 2219-T87 Aluminum, NASA Technical Paper 2715, April, 1987.
3.   Danford, M. D., The Corrosion Protection of 2219-T87 Aluminum By Anodizing, NASA Technical Memorandum TM-103540, June 1991.

1991

NASA/ASEE SUMMER FACULTY FELLOWSHIP PROGRAM

MARSHALL SPACE FLIGHT CENTER
THE UNIVERSITY OF ALABAMA

AUTOMATION OF CUTTING AND DRILLING OF COMPOSITE COMPONENTS

Prepared By:	Charles W. Warren
Academic Rank:	Assistant Professor
Institution:	The University of Alabama Department of Mechanical Engineering Tuscaloosa, Alabama
NASA/MSFC:	

Laboratory:
    Division:
    Branch:
	Materials and Processes
	Process Engineering
	Chemical and Non-Metals Processes

MSFC Colleagues:	Eutiquio Martinez Gail Gordon
Contract No.:	NGT-01-008-021 The University of Alabama

1 Introduction

This report outlines the research that was conducted during the ten weeks of the NASA / ASEE Summer Faculty Fellowship Program. The task was to develop a preliminary plan for an automated system for the cutting and drilling of advanced aerospace composite components. The components under consideration are being hand manufactured by Martin Marietta Manned Space Systems. The immediate goal is to automate the production of these components, but the technology developed can be readily extended to other systems.

Working with the engineers and technicians at NASA and Martin Marietta (MMC), a tentative plan has been developed to automate this process. In the sections below, a description of current methods at MSFC, current methods in industry, and the proposed plan for automation are given.

1.1 Composite Components Description

There is a desire to replace many of the components of the Space Shuttle System with components made from composite materials. The components under consideration here are manufactured by Martin Marietta for use on the External Tank. Three specific parts are considered here, but the technology developed could easily be extended to other components. The components studied are the LO2 Feedline Fairing, the Nosecone, and the Intertank Access Door.

These components are laid by hand using a prepreg material in a mold (tool) and a vacuum bagging process is used to remove voids. The component is placed into a large autoclave for curing while still in the mold. Once the part has been cured, it is removed from the mold and the excess is trimmed and appropriate holes are drilled. The difficulty lies in the fact that the parts are very large. Cutting and drilling to close tolerances (approximately .030 inches) is difficult for components that are odd shaped and almost five feet across. There are also plans to manufacture components that are much larger than the three in this study.

1.2 Current Methods of Processing (MSFC)

There are several methods of processing the components in use at MMC. Once the components have been cured, trim lines are placed on the components that identify the final edge to be achieved. A rough cut is then performed close to the trim line using either a band saw or a hand-held jig saw using a diamond impregnated blade. Conventional wood or metal cutting blades are not well suited for cutting composite materials.

Once the rough cut is made, hand-held diamond impregnated grinders are used to remove most of the remaining trim material and clean the edge. The final operation in the trimming process is to obtain a finished edge. This is done by a large amount of hand sanding.

The next operation is to drill several holes in the components for later use in the assembly process. Bushings are clamped onto the top and bottom of the surface being drilled to prevent the delamination problem and feedrates are carefully control to prevent heat buildup. The drilling process is slow and tedious due to the number of holes to be drilled in each component.

2 Current Methods of Cutting (Literature)

During the ten weeks of the summer program, an extensive literature survey was conducted into current methods of processing composite components. Much of the literature centered around the aerospace industry. These articles described the processing of composite components that are used on military aircraft. The second most described systems are those in the automobile industry. These articles described the automated cutting of plastics, but the technology can be extended to composites.

Most of the literature for cutting composites described water jet cutting systems. There were several papers that compared cutting with water jets, lasers, and routers. These three techniques are the best suited for automation.

3 System Specification

When automating a system such as this, there are many decisions to be made with respect to methods and equipment used. Fortunately, most of the required major equipment items for this project are already available at MSFC. There are three major operations here that should be performed by a robot. They are: locating the part to be cut, positioning the cutter, and positioning the drill. The devices for accomplishing this should be mounted with an automatic tool changer between the device and the robot. Although not entirely necessary, they greatly extend the life of the mounting hardware. Robot end effectors are notorious for being difficult to mount repeatedly.

The entire system should be coordinated by a central computer system that directs the operation. High level commands are sent to the individual device controllers for processing. Each device, (robot, water jet, drill), will have a separate computer controller. The waterjet and drill could share a controller since both operations will not occur simultaneously with this system.

Below is a list of components needed to complete the system. Also, recommendations are given for a specific device that could accomplish the task.

- **Robot** – A gantry type robot is by far the best suited for this task. They typically have a wide range of motion needed to process large parts and the rigid structure. These robots are typically more accurate than other type of robots, which allows tools to be precisely positioned. There is a Cimcorp XR225 robot installed in Building 4707. This is a very accurate robot that is ideal for this task. Several vendors of cutters and drills have used this model of robot to position their tools and highly recommended it.

- **Water Jet Cutter** – Water jet cutting systems are very versatile and work well with composites. There is, however, a large capital investment that must be factored into the decision to purchase such a system. The highest cost item is the 60,000 psi pump. Again, there is a very good system installed in Building 4707. Its pump could easily handle another cutting nozzle. The pump is manufactured by Flow International, but both major vendors of abrasive water jet cutters can use this pump. There is high pressure plumbing already installed on the Cimcorp robot as well, which will reduce development costs significantly.

- **Part Locating Device** – A vision system or the laser range finder would work well for part locating. Although either of these optical systems would work well, my feeling is that the laser system would be more economical. However, a vision system is only slightly more expensive and should identify part locations faster.

- **Drilling Device** – Although a turnkey drilling system is available from EOA Systems, Inc. for approximately $70,000, it would be difficult to justify the large capital expenditure for the part production volume in this study. It is intended for use in an aircraft production environment where thousands of high precision holes are drilled regularly.

  A smaller, less sophisticated device can be developed that would be adequate as an R & D tool. It would be capable of high precision drilling with hardware to prevent delamination.

- **Tool Changer** – Although not absolutely necessary, a tool changer is very useful when tools are to be swapped on the robot. The relatively low cost, ($2,000 to $5,000 depending on capacity and features), is justified easily by the time savings and extended mounting hardware life.

- **Computer Control Hardware** – IBM PC/AT compatible computers are very well suited to this task. Intel 80386 or 80486 based computers are readily available with a tremendous amount of third party hardware peripherals and

software available. These systems are well understood and economical to purchase and operate. They could be used as the high level coordinator as well as the controller for the water jet and the drill.

- **Software** – The control and coordination software for this system will need to be developed. A simple-to-operate, menu -driven software package should be developed for each computer. The software for the high level coordinating computer will handle the interface between the human operator and the rest of the systems. Software is also used that handles communication between the various control computers.

- **Communication Links** – There are many standards for communication links to choose from. RS–232 is a well understood standard used in the personal computer business. There is also a great deal of hardware and software available. The speed of this link is also adequate for the tasks in this study.

- **Off-line Programming** – The Deneb Software on the Silicon Graphics hardware is an excellent system for off-line programming. This is in place and needs no modification. Any program or path translation could easily be done by the software to be included on the high level coordinator.

4 Conclusions

There is an excellent opportunity for developing a state-of-the-art, automated system for the cutting and drilling of large composite components at MSFC. Most of the major system components are in place: the robot, the water jet pump, and the off-line programming system. The drilling system and the part locating system are the only major components that need to be developed. Also, another water jet nozzle and a small amount of high pressure plumbing need to be purchased from, and installed by, one of the two major vendors. Once the system components have been obtained, the system needs to be tied together in a coherent manner.

Although there is some startup effort involved, there will be a tremendous amount of potential in the system. The system will be capable of processing existing and many future parts developed.

1991

NASA/ASEE SUMMER FACULTY FELLOWSHIP PROGRAM

MARSHALL SPACE FLIGHT CENTER
THE UNIVERSITY OF ALABAMA

HP9-4-.30 WELD PROPERTIES AND MICROSTRUCTURE

Prepared By: George W. Watt, Ph.D.

Academic Rank: Assistant Professor

Institution: Utah State University
                                    Department of Industrial Technology

NASA/MSFC:

    Laboratory: Materials and Processes
    Division: Metallic Materials
    Branch: Metallurgy Research

MSFC Colleague: Tina W. Malone

Contract No.:   NGT-01-008-021
                                    The University of Alabama

HP9-4-.30, ultra high-strength steel, the case material for the Advanced Solid Rocket Motor (ASRM), must exhibit acceptable strength, ductility, toughness, and stress corrosion cracking (SCC) resistance after welding and a local post weld heat treatment (PWHT). Testing, to date, shows that the base metal (BM) properties are more than adequate for the anticipated launch loads. Tensile tests of test specimens taken transverse to the weld show that the weld metal overmatches the BM even in the PWHT condition. However, there is still some question about the toughness and SCC resistance of the weld metal in the as welded and post weld heat treated condition.

To help clarify the as welded and post weld heat treated mechanical behavior of the alloy, subsize tensile specimens from the BM, the fusion zone (FZ) with and without PWHT, and the heat affected zone (HAZ) with and without PWHT were tested to failure and the fracture surfaces subsequently examined with a scanning electron microscope (SEM). Table I shows the test results (the average of 5-6 test specimens) and, for comparison, average results from a large number of full scale BM tensile tests accomplished at MSFC. The full size specimen tensile test results and the subsize specimen tensile results for the BM are comparable indicating at most a small specimen size effect for the subsize tensile results. Without PWHT the FZ and HAZ materials have a reduced 0.2% offset yield strength (YS), a very high ultimate tensile strength (UTS), and significant loss of ductility as measured by either %El or %RA. The reduced YS is probably due to the presence of appreciable amounts of relatively soft retained austenite that begins to plastically deform at a lower stress than the higher strength martensite matrix surrounding it. The influence of retained austenite on the fracture of maraging steels

TABLE I

| Property | NASA full size | Subsize (0.16" dia.) | | | | |
		BM	FZ,NoPWHT	FZ,PWHT	HAZ,NoPWHT	HAZ,PWHT
YS(ksi)	206	211	181	221	188	215
UTS(ksi)	227	237	271	250	293	251
%El (1/2" GL)	22.8*	14.3	7.5	14.6	8.2	16.2
%RA	54.3	54.3	35.5	43.6	45.2	57.2

* The gage length (GL) for the NASA full size specimens was 2".

XX-1

has been reported in the literature.[1] It was suggested that the highly strained pools of austenite contain carbide or other particles that are sites for the creation of voids which grow, coalesce, and result in failure by microvoid coalescence. The data in Table I, also, clearly show that the PWHT used (950 °F for 2 hours) results in return of the FZ and HAZ to almost base metal YS and UTS values. The %El and %RA of the HAZ also indicate recovery of most of the BM ductility, but the %RA value for the post weld heat treated FZ are considerably below the BM values indicating the ductility of the FZ remains low. These results would suggest that a good PWHT should return the HAZ to desired strength and toughness, but probably not recover the FZ toughness.

SEM examination of the fracture surfaces of representative samples from the subsize tensile tests (BM, FZ with and without PWHT, and HAZ with and without PWHT) shows the following results and trends. All fracture surfaces exhibit a microvoid coalescence failure mode. In general, there appears to be a bi-modal distribution of dimple or void sizes on the fracture surface with small dimples being less than 1 micron in diameter and the large dimples being from 1-5 microns in diameter. Another clearly discernible characteristic was that the FZ and HAZ without PWHT specimens had a much higher fraction of the small dimples on the fracture surface than the BM. After PWHT, the HAZ showed an increase in the fraction of larger dimples while the FZ seemed to show a decrease. This reduction in FZ dimple size is probably due to sample to sample variation and should not be interpreted as caused by the PWHT. Preliminary estimates of the average dimple size on the fracture surface (D_0), which depends on the dimple size distribution, and the strain to fracture estimated from %RA (e_f) are given in Table II. These data show that as D_0 increases, at least within the range of sizes considered here, e_f increases. Garrison, et al,[2] have related void or dimple spacing to crack tip opening displacement. As dimple spacing increases dimple diameter will increase in direct proportion and, since, crack tip opening displacement is proportional to strain to fracture the data in Table II should follow a relationship similar to that determined by Garrison. He showed, at low void spacings, the relationship between void spacing and crack tip opening displacement should be linear; experimental data appeared to confirm this result. Thus,

TABLE II

Material	D^0 (micron)	e_f
BM	1.7	0.78
HAZ no PWHT	1.3	0.42
FZ no PWHT(1)	1.1	0.44
FZ no PWHT(2)	1.2	0.47
HAZ PWHT	1.4	0.70
FZ PWHT	1.0	.49

XX-2

C-4

for the dimple sizes in this work, it is expected that the relationship between e_f and D_o should be linear with a zero intercept. The data do indicate a linear least squares fit of $e_f=0.4D_o$. It appears from these data that the ductility of the HAZ is regained to a large extent by the PWHT while that of the FZ is only slightly improved. Consequently, the weak link, as far as toughness and stress corrosion cracking of the post weld heat treated weldment is concerned, would seem to be the fusion zone.

Limited tensile SCC tests using the ASTM 3.5% NaCl Alternate Immersion and the 5% Salt Spray Tests were performed at MSFC and indicate a possible problem in the weld metal. In the as welded condition most of the failures occurred in three weeks or less at stresses equal to or greater than 75% YS with the cracking tending to initiate in the HAZ. After PWHT there appeared to be an improvement, but failures still occurred at close to three weeks in some cases. However, after the PWHT the failures seemed to initiate more in the FZ. Several specimens were sectioned perpendicular to the fracture surface, polished, and etched in order to determine the location of the fracture initiation. These specimens were also used for microhardness measurements to determine if there was a relationship between hardness and the location of the crack initiation site. Gouch[3] has concluded that, for high strength steels, welding greatly increases susceptibility to SCC with the hardest regions of the weld zone being the most susceptible with microstructure having a secondary effect. He also found that PWHT improves SCC resistance since it results in a reduction in hardness in the FZ and HAZ.

Comparison of the microhardness data, taken in this instance from a limited number of the HP9-4-.30 weldments tested in SCC, with the apparent crack initiation point indicates that in the as welded condition the crack does appear to initiate in one of the harder regions of the FZ or HAZ. However, the PWHT seems to shift the failure location into the FZ even though there are still harder regions in the HAZ. Apparently, in the post weld heat treated condition the microstructure and/or microsegregation become more dominant than the hardness in controlling the SCC. Of course, the effect of the surface condition may also play a major role, and it may be that in the PWHT condition the exposed surface of the FZ is more susceptible to pitting so it is easier to initiate the cracks. Once the pits (or other surface defect) has been initiated the crack probably grows by a hydrogen embrittlement mechanism. Tromans[4] studied the stress corrosion cracking of HY-180 steel at various corrosion electrochemical potentials and found in all cases that the crack propagation was consistent with hydrogen embrittlement.

It has been suggested that a higher temperature PWHT and perhaps a different temper during BM processing could improve the SCC resistance of the weldments. It is possible to achieve some

improvement, but if the FZ susceptibility problem is associated with the microstructure/microsegregation then that cannot be changed by a PWHT.

REFERENCES

1. Kenyon, N., "Effect of Austenite on the Toughness of Maraging Steel Welds," Welding Journal, May 68, p. 193-a.

2. Garrison, W.M. Jr, Raghavan, K.S., and Maloney, J.L., "Fracture Toughness: A Discussion of the Influence of Particle kSpacing at Constant Particle Volume Fraction," submitted to Metall. Trans. A.

3. Gouch, T.G., "Stress Corrosion Cracking of Welded Joints in High Strength Steels," Welding Journal, July 74, p. 287-s.

4. Tromans, D., "Stress Corrosion Cracking of HY-180 Steel in Aqueous 3.5 Pct NaCl," Metall. Trans. A, Vol 12A, p. 1445.

1991

NASA/ASEE SUMMER FACULTY FELLOWSHIP PROGRAM

MARSHALL SPACE FLIGHT CENTER
THE UNIVERSITY OF ALABAMA IN HUNTSVILLE

COMPUTERIZED REDUCTION OF ELEMENTARY REACTION
SETS FOR COMBUSTION MODELING

Prepared by: Carl V. Wikstrom, Ph.D.

Academic Rank: Assistant Professor

Institution: University of Arkansas
                        Mechanical Engr. Dept.
                        Fayetteville, AR

NASA/MSFC:

        Laboratory: Propulsion
        Division: Propulsion Systems
        Branch: Performance Analysis

MSFC Colleague: Charles F. Schafer, Ph.D.
                        Klaus W. Gross

Contract No.:   NGT-01-008-021
                        The University of Alabama
                        in Huntsville

1. Introduction

Modeling of chemistry in Computational Fluid Dynamics can be the most time-consuming aspect of many applications. If the entire set of elementary reactions is to be solved, a set of stiff ordinary differential equations must be integrated. Some of the reactions take place at very high rates, requiring short time steps, while others take place more slowly and make little progress in the short time step integration.

Historically, the problem has been approached in several ways:

1) Single Step - Instantaneous Reaction: While computationally simple, this technique will over-predict conversion since the equilibrium point will be surpassed.

2) Total Equilibrium: This is the assumption used in ODE and TDE at MSFC. The assumption may be adequate in describing the overall performance of an engine, but may fail to provide the detail required for the spatial resolution which CFD analysis is to provide. That is, the assumption may not be valid for the local conditions resulting from the CFD calculations.

3) Reduced Mechanism - Finite Rate: The choice of the appropriate reduced set is difficult, since the local conditions are not constant throughout the CFD calculations. Since the importance of the elementary reactions may change within the computational space, the global set chosen may not be appropriate for the local conditions.

4) Partial Equilibrium - Finite Rate: A portion of the reactants are assumed to be in equilibrium, while the remainder are integrated in finite rate kinetics. This approach removes the very short time step calculations and allows integration of fewer equations at longer time steps. Since there is an interaction between the equilibrated and non-equilibrated species, an equilibrium calculation is performed at each time step. KIVA (Los Alamos) utilizes this approach. However, the proper choice of equilibrated and non-equilibrated reactions may change with the local conditions.

The goal of this work is to develop a procedure to automatically obtain sets of finite rate equations, consistent with a partial equilibrium assumption, from an elementary set appropriate to local conditions. The sets can be applied to the appropriate regions within the CFD space where the total equilibrium assumption is inappropriate.

2. Approach

The full elementary set of equations was solved for a single cell using CHEMKIN (Kee, et al, 1989) and PSR (Glarborg, et al.,

1986). It was necessary to assign each reaction as equilibrated, frozen (no reaction occurring), or finite rate. The assignment was made as follows:

Let the characteristic reaction time be defined as:

$$\tau_{rxn} \equiv \frac{C_t}{R_i}$$

Where $C_t \equiv$ Total molar concentration (moles/cm^3)
and $R_i \equiv$ Molar reaction rate (moles/c^3-s) for equation i.

and the characteristic residence time as:

$$\tau \equiv \frac{\dot{m}}{\rho V}$$

Where $\rho \equiv$ Density (g/cm^3)
          $V \equiv$ Volume of cell (cm^3)

and $\dot{m} \equiv$ mass flow rate into cell (g/s).

Then the assignment was made as follows:

$$\frac{\tau_{rxn}}{\tau} > 100 \quad \textit{Frozen}$$

otherwise the reaction was classified as not frozen. The value of 100 was arbitrary and may be changed in future applications. The frozen reactions and the species appearing only in the frozen reactions were discarded.

Let R_f indicate forward direction reaction rate and R_r indicate reverse reaction rate and R_{max} indicate the greater of the forward and reverse rate. The following criterion was used for equilibrated designation:

$$\frac{|R_f - R_r|}{R_{max}} < 0.05 \quad \textit{Equilibrated}$$

The species appearing in the equilibrated reactions were assumed to be in partial equilibrium (reactants with products).

The remainder of the reactions were classified as finite rate and were retained. The partially equilibrated species were used to further reduce the finite rate mechanism using the method outlined by Chen (Chen, 1988).

3. Test Case

The hydrocarbon portion of the Miller/Bowman (Miller, et al., 1989) mechanism was used for the development of the procedure. This elementary reaction set contains 151 reaction and 33 species.

The conditions chosen were:

$$\dot{m}=47kg/s \quad P=212.7atm. \quad V=41.48l$$

Feed Volume Fractions: C_2H_4 0.306 O_2 0.694

The resulting residence time is 1.3 ms.

Of the 151 reactions in the elementary reaction set, 79 were frozen and were discarded. 43 reactions were equilibrated and 29 were designated finite rate. The 29 finite rate reactions contained 20 species, 13 of which were equilibrated in the set of 43 reactions. These reactions were further reduced to the following set of "global" reactions:

1. $O_2 + 2C \leftrightarrow 2CO$

2. $2O_2 + C + 3CH \leftrightarrow 3CO + CH_2OH$

3. $C + C_2H_4 \leftrightarrow CH + C_2H_3$

4. $O_2 + C + C_2H_4 \leftrightarrow CH + CO + CH_2OH$

5. $CH + CO \leftrightarrow HCCO$

6. $2CH + CO \leftrightarrow C + CH_2CO$

7. $O2 + C + CH + HCCO \leftrightarrow CH_2 + 3CO$

Note that the Miller/Bowman mechanism was assembled for the purpose of modeling NO_x formation and C_1 hydrocarbons are important in "prompt" NO formation. The current approach should be able to maintain accurate prediction of C_1 concentrations, which would be lost in a total equilibrium approach, by using only the above global mechanism and a partial equilibrium assumption on the remaining species.

4. Conclusions and Future Work

The possibility of computerized reaction reduction has been demonstrated. However, the ability to use the reduced reaction set depends on the ability of the CFD approach in incorporate partial equilibrium calculations into the code. Therefore, the results should be tested on a code with partial equilibrium capability.

The predictive capability of the resulting reduced set is can be no better than that of the original elementary reaction set. The procedure should also be tested on other elementary reaction sets.

The current test was at conditions on the scale of a full combustion chamber. Testing of the procedure at the conditions of an individual cell is appropriate.

Under certain conditions, multiple sets of partially equilibrated species may result. The current procedure should be modified to facilitate multiple sets of partially equilibrated species.

5. References

Chen, J-Y, "A General Procedure for Constructing Reduced Reaction Mechanisms with Given Independent Relations", Combustion Science and Technology, 1988, Vol. 57, pp. 89-94.

Glarborg, P., Kee, R.J., Grcar, J.F., and Miller, J.A., "PSR: A Fortran Program for Modeling Well-Stirred Reactors", Sandia Report SAND86-8209, UC-4, February, 1986.

Kee, R.J., Rupley, F.M., and Miller, J.A., "Chemkin-II: A Fortran Chemical Kinetics Package for the Analysis of Gas-Phase Chemical Kinetics", Sandia Report SAND89-8009, UC-401, September, 1989.

Miller, J.A. and Bowman, C.T., "Mechanism and Modeling of Nitrogen Chemistry in Combustion", Progress in Energy and Combustion Science, 1989, Vol. 15, pp. 287-338.

1991

NASA/ASEE SUMMER FACULTY FELLOWSHIP PROGRAM

MARSHALL SPACE FLIGHT CENTER
THE UNIVERSITY OF ALABAMA IN HUNTSVILLE

Assessment of the NASA Code FDNS2D
for Computation of
Film Cooling Effectiveness

Prepared By:	Keith A. Woodbury, Ph.D., P.E.
Academic Rank:	Assistant Professor
Institution:	The University of Alabama Mechanical Engineering Deparment

NASA/MSFC:
  Office:
  Division:
  Branch:
	Combustion Devices Group
	Component Development Division
	Turbomachinery
	and Combustion Devices

MSFC Colleague:	Dave Sparks
Contract No.:	NGT-01-008-021 University of Alabama in Hunsville

Introduction. The role of Computational Fluid Dynamics (CFD) programs is usually one of analysis. Generally they are not used in the design phase of a project. There has been a concerted effort at MSFC to integrate CFD codes into the design phase of Combustion Devices, specifically, in the design of the STME nozzle. Before the results of such analyses can be accepted, the credibility of the CFD codes upon which they are based must be established.

This report details the effort to assess the capability of the NASA code FDNS2D to compute the heat transfer to a solid bounding surface. Specifically, high-speed flow over a flat plate is considered, and the resulting wall shear stress, and heat transfer are computed. These values are compared against analytical results (for wall shear stress) and experimental data (for heat transfer).

What follows in this report is a brief description of the FDNS2D code, with special emphasis on how it handles solid wall boundary conditions. The flow conditions and the FDNS solution are presented next, along with comparison to analytical and experimental data. Some intermediate observations are then made, followed by a recommendation for adoption of an alternate method for computing the wall heat flux. Some conclusions are made to close out the report.

FDNS. The computer code name, FDNS, stands for *F*inite *D*ifference *N*avier-*S*tokes. The code, written by SECA, Inc. in 1988 [1], is a pressure–based finite-difference solver. The code implements artificial viscosity in order to capture shocks in high-speed flows.

The version used in this effort is two-dimensional, hence the name FDNS2D. It solves the continuity, u-, v- momentum, energy, k-ε, and specie conservation equations. The k-ε turbulence models available in the code are both the "standard" and "extended" versions. Additionally, chemistry capability is provided by either equilibrium or finite-rate chemical reactions.

The implementation of solid wall boundary conditions in FDNS is by use of wall functions [2]. The particular implementation in the code is assumed valid whenever the dimensionless distance $y^+ = \rho y_p C_\mu^{1/4} k^{1/2}/\mu$ is greater than 11.63. If y^+ is less than this value, then a laminar expression is used. It is believed that this "patching" of the laminar expression for near wall grid points is highly inaccurate. Thus, to expect reasonable solutions from the FDNS2D code, wall functions must be employed, and this means that the computational mesh must be chosen so that the y^+ parameter is greater than 11.63.

Test Case. The test case used in this investigation is a simple flow over a flat plate. The fluid flowing is air, which approaches the plate with a Mach number $M = 6.42$ and a static temperature of $T = 258$ R. The specific case being studied is "Run 4" from a set of data collected at Calspan and published by Michael Holden [3]. To model his wind tunnel condition, the plate was treated as isothermal at a temperature of 540 R.

The computer mesh was generated using the GENIE3D program on the IRIS

workstations in the CFD branch (ED32) at MSFC. The mesh was coarse, with 121 equally spaced nodes in the lentghwise direction (x-direction) covering a distance of 3.75 feet, and 41 nodes in the cross-stream direction (y-direction) over a range of 0.5 feet. The mesh in the y-direction was graded using a hyperbolic tangent stretching scheme, with the node closest to the wall at a distance of 3.75E-5 feet. After solution of the problem, it was found that this y_p distance resulted in y^+ values in the range $23 < y^+ < 31$. This ensures that wall functions were utilized by the FDNS code.

The FDNS code produces an output file (the restart file, FORTRAN unit 9) which contains a table of all the solution variables at the nodal points. From these tabular values, and by making use of the wall functions as implemented in the program, the values of the wall shear stress, τ_w, and the wall heat flux, q_w, can be determined.

To judge the quality of these computations, comparison is made against the analytical solution of van Driest (from Shapiro [4]) for the wall shear stress, and against the experimental data of Holden [3] for wall heat flux. A plot of the friction coefficient $C_f = \tau_w / \frac{1}{2}\rho U_\infty^2$ versus distance along the wall is shown in Figure 1. As can be seen from that figure, the agreement between the FDNS predictions and the van Driest solutions is good. A plot of the wall heat transfer q_w versus distance along the wall is shown in Figure 2. The open circles, denoting the heat transfer predictions from the wall functions as implemented in the FDNS code, are seen to fall well below the experimental data of Holden.

Observations. Although the wall functions do an excellent job of modelling the wall shear stress for flow over a flat plate with high Mach numbers, the corresponding computations for wall heat flux are grossly in error. Therefore, the heat fluxes utilized in the FDNS code for boundary conditions are inaccurate. What this means, of course, is that the resulting temperature profiles in the fluid must be in error.

Is there hope? Given the poor result of the heat flux predictions from the FDNS code, and the fact that it is exactly these values that are needed in order to ultimately assess the effectiveness of film cooling in rocket nozzles, an alternative approach to computing the wall heat flux is desired. One method might be to scour the literature and find another representation for the wall function for the energy equation (there are many), but a simpler approach is suggested here. The method to be used is based on a Reynolds analogy.

For a compressible boundary layer (Shapiro [4], page 1100)

$$q_w = h(T_{aw} - T_w) \tag{1}$$

where T_{aw} is the *adiabatic wall temperature*, and T_w is the actual wall temperature. The adiabatic wall temperature is given by (Shapiro [4], page 1099)

$$T_{aw} = T_\infty + RU_\infty^2/2/c_p \tag{2}$$

which defines the *recovery factor*, R. ($R \approx 0.89$ for air.) The Reynolds Analogy, as suggested by Shapiro ([4], page 1100), and verified experimentally by Holden ([5],

Figure 12a), may be expressed as

$$\frac{C_f}{2} = \frac{\tau_w}{\rho U_\infty^2} \approx C_H = \frac{h}{c_p \rho U_\infty}. \qquad (3)$$

By combining these relations, the heat transfer may be inferred based on the wall friction as

$$q_w = \frac{\tau_w c_p}{U_\infty}(T_\infty - T_w) + \frac{\tau_w}{2}U_\infty R. \qquad (4)$$

This equation was used to reprocess the results from the previous execution of the FDNS code. The resulting values are plotted in Figure 2 as the open squares. As can be seen from the figure, the agreement with the experimental data from Holden is vastly improved over the strict application of the wall function.

Conclusions. The following conclusions can be drawn from this investigation:

- FDNS2D using wall functions does a good job of predicting τ_w for high speed boundary layer flows.

- FDNS2D using wall functions does a poor job of predicting q_w for high speed boundary layer flows.

- The Reynolds Analogy may be employed to obtain reasonable estimates of the heat fluxes based on the FDNS2D output.

- If FDNS2D is expected to give reasonable values for the temperature field in the fluid, modification of the existing wall function boundary condition will be necessary.

References

[1] Y. Chen, R. Farmer, and J. A. Freeman, "The use of variational principles in improving computational fluid dynamics methodology," Tech. Rep. SECA-TR-90-05, SECA, May 1990. prepared for NASA/MSFC, Contract NAS8-37408.

[2] B. E. Launder and D. B. Spalding, "Numerical computation of turbulent flows," *Computer Methods in Applied Mechanics and Engineering*, vol. 3, pp. 269–289, 1974.

[3] M. S. Holden, "A data base of experimental studies of shock wave/wall jet interaction in hypersonic flow," Tech. Rep., Calspan-UB Research Center, Buffalo, NY, April 1990.

[4] A. H. Shapiro, *The Dynamics and Thermodynamics of Compressible Flow*. Brown, 1954.

[5] M. S. Holden, "Shock wave-turbulent boundary layer interaction in hypersonic flow," Tech. Rep. 77-45, AIAA, January 24-26 1977. presented at AIAA 15th Aerospace Sciences Meeting.
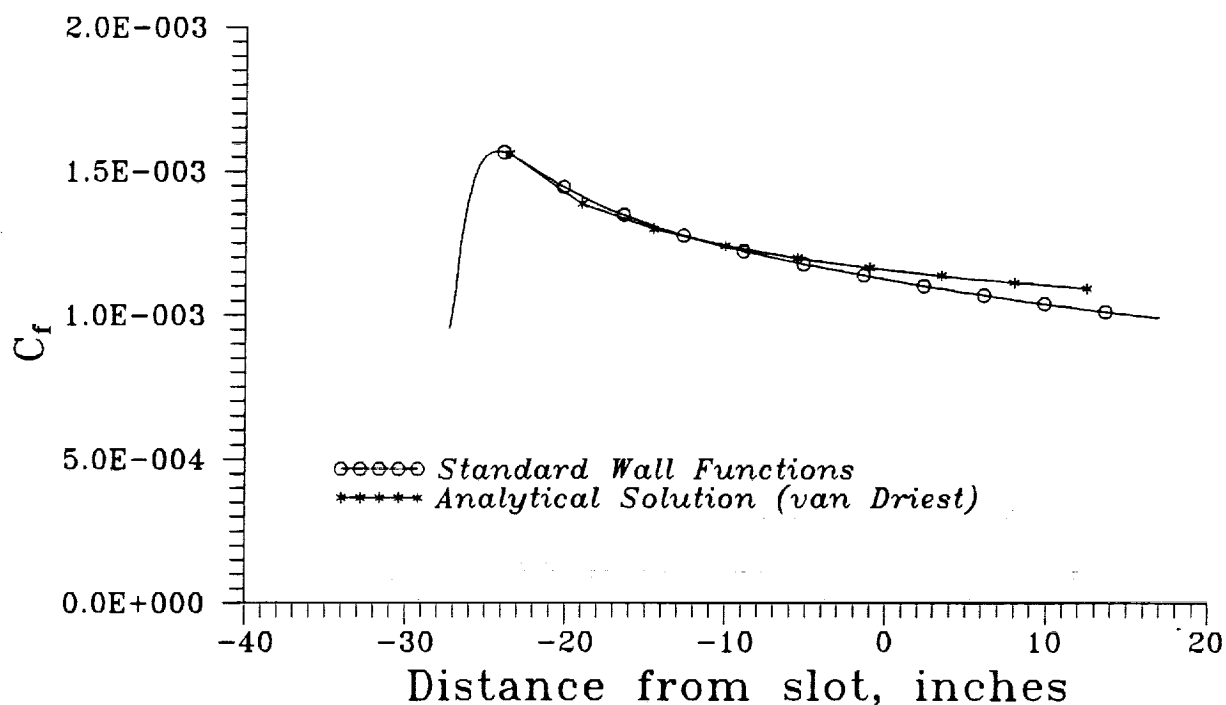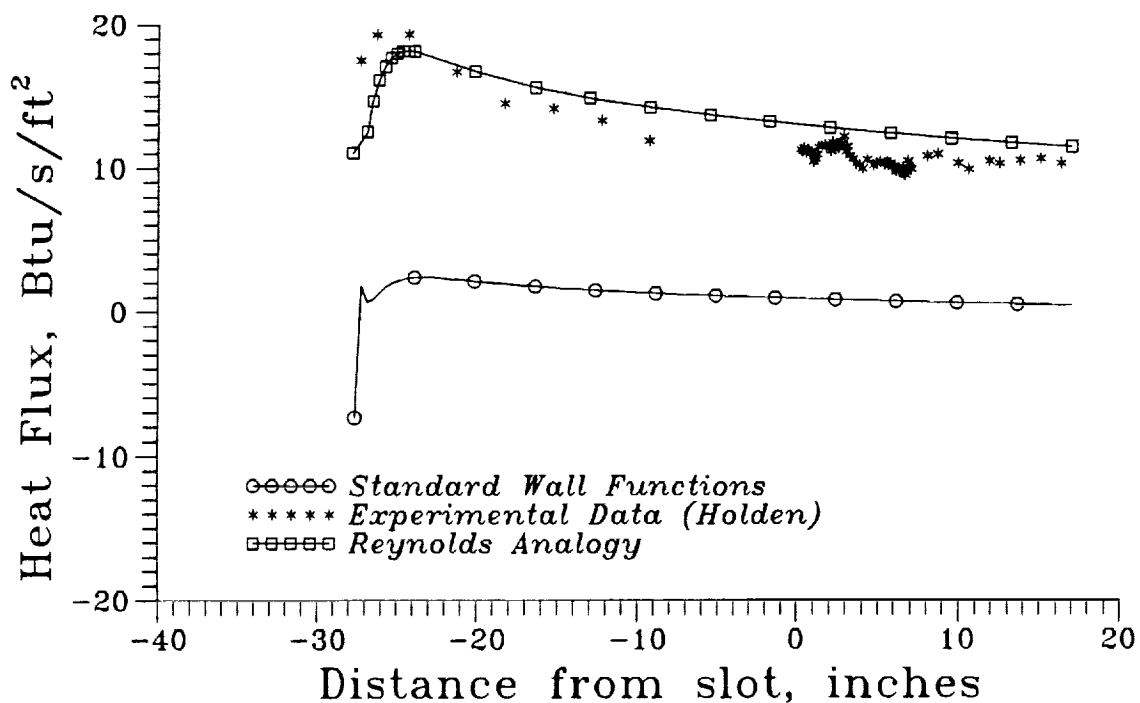
Figure 1: Surface Shear Stress Comparison

Figure 2: Surface Heat Flux Comparison

ZZ-4